Mid-Miocene explosive super-eruptions from the Yellowstone hotspot track: the rhyolitic ignimbrite record in south central Snake River Plain, Idaho, USA

Thesis submitted for the degree of

Doctor of Philosophy

at the University of Leicester

by

Thomas Ryan Knott MGeol

Department of Geology

University of Leicester

January 2014

Mid-Miocene explosive super-eruptions from the Yellowstone hotspot track: the rhyolitic ignimbrite record in south central Snake River Plain, Idaho, USA

Thomas Ryan Knott MGeol

Abstract

Explosive super-eruptions (≥450 km^3) are amongst the most catastrophic events at the Earth's surface, with immediate and devastating regional environmental consequences. Recent catastrophic super-eruptions at Yellowstone are well-known, but the previous (Miocene) history of large explosive eruptions from the Yellowstone hotspot is less-well understood, even though some in the central Snake River Plain (cSRP) may have been similar in size, or larger. To test this, local successions of rhyolitic welded ignimbrites in the southern cSRP have been studied to distinguish and characterise individual eruption-units using a combination of fieldwork, whole-rock and mineral chemistry, rock magnetism and geochronology data to correlate them regionally. In the Rogerson Graben, the revised Rogerson Formation comprises five eruption-units, each designated as a member. In the Cassia Hills ~20 km further east, the revised Cassia Formation comprises thirteen eruption-units, and a new deep drill-hole near Kimberly, reveals three rhyolitic eruption-units. Robust correlations between these sites and to the north of the Snake River Plain have revealed the presence of three new regionally widespread ignimbrite sheets: (1) the Brown's View Ignimbrite (10.3±0.2 Ma; 2700 km^2; 40 km^3 DRE); (2) the McMullen Creek Ignimbrite (9.0 ±0.1 Ma; 12,000 km^2; 589 km^3 DRE); and (3) the Grey's Landing Ignimbrite (~9.0 Ma; 18,000 km^2; 708 km^3 DRE).Using standard techniques to calculate eruption magnitudes, two of these record super-eruptions: the McMullen Creek eruption (magnitude 8.4, 1179 km^3 DRE) and the Grey's Landing eruption (magnitude 8.5, 1416 km^3 DRE). These represent the largest super-eruptions within the cSRP and are also among the largest eruptions of the entire Snake River-Yellowstone volcanic province. The addition of the three correlations presented here has further reduced the total number of previously inferred eruption-units from 42 to 29. Therefore, mid-Miocene rhyolitic explosive eruptions in the central Snake River Plain were less numerous but significantly larger than previously thought.

Acknowledgements

This thesis would not have been possible without the professional and personal support offered to me by the huge number of fantastic people who have surrounded me over the past four years.

Firstly, I would like to thank my supervisors Dr Michael Branney and Dr Marc Reichow for conceiving the project, and for accepting an unsuspecting student as your PhD researcher. Your continued advice, support, and enthusiasm throughout this work were much appreciated and I have very much enjoyed working with you both.

I would also like to say thank you to my colleagues David Finn and Rob Coe for their generous time spent out in the field, and for the excellent palaeomagnetic results they have produced. Thank you also to Mike McCurry for useful discussions out in the field, and a big thanks to him and his family for putting me up during my visits to Idaho State University. A number of others also deserve a grateful mention for their useful scientific discussions and analytical support, including: Andy Saunders, Mike Norry, Bill Bonnichsen, Rich Walker, Nick Marsh, Colin Cunningham, Rob Wilson, Michael Storey, Dan Barfod, and Andrew Tindle. Also, thank you to all my field and laboratory assistants I have had throughout this study, I'm sorry I cannot mention you all by name.

My long field seasons out in Idaho were made all the more pleasant due to my 'adoption' by my 'Idaho family'. Therefore, I would like to say a massive thank you to Tammie Aasa, and Janie, Brian, Whitney, Nathan, and the rest of the Castleberry family for their friendship and hospitality, and for all the laughs, food and beer a guy could ever ask for. In addition, fieldwork literally would not have been possible without the friendship of David and Butch Schwartz, thank you for taking such good care of the 'A-team van'.

I would also like to say thank you to my good friend Charlotte Watts for always laughing at my stupid jokes, and for keeping me sane in the last few months. Also, a massive thanks to my parents Nicola and Kevin Knott and my sister Charlotte for their constant love and support.

Finally, to my fiancée Helen; I could not have done this without you. Your love and support have been unwavering and thank you for sticking by this grumpy sod particularly towards the end. I love you so much.

Table of Contents

List of Figures

1. Introduction

Super-eruptions are amongst the most catastrophic events at the Earth's surface, with devastating regional environmental consequences and likely effects on global climate. But to assess their role in both crustal evolution and environmental change we need to know much more about their sizes, the eruption styles represented, and how frequently they occur.

It's well-known Yellowstone has erupted catastrophically in recent times (Christiansen, 2001), but perhaps less widely appreciated is that these were just the latest of a large number of super-eruptions that have burned a track along the Snake River eastwards from northern Nevada to Wyoming from 16 Ma to present (Pierce & Morgan; 2002). Some of the earlier eruptions may have been as large, or larger than Yellowstone, but we know astonishingly little about them, how many occurred, and their true extents. Despite being one of the Earth's most accessible, youngest and best-preserved silicic large igneous provinces most remains unstudied, un-mapped, and there is limited work that resolves the basic volcanic stratigraphy.

1.1. Research questions

This study forms part of a University of Leicester based investigation into "Scales and frequencies of Snake-River type super-eruptions of the Yellowstone hot-spot track, USA" (NERC grant NE/G005372/1), which has the following research questions:

(1) How large were Miocene super-eruptions in the Yellowstone–Snake River volcanic province?

(2) How many were there?

(3) How frequently did they occur?

(4) Do the eruption frequencies and volumes change over time? (e.g., is Yellowstone hotspot activity waning?)

This chapter highlights the global importance of 'super-eruptions' and their global frequencies, before summarising what is currently known about volcanism from the Yellowstone–Snake River volcanic province. Particular attention is paid to the central Snake River Plain (cSRP) where recent work suggests that volcanic activity in this region

may have been more voluminous than more recent volcanism at Yellowstone (Nash et al., 2006), and where records of 'super-eruptions' are starting to be identified (Ellis et al., 2012a). By building upon and identifying gaps in the previous work I have defined key objectives that are the main focus of my work (see section 1.9).

1.2. 'Super-eruptions': defining the largest-explosive eruptions on our planet

The term 'super-eruption' is becoming a commonly used term to describe large explosive eruptions that yield >450 km^3 of silicic magma and, along with asteroid impacts, are the largest catastrophic events that affect the Earth's surface (Sparks et al. 2005; Self, 2006). On the widely used Volcanic Explosivity Index (VEI), which is a measure of the explosiveness of an eruption, the largest eruptions on our planet are VEI 8 based on tephra volumes >1000 km^3 (Newhall & Self, 1982). However the VEI scale only considers 'bulk-volume' and fails to consider the density of the tephra deposits, which with different degrees of welding can range from 600 – >2000 kg m^{-1} (Mason et al., 2004). Therefore, a tephra deposit with a 'bulk-volume' of ~1000 km^3 may have a 'dense rock equivalent' (DRE) volume of ~600 km^3 and should not be classified as a VEI 8 eruption. Modern classification of the size of explosive eruptions is based on a logarithmic magnitude scale of erupted mass as defined by Pyle (1995, 2000). The magnitude scale (M) is defined by:

$M = \log_{10}(m) - 7.0$; where (m) is the erupted mass in kg.

Therefore it is preferable to define super-eruptions as events ≥M8, which have eruptive masses between 10^{15} – 10^{16} kg (Pyle, 2000; Mason et al., 2004).

1.3. Consequences, tectonic settings and frequency of 'super-eruptions'

Eruption of colossal volumes of tephra can occur within a few days (e.g., Sparks & Wilson, 1976; Wilson, 2001) with devastating regional and environmental effects. For example the ~74 ka Younger Toba Tuff eruption produced ~2800 km^3 of tephra, covering >1% of the Earth's surface with >10 cm of ash (Rose & Chesner, 1987). As a consequence large eruptions of this size have been shown to alter global climate and cause periods of significant global cooling (e.g. 'volcanic-winter' Rampino & Self, 1992, 2000; Self, 2006; Robock, 2005, 2013), and the Toba eruption has been attributed to the decline in human civilisation around 70 ka (Ambrose, 1998). The production and storage of such large volumes of magma, necessary to produce super-eruptions, also plays an

important role in crustal evolution and planetary differentiation (Bachmann & Bergantz, 2008) and events of this size have likely been occurring throughout Earth history.

Large explosive silicic eruptions are associated with various tectonic settings. Some are associated with continental break-up (e.g. the Chon Aike province of South America–Antarctic Peninsula, Pankhurst et al., 1998; Riley & Leat, 1999) and others are associated with continental convergent margins (e.g., the Taupo volcanic zone, Wilson et al., 1995; and the Sierra Madre Occidental, Mexico, Swanson et al., 2006). However, there is limited data on hotspot-related intra-plate silicic volcanism, despite a growing realisation that large-scale silicic volcanism may be an important component of many large igneous provinces (LIPs) across the globe and may be comparable to volumes of continental flood basalts (e.g. the Paraná-Etendeka province, Milner et al., 1995; Bryan et al., 2002).

The most recent collation of the largest eruptions on Earth totals 47 M8 explosive silicic eruptions, erupted between the Ordovician - Pleistocene, with 42 occurring within the past 36 Ma (Mason et al., 2004). However, as interest in super eruptions grows additional examples are being identified (e.g. in the Great Basin, USA, Best et al., 2013). Estimates of the frequency of super-eruptive events range from 1 eruption/50 ka (based on nine M8 eruptions over the past 2 Ma, Decker, 1990) to ≥1.1 eruptions/Myr (based on 42 M8 events over the past 36 Ma, Mason et al., 2004). Most super-eruptions occurred within two 'flare-ups' in global activity at 36–25 Ma and 13.5–0.6 Ma, and eruptive frequency within an individual flare-up can vary between 1.4–22 events/Ma (Mason et al., 2004). It is clear from these studies that to develop a better understanding of the global frequency of super-eruptions it is necessary to identify the deposits of more super-eruptions in the geological record, in particular super-eruptions at continental intra-plate settings.

To contribute to this, the present study investigates the Snake River–Yellowstone volcanic province, USA, one of the youngest (~16Ma–present) and best preserved silicic large igneous provinces, where super-eruptions have been both demonstrated and predicted (e.g., Bonnichsen et al., 2008; Ellis et al., 2012a).

1.4. Columbia River Basalts and the Yellowstone – Snake River volcanic province

For the past ~17 Ma, the inland northwest of North America has been the site of a large igneous province, herein referred to as the Yellowstone – Snake River volcanic province. The Yellowstone – Snake River volcanic province is arguably the best example of an

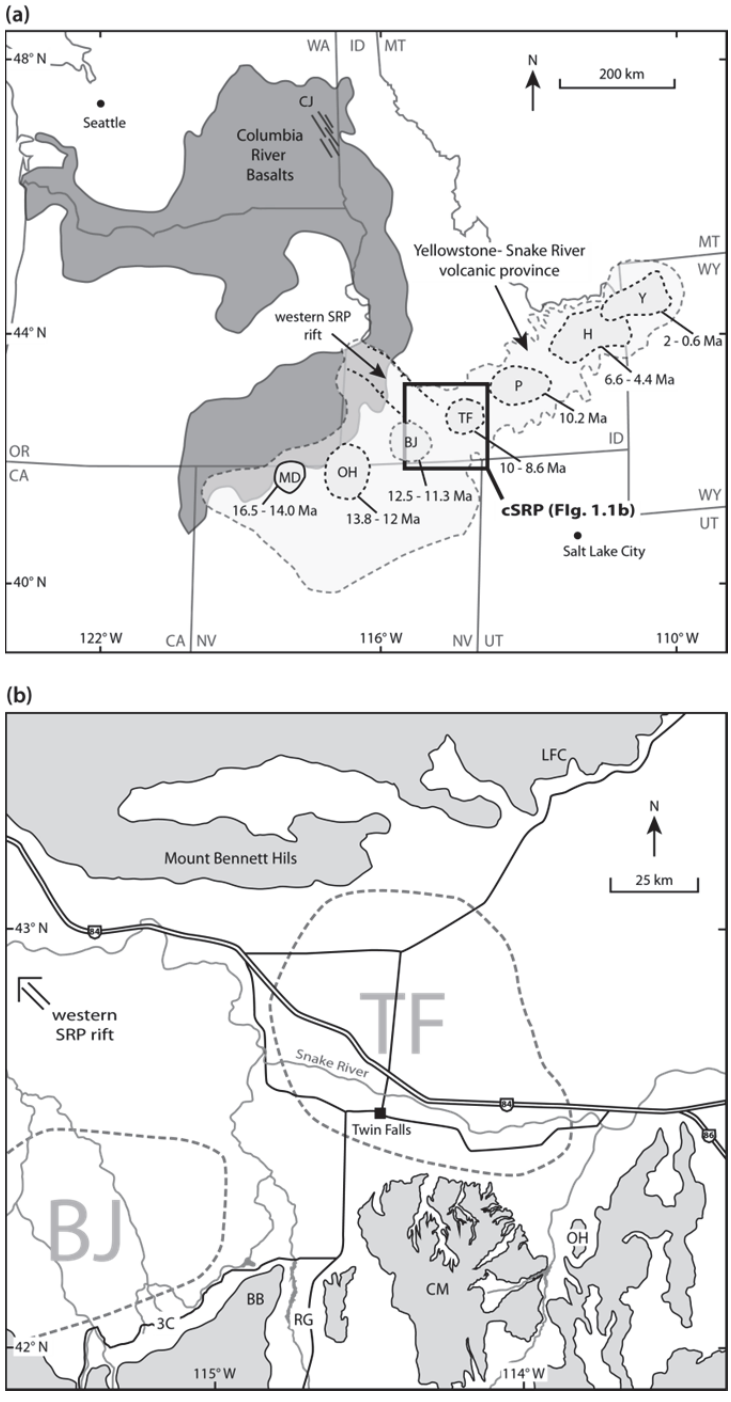

Figure 1.1. (a) The Yellowstone–Snake River bimodal volcanic province showing the central Snake River Plain (cSRP) and the locations of all proposed volcanic centres. Volcanics centres are termed: MD, McDermitt; OH, Owyhee-Humbolt; BJ, Bruneau-Jarbidge; TF, Twin Falls; P, Picabo; H, Heise; and Y, Yellowstone, after Bonnichsen et al (1989) and Morgan & McIntosh (2005). Dark grey area shows the extent of the Columbia River Basalts that erupted along the Chief Joseph (CJ) dyke swarm (Camp et al., 2003). **(b)** Simplified location map of the cSRP (study area of the present study) showing the locations of all place names mentioned in the text, including: 3C, Three Creek road; BB, Browns Bench massif; RG, Rogerson Graben; CM, Cassia Mountains; OH, Oakley Hills; and LFC, Little Fish Creek canyon.

intra-plate, continental hot-spot track (Morgan, 1971; Hall, 1996; Pierce & Morgan; 2002) and records time-transgressive, mid-Miocene–present, bimodal (rhyolite–basalt) volcanism that extends from northern Nevada across southern Idaho to Wyoming (Fig. 1.1a). The province is also associated with the voluminous Columbia River Basalts in Washington State, USA (Fig. 1.1a) which are thought to mark the inception of mid-Miocene volcanism in the northwest USA (Pierce & Morgan, 1992, 2002).

1.4.1. *The inception of volcanism in the Yellowstone-Snake River volcanic province*

Volcanic activity in the Yellowstone-Snake River volcanic province is thought to have begun around 16.6 Ma with the eruption of the Columbia River Basalts that form a plateau of voluminous (>230,000 km^3) basaltic lavas, covering large areas of southeast Washington State, northern and south-eastern Oregon and adjacent parts of western Idaho, and erupted along the NNW oriented Chief Joseph dike swarm (Fig. 1.1a) until ~6 Ma (Hooper et al., 2002; Camp et al., 2003; Reidal et al., 2013). During this 10.5 million year period ~98% of the total Columbia River Basalt volume is thought to have been emplaced in the first two million years (between 16.6–14.5 Ma, Swanson et al. 1979; Hooper et al. 2002; Barry et al., 2013). This rapid outpouring of basaltic magma is also broadly contemporaneous with silicic magma erupting over a wide region of southern Oregon and northern Nevada (Brueseke et al. 2008; Shervais and Hanan 2008; Brueseke and Hart 2009; Coble and Mahood 2012) along with peralkaline silicic volcanics erupting from the McDermitt caldera complex (Fig. 1.1a) from 16.5–14.0 Ma, which mark the earliest silicic volcanism of the NE-SW trending Yellowstone hot-spot track (Rytuba & McKee, 1984).

The inception and persistence of bimodal volcanism along the Yellowstone-Snake River volcanic province (from ~17 Ma to present) has often been attributed to an upwelling mantle plume (Armstrong et al. 1975; Engebretson et al., 1984; Pierce and Morgan 1992, 2002). The eruption of the Columbia River Basalts is thought to have been in response to the impact of the larger Yellowstone plume-head at the base of the North American lithosphere; with sustained volcanism along the Yellowstone hot-spot track attributed to the fixed Yellowstone-plume tail as the North American plate migrated to the west (Engebretson et al., 1984; Pierce & Morgan, 2002; Geist & Richards, 2013). However, it has been noted that the Columbia River Basalts lie north of the NE-SW projected trend of time-transgressive volcanism, and therefore more recent non-plume models have been invoked to explain the generation and eruption of large volumes of basaltic and silicic

magmas in the Yellowstone-Snake River volcanic province. Some have suggested that large volumes of melt may have been generated by enhanced back-arc convection due to rollback of the subducting Farallon slab and extension in the over-riding North American plate (Smith, 1992; Long et al., 2012), whereas others have invoked copious edge-driven convection around the margins of fragmented sections of the Farallon slab (James et al., 2011). More recent studies have indicated that the down-going Farallon slab may have simply deflected the Yellowstone-plume northwards and subsequently separated the plume-head from the plume-tail (Geist & Richards, 2013). This caused the synchronous eruptions of the Columbia River Basalts (melting of the voluminous plume-head) to the north and silicic magmas from the McDermitt eruptive-centre to the south (melting from the fixed plume-tail). Ultimately, the fundamental cause of volcanism in the Yellowstone-Snake River volcanic province remains contentious. However, all agree that the generation of voluminous silicic magmas, which are the primary focus of this thesis, require a significant thermal input from upwelling mantle-derived basalts that subsequently drives melting within the crust (Bonnichsen et al., 2008; Leeman et al., 2008; Watts et al., 2011). The resultant silicic melts may then be further modified by fractionation within shallower magma reservoirs (McCurry & Rogers, 2009).

1.4.2. Eruptive centres of the Yellowstone – Snake River volcanic province

After ~14 Ma, volcanic activity at the McDermitt eruptive-centre waned (Rytuba & McKee, 1984) and volcanism progressed along a north-eastward younging trend, which now defines the Yellowstone-Snake River volcanic province. Eruptions have been tentatively proposed to originate from six discrete 'eruptive centres' (Fig. 1.1a) located within the topographically depressed Snake River Plain (Pierce & Morgan, 1992). These eruptive centres are termed, from oldest to youngest: (1) the Owyhee Humbolt centre (Brueseke et al., 2004); (2) the Bruneau Jarbidge centre (Bonnichsen, 1982b); (3) the Twin Falls centre (McCurry et al., 1996); (4) the Picabo centre (Pierce & Morgan, 1992; Drew et al., 2013); (5) the Heise centre (Morgan & McIntosh, 2005); and (6) the Yellowstone volcanic field (Christiansen, 2001). To date, the only good evidence for calderas is within the Heise eruptive centre and the Yellowstone volcanic field, both of which are interpreted as a series of nested calderas (Christiansen, 2001; Morgan & McIntosh, 2005). In addition, the INEL-1 drill core, recovered on the margin of the Picabo eruptive-centre, revealed ~2.5 km of rhyolitic ignimbrite (Doherty et al., 1979) at least 2.1 km of which were deposited between 8.0–8.6 Ma and are thought to be evidence

for an intra-caldera fill sequence (McCurry and Rodgers, 2009). The older eruptive-centres in the central Snake River Plain (e.g., the Twin Falls and Bruneau-Jarbidge eruptive-centre) are extremely tentative as late stage basaltic lavas obscure any evidence for calderas in this region (Bonnichsen et al., 2008). However, present efforts are being made to find evidence for calderas in the Twin Falls eruptive centre (e.g., the Kimberly bore-hole, see Chapter 5; Shervais et al., 2013). Activity at each eruptive-centre included a period of explosive silicic volcanism that deposited voluminous rhyolitic ignimbrites, and associated fallout layers, exposed within canyons incised into topographic highs to the north and south of the Snake River Plain (e.g., Bonnichsen & Citron, 1982; Honjo et al., 1992; Williams et al., 1990; Cathey & Nash, 2004; Andrews et al., 2008; Ellis et al., 2010), followed by eruptions of rhyolitic lavas and later voluminous basalt lavas that filled the Snake River Plain (Bonnichsen et al., 2008).

1.5. 'Super-eruptions' and eruptive frequency of the Yellowstone volcanic field

The term 'super-eruption' was first coined in the Yellowstone–Snake River volcanic province (Bonnichsen, 2000) and following more recent BBC documentaries (e.g., "Super-volcano" in 2005) the Yellowstone volcanic field has become popularly associated with super-eruptions. The Yellowstone volcanic field has produced several large-explosive silicic eruptions over the past ~2 Ma, including: (1) the 2.1 Ma, 2500 km^3, Huckleberry Ridge Tuff; (2) the 1.3 Ma, 280 km^3, Mesa Falls Tuff; and (3) the 0.6 Ma, 1000 km^3, Lava Creek Tuff (Christiansen, 2001). The Huckleberry Ridge Tuff comprises three members (A, B and C), but recent age determinations have shown that Member C is an individual eruption-unit, thus the volume of the Huckleberry Ridge Tuff is reduced to 2210 km^3 (Ellis et al., 2012b; Ellis & Mark, 2013). Regardless, both the Huckleberry Ridge and Lava Creek Tuffs record magnitude 8 (M8) eruptions and are among the largest explosive eruptions on Earth (Mason et al., 2004).

The frequency of large explosive eruptions at Yellowstone, based on the last three, is approximately 1–2 eruptions/Ma. In comparison, eruption frequency in the older central Snake River Plain (cSRP) has been estimated as 10–20 eruptions/Ma (Nash et al., 2006). This ~4 Ma period (~12–8 Ma) of high eruption frequency has been termed an ignimbrite 'flare-up' in the cSRP (Nash et al., 2006; Bonnichsen et al., 2008), the onset of which coincides with the opening of the western Snake River Plain rift (Fig. 1.1a).

1.6. Rifting of the western Snake River Plain and its relation to the central Snake River Plain ignimbrite 'flare-up'

The western Snake River Plain rift is a 200 km long, 70 km wide fault-bound graben that trends NW-SE across south-western Idaho, USA and is thought to have formed as the result of NE-SW extension driven by magmatism of the Yellowstone-hotspot, between ~12–7 Ma (Wood & Clemens, 2002; Bonnichsen & Godchaux, 2002; Nash et al., 2006). The western Snake River Plain rift intersects the NE-SW trending Snake River Plain around the inferred Bruneau-Jarbidge and Twin Falls eruptive centres (Fig. 1.1a and b), and coincides with an increase in ignimbrite forming eruptions from these eruptive centres (Bonnichsen & Godchaux, 2002). The peak of this ignimbrite flare-up is best recorded by the 12.7–10.5 Ma, ~500 m-thick, Cougar Point Tuff succession thought to have erupted from the proposed Bruneau-Jarbidge eruptive centre (Bonnichsen & Citron, 1982; Cathey & Nash, 2004). The Cougar Point Tuff succession consists of ten intensely-welded rhyolitic ignimbrite eruption-units, that span the SW Idaho and NE Nevada border, and has associated ash-fall layers dispersed over much of the western interior of the USA (Perkins et al., 1998; Perkins & Nash, 2002; Cathey & Nash, 2004). A total of 14 ash-fall layers, including correlatives of the Cougar Point Tuffs, have been identified (Perkins & Nash, 2002). This suggests an average discharge rate of ~2800 km^3/Ma between 12.7 –10.5 Ma. This ignimbrite flare-up was also contemporaneous with an increased magmatic temperature (900 – >1000 °C) as estimated from deposits of the proposed Bruneau-Jarbidge and Twin Falls eruptive centres (Nash et al., 2006; Bonnichsen et al., 2008; Ellis et al., 2010). However, the full temporal and geographic extent of this ignimbrite flare-up is difficult to constrain as it is based on a record of individual eruptions defined in localised volcanic stratigraphies (e.g., the Cougar Point Tuffs and the Browns Bench stratigraphy, Bonnichsen et al., 2008; the Rogerson Graben stratigraphy, Andrews et al., 2008; the Cassia Mountains stratigraphy, Williams et al., 1990; Wright et al., 2002; Ellis et al., 2010, and others) some of which may be correlatives of one another, thus reducing the total number of explosive eruptions (Bonnichsen et al., 2008; Ellis et al., 2012a).

1.7. Identifying 'super-eruptions' in the central Snake River Plain (cSRP)

To determine the number, size and frequency of super-eruptions during the ~12 – 8 Ma ignimbrite flare-up more super-eruptions must first be identified within the established, localised, stratigraphies. However, hitherto, there have been limited attempts at

correlating individual ignimbrite sheets across the southern margins of the central Snake River Plain (Ellis et al., 2012a) and no correlations have yet been made across the Snake River Plain to massifs to the north.

The first attempt at grouping similar ignimbrites and lavas in the central Snake River Plain (cSRP) combined $^{40}Ar/^{39}Ar$ geochronology, whole-rock geochemistry and physical characteristics of ~95% of known rhyolitic ignimbrites and lavas in the cSRP to form 13 'composition and time' ('CAT') groups, which were defined based on progressively younger age ranges and similar ranges in TiO_2 (Bonnichsen et al., 2008). Magnetic polarity (determined in the field) also played a role, and where a single CAT group includes units with normal and reversed polarities it is further sub-divided (e.g., CAT group 10A and 10B, Bonnichsen et al., 2008). Each CAT group contains up to eight individual eruption-units and it has been suggested that some, or all, of the individual units within a single CAT group may in fact derive from single extensive rhyolitic sheets (Bonnichsen et al., 2008; Ellis et al., 2012a). Recently, three large-volume rhyolitic ignimbrites have been identified by correlating individual ignimbrite eruption-units along the south cSRP that are within CAT groups 5, 7 and 8 (Ellis et al., 2012a). These three ignimbrite sheets have been termed the 'Cougar Point Tuff XI' (11.41 ± 0.08 Ma), the 'Cougar Point Tuff XIII' (10.96 ± 0.07 Ma), and the 'Steer Basin Tuff' (10.66 ± 0.09 Ma) (Ellis et al., 2012a). Their dense rock equivalent (DRE) volumes were estimated as ~350 km^3 (Cougar Point Tuff XI), ~1,000 km^3 (Cougar Point Tuff XIII), and ~350 km^3 (Steer Basin Tuff). On the magnitude scale these are magnitude 7.9 (Cougar Point Tuff XI), 8.4 (Cougar Point Tuff XIII), and 7.9 (Steer Basin Tuff). All three are very large explosive eruptions and Cougar Point Tuff XIII is a super-eruption similar, if not larger, in magnitude to the Lava Creek Tuff super-eruption (Christiansen, 2001; Ellis et al, 2012a). However, to date, no correlations have been identified between the younger (~10.6–8 Ma) ignimbrites of the south cSRP and no correlations have been extended across the SRP to ignimbrites located in the north (e.g., the Mount Bennett Hills, Honjo et al., 1992; Bonnichsen et al., 2008).

1.8. Snake River-type volcanism – a brief review

Snake River (SR)-type volcanism is a recently described category of large-scale rhyolitic volcanism, defined on the basis of distinctive volcanic facies displayed by Miocene volcanic rocks in the central Snake River Plain (Branney et al., 2008). SR-type volcanic

facies are distinct from typical silicic volcanism described extensively in the literature (e.g., Cas & Wright, 1987; Branney & Kokelaar, 2002), and records unusual, voluminous and particularly environmentally devastating styles of eruption that remain poorly understood. However, Branney et al. (2008) highlighted that other examples of SR-type volcanism may have occurred in other volcanic fields, which includes deposits in; Etendeka-Paraná (Ewart et al. 1998); the English Lake District (Branney et al., 1992); and the Proterozoic Keewanawan volcanics of Minnesota, USA (Green & Fitz, 1993).

Compositionally, all SR-type rhyolites are metaluminous to slightly peraluminous with an anhydrous phenocryst assemblage of some or all of the following minerals: quartz, plagioclase, sanidine, pigeonite, augite, fayalite, ilmenite, magnetite and accessory apatite and zircon (Cathey & Nash, 2004; Bonnichsen et al., 2008; Andrews et al., 2008; Ellis et al., 2010, 2012a). In addition, SR-type rhyolites are also associated with a strong depletion in $\delta^{18}O$ (Ellis et al., 2013). Both SR-type ignimbrites and lavas have $\delta^{18}O$ values ranging between -1.2 and 4.8 ‰ (Boroughs et al., 2005, 2012), which is significantly lower than the 7–10 ‰ $\delta^{18}O$ of typical rhyolites (Boroughs et al., 2005).

SR-type lavas have been extensively described in the cSRP (e.g., Bonnichsen, 1982a; Ekren et al., 1984; Bonnichsen et al. 1989; Henry & Wolff, 1992; Manley & McIntosh, 2002) and are considerably more extensive (10's of km) and more voluminous (>10 km^3) than rhyolite domes and coulees typically associated with silicic volcanic fields elsewhere (Branney et al., 2008). They have low aspect ratios and extend for long distances (e.g., the >75km^3, Dorsey Creek Rhyolite extends for ~40 km, Bonnichsen, 1982a). The lavas are typically blocky, with thick (>5 m) upper and lower glassy auto-breccias separated by a devitrified lithoidal (microcrystalline) centre (Bonnichsen, 1982a). The lithoidal centres are dominantly flow-banded, and commonly exhibit columnar joints and sub-horizontal sheet joints that tend to follow the flow-banding (Bonnichsen, 1982a).

SR-type fall deposits (Fig. 1.2d) typically consist of millimetre-scale parallel laminations of fine–medium rhyolitic ash (Branney et al., 2008). Many contain glassy cuspate shards (1–5 mm in size) and some also contain layers of framework-supported ash coated pellets (Fig, 1.2c). Pumice lapilli fall deposits, that characterise many silicic volcanic fields elsewhere, are extremely rare in the cSRP (Branney et al., 2008). However, such deposits are exposed beneath the Grey's Landing ignimbrite (Andrews et al., 2008) and 'Cougar Point Tuff XV' (Bonnichsen & Citron, 1982).

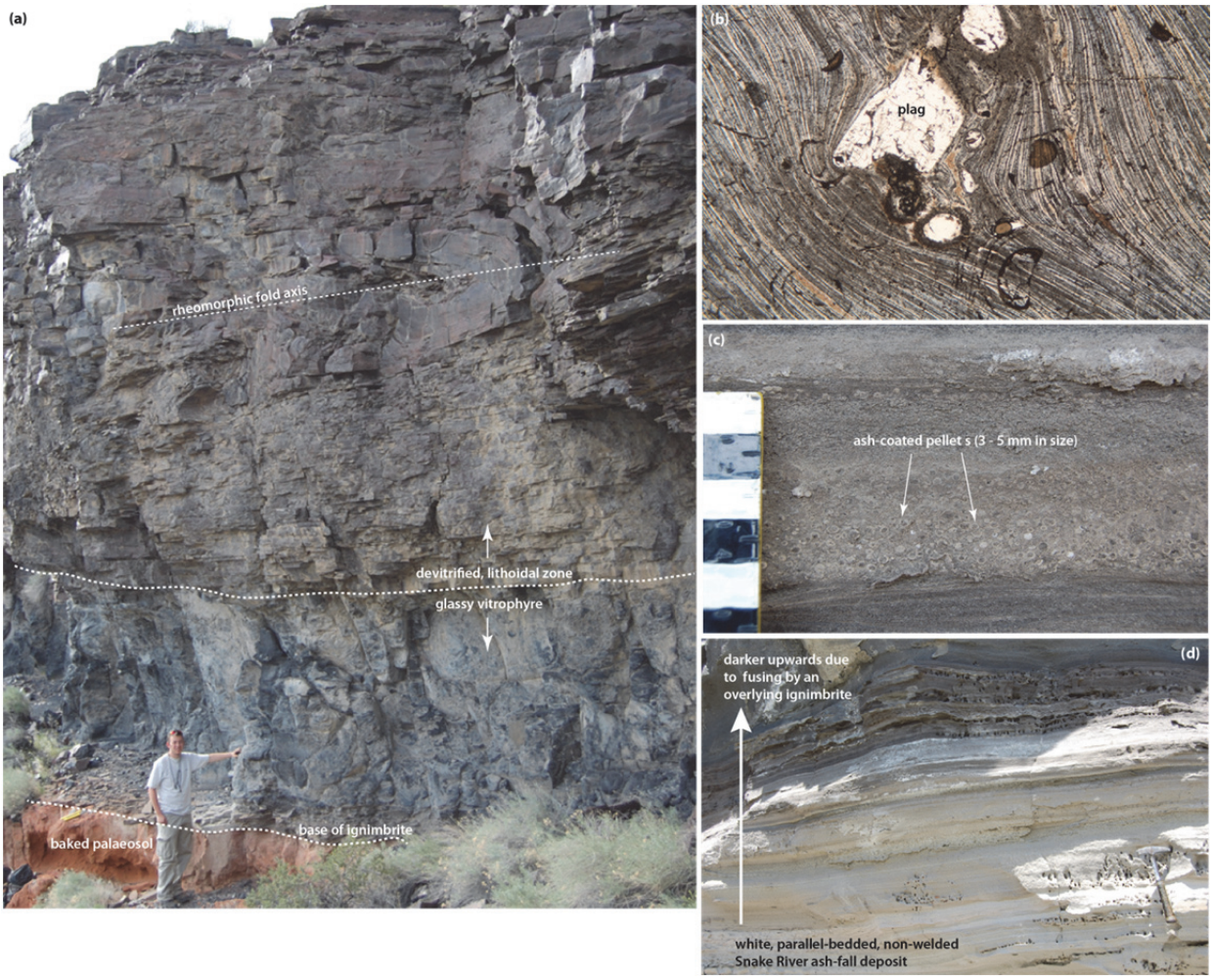

Figure 1.2. (a) A typical Snake River (SR)-type ignimbrite showing a black, glassy basal vitrophyre overlain by a devitrified lithoidal zone that typically contains metre-scale rheomorphic folds. Individual SR-type eruption-units are identified by a palaeosol below and above. **(b)** Individual glass shards are transposed and attenuated by rheomorphic deformation producing a flow-lamination, similar to that seen in silicic lavas, that wraps around phenocrysts. This has led to many SR-type ignimbrites being described as lava-like (Branney et al., 2008). **(c)** Some SR-type ash-fall deposits contain layers of ash-coated pellets (e.g., the Wooden Shoe Member, Cassia Mountains, see Chapter 4) that implies the involvement of water during eruption. **(d)** SR-type fall deposits are non-welded and parallel-laminated and are typically obscured under present slopes. Where overlain by SR-type welded ignimbrites these fall deposits are commonly fused and appear darker.

Welding of SR-type fall deposits is also varied, but the majority are non-welded and poorly exposed, obscured beneath modern grassy slopes (e.g., Andrews et al., 2008; Ellis et al., 2010). However, when in contact with intensely-welded, SR-type ignimbrites these deposits are commonly fused (Fig. 1.2d), but still preserve bedding (e.g., beneath the Grey's Landing ignimbrite, Andrews et al., 2008; Chapter 3.7).

SR-type ignimbrites are commonly intensely-welded (Branney et al., 2008) and are off the scale of welding intensity proposed by Quane and Russell (2005). This high degree of welding has been attributed to high magmatic temperatures (~900–1000 °C, Cathey &

Nash, 2004; Andrews et al., 2008; Ellis et al., 2010). As a result the intensely-welded ignimbrites are more resistant to erosion and form prominent cliff-forming rhyolitic units exposed on the southern and northern margins of the cSRP (Fig. 1.2a). Typical exposures consist of upper and lower black, glassy, vitrophyres separated by a lithoidal centre (Branney et al., 2008). In addition, devitrification features such as spherulites and lithophysae are also common at the contacts been glassy and devitrified zones. Both pumice and lithic lapilli are extremely rare in SR-type ignimbrites (Branney et al., 2008; Andrews et al., 2008; Ellis et al., 2010), which are well sorted compared to conventional ignimbrites elsewhere (e.g., the massive lapilli tuffs of the Poris Formation, Tenerife, Brown & Branney., 2013). Many are also highly rheomorphic (e.g., the Grey's Landing ignimbrite, Andrews et al. 2008) and preserve microscopic to metre-scale rheomorphic folds. Primary vitroclastic textures are usually not visible in the field, however petrographic observation of upper and lower glassy vitrophyres often reveals cuspate glass shards and/or broken phenocrysts, which are indicative of a pyroclastic origin (e.g., Fisher & Schminke, 1984; Allen & McPhie; 2003). However, these shards are commonly deformed due to progressive aggradation and rheomorphic deformation of SR-type ignimbrites during their emplacement (Branney et al., 2008; Andrews et al., 2008). This leads to the development of a eutaxitic foliation or flow banding depending on the degree of deformation (Fig. 1.2b). The paucity of macroscopic vitroclastic textures and the presence of pervasive flow banding means that some SR-type ignimbrites have been described as lava-like (*sensu* Branney & Kokelaar, 1992), and some have been interpreted as rhyolitic lavas (e.g., the Three Creek Rhyolite, Bonnichsen, 1982a) only to be revised as ignimbrites in subsequent studies (e.g., the Three Creek ignimbrite, Bonnichsen et al., 2008). Criteria for discriminating between lava-like ignimbrites and rhyolitic lavas, in the cSRP, include the preservation of vitroclastic textures (e.g., glass shards, broken phenocrysts, and entrained pyroclasts) that indicate an ignimbrite, and the presence of a basal auto-breccia that typify SR-type lavas (Andrews et al., 2008; Branney et al., 2008).

1.9. Research objectives

This thesis considers the following research questions:

(1) How large were super-eruptions in the central Snake River Plain (cSRP)?

(2) How many were there?

(3) How frequently did they occur?

(4) How do they compare with eruption volumes and frequencies from the Yellowstone volcanic field?

Previous work has established numerous, localised, volcanic stratigraphies (e.g., the Cougar Point Tuffs and the Browns Bench stratigraphy, Bonnichsen et al., 2008; the Rogerson Graben stratigraphy, Andrews et al., 2008; the Cassia Mountains stratigraphy, Williams et al., 1990; Wright et al., 2002; Ellis et al., 2010; and others) and efforts have been made to establish the existence of super-eruptions originating from the cSRP (Bonnichsen et al., 2008; Ellis et al., 2012a). However, in order to gain a more complete understanding of the number, scale and frequency of super-eruptions originating from this region it is necessary to identify additional examples within the younger volcanic stratigraphies. In order to achieve this, the present study highlights the following research objectives:

(1) To document and interpret local volcanic stratigraphies in the southern cSRP, with particular attention paid to the stratigraphy of the Rogerson Graben and the Cassia Mountains, Idaho.

Individual eruption-units in these areas will be described and characterised. Previous accounts of these local stratigraphies (Williams et al., 1990; Wright et al., 2002; Andrews et al., 2008; Ellis et al., 2010) give a good volcanic frame work, but there are still several gaps in understanding (e.g., the number of individual eruption-units). These local stratigraphies will be revised, enabling comment on the petrogenetic history and/or the tectonic history of these areas. However this is not the primary focus of this thesis.

(2) To document and interpret the volcanic stratigraphy revealed by the new Kimberly deep drill-hole, in southern Idaho, with the aim to correlate these with volcanic successions exposed elsewhere and identify any potential caldera-fills.

Hitherto, no caldera has been identified within the cSRP. Ignimbrites in the south cSRP have been inferred to originate from the proposed Bruneau-Jarbidge and Twin Falls eruptive centres (e.g., Bonnichsen et al., 2008). Therefore the existence of intra-caldera deposits and their inclusion in eruption volume estimates for individual eruptions has always been inferred (e.g., Ellis et al., 2012). If a caldera fill can be identified within the

Kimberly bore hole it would be the first proof of a caldera in the cSRP, and would provide constraints on the volumes of intra-caldera ignimbrites.

(3) To develop a multi-technique approach to correlating ignimbrite eruption-units, where such correlations are not possible by conventional field volcanological techniques.

The monotonous nature of SR-type ignimbrites (e.g., intense-welding and lack of distinctive pumice or lithic lapilli) means that individual eruption-units are difficult to identify and correlate by conventional, field-based, methods (e.g., Hildreth & Mahood, 1985). Therefore, the present study utilises a multi-technique approach including detailed fieldwork, whole-rock and mineral chemistry, and palaeomagnetic and geochronology data in order to identify and characterise individual eruption-units (Chapter 2).

(4) To use (1)-(3) to correlate between local volcanic successions in the cSRP and thereby establish, for the first time, the areas covered, volumes and masses of post-10.6 Ma very large rhyolitic eruptions.

The three voluminous eruptions defined by Ellis et al. (2012a) demonstrate that large volume 'super-eruptions' did originate from the cSRP. The primary objective of this thesis is to investigate whether 'super-eruptive' events are expressed in the younger volcanic stratigraphies between ~10.6–8 Ma. If individual ignimbrite eruption-units can be correlated then new super-eruptions may be identified. This will also contribute significantly to the regional stratigraphy and facilitate comments on the overall volcanic activity of the cSRP and how this compares to activity in the Yellowstone volcanic field over the past ~2 Ma.

2. Methodology: a multi-technique approach to correlating Snake River-type eruption-units

In order to establish volumes of potentially wide-spread SR-type tephras in the central Snake River Plain (cSRP) individual eruption-units must be classified and 'finger-printed' in order to allow correlation between them. In many other volcanic fields individual eruption-units are correlated by using fall-deposits as stratigraphic markers, as the internal characteristics of these deposits are much more predictable over large distances (Branney & Kokelaar, 2002). However, the limited exposure of fall deposits in the cSRP means that the primary focus of this study is on the better exposed SR-type ignimbrites.

Early reviews highlight some of the challenges that are faced when correlating ignimbrites (Hildreth & Mahood, 1985) and conclude that distinctive pumice and lithic lapilli and phenocrysts are among the best diagnostic criteria, as are high-precision ages and thermal remnant magnetic (TRM) directions. Recent reviews on correlating tephras, for the purpose of tephrochronology, have indicated that 'finger-printing' tephras is better achieved by utilising micro analytical techniques of phenocrysts and/or matrix glasses (Lowe, 2011). This principle has been successfully demonstrated in distinguishing between multiple ignimbrites in the northern Pannonian Basin, Eastern-Central Europe (Harangi et al., 2005). Some studies have demonstrated that high precision $^{40}Ar/^{39}Ar$ dating alone is capable of distinguishing between individual ignimbrite sheets (e.g., the Huckleberry Ridge Tuff in the Yellowstone volcanic field, Ellis et al., 2012b), and subsequent studies have argued that while high-precision ages are important, ignimbrites can be successfully correlated by their characteristic palaeomagnetic directions (Ort et al., 2013). However, it has been concluded that ignimbrite correlations are ultimately strengthened by combining multiple analytical techniques (Hildreth & Mahood, 1985; de Silva & Francis, 1989).

In the cSRP the sheer scale of the study area (~18,000 km^2) means that correlations must be attempted between ignimbrites exposed in localised successions some 20–100 km apart (Fig. 1.1b). In addition, the monotonous nature of SR-type ignimbrites (e.g., intense-welding and the lack of pumice and lithic lapilli) means that individual eruption-units are difficult to identify and correlate by conventional, field-based, methods (e.g., Hildreth & Mahood, 1985). Studies in the cSRP have therefore utilised multiple-techniques including $^{40}Ar/^{39}Ar$ geochronology, whole-rock and mineral chemistry and

palaeomagnetic polarity in order to correlate individual ignimbrite sheets (Ellis et al., 2012a).

In summary, what is clear from studies conducted in the cSRP, and other volcanic fields around the globe, is that robust correlations between ignimbrites can only be achieved by combining supportive evidence from as many analytical techniques as possible. Therefore the present study utilises detailed field observations, whole-rock and mineral chemistry, palaeomagnetic data (polarity and mean flow directions) and geochronology data in order to characterise and correlate these particularly challenging SR-type ignimbrites. These techniques are briefly outlined below and full methodologies are provided in Appendix B.

2.1. Field characterisation

A total of 32 weeks fieldwork was conducted in southern Idaho, USA in order to revise and characterise individual eruption-units in the southern cSRP. Individual eruption-units were identified on the basis of a palaeosol above and below (i.e., unconformity-bound units, after Salvador, 1994). This means that any ash-fall deposits and ignimbrites between two palaeosol horizons are considered part of the same eruption. In addition, each eruption unit was described and logged with particular attention paid to any variations in welding, phenocryst content and phases, and other rare distinctive physical features (e.g., glass shards, and any distinctive pumice and lithic lapilli). Individual eruption-units were logged at multiple localities with increasing distance away from the Snake River Plain in order to access any lateral variations in their distinctive features.

2.2. Whole-rock geochemistry

Whole-rock samples were collected across all eruption-units discussed in this thesis, and were prepared for X-ray fluorescence (XRF) spectrometry and analysed on a PANalytical PW4400 Axios XRF spectrometer at the University of Leicester. Major element concentrations were determined on glass fusion beads and trace element concentrations were determined on pressed powder pellets (see Appendix B.1).

2.3. Mineral geochemistry

Phenocryst compositions were determined on 30 micron carbon-coated thin sections cut from representative samples of each eruption-unit. Major element concentrations were determined by Electron Microprobe Analysis (EMPA) and phenocrysts were analysed on a Cameca SX100 electron microprobe at the Open University, Milton Keynes (see

Appendix B.2). Trace element concentrations were also determined on phenocrysts from select units during a pilot study to determine their usefulness when attempting to discriminate between eruption-units. Trace element concentrations were determined by Laser Ablation-Inductively Coupled Plasma-Mass Spectrometry (LA-ICP-MS) and phenocrysts were analysed using a NewWave UP-213, 213 nm laser ablation system, and a Thermo X Series 2 Inductively Coupled Plasma-Mass Spectrometer at Idaho State University, USA (see Appendix B.3).

2.4. $^{40}Ar/^{39}Ar$ feldspar and U-Pb zircon geochronology

Samples for argon geochronology were collected from all rhyolitic units of the Kimberly borehole, and three members of the Cassia formation were selected for the secondary ion mass spectrometry (SIMS) measurements on zircon. Full analytical methods and data reduction are described in Appendix B.4 and B.5.

Argon measurements were carried out by laser fusion on individual feldspar at the NERC Argon Isotope Facility at the Scottish Universities Environmental Research Centre (SUERC), East Kilbride, UK. Experiments were conducted by Dan Barfod and data collected on an ARGUS 5-collector mass spectrometer. All argon ages referred to in this study (new and published) are relative to the age of the Fish Canyon sanidine monitor with a recommended age of 28.172 ± 0.028 Ma determined by Rivera et al. (2011).

U-Pb dating of zircons was performed at the Edinburgh Ion Microprobe Facility (EIMF) using the CAMECA IMS-1270 ion microprobe and using GJ-1 as the reference zircon.

2.5. Palaeomagnetic polarity and mean flow directions

Palaeomagnetic polarity and mean flow directions of all units mentioned in this thesis were determined on ~1000 orientated drill cores (10 cm in length) taken across all units mentioned in this thesis, with an average of 12 cores taken from any one unit. All Laboratory work was conducted, and subsequent data provided, by David Finn and Rob Coe working at the University of California, Santa Cruz (Appendix B.6).

3. Rhyolitic volcanic succession of the Rogerson Formation in southern Idaho USA, and constraints on the tectonic evolution of the Rogerson Graben.

3.1. Introduction

The Rogerson Graben is a significant N–S trending basin in southern Idaho that extends into northern Nevada (Fig. 3.1). It is thought to have formed due to approximately east-west extension, and likely coincides with the opening of the western Snake River Plain rift (Bonnichsen & Godchaux, 2002). The graben is bounded to the east and west by topographic highs made up of gently west-dipping rhyolitic ignimbrites. The western margin is a prominent fault scarp (~400 m relief), termed the Browns Bench escarpment (Bonnichsen et al., 2008), which exposes eight ignimbrites of the Browns Bench stratigraphy (Bonnichsen et al., 2008). To the east a second dominant fault, here termed the Shoshone Hills fault separates the graben from the topographically higher Shoshone Hills (Fig. 3.1). The graben is open to the north where it is buried by later basalt lavas, and to the south where it joins a wider basin stretching south of Jackpot, Nevada (Fig. 3.1). Throughout its development the Rogerson Graben was infilled by Miocene silicic volcanics that were previously thought to be part of the Idavada volcanic group (Malde & Powers, 1962).

The first interpretation of the volcanic stratigraphy within the graben identified that the Miocene volcanics consisted of dominantly Snake River-type ignimbrites and associated ash deposits, thought to have originated from the central Snake River Plain (cSRP), and these were divided into seven individual rhyolitic eruption-units and subsequently designated as members of the Rogerson Formation (Andrews et al., 2008). From stratigraphically oldest to youngest these members were termed: the Jackpot Member, the Rabbit Springs Member, the Brown's View Member, the Backwaters Member, the Grey's Landing Member, the Coyote Creek Member and the Sand Springs Member (Andrews et al., 2008).

3.2. Rationale

The purpose of the present study was to define the characteristic features of each eruption-unit, in order to 'finger-print' them, with the aim to correlate these eruption-

units with other silicic eruption-units exposed across the central Snake River Plain (cSRP). However, by combining field mapping and logging with whole-rock and mineral chemistry and some palaeomagnetic data potential discrepancies with the pre-existing Rogerson Formation stratigraphy (of Andrews et al., 2008) have been identified. The present study therefore redefines the volcanic stratigraphy and reduces the number of eruptions, recorded by the Rogerson Formation, from seven to five eruption-units. The established nomenclature (of Andrews et al., 2008) has been maintained for simplicity. The revised members of the Rogerson Formation (Fig. 3.2) are herein termed; the Jackpot Member, the Rabbit Springs Member, the Brown's View Member, the Backwaters Member and the Grey's Landing Member. Formal descriptions of each eruption-unit as well as supporting evidence for these revisions are presented below.

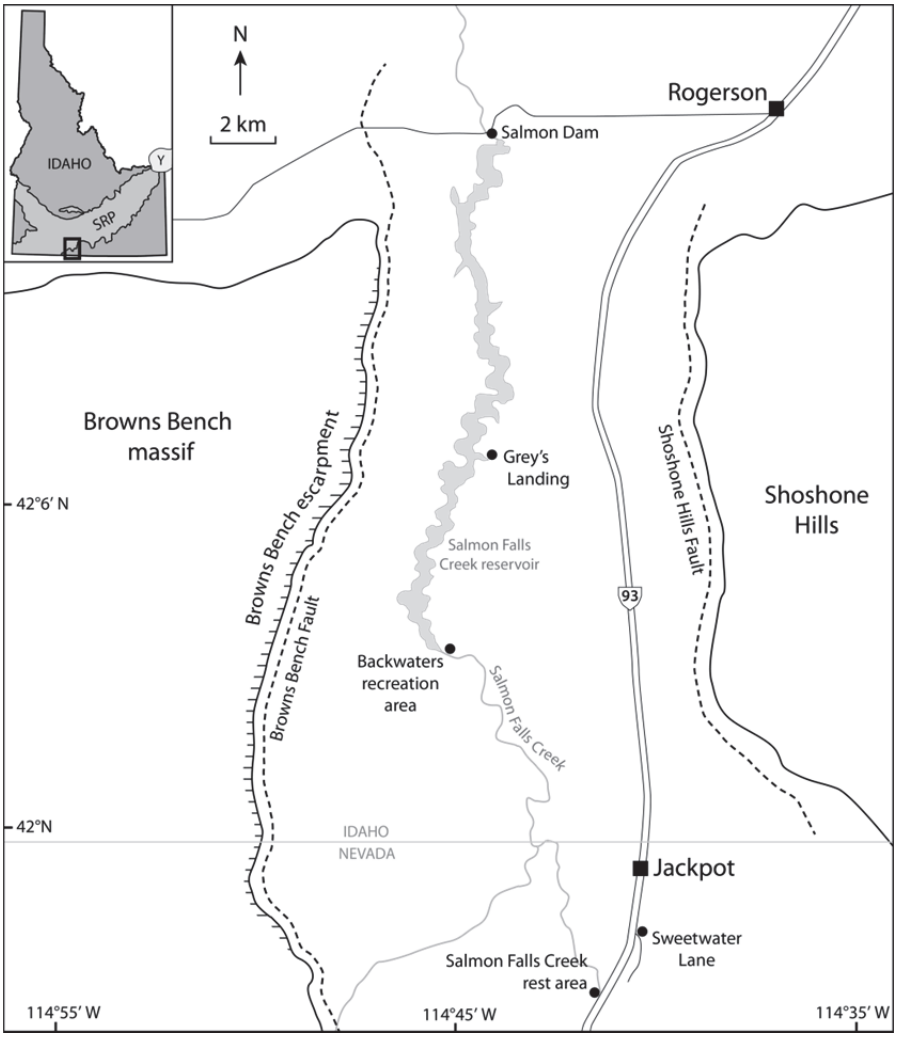

Figure 3.1. Simplified location map of the Rogerson Graben and surrounding areas showing all towns, and place names mentioned in the text. Inset: Location of the Rogerson Graben (black square) in relation to the Snake River Plain (SRP) in southern Idaho, Y = Yellowstone volcanic field.

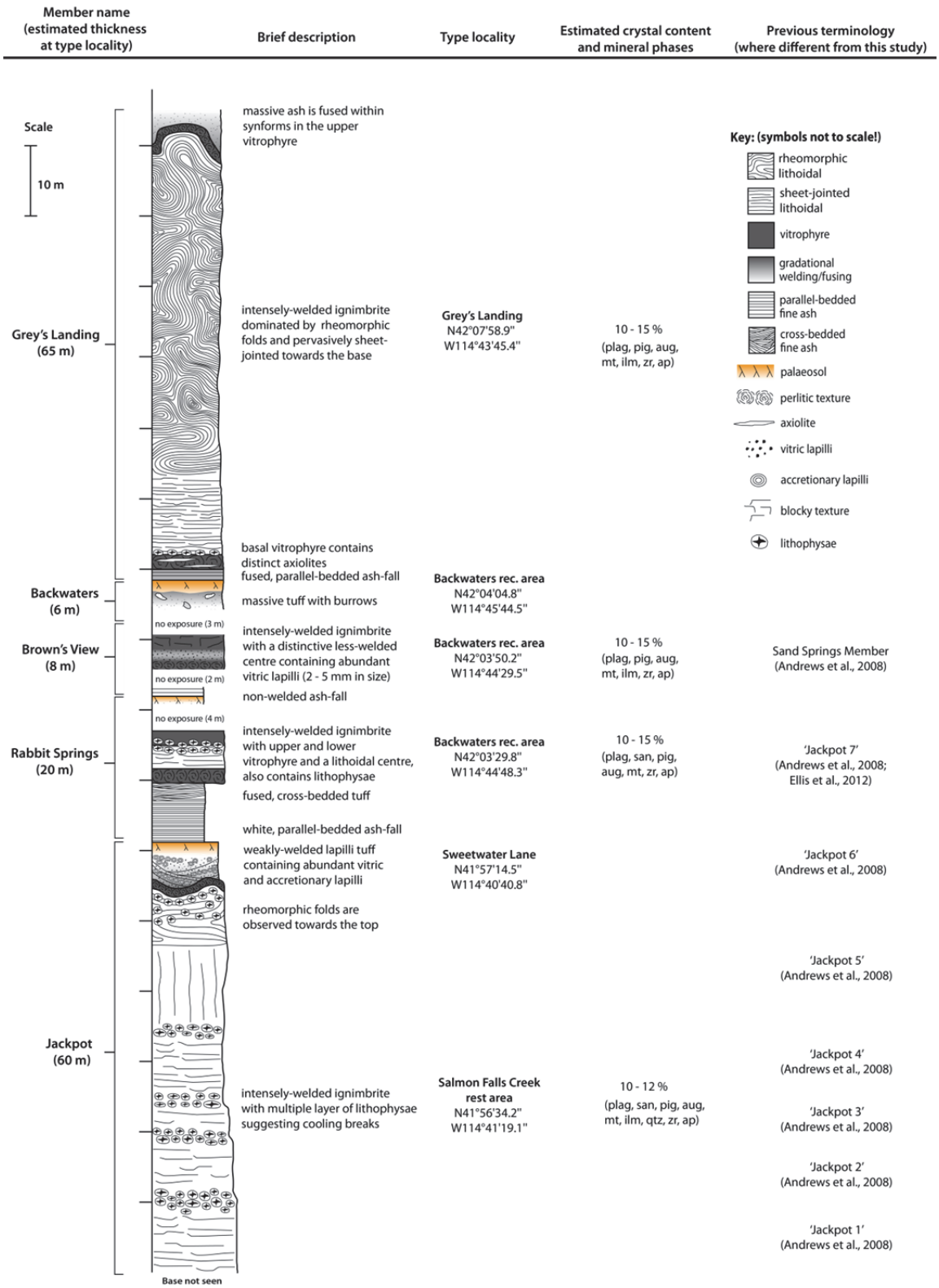

Figure 3.2. Generalised vertical section of the Rogerson Formation showing the main physical features of each of the five members. Phenocryst abbreviations are: plag – plagioclase, pig – pigeonite, aug – augite, mt – magnetite, ilm – ilmenite, qtz – quartz, zr – zircon, ap – apatite.

3.3. The Jackpot Member

The Jackpot Member is an intensely-welded rhyolitic ignimbrite and is the oldest member of the Rogerson Formation (Andrews et al., 2008). The member was previously subdivided into seven informal sub-units on the basis of multiple layers of lithophysae, interpreted as brief cooling breaks (Andrews et al., 2008). These sub-units were informally named 'Jackpots 1–7' (Andrews et al., 2008, Fig. 3.2). However, a subsequent study has grouped these sub-units and suggested that the Jackpot Member records two separate eruption-units (Ellis et al., 2012a). For example, Jackpots 1–6 were correlated as part of the 'Cougar Point Tuff XIII' and Jackpot 7 was correlated as part of the 'Steer Basin Tuff', both of which are recently defined widespread ignimbrite eruption-units (Ellis et al., 2012a).

Although the present study agrees with the interpretation (of Ellis et al., 2012a) that Jackpots 1–6 represent a single albeit pulsed eruption-unit, whole-rock data (section 3.8, Fig. 3.15b) and palaeomagnetic mean flow directions (Finn & Coe, unpublished, Fig. 3.3) obtained on sub-units 1 and 5 at the type locality (Salmon Falls Creek rest area, south of Jackpot, Nevada, Fig. 3.1) differ. This may suggest that Jackpots 1–5 potentially record two discrete eruption-units. However, this difference is only recorded at the type locality and based on very limited data is therefore considered insufficient evidence for any subdivision of the Jackpot Member. Thus, the division into discrete sub-units as suggested by Andrews et al. (2008) is deemed unnecessarily complex and Jackpots 1–6 are redefined as a single, ~60 m thick eruption-unit termed the Jackpot Member for the purpose of this study (Fig. 3.4).

With regards to Jackpot 7, this sub-unit was previously thought to underlie the younger Rabbit Springs Member (Andrews et al., 2008). However, detailed field observations, whole-rock and mineral chemical data and palaeomagnetic data presented here (see section 3.4.2) strongly support the reinterpretation of Jackpot 7 as a lateral extension and correlative of the Rabbit Springs Member.

3.3.1. Description

At the type section (Fig. 3.4 inset) the Jackpot Member is ~50 m thick massive tuff (base not seen) and consists of red-brown lithoidal rhyolite throughout. The lower 35 m is pervasively sheet jointed with multiple 1–2 m thick layers of lithophysae at different heights through the member (Fig. 3.4). Upwards the member has well-developed

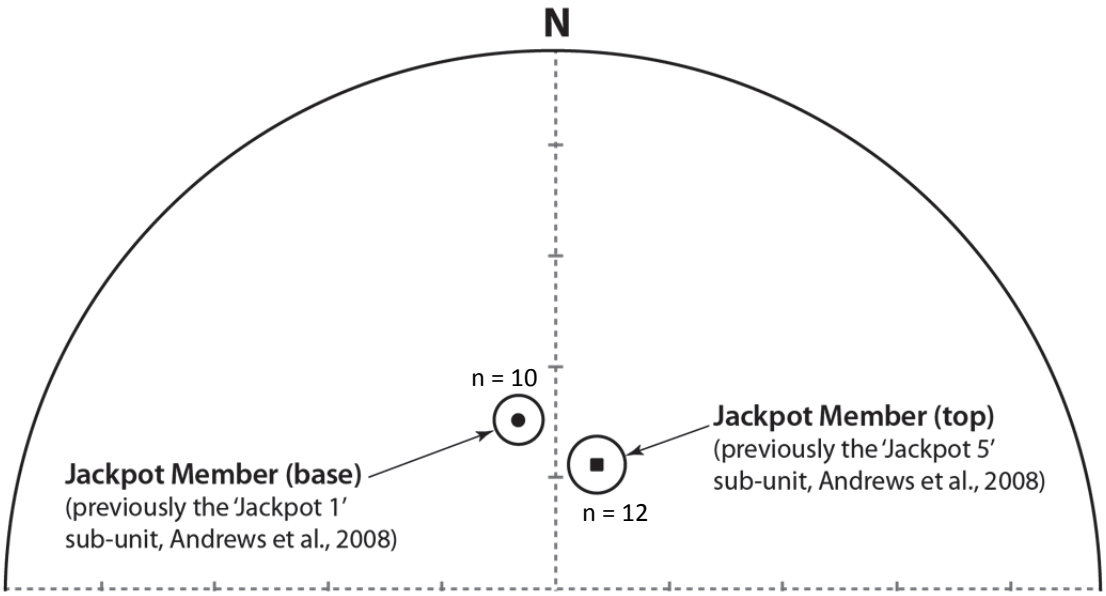

Figure 3.3. Stereonet showing the differing palaeomagnetic mean flow directions (black symbols with error circles) between the base and top of the Jackpot Member at its type locality at Salmon Falls Creek rest area.

columnar joints, which are less pronounced in the upper 10 m where metre-scale rheomorphic folds are dominant (Fig. 3.4). Above, a ~15 m gap in exposure is inferred to conceal the upper parts of the Jackpot Member, which are better exposed 2 km further north at Sweetwater Lane (Fig. 3.1). Here the rheomorphic lithoidal zone is ~3 m-thick and contains abundant spherulites and lithophysae that extend into the sharply overlying 2 m-thick upper vitrophyre (Fig. 3.5a). Some of these lithophysae are also infilled with lime-green chalcedony. The upper vitrophyre is overlain by a diffusely cross-bedded, less-welded, lapilli-tuff (Fig. 3.5b). The lapilli tuff was previously defined as the Jackpot 6 sub-unit (Andrews et al., 2008) and is the most characteristic feature of the Jackpot Member. It is distinctively orange in colour; however the lower 20 cm are grey due to back-fusing by the underlying intensely-welded zone. It also varies in thickness from 2–3 m-thick as it infills underlying rheomorphic synforms and antiforms (Fig. 3.4). It also contains abundant black, non-vesicular, vitric lapilli (5–10 mm in size) and accretionary lapilli (≤1 cm in diameter) that are concentrated into lenses where the member is cross-bedded (Fig. 3.5c). Upwards the lapilli-tuff develops into a palaeosol, which is better exposed further north at the Backwaters recreation area (Fig. 3.1), and is sharply overlain by the Rabbit Springs Member.

Crystal content is estimated at 10–12 % (0.5–3 mm crystals) and is consistent throughout the Jackpot Member. Phenocrysts comprise a mineral assemblage of

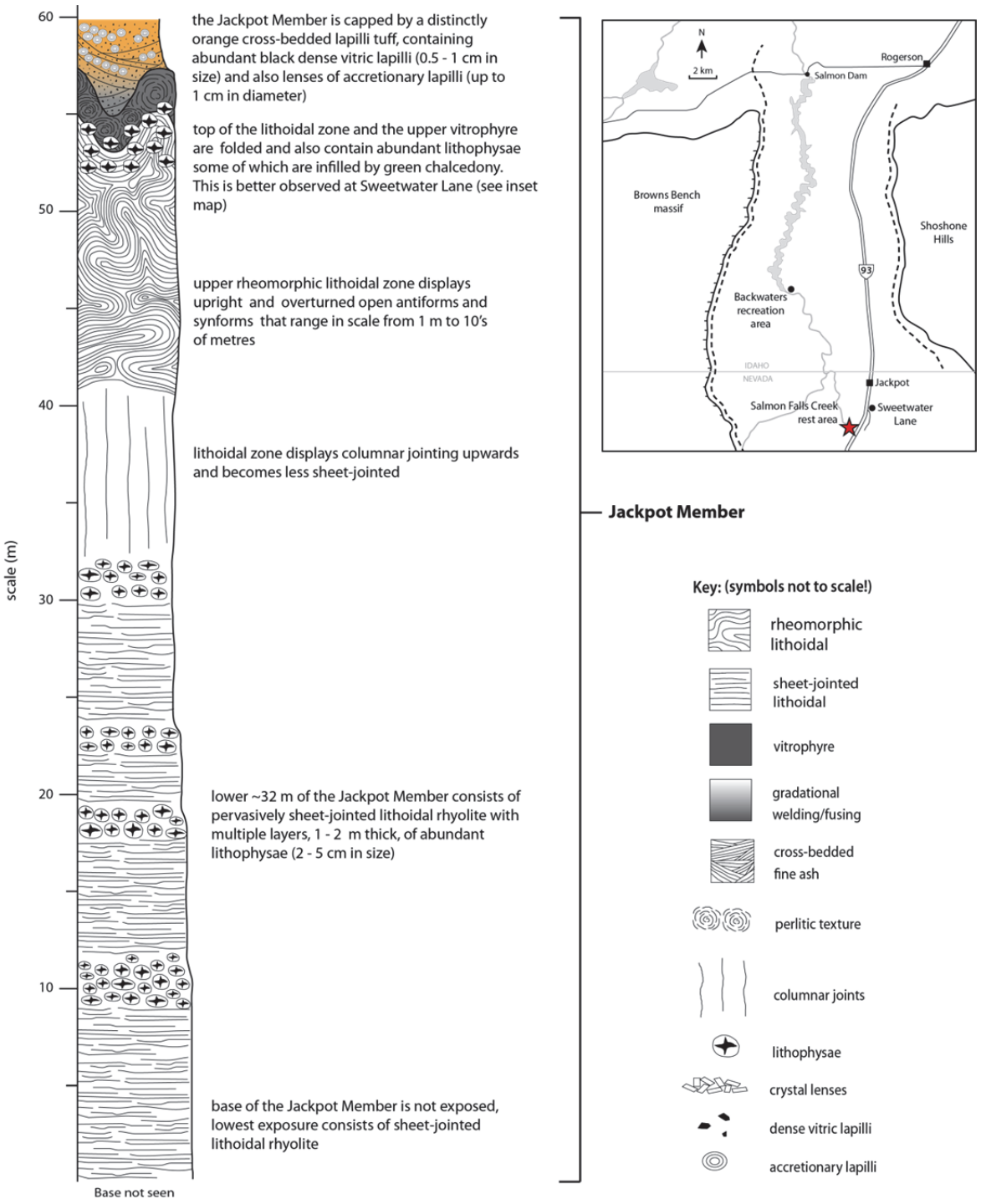

Figure 3.4. Graphic log of the Jackpot Member. Inset shows the type locality (red star) for the member at Salmon Falls Creek rest area. In addition the upper vitrophyre and the overlying lapilli-tuff are not exposed at the type section and are exposed at Sweetwater Lane.

plagioclase, sanidine, pigeonite, augite, magnetite, ilmenite, rare quartz and accessory apatite and zircon, which is broadly similar to most members of the Rogerson Formation (section 3.9). However, the presence of ilmenite and quartz is unique to the Jackpot Member and helps to distinguish it from other Rogerson Formation members.

3.3.2. Lateral variations

The Jackpot Member is best exposed at isolated localities south of Jackpot, Nevada. Further north, exposures are limited to the upper parts of the Jackpot Member, therefore lateral thickness variations of the member are difficult to determine. However, the correlation of 'Cougar Point Tuff XIII' (Ellis et al., 2012a) suggests that the Jackpot Member is part of a widespread ignimbrite sheet with minimal thickness variations from east to west. The only significant lateral variation is exhibited by the capping lapilli-tuff. At the Backwaters recreation area (Fig. 3.1) the lapilli tuff overlies a ~4 m-thick exposure of the upper rheomorphic lithoidal zone and upper vitrophyre (Fig. 3.7a). It has a similar orange colour, although this is not as intense as at its type section (Sweetwater Lane). More importantly the vitric lapilli are less abundant and smaller, between 1 and 5 mm in size, and accretionary lapilli are absent. This suggests that deposition of these distinctive lapilli was not uniform throughout the Rogerson Graben.

3.3.3. Interpretation

The Jackpot Member is interpreted to record a single explosive eruption due to an absence of palaeosols, fallout layers or reworked horizons between the different lithologies, which indicates that there were no significant time gaps during its emplacement. However, the cooling breaks indicated by multiple layers of lithophysae suggest it is an example of a compound cooling unit (*sensu* Smith, 1960; Wilson & Hildreth, 2003), formed by several ignimbrite pulses. In addition, the lower degree of welding and the abundant vitric and accretionary lapilli within the capping lapilli-tuff may also imply some late stage magma-water interaction, which has been suggested for other cSRP ignimbrites (e.g., the Deadeye ignimbrite, Ellis & Branney, 2010).

3.4. The Rabbit Springs Member

The Rabbit Springs Member (Andrews et al., 2008) is ~20 m thick at its type section at the Backwaters recreation area (Fig. 3.1, and 3.6 inset) and consists of ~9.5 m of non-welded rhyolitic ash overlain by a 10 m thick intensely-welded rhyolitic ignimbrite (Fig. 3.6). The member can be distinguished from other nearby rhyolitic ignimbrites by

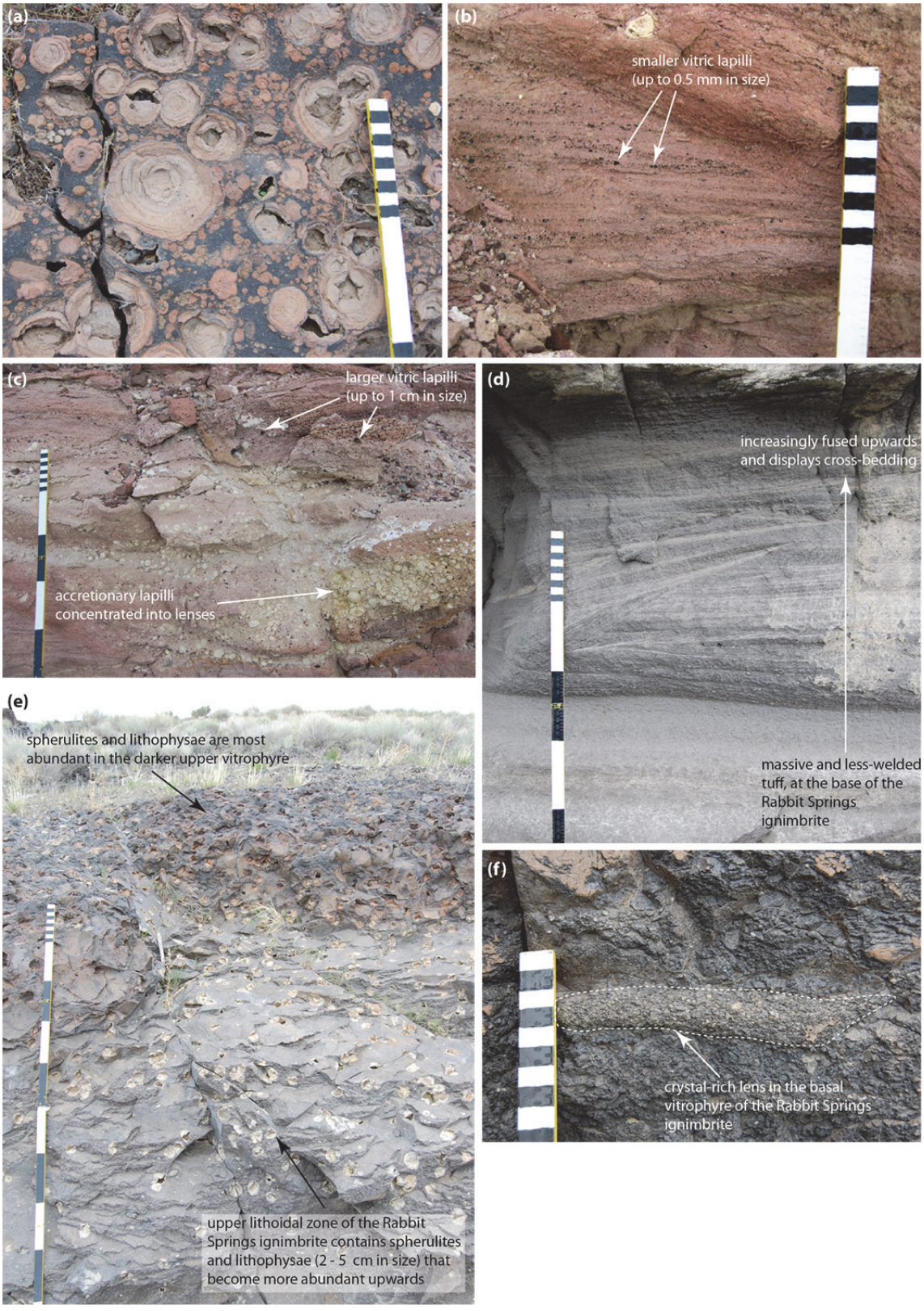

Figure 3.5. (a) Abundant spherulites and lithophysae in the upper vitrophyre of the Jackpot Member. **(b)** Orange and cross-bedded lapilli-tuff at the top of the Jackpot Member, here vitric lapilli are smaller but can be up to 1 cm in size. **(c)** The Jackpot Member lapilli-tuff also contains abundant accretionary lapilli that are typically concentrated into lenses. Examples of the larger vitric lapilli can also be seen towards the top of the photo. **(d)** Less-welded base of the Rabbit Springs ignimbrite that becomes more welded upwards. Cross-bedding also suggests that the pyroclastic density current was fully dilute at the time of deposition. **(e)** Spherulites and lithophysae are observed in the upper lithoidal zone of the Rabbit Springs ignimbrite and become more abundant upwards into the overlying upper vitrophyre. **(f)** Example of one of the crystal-rich lenses in the basal vitrophyre of the Rabbit Springs ignimbrite. These lenses are more coherent than the surrounding vitrophyre and stand prominent from the exposures.

abundant spherulites and lithophysae in its upper vitrophyre, and the fact that it is the youngest member of the Rogerson Formation to contain sanidine phenocrysts, which are absent from all overlying members (section 3.9). It sharply overlies an orange palaeosol developed in the top of the Jackpot Member and underlies the Brown's View Member (Andrews et al., 2008).

3.4.1. Description

The basal 7 m of the Rabbit Springs Member consists of white, non-welded, fine ash with centimetre-scale parallel laminations (Fig. 3.6). This passes up into grey tuff (2.5 m thick) with the change in colour attributed to a slight increase in welding (Fig. 3.5d). The upper weakly-welded zone also shows low angle cross-bedding (Fig. 3.5d) and contains lenses (1–2 cm thick) of accretionary lapilli, <1 cm in diameter, and sparse dense vitric lapilli up to 1 cm in size. This is sharply overlain by a crystal-poor (2–3% crystals) basal perlitic vitrophyre of the Rabbit Springs ignimbrite. The basal vitrophyre, 3 m-thick, also contains crystal-rich lenses (up to 10 cm in length) located ~40 cm above the basal contact that are more coherent than the surrounding vitrophyre (Fig. 3.5f). Large spherulites, 3–15 cm in size, mark the transition from the basal vitrophyre to the overlying relatively crystal-rich (10–15%) lithoidal centre, which is 4.5 m-thick (Fig. 3.6). Most of the lithoidal centre is pervasively sheet jointed, with a 2 m-thick blockier jointed zone towards the base. The upper 2 m of the lithoidal zone contains abundant spherulites and lithophysae (3–5 cm in size), which extend above its upper contact and into the overlying, 2.5 m-thick, upper vitrophyre (Fig. 3.5e). The upper vitrophyre has the same crystal content as the lithoidal centre, and is sharply overlain by 1 m of massive, non-welded, fine ash. A ~4 m gap in exposure separates this non-welded ash from a palaeosol beneath the Browns View Member. Although not observed during the present study, a sequence of volcaniclastic sediments separated by palaeosols and major erosional contacts has been documented within this obscured zone and interpreted as periods of repose separated by major flooding events that reworked non-welded fallout ash (Andrews et al., 2008).

3.4.2. Lateral variations

Previous interpretations suggested that the Rabbit Springs Member does not extend further south than the Backwaters recreation area (Andrews et al., 2008). However, the present study demonstrates that the Rabbit Springs Member is in fact a correlative of the 'Jackpot 7' unit (of Andrews et al., 2008).

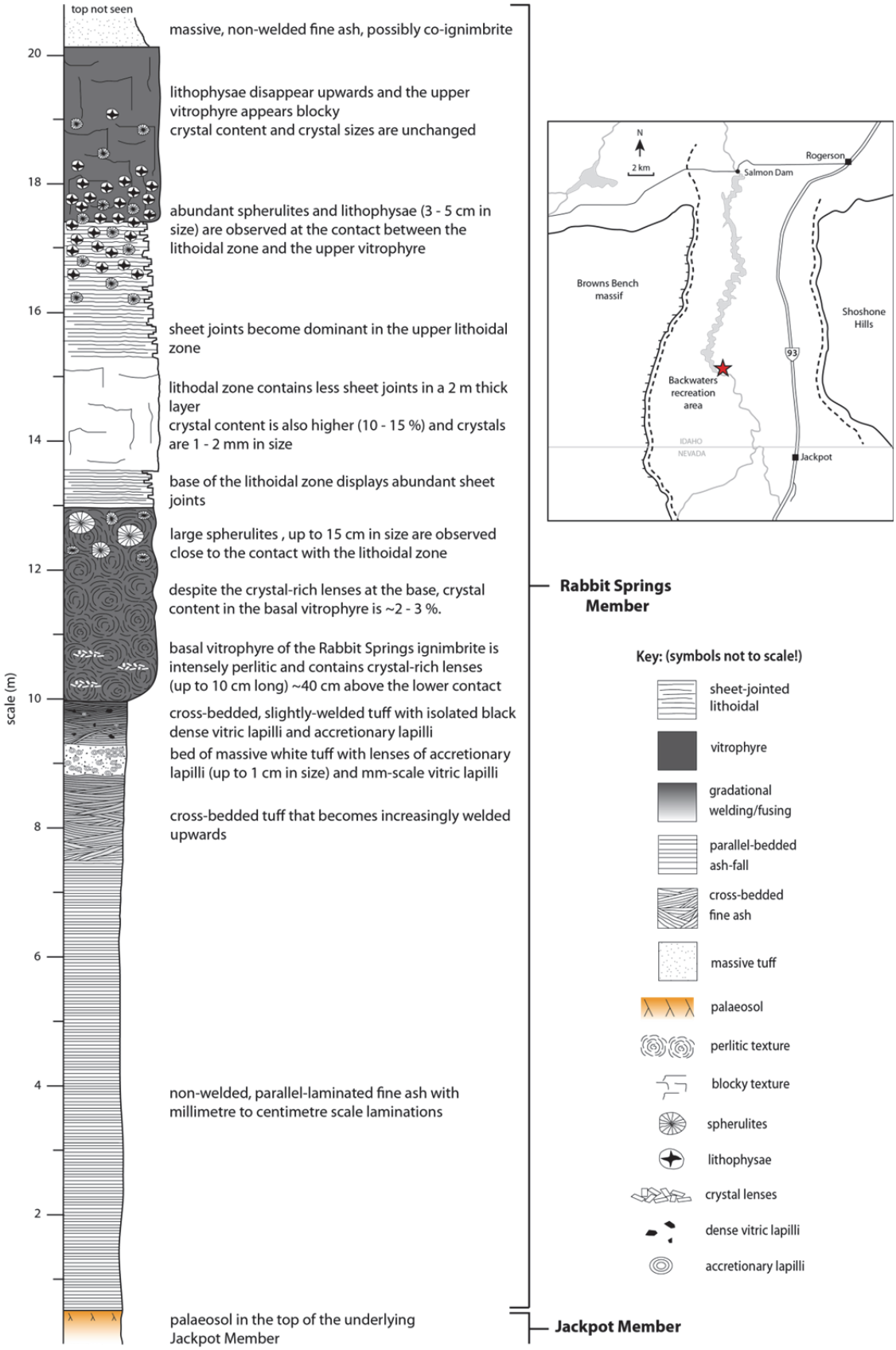

Figure 3.6. Graphic log of the Rabbit Springs Member. Inset shows the type locality (red star) for the member at the Backwaters recreation area.

Jackpot 7 was previously described and sampled (Andrews et al., 2008; Ellis et al., 2012a) in a small canyon located ~6 km north-west of the Salmon Falls Creek rest area (GR: N42°57'40" W114°45'52"). Here it comprises a 3 m-thick basal vitrophyre containing crystal-rich lenses overlain by a 3 m-thick lithoidal zone (Fig. 3.7a). These field characteristics, in particular the crystal-rich lenses, are very similar to the Rabbit Springs Member at its type locality. In addition, when comparing whole-rock data for these two units, it becomes apparent that they share amongst others closely similar incompatible trace element ratios of Zr/Y and Th/Nb (Fig. 3.7b). Both units also have indistinguishable palaeomagnetic mean flow directions (Finn & Coe, unpublished data, Fig. 3.7c). Therefore, the present study redefines Jackpot 7 as a lateral extension and correlative of the Rabbit Springs Member. Thus, the member extends ~10 km further south than previously thought (Andrews et al., 2008).

Exposures of the Rabbit Springs Member east of Highway 93 show that the member thins eastwards to ~4 m (Fig. 3.9). Here it consists entirely of massive, perlitic vitrophyre with abundant spherulites (2–3 cm in size) and no lithoidal zone. Crystal content (10–15 %, 1–2 mm in size) appears to remain unchanged. This is also consistent with the previous interpretation of this member (Andrews et al., 2008).

3.4.3. Interpretation

The basal 7 m of non-welded, parallel laminated, fine ash is interpreted as the deposit of sustained sub-aerial fallout; however the limited exposure of this ash means that some degree of reworking cannot be ruled out. The overlying 2.5 m of slightly-welded tuff is interpreted as the early deposits of the Rabbit Springs ignimbrite, and the preserved low angle cross-bedding suggests that the density current at the time was fully dilute. Also, the lenses of accretionary lapilli and vitric lapilli may suggest a degree of magma-water interaction during the eruption, similar to the Deadeye ignimbrite of the Cassia Mountains, Idaho (Ellis & Branney, 2010). Upwards the ignimbrite is more intensely-welded and is interpreted as a simple cooling unit (*sensu* Smith, 1960; Wilson & Hildreth, 2003), which was likely deposited from a single prolonged high-temperature density current. The capping non-welded fine ash is also interpreted as fallout ash, although this may have been co-ignimbrite.

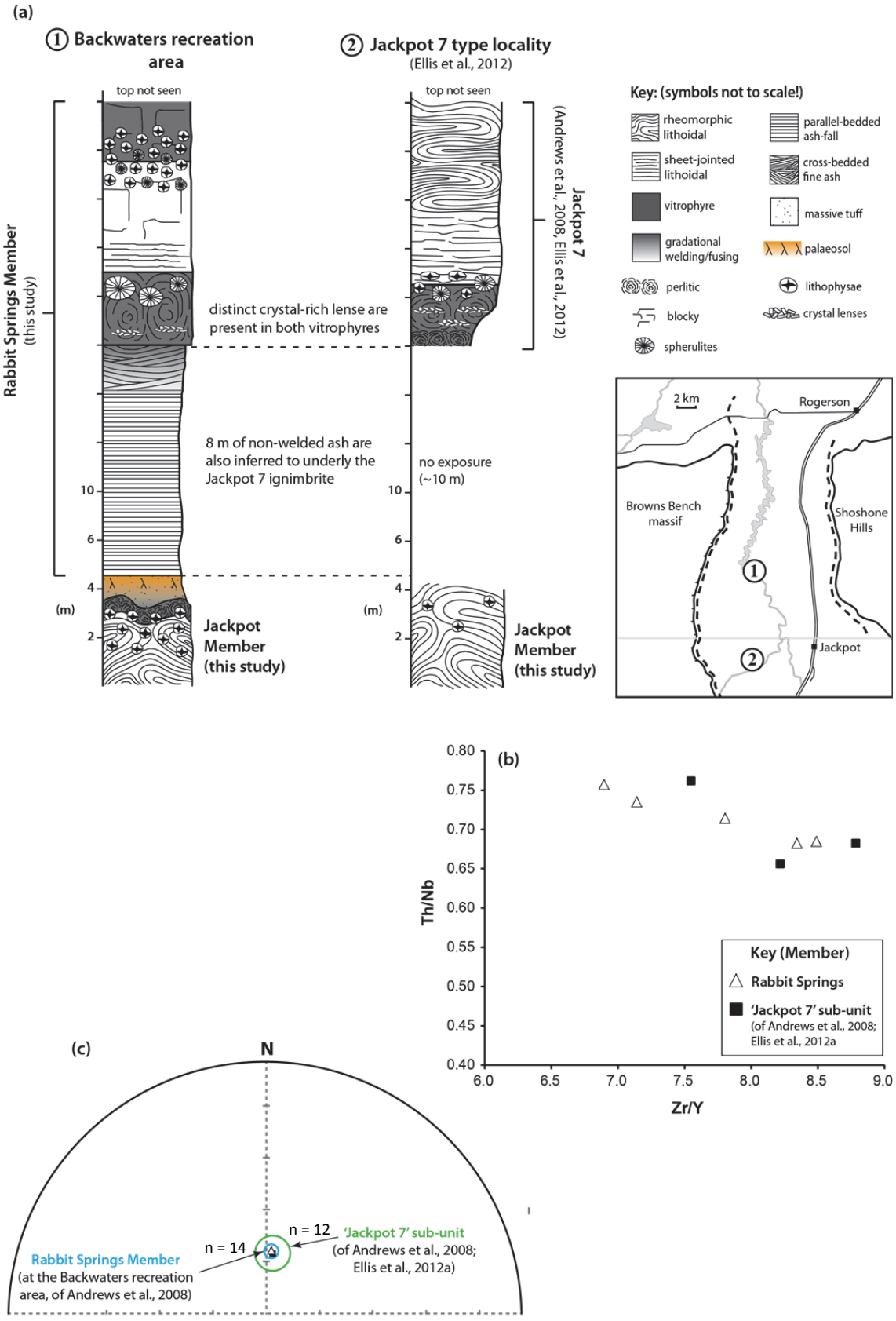

Figure 3.7. (a) Graphic logs of the Rabbit Springs Member and the 'Jackpot 7' sub-unit (of Andrews et al., 2008), at each of their respective type localities (see inset map), demonstrating the similar physical characteristics shared by both units. **(b)** Zr/Y versus Th/Nb showing the chemical similarities between the Rabbit Springs Member and the 'Jackpot 7' sub-unit (Jackpot 7 data source: Bonnichsen et al., 2008). **(c)** Stereonet showing the indistinguishable palaeomagnetic mean flow directions (Finn & Coe, unpublished) exhibited by the Rabbit Springs Member and the 'Jackpot 7' sub-unit.

3.5. The Brown's View Member

The Brown's View Member (Andrews et al., 2008) is ~9 m-thick, at the Backwaters recreation area (type locality, Fig. 3.1, and 3.8 inset), and consists of non-welded, parallel-laminated, rhyolitic ash overlain by a rhyolitic ignimbrite. The ignimbrite has a distinct complex welding profile with upper and lower vitrophyres separated by a less-welded centre containing abundant non-vesicular vitric lapilli, 5–10 mm in size (Fig. 3.8). This welding profile is unique in the Rogerson Formation and helps distinguish the member from other members nearby. The Brown's View Member is also the horizon in the phenocryst assemblage of the Rogerson Formation where sanidine disappears (section 3.9), and is therefore an important stratigraphic marker. It sharply overlies a 1 m-thick orange palaeosol developed in the top of undifferentiated volcaniclastic sediments that overly the Rabbit Springs Member, and is overlain by the Backwaters Member (contact not seen). The Brown's View Member has been informally sub-divided into layers A-D to facilitate its description.

3.5.1. Description

Non-welded, parallel bedded, rhyolitic ash, ~1 m-thick (layer A, Fig. 3.8), is separated from the overlying Browns View ignimbrite by a 2 m gap in exposure that likely conceals more non-welded, parallel bedded, ash. The lowest exposure of the Browns View ignimbrite is a 1 m-thick perlitic basal vitrophyre (layer B, Fig. 3.8) that is relatively crystal poor (2–5 % crystals). The majority of phenocrysts are 1–2 mm in size, comprising a mineral assemblage of plagioclase, pigeonite, augite, magnetite and smaller (<1 mm) accessory apatite and zircon. Pigeonite and augite crystals are also Mg-rich (see section 3.9), which is a defining characteristic of the Brown's View Member and helps distinguish it from other members of the Rogerson Formation.

The basal vitrophyre of the member is overlain by a 1 m-thick less-welded lapilli-tuff (layer C, Fig. 3.8) containing abundant black angular vitric lapilli, 5–10 mm in size (Fig. 3.11c). Upper and lower marginal zones of layer C contain less vitric lapilli and are more welded than the centre. Crystal content increases upwards through layer C to a maximum (~10 %, sizes unchanged) in the overlying upper vitrophyre (layer D, Fig. 3.8). Layer D has a rapid gradational lower contact with layer C, and its base is perlitic with sparse lithophysae, 1–2 cm in size. The perlitic texture decreases upwards and the upper metre of layer D has a blockier appearance. A ~3 m gap in exposure separates the

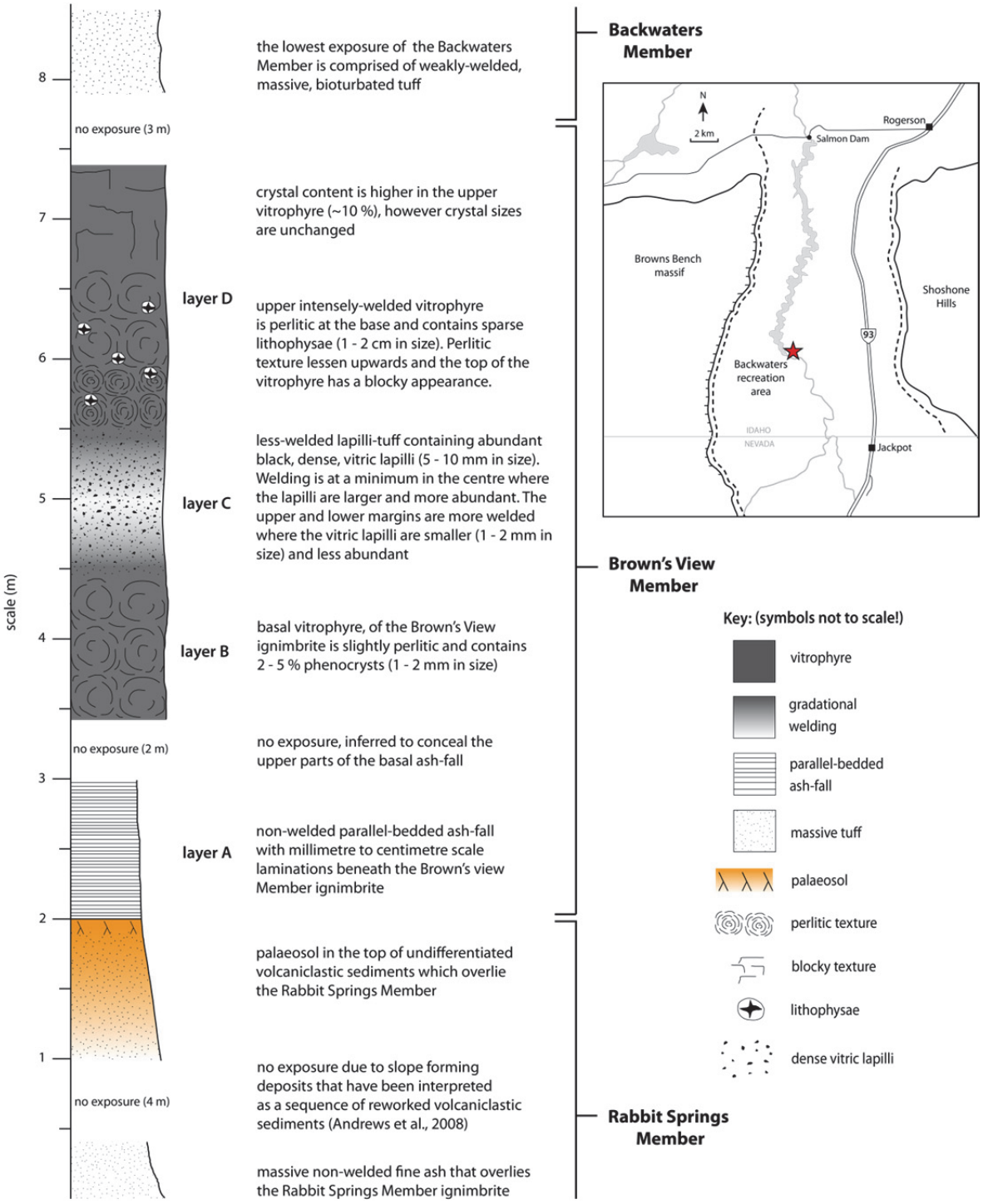

Figure 3.8. Graphic log of the Brown's View Member. Inset shows the type locality (red star) for the member at the Backwaters recreation area.

upper vitrophyre from the overlying Backwaters Member, and this gap is inferred to conceal the upper-most parts of the Brown's View Member.

3.5.2. Lateral variations

The Brown's View Member is exposed both within the Rogerson Graben and also outside the graben to the north-west, where it onlaps and oversteps the older stratigraphy of the Browns Bench massif (Andrews et al., 2008). Previous interpretations also suggested that the member thinned eastwards across the Rogerson Graben and pinched-out east of Highway 93 (Andrews et al., 2008). However, by revising the stratigraphy east of Highway 93 (Fig. 3.9) the present study demonstrates that the member in fact thickens eastwards.

Previous descriptions (Andrews & Branney, 2005) of the stratigraphy east of Highway 93 identified a palaeosol (thought to be at the top of the Backwaters Member, Andrews et al., 2008) overlain by ~2 m of reworked volcaniclastic sediment, a ~1 m-thick parallel-bedded ash-fall deposit, and a 5 m-thick vitrophyre (Fig. 3.9). The ash-fall deposit and the overlying vitrophyre were interpreted as thinned lateral correlatives of the Grey's Landing Member (Andrews et al., 2008; Fig.3.9). At this eastern locality the 5-m-thick vitrophyre is overlain (contact not seen) by the Sand Springs Member previously defined by Andrews et al. (2008) (Fig. 3.9). These authors described the Sand Springs Member as an ~8 m-thick rhyolitic ignimbrite that has a gradational welding profile from a less-welded base to an intensely-welded upper vitrophyre, and contains abundant dense vitric lapilli (5–10 mm in size). However, through extensive field observations it was noted in the present study that the vertical sequence of lower and upper intensely-welded layers (e.g., the 5m-thick vitrophyre and the upper vitrophyre of the Sand Springs Member), separated by a less-welded lapilli-tuff containing abundant vitric lapilli is closely similar to vertical profile of the Brown's View Member at its type locality (Fig. 3.8). Therefore, the present study redefines the 5 m-thick vitrophyre and the overlying Sand Springs Member (of Andrews et al., 2008) as lateral correlatives of the Brown's View Member (Fig. 3.9). Thus, the Brown's View Member is now thought to thicken eastwards from ~9 m to ~20 m.

Support for this interpretation is provided by a comparison of whole-rock data, from the Brown's View and Sand Springs members, demonstrating that they have closely similar incompatible trace element ratios of Zr/Y and Th/Nb (Fig. 3.10a). The Brown's View

and Sand Springs members also have indistinguishable palaeomagnetic mean flow directions (Finn & Coe, unpublished data, Fig. 3.10b). In addition, the Sand Springs Member also contains high-Mg pyroxenes (augite and pigeonite) that are characteristic of the Brown's View Member (Fig. 3.10c) at its type locality. Whole-rock chemical data from the 5 m-thick vitrophyre are also identical to data from the Brown's View Member, and more importantly are distinct from data obtained from the Grey's Landing Member at its type locality (Fig. 3.10a). Therefore, the ~5 m-thick vitrophyre cannot be a thinned lateral correlative of the Grey's Landing Member as previously thought (Andrews et al., 2008), and is interpreted in the present study as a lateral extension of layer B of the Brown's View Member.

3.5.3. Interpretation

The non-welded, parallel bedded, white ash (layer A) at the base of the Brown's View Member is interpreted as originating from sustained sub-aerial fallout. However, cross laminations observed in the eastern exposures (Fig. 3.9) may also suggest a degree of localised reworking. The complex vertical welding profile of the overlying ignimbrite (Fig. 3.8) indicates that it is a compound cooling-unit (*sensu* Smith, 1960; Wilson & Hildreth, 2003). The two intensely-welded zones (upper and lower) indicate emplacement temperatures sufficiently hot to cause intense welding, whereas the central less-welded lapilli-tuff indicates a decrease in the emplacement temperature. This is interpreted as the effect of the incorporation of large volumes of cool vitric lapilli that may have acted as a heat sink, lowering the temperature of the density current and the accumulating deposit (e.g., Marti et al., 1991). Although the origin of the vitric lapilli remains unclear this interpretation assumes that the vitric lapilli were accidental in origin and were entrained into the density current during eruption. It is also observed that as the size and abundance of the vitric lapilli decreases the degree of welding increases (Fig. 3.8). This therefore supports the interpretation that the vitric lapilli lowered the emplacement temperature of the ignimbrite and prevented intense welding.

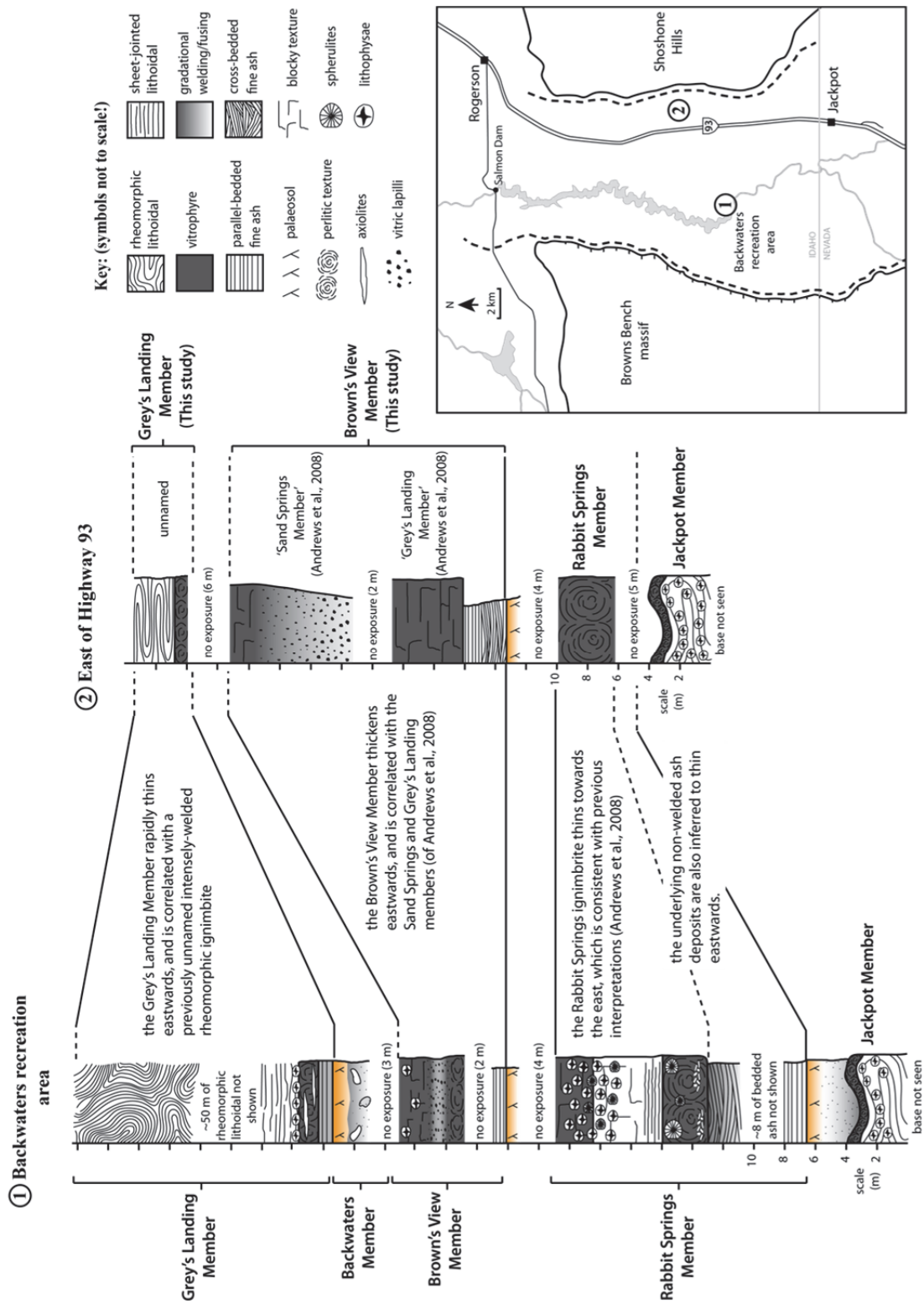

Figure 3.9. Graphic logs showing the volcanic successions at the Backwaters recreation area and east of Highway 93 (see inset map for localities). These demonstrate the west–east lateral thickness and internal lithological variations exhibited by all members of the Rogerson Formation.

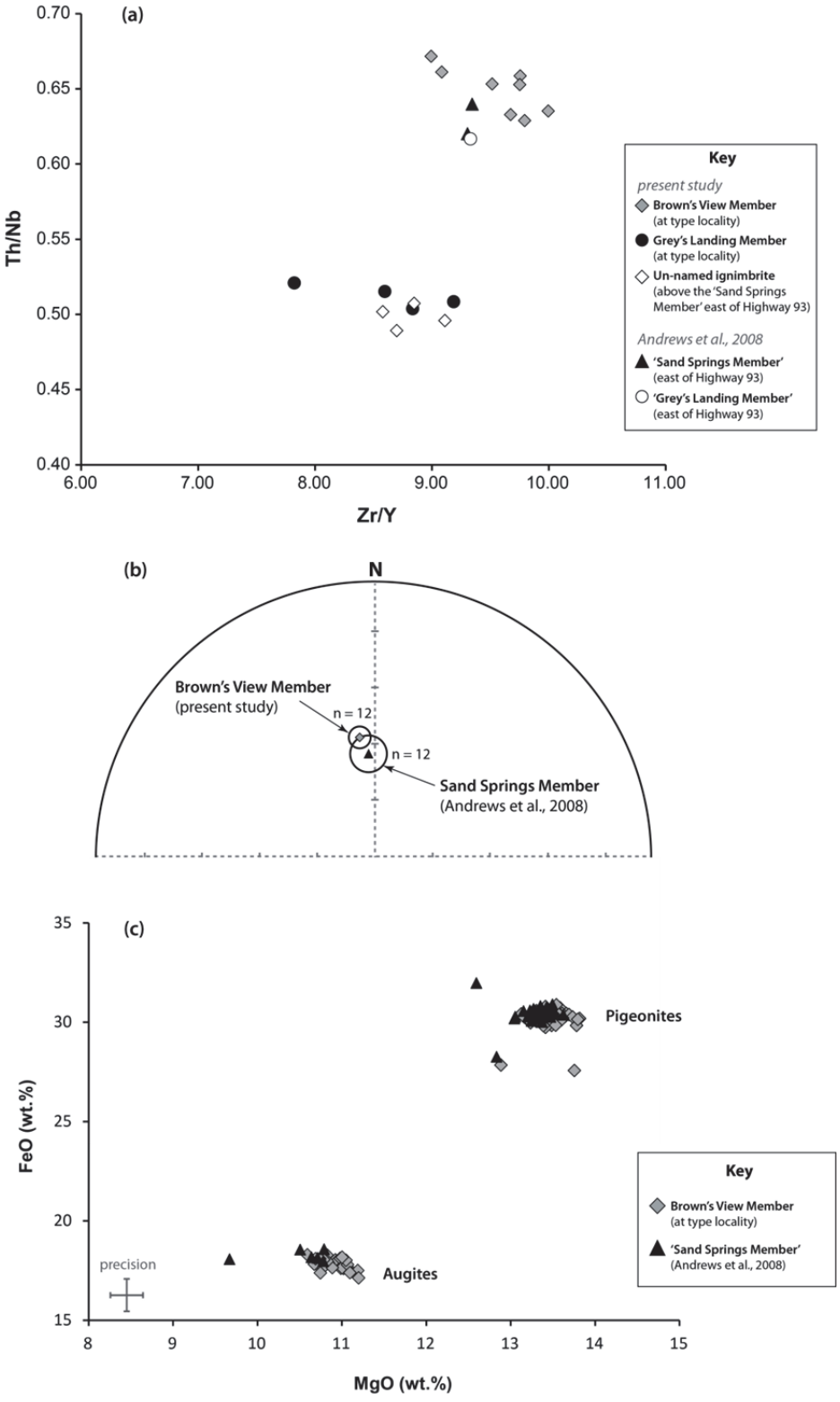

Figure 3.10. (a) Zr/Y versus Th/Nb showing the chemical similarities between the Brown's View Member of the present study and the thin Grey's Landing Member and overlying Sand Springs Member of Andrews et al., (2008). Note that the 'Grey's Landing Member' east of Highway 93 (Andrews et al., 2008) is distinct from the Grey's Landing Member at its type section, and therefore the two cannot be correlatives. In addition, data from the previously un-named ignimbrite that overlies the 'Sand Springs Member' are indistinguishable from the Grey's Landing Member, and supports the interpretation that they both are correlatives of one another. **(b)** Stereonet showing the indistinguishable palaeomagnetic mean flow directions (Finn & Coe, unpublished) of the Brown's View Member and the Sand Springs Member (of Andrews et al., 2008). (c) MgO versus FeO plot showing the indistinguishable high-Mg pyroxenes in both the Brown's View and Sand Springs members.

3.6. The Backwaters Member

The Backwaters Member (Andrews et al., 2008) is poorly exposed throughout the Rogerson Graben, and is only exposed at its type section at the Backwaters recreation area (Fig. 3.1). Here it is ~6 m thick and overlies the Brown's View Member (contact not seen) and is sharply overlain by the Grey's Landing Member (Fig. 3.12). Due to the limited exposure, the Backwaters Member is not considered further in this thesis, however a brief description and interpretation are provided below.

3.6.1. Description

The lower 4 m of the member comprise non-welded, pale orange, massive tuff that contains sparse pumice lapilli, up to 2 cm in size. The member has also been heavily bioturbated and mammalian burrows are observed throughout the unit (Fig. 3.11a). The non-welded tuff is sharply overlain by a darker welded tuff, 1 m-thick, that is capped by a 1-m thick baked orange palaeosol (Fig. 3.11a) with preserved grass imprints on its upper surfaces. The baked palaeosol and upper welded zone are thought to be due to fusing by the downward conduction of heat from the overlying intensely-welded Grey's Landing Member (Andrews et al., 2008).

3.6.2. Interpretation

The Backwaters Member was previously interpreted as a non-welded ignimbrite (Andrews et al., 2008); however the degree of bioturbation makes it difficult to be certain. The baked palaeosol at the top of the member suggests there was a significant repose period between the Backwaters and Grey's Landing eruptions, however neither member has been dated (section 3.10).

3.7. The Grey's Landing Member

The Greys Landing Member (Andrews et al., 2008) is the youngest member of the Rogerson Formation. At its type section at Grey's Landing, (Fig. 3.1 and 3.12 inset), it is ~65 m thick and consists of a well-bedded basal ash-fall deposit overlain by an intensely-welded rhyolitic rheomorphic ignimbrite (Fig. 3.12) and overlies a baked palaeosol developed at the top of the underlying Backwaters Member (Andrews et al., 2008). The Grey's Landing member can be distinguished from all other Rogerson Formation members as it contains four discrete modes of pyroxene (section 3.9).

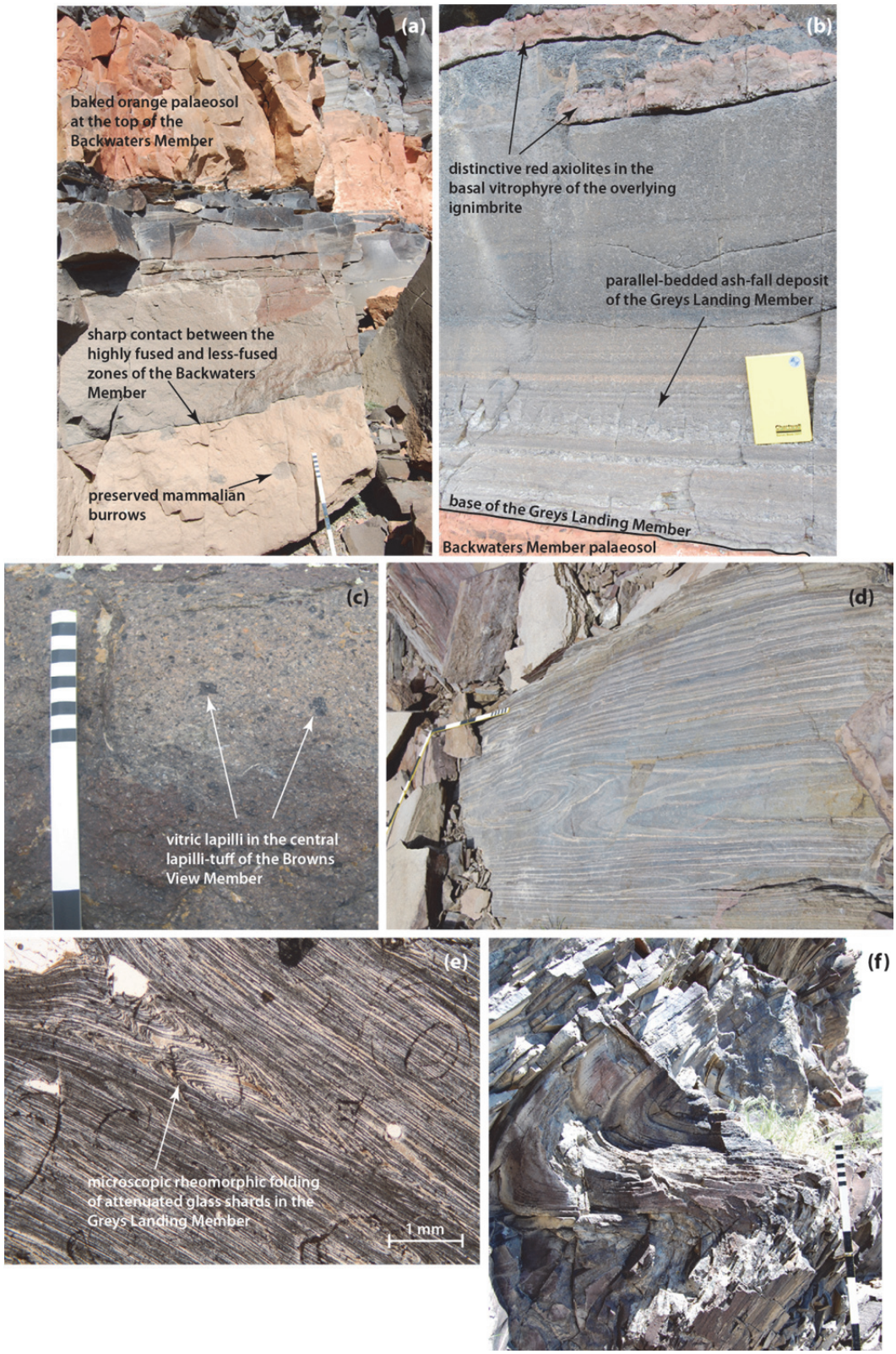

Figure 3.11. (a) Exposure of the Backwaters Member showing the lower less-fused zone sharply overlain by the upper highly-fused zone and capped by a distinctive baked orange palaeosol. Fusing was due to the deposition of the overlying high-temperature Grey's Landing Member. **(b)** Lower ~1 m of the Grey's Landing Member showing the basal parallel-bedded ash-fall deposit overlain by an intensely-welded rhyolitic ignimbrite containing distinctive red axiolites. **(c)** Abundant black vitric lapilli within the central less-welded lapilli-tuff of the Brown's View Member. **(d)** Intense flow-banding and isoclinal rheomorphic folds within the lower structural 'flat-zone' of the Grey's Landing Member. **(e)** Intense welding and rheomorphism has transposed and attenuated glass shards within the Grey's Landing Member generating a parataxitic foliation that wraps around the phenocrysts (top left). Isoclinal fold pairs in the centre indicate rheomorphic folding was also occurring on a microscopic scale. **(f)** Metre-scale open rheomorphic folds in the upper lithoidal 'steep-zone' of the Grey's Landing Member.

3.7.1. Description

The base of the member is a 0.4 m-thick well-bedded ash-fall deposit with alternating crystal rich and fine ash layers, all of which have been fused to vitrophyre by the overlying Grey's Landing ignimbrite (Fig. 3.11b). There are also localised scours into the ash that are draped by younger beds. The fused ash-fall is sharply overlain by the basal vitrophyre of the Grey's Landing ignimbrite, which is 2 m-thick and contains distinctive red axiolites (Fig. 3.11b) that extend laterally up to 3 m. Petrographic observations of the basal vitrophyre reveal that individual glass shards have been elongated, due to intense rheomorphic shearing (Andrews & Branney, 2011), and now define a parataxitic foliation that wraps around the existing phenocrysts (Fig. 3.11e). Crystal content and sizes (10–15 %, 1–3 mm in size) are consistent throughout the member, and comprises a mineral assemblage of plagioclase, pigeonite, augite, magnetite and accessory apatite and zircon. The upper contact of the basal vitrophyre is sharp and highlighted by red spherulites, 3–5 cm in diameter. The overlying lithoidal zone is ~57 m thick (Fig. 3.12), and is pervasively flow-banded and flow-folded with folds that range from microscopic (Fig. 3.11e) to metre-scales and includes abundant sheath folds. The lithoidal zone can also be sub-divided into two structural domains. This includes a lower 'flat-zone' with sub-horizontal recumbent isoclinal folding and sheath folds (Fig. 3.11d), and an upper 'steep-zone' with upright to overturned open antiforms and synforms (up to 10 m in scale, Fig. 3.11f). The lithoidal zone is sharply overlain by a thin (≤ 1 m thick) upper vitrophyre that is not exposed at the type section but can be seen at the Salmon Dam (Fig. 3.1). Here the upper vitrophyre is highly perlitic and follows the folding in the upper lithoidal zone (Fig. 3.12). The folding also disturbs the overlying fine ash (2–3 m thick) that is preserved and fused within synforms in the upper vitrophyre. This ash passes up into an orange palaeosol that is locally overlain by younger basalt lavas.

3.7.2. Lateral variations

The Grey's Landing Member is exposed both within the Rogerson Graben and outside the graben to the north, where it onlaps and oversteps the older stratigraphy of the Browns Bench escarpment (Andrews et al., 2008). Previous interpretations of the ignimbrite also suggest that it correlates to a ~5 m-thick vitrophyre exposed along Highway 93 (Andrews et al., 2008; Andrews & Branney, 2011). However, revisions made by the present study demonstrate that this vitrophyre and the overlying lapilli-tuff

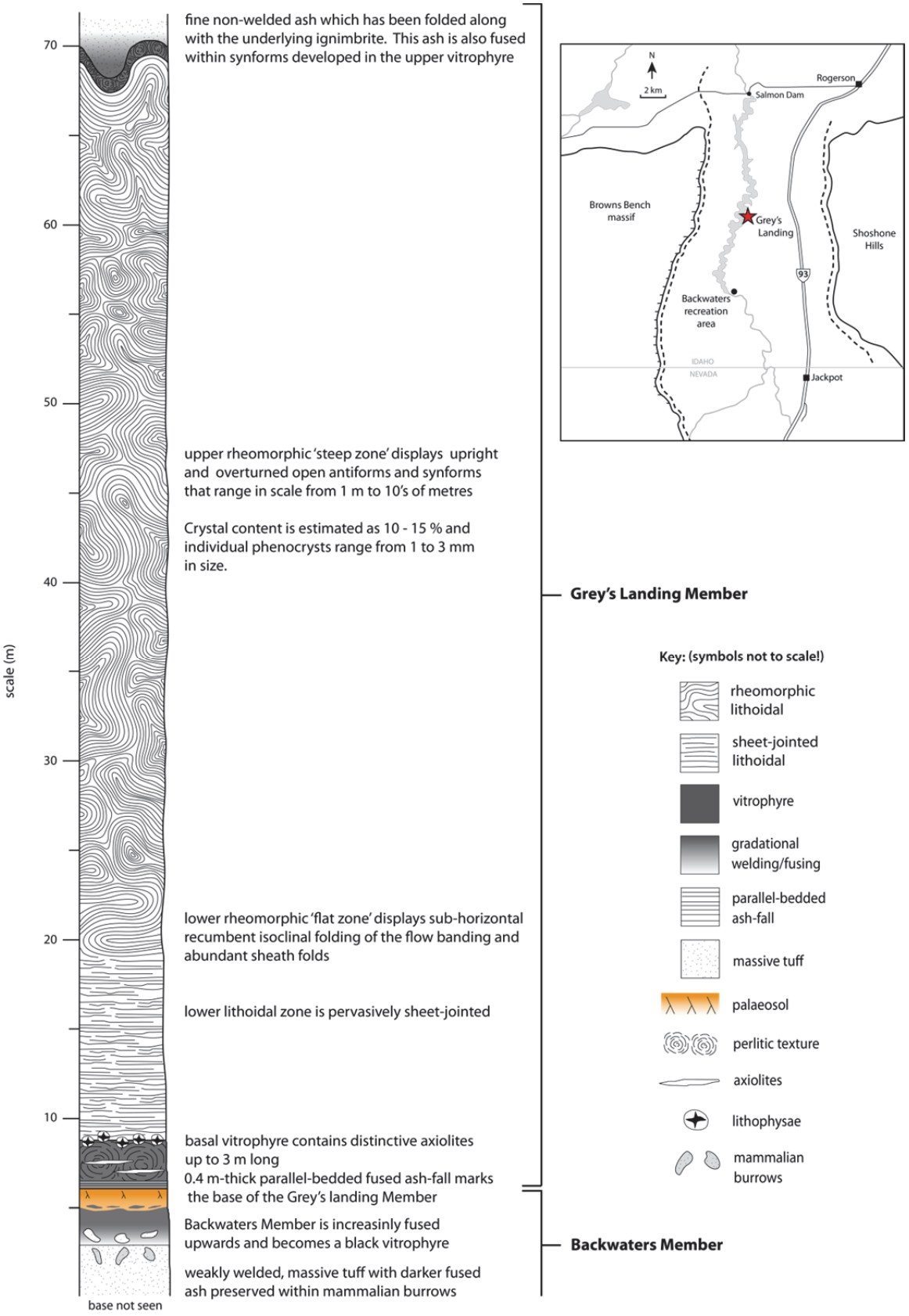

Figure 3.12. Graphic log of the Grey's Landing Member. Inset shows the type locality (red star) for the member at Grey's Landing.

are in fact lateral correlatives of the Brown's View Member (see section 3.5.2). A previously unnamed intensely-welded ignimbrite was also identified east of Highway 93 that is separated from the underlying Brown's View Member by a 10 m gap in exposure, inferred to conceal the Backwaters Member (Fig. 3.9). This ignimbrite is composed of a 1 m-thick basal vitrophyre, sharply overlain by a 2 m thick rheomorphic lithoidal zone (top not seen, Fig. 3.9). In addition, whole-rock (Fig. 3.10a) and mineral chemical data (Fig. 3.13), obtained from this unnamed ignimbrite, are indistinguishable from the Grey's Landing Member, at its type locality. These data combined with the stratigraphic position of this unnamed ignimbrite imply that it is a lateral correlative of the Grey's Landing Member. Therefore the Grey's Landing Member is redefined in the present study as the capping member of the Rogerson Formation, and thins rapidly eastwards from ~65 m to ~3 m.

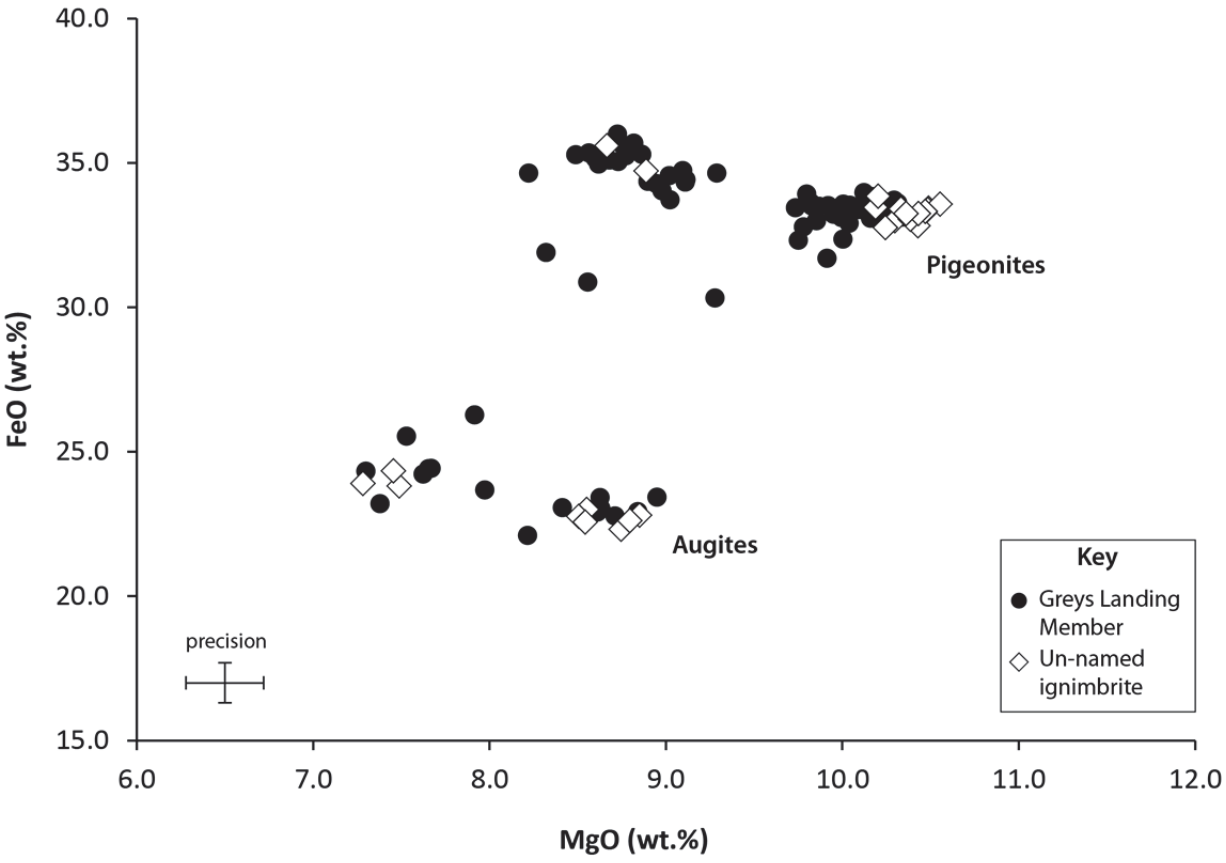

Figure 3.13. MgO versus FeO plot showing the indistinguishable pigeonite and augite compositions of the Grey's Landing Member and the previously unnamed ignimbrite that overlies the Brown's View Member east of Highway 93 (Fig. 3.9). This supports the interpretation that the unnamed ignimbrite is a lateral correlative of the Grey's Landing Member

3.7.3. Interpretations

The Grey's Landing Member is a simple cooling unit (*sensu* Smith, 1960; Wilson and Hildreth, 2003) and interpreted as the product of a single explosive eruption (Andrews et al., 2008). The basal bedded ash-fall deposit is the result of sustained sub-aerial fallout; based on the mantling of the substrate, excellent sorting and laterally continuous laminations. The overlying massive ignimbrite is the result of a single high temperature pyroclastic density current (Andrews & Branney, 2011). Welding of the ignimbrite occurred during deposition and rheomorphic deformation continued post-emplacement with the development of rheomorphic folds (Andrews & Branney, 2011). Rheomorphic folding was also occurring during the deposition of the capping fine ash deposits, as these are fused and folded by the underlying ignimbrite. These ash deposits are interpreted as late stage sub-aerial fallout and may also have been co-ignimbrite.

3.8. Whole-rock chemistry

Whole-rock samples were collected from the Rogerson Formation and prepared for X-ray fluorescence (XRF) spectrometry and analysed on a PANalytical PW4400 Axios XRF spectrometer at the University of Leicester (see Appendix B.1). Samples were preferentially collected from the base and top of individual members, at multiple localities, in order to characterise the individual eruption-units and assess any vertical or lateral chemical zonation. The poor exposure of the non-welded facies meant that these were not targeted for sampling. This also includes the Backwaters Member as exposures are limited to the Backwaters recreation area and likely do not correlate with any widespread ignimbrite sheets across the cSRP.

3.8.1. Major elements

The rhyolites of the Rogerson Formation have SiO_2 contents ranging between 70.19–76.63 wt.% and have relatively high concentrations of TiO_2, MgO and Fe_2O_3 (Table C.1), which is consistent with data obtained on other rhyolitic ignimbrites from the central Snake River Plain (e.g., Bonnichson & Citron, 1982; Cathey and Nash, 2004; Wright et al., 2002; Andrews et al., 2008; Ellis et al., 2010; Fig. 3.14a). Alumina Saturation Indices (ASI) range between 0.93 and 0.99 with higher values of 1.04 in the Jackpot Member (Table C.1). This suggests that most eruption-units are metaluminous whereas the older Jackpot Member is slightly peraluminous. Loss on ignition (LOI), of

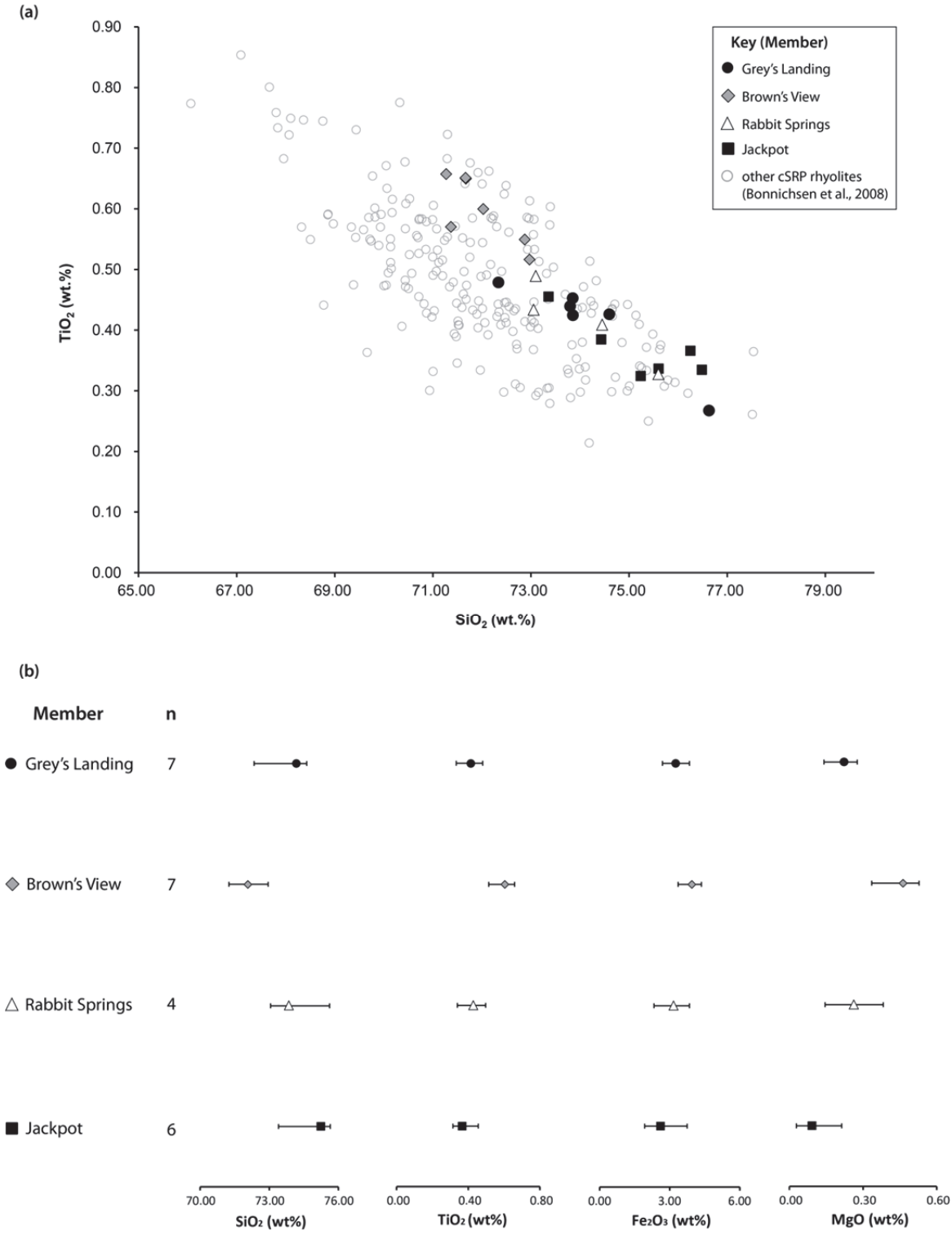

Figure 3.14. (a) SiO_2 vs TiO_2 plot showing the variations between the Rogerson Formation members (this study) and their similarity to the majority of other cSRP rhyolitic ignimbrites (data from Bonnichsen et al., 2008). **(b)** Variations in select major element concentrations with stratigraphic height through the Rogerson Formation. Symbols represent the mean concentrations and the black bars represent the range in concentration exhibited by all samples of each member.

all members, are typically <2.5 wt.% (Table C.1), which implies that post-emplacement alteration was negligible.

Major element concentrations are remarkably consistent within individual members; displaying only subtle vertical variations (e.g., <2 wt.% SiO_2) from base to top at any one locality. However, up succession, major element concentrations show systematic variation between members of the Rogerson Formation. From the Jackpot Member to the Browns View Member SiO_2 generally decreases whereas MgO, TiO_2 and Fe_2O_3 all increase (Fig. 3.14b). These variations are consistent with the magmatic system, producing these rhyolites, becoming increasingly more mafic over time; a pattern also noted by previous studies that suggest a province wide trend to more mafic compositions in the central Snake River Plain (cSRP) over time (Bonnichsen et al., 2008; Nash et al., 1996). The overlying Greys Landing Member then shifts from this trend, with higher SiO_2 and lower MgO and TiO_2.

3.8.2. Trace elements

All members of the Rogerson Formation plot (Fig. 3.15a inset) within the 'within plate granites' field of Pearce et al. (1984) and with high Ga/Al ratios (>3) can be classified as A-type (after Whalen et al., 1987). Totals of high field strength elements (Zr+Nb+Y+Ce) range from 700–996 ppm, which is also within the anorogenic granites range (500–1000 ppm) defined by Eby (1990).

Bulk-silicate-Earth normalised trace element patterns show that all members of the Rogerson Formation have similar trace element abundances, with high Rb, Th, U and Pb, and relatively lower Ba, Nb and Sr (Fig. 3.15a). Despite the overall similarities it is possible to distinguish individual members by using the relatively incompatible elements Th, Nb, Zr and Y as discriminators. Data from the Jackpot Member defines two chemical groups, with lower Zr/Y and Th/Nb ratios towards the base and higher ratios towards the top (Fig. 3.15b). This may suggest that the Jackpot Member may be chemically zoned; however the base was only sampled at the type locality and is not exposed elsewhere, therefore any zonation cannot be further constrained. In addition, Zr/Y and Th/Nb ratios obtained from overlying Rabbit Springs Member also show a range (Fig. 3.15b), and from base to top Zr/Y ratios increase and Th/Nb ratios decrease. Data from the younger Brown's View and Grey's Landing members demonstrate minimal variation, although a single anomalous outlier is observed in the Grey's

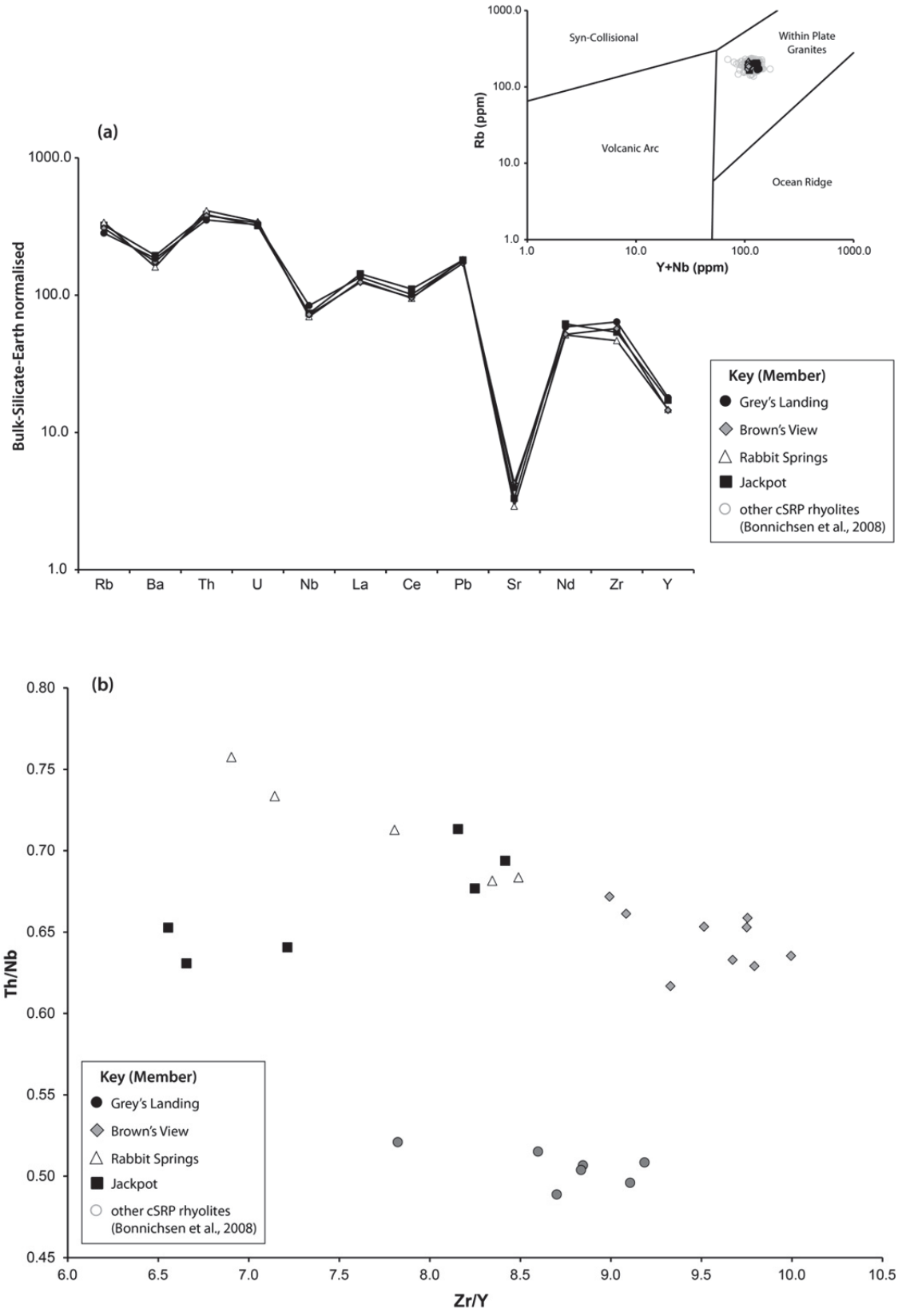

Figure 3.15. (a) Bulk-Silicate-Earth (Sun & McDonough, 1995) normalised trace element patterns for all members of the Rogerson Formation demonstrating that all have broadly similar trace element abundances. Inset shows all Rogerson Formation members plot within the 'Within Plate Granites' field (of Pearce et al., 1984) and all are similar to the majority of other rhyolitic ignimbrites in the cSRP. **(b)** Zr/Y vs Th/Nb plot demonstrating the chemical groups defined by each of the Rogerson Formation members. The largest variations are observed in the Jackpot and Rabbit Springs Members, however the younger Brown's View and Grey's Landing Members define chemical fields that are distinct from all other Rogerson Formation members.

Landing Member data with a lower Zr/Y ratio. However, the majority of data from the Grey's Landing and Brown's View members define unique chemical groups that are distinct from all other Rogerson Formation members (Fig. 3.15b).

3.9. Petrology and mineral chemistry

Crystal content in all members is typically 10–15 %, although both the Rabbit Springs and Brown's View Members show a vertical increase in crystal content from base to top. All members also share a broadly similar anhydrous mineral assemblage of plagioclase, pigeonite, augite, magnetite and accessory apatite and zircon. In addition the older members (the Jackpot and Rabbit Springs members) also contain sanidine, and the Jackpot Member is unique as it is the only member to contain ilmenite and quartz crystals.

Mineral chemical data was obtained by electron microprobe analysis, using a Cameca SX100 electron microprobe at the Open University, Milton Keynes, UK (see Appendix B.2). Data was only obtained from feldspars, pyroxenes and Fe-Ti oxides as these are the three most abundant mineral phases in all members of the Rogerson Formation. Data show that individual eruption-units can be distinguished by the presence of discrete compositional modes within these abundant mineral phases, in particular the pyroxenes. Therefore data from each of these dominant mineral groups are described individually below.

3.9.1. Feldspars

Feldspar crystals, in all members, occur as two textural types here termed 'Type 1' and 'Type 2' crystals. Type 1 crystals (Fig. 3.16b) are euhedral to subhedral laths, 1–3 mm in size, and contain inclusions of glass and/or smaller crystals (e.g., pyroxene, Fe-Ti oxides, or apatite). These inclusions are commonly concentrated within the core of Type 1 crystals, similar to the 'cellular feldspars' described by Wright et al (2002), which these authors attribute to rapid growth. Some Type 1 crystals also show weak zonation, although this is not a common observation and core to rim variation is typically <1% An (Table C.5). Where zoning is present inclusions of glass seem to be concentrated within single zonation rings.

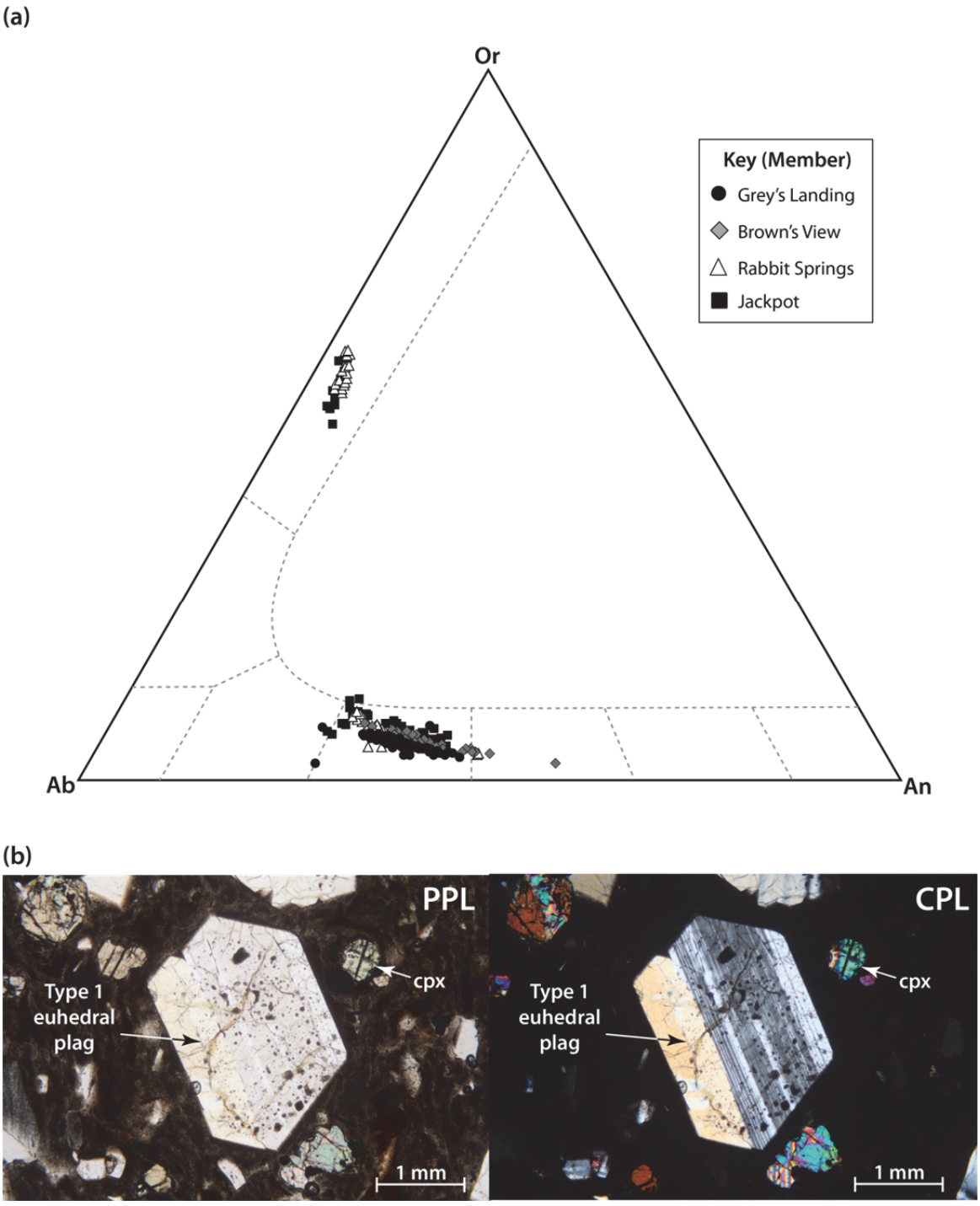

Figure 3.16. (a) Feldspar ternary diagrams showing the dominance of plagioclase (andesine) in all members of the Rogerson Formation. Sanidine is also present in the Jackpot and Rabbit Springs members, but is absent from all overlying members. **(b)** Photomicrographs in plane polarised (PPL) and cross polarised (CPL) light showing an example of a euhedral 'Type 1' plagioclase (plag) crystal containing brown glass inclusions. Smaller pyroxene crystals (cpx) also surround the plagioclase crystal and are isolated within the glassy matrix.

Type 2 crystals are smaller (0.2–0.5 mm) euhedral–subhedral crystals, most of which have at least one broken margin and are likely fragments of larger crystals. These crystals show no zoning and are commonly isolated within the matrix.

Plagioclase is ubiquitous throughout the entire Rogerson Formation (Table.C.5) and is dominantly andesine (An_{31}–An_{48}) with oligoclase (An_{25}–An_{28}) also present in the older Jackpot Member. This broad compositional range means that plagioclases are not particularly useful when discriminating between individual members of the Rogerson Formation (Fig. 3.16a). However, sanidine (An_2–An_6, Or_{51}–Or_{61}; Table C.5) is also present in the Jackpot and Rabbit Springs members, but is absent from the younger Brown's View and Grey's Landing members (Fig. 3.16a). This therefore provides a distinct stratigraphic horizon between the Rabbit Springs and Brown's View members where sanidine disappears from the phenocryst assemblage, and is useful when distinguishing between the older and younger eruption-units.

3.9.2. Pyroxenes

Pyroxene crystals, in all members, are typically subhedral and small (0.5–1 mm in size) with slightly rounded crystal faces. They occur both as single crystals and as part of crystal aggregates with Type 1 feldspars (Fig. 3.17b). Compositionally they occur as two types; Ca-rich augite and Ca-poor pigeonite (Table C.6), both of which are ubiquitous throughout the Rogerson Formation. MgO concentrations of these pyroxenes are useful for discriminating between some members of the Rogerson Formation.

The pyroxenes of both the Jackpot and Rabbit Springs members are indistinguishable and define two compositional modes: a single mode of pigeonite and a single mode of augite, although augite is slightly less abundant in the Jackpot Member (Fig. 3.17a). The overlying Brown's View Member, however, is unique as it contains pigeonites and augites that have the highest MgO concentrations of any other member of the Rogerson Formation (Fig. 3.17a). The compositions of pyroxenes within the overlying Grey's Landing Member are similar to those of the Jackpot and Rabbit Springs members. However the Grey's Landing Member is unique from all other members of the Rogerson Formation as it contains two compositional pairs of pigeonite and augite. Pair 1 includes pigeonites (P1, Fig. 3.17a) with MgO concentrations between 8.22 and 9.29 wt.% (Table C.6), and augites (A1, Fig. 3.17a) with lower MgO concentrations between 7.28 and 7.97 wt.% (Table C.6). Whereas, pair 2 includes pigeonites (P2, Fig. 3.17a)

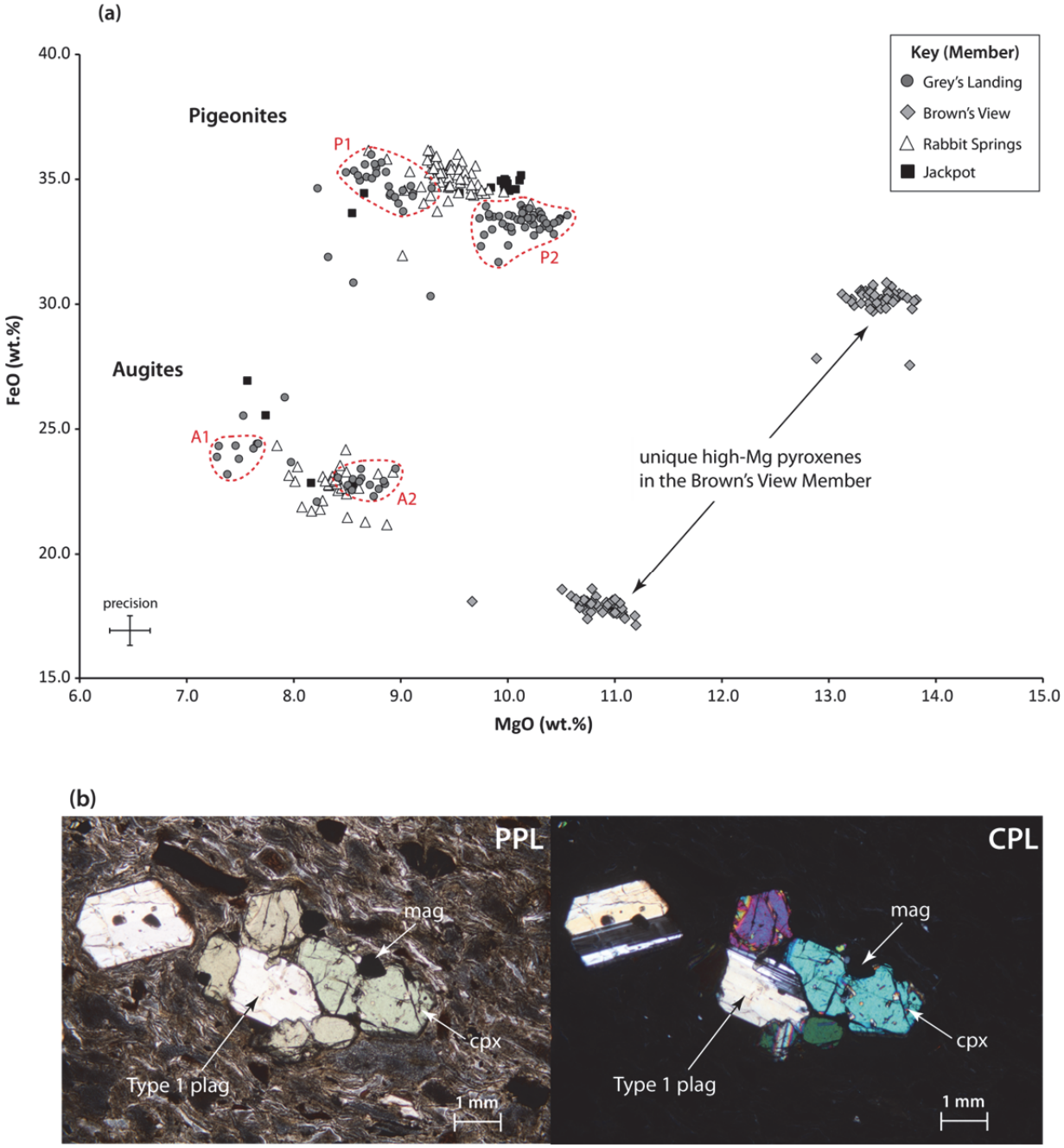

Figure 3.17. **(a)** Pigeonite and augite compositions from all members of the Rogerson Formation. Compositions of pigeonites and augites in the Jackpot, Rabbit Springs, and Grey's Landing Members are broadly similar. However, the Grey's Landing Member can be distinguished from the other members as it contains two modes of pigeonite (P1 and P2) and two modes of augite (A1 and A2). Pyroxenes in the Brown's View Member are unique as they have significantly higher MgO concentrations. **(b)** Photomicrographs in plane polarised (PPL) and cross polarised (CPL) light.showing an example of a typical Rogerson Formation crystal aggregate composed of Type 1 plagioclase (plag) and smaller subhedral crystals of pyroxene (cpx) and magnetite (mag).

with MgO concentrations between 9.74 and 10.56 wt.% (Table C.6), and augites (A2, Fig. 3.17a) with lower MgO concentrations between 8.22 and 8.95 wt.% (Table C.6). Multiple modes of pigeonite and augite are not seen in any other Rogerson Formation Member, however they have been noted within other cSRP ignimbrites (e.g., the Cougar Point Tuffs, Cathey & Nash, 2004).

3.9.3. Fe-Ti oxides

These crystal are commonly subhedral–anhedral and small (0.2–0.5 mm), although few reach a maximum of 1 mm. The dominant compositional phase is Ti-rich magnetite (16.06–33.58 wt.% TiO_2), which is present in all members of the Rogerson Formation. Ilmenite is also reported to be present in all members except the Grey's Landing member (Andrews et al., 2008), but was only found within the Jackpot Member in the present study.

3.10. Geochronology and periodicity of the Rogerson Formation

Previous studies (Bonnichsen et al., 2008; Ellis et al., 2012a) have provided age determinations on the older members of the Rogerson Formation and these are summarised in Table 3.1. An $^{40}Ar/^{39}Ar$ sanidine age of 10.97 ± 0.05 Ma (Ellis et al., 2012a) was obtained on the Jackpot Member (sub-unit 5 of Andrews et al., 2008), which marks the oldest record of silicic volcanism within the Rogerson Graben. In addition, $^{40}Ar/^{39}Ar$ sanidine ages were also obtained (Bonnichsen et al., 2008) for the 'Jackpot 7' sub-unit (10.62 ± 0.1 Ma) and the Rabbit Springs Member (10.49 ± 0.13 Ma). Both of these ages are indistinguishable and support the interpretation that 'Jackpot 7' is a lateral correlative of the Rabbit Springs Member (section 3.4.2). Hitherto, no age determinations exist for the younger Brown's View, or Grey's Landing Members. However, suggestions have been made by the 'composition and time' ('CAT') groups of Bonnichsen et al. (2008). They report that the Brown's View Member, belonging to 'CAT' group 10A, erupted sometime between 10–9.5 Ma and the Grey's Landing Member, belonging to 'CAT' group 12B, erupted sometime between 9.0–7.5 Ma.

Considering all above ages, the Rogerson Formation records a period of Miocene silicic volcanism that lasted for approximately ~3.5–2 million years. The five individual members emplaced during this time period yield an average frequency of one explosive

eruption every ~700–400 ka, which is similar to the 480 ka repose period between the Jackpot and Rabbit Springs members (Table 3.1). However, additional geochronology data are needed in order to further constrain the periodicity of eruptions recorded by the Rogerson Formation.

Table 3.1. Complied age determinations of members of the Rogerson Formation.

Member	Age	Method	Reference	Repose period (Ma)
Greys Landing	~9.0 – 7.5 Ma	'CAT group 12B'	Bonnichsen et al. (2008)	
Browns View	~10.0 – 9.5 Ma	'CAT group 10A'	Bonnichsen et al. (2008)	
Rabbit Springs	10.49 ± 0.13 Ma	$^{40}Ar/^{39}Ar$ sanidine	Bonnichsen et al. (2008)	
'Jackpot 7' sub-unit	10.62 ± 0.10 Ma	$^{40}Ar/^{39}Ar$ sanidine	Ellis et al. (2012)	~0.48 ± 0.14
'Jackpot 5' sub-unit	10.97 ± 0.05 Ma	$^{40}Ar/^{39}Ar$ sanidine	Ellis et al. (2012)	

3.11. Tectonic evolution of the Rogerson Graben

The N–S trending Rogerson Graben is bound by two dominant normal faults (Bonnichsen et al., 2008; Andrews et al., 2008), herein termed the Browns Bench fault and the Shoshone Hills fault. The Browns Bench fault is located in the western Rogerson Graben, and easterly down-throw has generated the present Browns Bench escarpment (~400 m relief). The Shoshone Hills fault is located to the east with westerly down-throw against the more subdued Shoshone Hills (Fig. 3.1). Development of the graben is thought to have coincided with a period of extension between ~12–7 Ma (Bonnichsen and Godchaux, 2002), during which NE-SW Basin-and-Range extension was enhanced by voluminous magmatic activity at the Yellowstone hot-spot and formed the 70 km wide west Snake River Plain rift.

All members of the Rogerson Formation, within the graben, were previously thought to thicken westwards, and so accumulated during the development of an asymmetric half-graben, with a westward dipping floor, controlled by the Browns Bench fault (Andrews et al., 2008). However, the present study allows further comment on the graben's tectonic evolution, which was likely more complex than previous thought (Andrews et al., 2008). A revised model for the evolution of the graben is proposed here as a series of progressive stages (Fig. 3.19 a–e) that account for lateral thickness variations of ignimbrites of the Rogerson Formation, and each are outlined below.

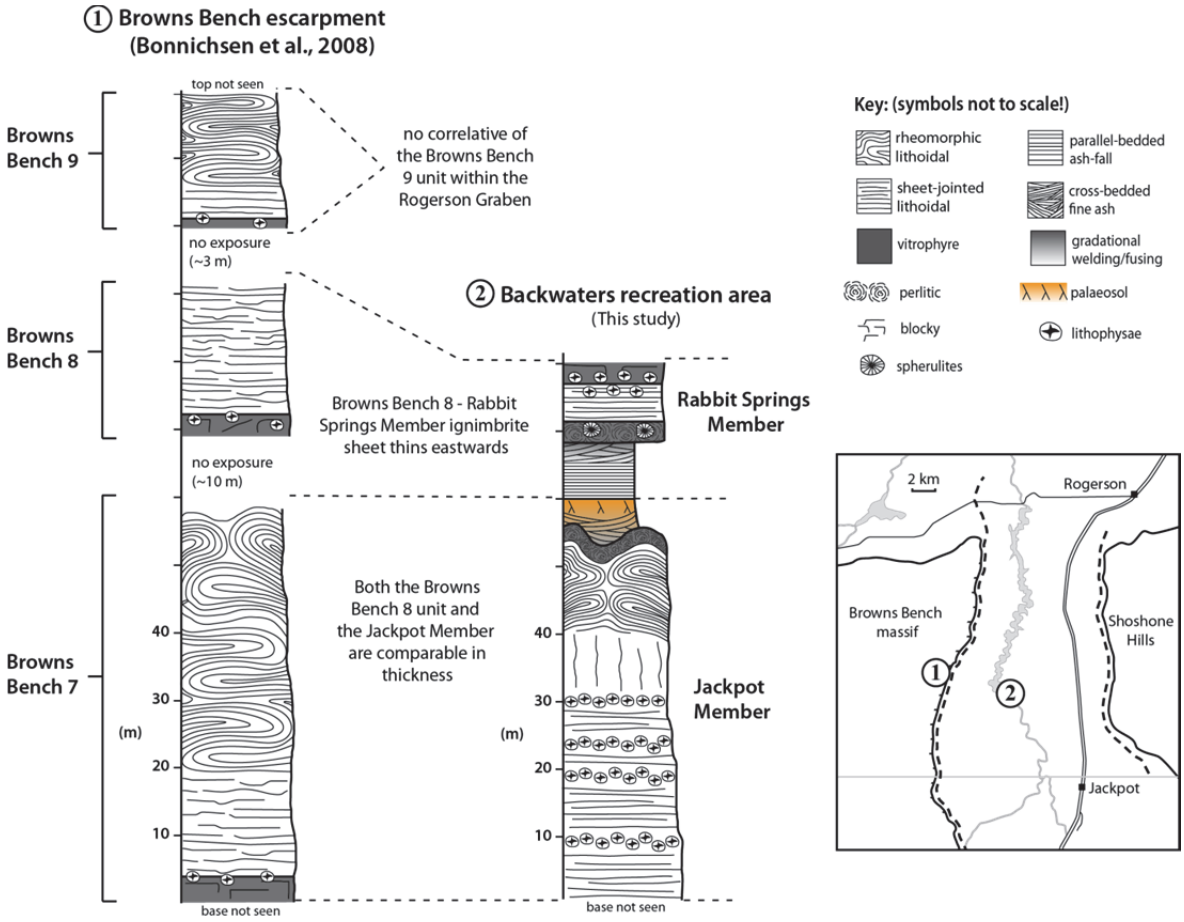

Figure 3.18. Graphic logs of the Browns Bench 7, 8 and 9 units (modified after Bonnichsen et al., 2008) and the Jackpot and Rabbit Springs Members within the Rogerson Graben (see inset map for localities). Full thickness of the Jackpot Member is adapted from its type section at the Salmon Fall Creek rest area (Fig. 3.4). Browns Bench 7 and the Jackpot Member are correlatives of one another (Ellis et al., 2012) and both are of similar thickness (base not seen). Browns Bench 8 and the Rabbit Springs Member have also been correlated together (Ellis et al., 2012) and the ignimbrite sheet thins eastwards.

3.11.1. Pre-Rogerson Graben extension

Pre-Miocene basement is not seen within the Rogerson Graben and the floor of the graben is thought to consist of the oldest Jackpot Member, which likely overlies pre-Rogerson Formation eruption-units of the Browns Bench succession (Andrews et al., 2008; Bonnichsen et al., 2008). Recent correlations have demonstrated that the Jackpot Member is correlated with the 'Browns Bench 7' eruption-unit, exposed on the Browns Bench escarpment, and the younger 'Browns Bench 8' eruption-unit is correlated with the Rabbit Springs Member (previously termed Jackpot 7, Andrews et al., 2008; Ellis et al., 2012; Fig. 3.18). The thickness of the Browns Bench 7 unit is similar to the thickness of the Jackpot Member within the graben (Fig. 3.18), although basal contacts of these units are not exposed. This implies that the Browns Bench fault probably did

not exist prior to the emplacement of the Browns Bench 7–Jackpot Member ignimbrite sheet (Fig. 3.19a). However, the Browns Bench 8–Rabbit Springs Member thins eastwards; therefore it is proposed that E-W extension, prior to its emplacement, generated a topographic slope towards the west (Fig. 3.19a). Age determinations on the Browns Bench 7–Jackpot Member and the Browns Bench 8–Rabbit Springs Member constrain the development of this depression to sometime between 10.97±005 Ma and 10.49±0.13 Ma (Fig. 3.19a).

3.11.2. Initiation of the Browns Bench fault (prior to ~10.34 Ma)

Browns Bench 8 is overlain by the 20 m-thick, 10.34±0.09 Ma, Browns Bench 9 eruption-unit (Bonnichsen et al., 2008; Fig. 3.18). However, no correlative of this unit has been identified within the Rogerson Graben. To explain this it is proposed that continued E-W extension caused the development of the Browns Bench fault, and that early displacement (prior to10.34±0.09 Ma) was to the west (Fig. 3.19b). This created a topographic barrier against which the Browns Bench 9 ignimbrite was emplaced (Fig. 3.19b).

3.11.3. Initiation of the Shoshone Hills fault and an E-sloping graben (prior to ~10 Ma)

Continued extension initiated the Shoshone Hills fault with a westerly down-throw generating an asymmetric half-graben with an eastward dipping floor (Fig. 3.19c). This is evidenced by the eastward thickening Brown's View Member (Fig. 3.19c), which suggests that the graben developed prior to its emplacement sometime between 10–9.5 Ma. The successive development of the Browns Bench fault and later the Shoshone Hills fault is also consistent with models for the development of planar fault arrays during uniform extension (e.g., McClay & Ellis, 1987).

3.11.4. Development of a W-sloping Rogerson Graben (prior to ~9 Ma)

Field observations in the present study have shown that the younger Grey's Landing Members thicken westwards, and this was also recognised in previous interpretations of the Rogerson Graben stratigraphy (Andrews et al., 2008). Therefore this suggests that prior to its emplacement (between 9.5 and 7.5 Ma, Bonnichsen et al., 2008) there was a topographic depression in the western Rogerson Graben.

In the present model continued E-W extension is proposed to have caused the reactivation of the Browns Bench fault, with down-throw now to the east (Fig. 3.19d). This marks the early development of the asymmetric Rogerson Graben, seen today, with

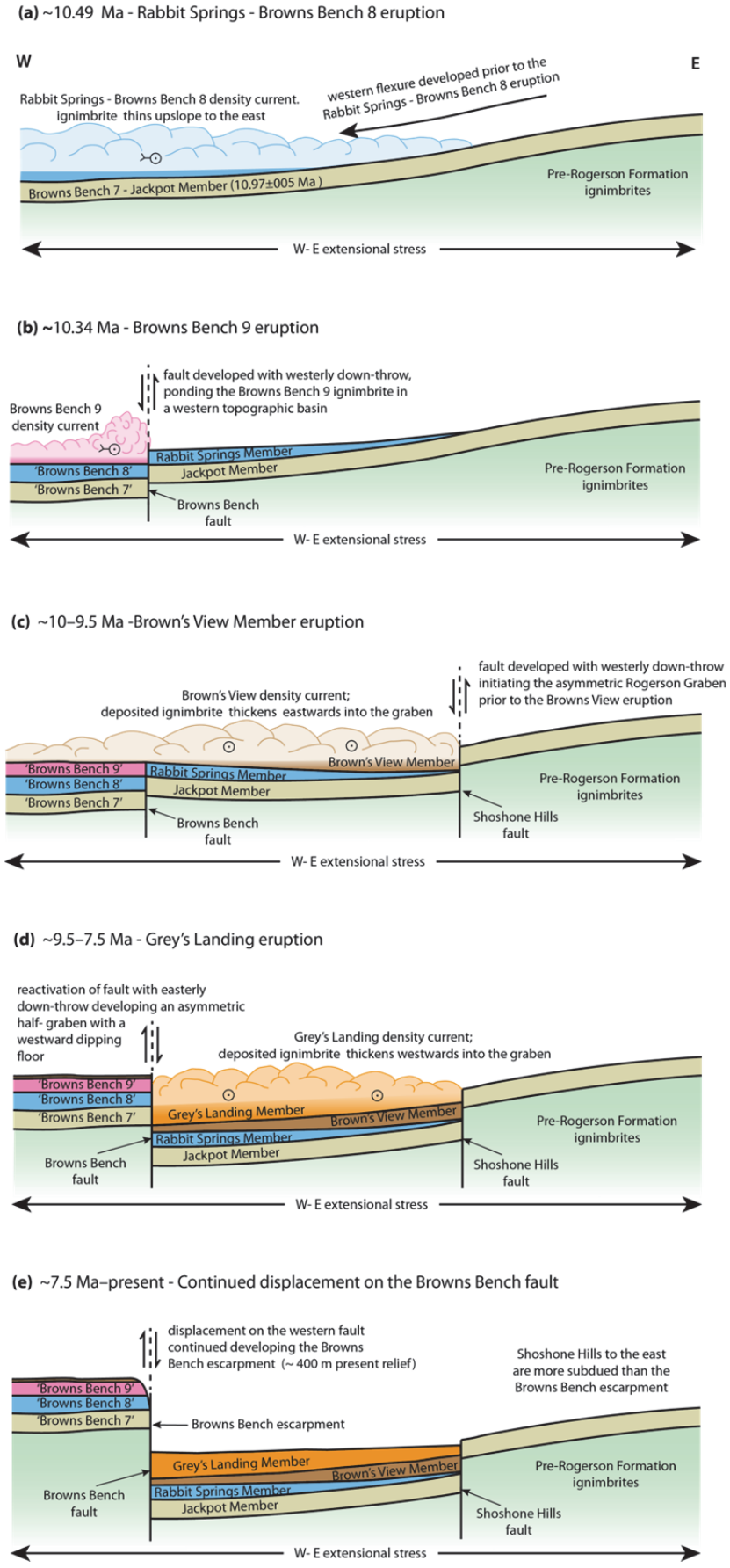

Figure 3.19. Model for the tectonic evolution of the Rogerson Graben as a series of progressive stages (a–e) that account for the lateral thickness variations of ignimbrites of the Rogerson Formation.

a westward dipping floor controlled by the Browns Bench fault. The graben was then successively infilled by the Grey's Landing Member, which ponded against the Browns Bench escarpment (Fig. 3.19d).

3.11.5. Continued displacement on the Browns Bench fault (~7.5 Ma – present)

At present, the relief of the Browns Bench fault escarpment is ~400 m (Fig. 3.19e). Therefore displacement on the Browns Bench fault continued post-emplacement of the Grey's landing Member, however this period of displacement is difficult to constrain as there are no age constraints on the Grey's landing Member, and no other younger units that would have been affected by this displacement.

3.12. Conclusions

The Rogerson Formation records a period of silicic explosive volcanism that originated from the cSRP between ~11–8 Ma. An investigation of the silicic pyroclastic succession within the Rogerson Graben has yielded the following conclusions (1–3):

(1) The volcanic succession within the Rogerson Graben comprises 5 individual eruption-units, each of which records a single explosive silicic eruption. This is two less than was defined in previous accounts (Andrews et al., 2008). Each eruption-unit constitutes a member of the re-defined Rogerson Formation.

(2) Individual units can be distinguished from one another using a combination of physical field characteristics, whole-rock and mineral chemistry, and some palaeomagnetic and geochronology data.

(3) Lateral thickness variations of ignimbrites within the Rogerson Graben imply that the tectonic evolution of the graben was more complex than previously thought (Andrews et al., 2008). Therefore, a new model is presented here that proposes the Rogerson Graben developed due to E-W extension, and alternate displacements on the Browns Bench and Shoshone Hills faults, resulting in an asymmetric half-graben with a westward dipping floor.

4. Rhyolitic volcanic succession of the Cassia Mountains in southern Idaho USA, and the petrogenetic evolution of the Cassia Formation rhyolites.

4.1. Introduction

The Cassia Mountains are a region of broad (~1500 km^2) domal uplift with a relief of ~1100 m (Wright et al., 2002), located within southern Idaho, with their southern margin in northern Nevada (Fig. 4.1). Late Palaeozoic basement is unconformably overlain by Miocene volcanics. The oldest rocks are mid-Ordovician marine limestones and orthoquartzites, exposed in the western limit of the range (Younquist & Haegele, 1956; Mytton et al., 1990; Williams et al., 1991), but most of the exposed basement is lower Permian sandstones and limestones (Younquist & Haegele, 1956; Mytton et al., 1990). The Miocene volcanic cover consists of Snake River (SR)-type (Branney et al., 2008) rhyolitic ignimbrites and associated ash-fall deposits, inferred to have originated from the Snake River Plain (Pierce & Morgan, 1992; McCurry et al., 1996), which are exposed within steep sided canyons (e.g., Rock Creek canyon, Fig. 4.1). Faulting is extensive and consists of numerous, small offset (e.g. 10s – 100s of metres), high-angle normal faults (Mytton et al., 1990; Williams et al., 1990, 1991, 1999). The most prominent faults strike north to northwest and northeast. Some faults are isolated within the pre-Tertiary rocks, while others penetrate into the overlying Miocene ignimbrite sequence. This indicates that faulting both predates and postdates emplacement of the Miocene volcanics. Faults that postdate the ignimbrites are often parallel to canyon walls and cause repetition of individual ignimbrite sheets; awareness of this is important when establishing the volcanic stratigraphy at any one locality.

Early studies of the Cassia Mountains volcanics identified and dated them as Miocene deposits (Anderson, 1931; Armstrong, 1975), and these were referred to as 'Idavada Volcanics' (Malde & Powers, 1962). Subsequent studies applied informal localised names to individual units located in the south (i.e., Goose Creek basin, Hackett et al., 1989; Trapper Creek, Perkins et al., 1995; Fig. 4.1). The Cassia Mountains were formally mapped and a volcanic stratigraphy established in the early 90's that documents five intensely-welded volcanic units separated by three non-welded tuff units (Mytton et al., 1990; Williams et al., 1990, 1991, 1999). From oldest to youngest these volcanic units

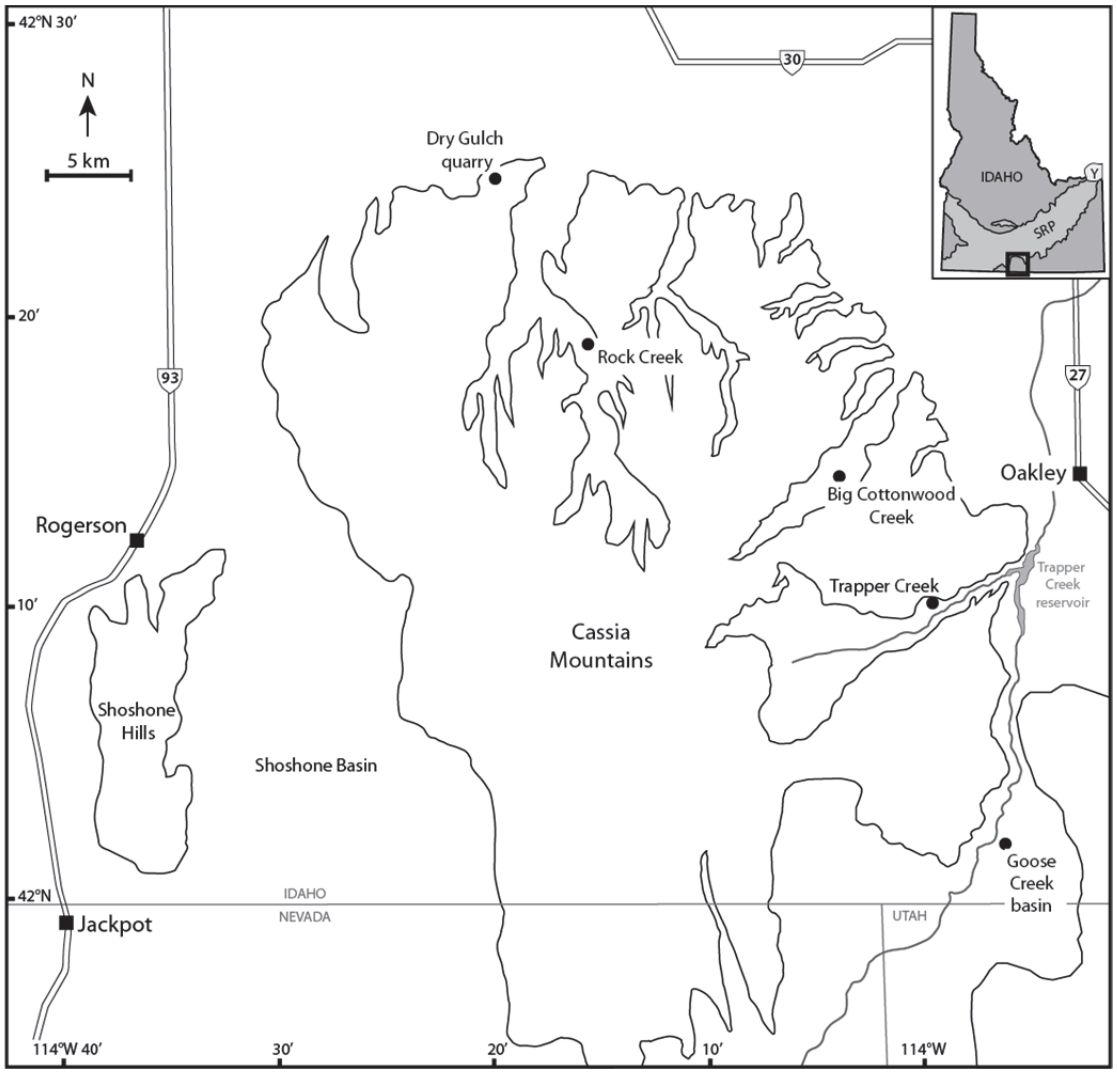

Figure 4.1. Simplified location map of the Cassia Mountains showing all major canyons, towns, and place names mentioned in the text. Inset shows the location of the Cassia Mountains (Black square) in relation to the Snake River Plain (SRP) in southern Idaho, Y = Yellowstone volcanic field.

were termed; (1) the 'Tuff of Ibex Peak'; (2) the 'Tuff of Magpie Basin'; (3) the 'Tuff of Big Bluff'; (4) 'Tt_1'; (5) the 'Tuff of Steer Basin'; (6) 'Tt_2'; (7) the 'Tuff of Wooden Shoe Butte' (separated into 'lower' and 'upper' members) and (8) the 'Tuff of McMullen Creek'. However, more recent studies (e.g., Wright et al., 2002; Ellis et al., 2010) have proposed significant revisions to this established stratigraphy. For example, palaeosol horizons were recorded within the 'Tt_2' unit (Ellis et al., 2010) and it was therefore sub-divided it into three separate eruption-units termed; the Niles Gulch Member; the Antelope Member; and the Deadeye Member (Ellis & Branney, 2010). It was also noted that the lower and upper members of the overlying Tuff of Wooden Shoe Butte are chemically distinct; however these remained designated as a single eruption-unit (Ellis et al., 2010). In addition, the younger 'Tuff of McMullen Creek' has been sub-divided into five

members, termed McMullen members 1–5 (Wright et al., 2002), and suggestions have been made for more (Ellis et al., 2010).

4.2. Rationale

Recent studies have demonstrated that the Big Bluff and Steer Basin members can be correlated as part of more widespread ignimbrite sheets (Ellis et al., 2012a). However, to date, no correlations have been suggested within the younger members. The purpose of the present study was to define the characteristic features of each eruption-unit, in order to 'finger-print' them, with the aim to correlate these eruption-units with other silicic eruption-units exposed across the central Snake River Plain (cSRP) (Chapter 6). However, field mapping and logging combined with whole-rock and mineral chemistry and some palaeomagnetic data, as part of this study, have identified potential discrepancies in the number of eruption-units identified within the Cassia Mountains volcanic succession (Wright et al., 2002; Ellis et al., 2010).

The present study identifies thirteen individual rhyolitic eruption-units and each is designated as a member of the Cassia Formation (after Ellis et al., 2010). The established nomenclature (of Williams et al., 1990, and Ellis et al., 2010) for the majority of the units is maintained; however new terminology has been established for the newly-defined eruption-units (Fig. 4.2). Therefore, the following chapter presents a revised Cassia Formation comprising thirteen members (Fig. 4.2) herein termed: (1) the Ibex Peak Member, (2) the Magpie Basin Member, (3) the Big Bluff Member, (4) the Steer Basin Member, (5) the Niles Gulch Member, (6) the Antelope Member, (7) the Deadeye Member, (8) the Wooden Shoe Butte Member, (9) the Little Creek Member, (10) the Dry Gulch Member, (11) the Indian Springs Member, (12) the McMullen Creek Member, and (13) the Lincoln Reservoir Member. Descriptions of each member as well as supporting evidence for these revisions are presented below. In addition, the limited exposure of the non-welded members (e.g., the Ibex Peak Member, Mytton et al., 1990; and the Deadeye Member, Ellis & Branney, 2010) means they were not formally described or sampled as part of this study. However, descriptions and interpretations of these units are provided with reference to the existing literature.

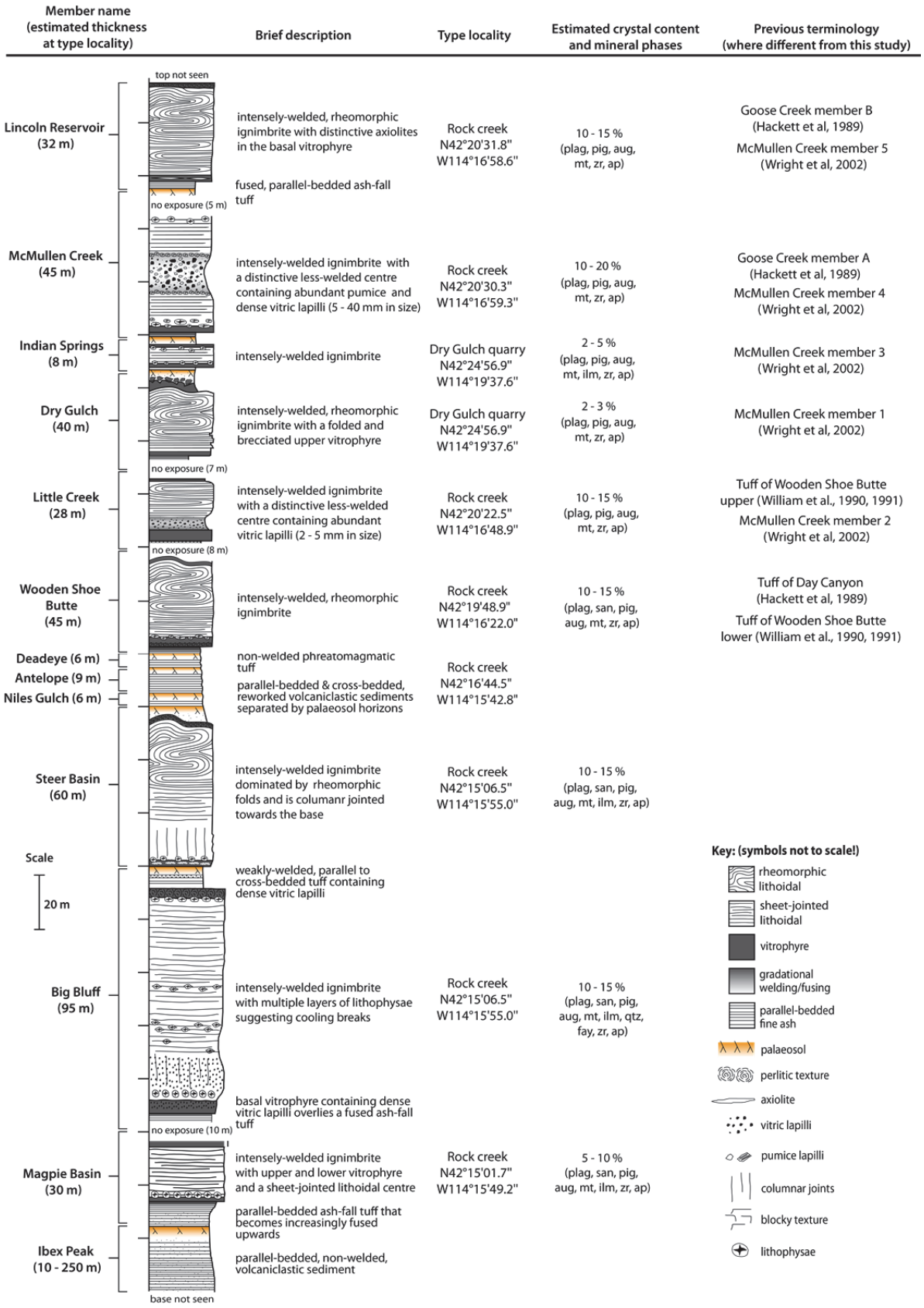

Figure 4.2. Generalised vertical section of the Cassia Formation showing the main physical features of each of the thirteen members. Phenocryst abbreviations are: plag – plagioclase, pig – pigeonite, aug – augite, mt – magnetite, ilm – ilmenite, qtz – quartz, fay – fayalite, zr – zircon, ap – apatite.

4.3. The Ibex Peak Member

The Ibex Peak Member (Mytton et al., 1990) was not formally described as part of this study and is predominantly exposed in the south-east Cassia Mountains. It unconformably overlies Permian limestone, and is conformably overlain by the Magpie Basin Member. In addition, the member is also locally overlain unconformably by the Big Bluff Member. The 'Tuff of Ibex Peak' is described as a white-grey massive to bedded ash, which is locally cross-bedded and contains interbeds of conglomerate and carbonaceous shale (Mytton et al., 1990). It also varies in thickness from <10 m to ~250 m-thick, and generally thickens eastwards (Mytton et al., 1990).

4.3.1. Interpretation: Previous interpretations of the Ibex Peak Member attribute it to deposition from sustained sub-aerial plinian fallout (Mytton et al., 1990). However the presence of cross-bedding and interbedded sedimentary facies (e.g., conglomerate and shale) suggests it is more likely volcaniclastic sediment formed by reworking of non-welded ash into the Goose Creek Basin (Hilbrand & Newman, 1985).

4.4. The Magpie Basin Member

The Magpie Basin Member (Ellis et al., 2010) is ~30 m thick at its type locality in Rock Creek, Cassia Mountains, Idaho (Fig. 4.3 inset) and is composed of a well-bedded basal rhyolitic ash-fall tuff and an intensely-welded rhyolitic ignimbrite. It overlies a palaeosol in the top of the Ibex Peak Member (Williams et al, 1991) and is overlain by the Big Bluff Member (contact not seen). The member is poorly exposed, due to it infilling palaeo-topography that developed within the Ibex Peak Member (Williams et al, 1991), and is commonly overlapped and obscured by the younger Big Bluff Member.

4.4.1. Description

The lowest exposure of the member is 5 m of parallel-bedded, non-welded, fine ash and pumice layers that change colour from white to grey upwards, probably due to fusing by the overlying Magpie Basin ignimbrite (Fig. 4.3; Fig. 4.5a). The base of the ignimbrite is a 2 m-thick vitrophyre with an estimated crystal content of ~5 % (1–4 mm crystals) comprising a mineral assemblage of sanidine, plagioclase, augite, pigeonite, ilmenite, magnetite, rare quartz and accessory apatite and zircon (section 4.17). This crystal content and crystal size range is consistent throughout the entire member. The basal vitrophyre is sharply overlain by an 18 m-thick lithoidal zone. The contact is also marked by large

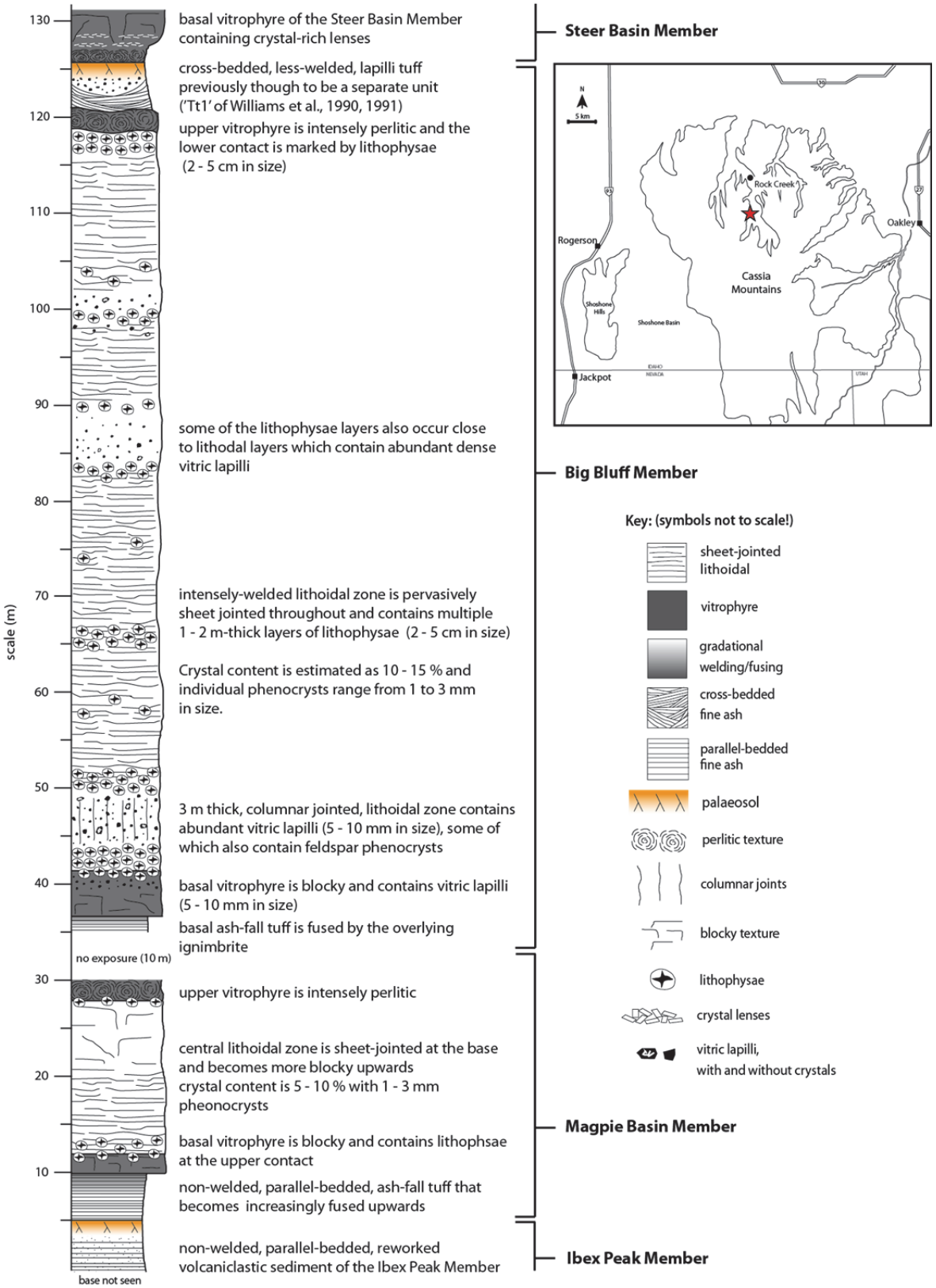

Figure 4.3. Graphic logs of the Magpie Basin and Big Bluff Members. Inset shows the type locality (red star) for these members within Rock Creek canyon

lithophysae, 15–20 cm in size (Fig. 4.3). The lower 10 m of the lithoidal zone is pervasively sheet jointed; however the density of joints decreases upwards and the upper 8 m has a blocky fracture. The top of the lithoidal zone is also marked by a 2 m-thick layer of lithophysae (2–3 cm in size) that passes sharply upwards into a 1 m-thick perlitic upper vitrophyre (Fig. 4.3). A ~10 m gap in exposure separates the Magpie Basin Member from the overlying Big Bluff Member, and likely conceals the upper-most parts of the Magpie Basin Member and base of the Big Bluff Member. Therefore a contact is inferred approximately 5 m above the upper vitrophyre.

4.4.2. Lateral variations

Exposures of the member are limited to the central Cassia Mountains (Williams et al., 1991). At the type locality the Magpie Basin ignimbrite exhibits rapid lateral thickness variations, within ~100 m, which also changes its internal lithofacies. At its thickest (~20 m-thick) it has a simple welding profile of an upper and lower vitrophyre separated by a central lithoidal zone (Fig. 4.4). If traced laterally it thins to ~10 m and is composed of vitrophyre throughout with a 2 m-thick layer of abundant lithophysae (10–20 cm in size) and thick axiolites (30–40 cm-thick) in the centre that may suggest the incomplete development of the lithoidal zone seen in thicker exposures (Fig. 4.4; Fig. 4.5b).

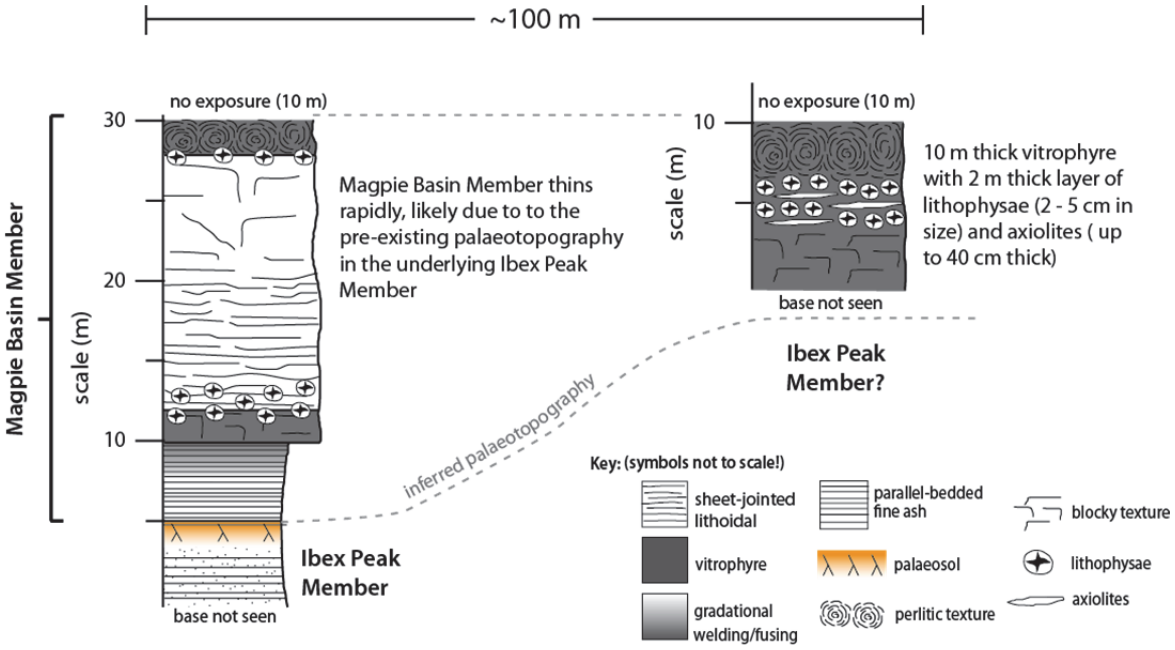

Figure 4.4. Graphic logs showing the rapid lateral thickness variations of the Magpie Basin Member. This variation is thought to be due to the underlying palaeotopography developed within the Ibex Peak Member (inferred by dashed line).

Figure 4.5. (a) Ash-fall tuff at the base of the Magpie Basin Member., which becomes fused upwards. **(b)** Thin (<10 m-thick) exposure of the Magpie Basin ignimbrite likely deposited on a palaeotopographic high (Fig. 4.4). **(c)** ~90 m-thick exposure of the Big Bluff Member, multiple erosional benches are indicative of its compound nature. **(d)** Dense vitric lapilli within the lower lithoidal zone of the Big Bluff Member. **(e)** Cross-bedding within the upper lapilli-tuff of the Big Bluff Member.

4.4.3. Interpretation

The Magpie Basin Member is interpreted to record a single eruption due to an absence of palaeosols, fallout layers or reworked horizons between the different lithologies, which indicates that there were no significant time gaps during its emplacement. The basal 5 m of parallel-bedded pumice and ash layers are interpreted as pumice-fall and ash-fall deposited from sustained sub-aerial fallout. The overlying intensely-welded ignimbrite is an example of a simple cooling unit (*sensu* Smith, 1960; Wilson & Hildreth, 2003) deposited from a high temperature pyroclastic density current. The rapid lateral changes in thickness exhibited by the ignimbrite are likely in response to underlying palaeotopography; with the thickest exposures deposited in palaeovalleys and the thinnest exposures deposited on palaeotopographic highs (Fig. 4.4).

4.5. The Big Bluff Member

The Big Bluff Member (Ellis et al., 2010) is the thickest welded member of the Cassia Formation (~95 m thick, Fig. 4.5c) and at its type locality in Rock Creek, Cassia Mountains (Fig. 4.3 inset) consists of a basal, parallel-bedded, rhyolitic ash-fall tuff overlain by an intensely-welded rhyolitic ignimbrite with a complex welding profile of intensely-welded zones and less-welded zones (Fig. 4.3). The member overlies the Magpie Basin Member (contact not seen) and is overlain by the Steer Basin Member (Ellis et al., 2010). It can also be distinguished from other nearby rhyolitic eruption-units by its large thickness, complex welding profile, including multiple layers of lithophysae and layers containing abundant, non-vesicular, vitric lapilli.

4.5.1. Description

The lowest exposure of the Big Bluff Member is a 1.5 m-thick parallel-bedded ash-fall tuff, which has been fused by the overlying Big Bluff ignimbrite (Fig. 4.3). The base of the ignimbrite is a 4 m-thick vitrophyre containing abundant non-vesicular vitric lapilli, 5–10 mm in size (Fig. 4.3). Crystal content of the vitrophyre is estimated at 10–15 %, with crystals 1–4 mm in size. This crystal content and size range is consistent throughout the Big Bluff Member, from base to top, and comprises a mineral assemblage of sanidine, plagioclase, augite, ilmenite, magnetite, quartz, rare fayalitic olivine and accessory apatite and zircon. The presence of fayalitic olivine is unique to the Big Bluff Member and is not observed in any other members of the Cassia Formation. In addition, the member contains

only augite, which is also distinct as all other Cassia Formation members contain both pigeonite and augite (section 4.17).

The basal vitrophyre is sharply overlain by a ~78 m-thick lithoidal zone, and the contact is marked by a 3 m-thick layer of lithophysae, 5–15 cm in size (Fig. 4.3). Above this lithophysal layer the lithoidal zone is blocky with well-developed columnar jointing and also contains abundant vitric lapilli, 5–20 mm in size (Fig. 4.5d). It is likely that these vitric lapilli are a continuation of those seen in the basal vitrophyre, but are obscured by the 3 m-thick lithophysal layer. Vitric lapilli disappear upwards and are mostly absent from the remaining lithoidal zone. However, there are discrete layers where they are more abundant at various heights through the member, and some of these layers are also associated with layers of lithophysae (Fig. 4.3). Sheet-jointing is also pervasive throughout the lithoidal zone, and in the upper 10 m these highlight metre-scale rheomorphic folds. The lithoidal zone is sharply overlain by a 2 m-thick perlitic upper vitrophyre, which is overlain by a 5 m-thick less-welded lapilli-tuff (Fig. 4.5e) that is locally cross-bedded and contains abundant vitric lapilli, 5–10 mm in size. The base is also slightly back-fused by the underlying ignimbrite suggesting it was emplaced while the ignimbrite was still hot (e.g., similar to the 'Jackpot 6' unit of Andrews et al., 2008). This lapilli-tuff was previously described as a separate unit termed the 'Tt_1' unit (Williams et al., 1991), although the lack of a palaeosol or ash-fall layers between it and the underlying ignimbrite, and the back-fusing, suggests there was no significant repose period between their emplacements. Therefore the present study redefines the 'Tt_1' unit as part of the Big Bluff Member.

4.5.2. Lateral variations

The Big Bluff Member is well exposed throughout the Cassia Mountains (Williams et al, 1991), although was not extensively mapped as part of this study. The majority of members within the Cassia Formation show thinning away from the Snake River Plain (e.g., the Wooden Shoe Butte Member, section 4.10.2). Therefore it is inferred that the Big Bluff Member exhibits the same lateral thickness variation, although the effect of thickness variations on its internal lithofacies remains unknown. The capping lapilli-tuff has been described as varying in thickness from 10–25 m due to subsequent reworking into palaeotopographic basins (Williams et al., 1991).

4.5.3. Interpretation

The Big Bluff Member is interpreted to record a single explosive eruption due to an absence of palaeosols or reworked horizons between the different lithologies, which indicates that there were no significant time gaps during its emplacement. The basal 1.5 m of parallel-bedded ash is interpreted as ash-fall tuff deposited from sustained sub-aerial fallout. The overlying Big Bluff ignimbrite is a compound cooling unit (*sensu* Smith, 1960; Wilson & Hildreth, 2003; Fig. 4.5c) and the multiple layers of lithophysae throughout the member are interpreted as cooling breaks, which formed during brief periods of repose between ignimbrite pulses. These lithophysal layers are also commonly located adjacent to layers rich in vitric lapilli. If these vitric lapilli represent cooler accidental lithics they may have acted as heat sinks (e.g., Marti et al., 1991) causing a lower emplacement temperature for these layers that may have chilled the underlying and later overlying margins of the ignimbrite, defining a cooling break. The capping lapilli tuff is interpreted as being deposited from a fully-dilute density current (*sensu* Branney & Kokelaar, 2002), which was later locally reworked into a volcaniclastic sediment.

4.6. The Steer Basin Member

The Steer Basin Member (Ellis et al., 2010) is a ~60 m thick intensely-welded rhyolitic ignimbrite sheet, and is one of the thicker members of the Cassia Formation. At its type locality in Rock Creek (Fig. 4.6 inset) it consists of an upper and lower vitrophyre separated by a lithoidal centre (Fig. 4.6). It overlies a palaeosol in the top of the Big Bluff Member and is overlain by the non-welded Niles Gulch Member (Ellis et al, 2010). The Steer Basin Member can be distinguished from other nearby rhyolitic units by a distinctive perlitic obsidian layer at its base and by crystal-rich lenses within its basal vitrophyre (Fig. 4.7a).

4.6.1. Description

The lowest exposure of the Steer Basin Member is an aphyric, highly perlitic, obsidian layer, 0.3m-thick, which is sharply overlain by a 2 m-thick basal vitrophyre (Fig. 4.6). The lower 0.5 m of the vitrophyre contains crystal-rich lenses, up to 10 cm in length (Fig. 4.7a) that are characteristic of the Steer Basin Member and define diffuse cross-bedding. Despite these crystal-rich lenses, overall crystal content throughout the member is estimated at 10–15% with a mineral assemblage comprising plagioclase, sanidine, pigeonite, augite, magnetite, ilmenite and accessory apatite and zircon. The vitrophyre is

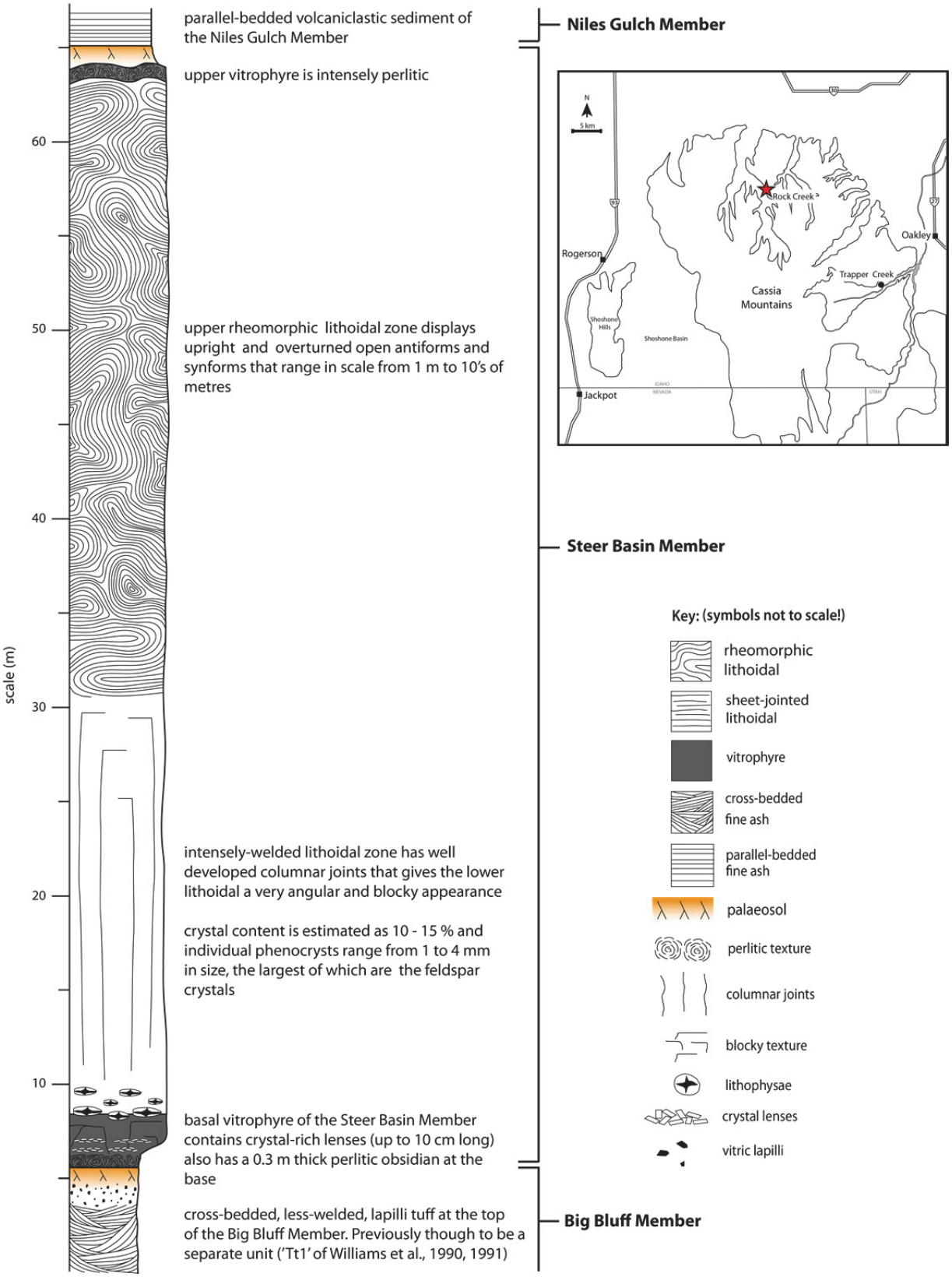

Figure 4.6. Graphic log of the Steer Basin Member. Inset shows the type locality (red star) for the member within Rock Creek canyon

sharply overlain by a 54 m-thick lithoidal zone and the contact is marked by abundant lithophysae, 5–10 cm in size. The lower 20 m of the lithoidal zone exhibits well developed columnar joints (Fig. 4.7b) and also has sparse sheet jointing. The upper 34 m of the lithoidal zone shows upright to overturned open rheomorphic antiforms and synforms, up to 10 m in scale (Fig. 4.6). The lithoidal zone is sharply overlain by a 1 m-thick upper vitrophyre that follows the underlying folds, and this is overlain by ~1 m of non-welded massive ash that develops upwards into a weak palaeosol and caps the Steer Basin Member.

4.6.2. Lateral variations

The Steer Basin Member is exposed throughout the Cassia Mountains (Williams et al., 1990) and thins towards the south. In Trapper Creek (Fig. 4.1) it thins to ~14 m, however its internal lithofacies are unchanged and the characteristic basal perlitic obsidian and crystal-rich lenses are still observed. In addition, recent correlations have proposed that the Steer Basin Member is part of a much more widespread ignimbrite sheet that extends ~80 km across the southern cSRP (Ellis et al., 2012a).

4.6.3. Interpretation

The Steer Basin Member is inferred to record a single explosive eruption due to an absence of palaeosols, fallout layers or reworked horizons between the different lithologies, which indicates that there were no significant time gaps during its emplacement. The basal 0.3 m-thick obsidian layer is interpreted to likely have been a very fine basal ash-fall tuff deposited from sustained sub-aerial fallout, which was subsequently fused to obsidian during the emplacement of the Steer Basin ignimbrite. The crystal rich lenses at the base of the ignimbrite are interpreted to represent the initial ground-surge of the Steer Basin ignimbrite (e.g., 'Layer 1' of Sparks et al, 1973). The entire ignimbrite is also an example of a simple cooling unit (*sensu* Smith, 1960; Wilson & Hildreth, 2003) likely emplaced from a single high-temperature pyroclastic density current, as there is no evidence for any internal cooling breaks from base to top.

4.7. The Niles Gulch Member

The Niles Gulch Member (Ellis et al., 2010) is ~6 m-thick and overlies a palaeosol in the top of the Steer Basin Member and is overlain by the non-welded Antelope Member (Ellis et al., 2010); however it was not formally described as part of the present study. Previous

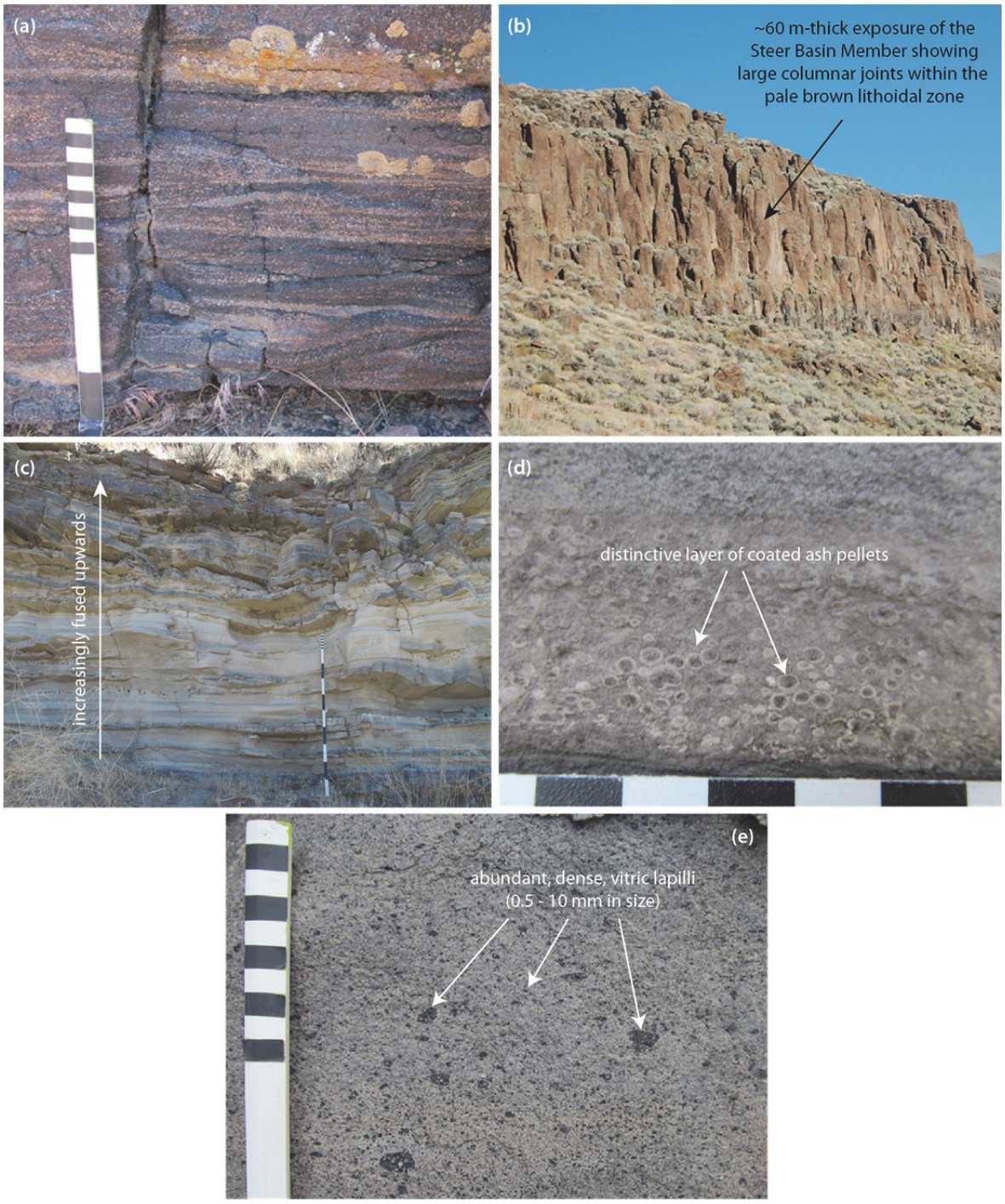

Figure 4.7. (a) Crystal-rich lenses in the basal vitrophyre of the Steer Basin Member. **(b)** ~60 m-thick exposure of the Steer Basin Member showing the large columnar joints throughout the lithoidal zone. **(c)** Basal ash-fall tuff of the Wooden Shoe Butte Member, note how the tuff becomes darker and increasingly fused upwards. **(d)** Distinctive layer of coated ash pellets within the upper fused ash-fall tuff of the Wooden Shoe Butte Member. **(e)** Abundant, dense, vitric lapilli (0.5–10 mm in size) in the central less-welded lapilli-tuff of the Little Creek Member.

observations describe thin beds of moderate to well-sorted gravel overlain by interbedded sandstones and mudstones with irregular thickness variations that are capped by a palaeosol (Ellis, 2009).

4.7.1. Interpretation

The Niles Gulch Member has been interpreted as reworked volcaniclastic sediment that was likely deposited within a lacustrine environment (Ellis et al., 2010).

4.8. The Antelope Member

The Antelope Member (Ellis et al., 2010) is ~6 m-thick and overlies a palaeosol in the top of the Niles Gulch Member and is overlain by the Deadeye Member (Ellis et al., 2010); however it was not formally described as part of the present study. Previous observations describe a non-welded unit comprising normally graded sandstone and mudstone interbeds overlain by massive sandstone with diffuse cross-laminations and ripple laminations (Ellis, 2009). Lenses of coarse sand and clast-supported gravel also occur near the top, and the unit is capped by a palaeosol.

4.8.1. Interpretation

The Antelope Member has also been interpreted as reworked volcaniclastic sediment deposited within a lacustrine environment (Ellis et al., 2010).

4.9. The Deadeye Member

The Deadeye Member (Ellis & Branney, 2010) is ~6 m-thick and overlies a palaeosol in the top of the Antelope Member and is overlain by the basal ash-fall tuff of the Wooden Shoe Butte Member (Ellis et al., 2010, section 4.10). Although not formally described as part of the present study, it has been well described in previous studies (Ellis et al., 2010; Ellis & Branney, 2010) as a non-welded massive to diffusely cross-bedded ignimbrite that contains abundant angular, non-vesicular, vitric lapilli, and also accretionary lapilli. The ignimbrite is also overlain by a parallel-bedded ashfall tuff, which contains coated ash pellets and ash clumps (Ellis & Branney, 2010).

4.9.1. Interpretation

The Deadeye Member is interpreted as the first-recorded example of explosive silicic phreatomagmatism in the cSRP (Ellis & Branney, 2010), and the non-welded character of the member in comparison with other Snake-River-type intensely-welded ignimbrites

suggests a lower emplacement temperature during an eruption in a lacustrine environment. This is supported by the abundant accretionary lapilli and the coated ash pellets and ash clumps in the upper ash-fall tuff, all of which record the moist aggradation of ash due to the involvement of water during the eruption (Ellis & Branney, 2010).

4.10. The Wooden Shoe Butte Member

The Wooden Shoe Butte Member was previously thought to be a single eruption-unit, ~65 m-thick, comprising two flow units termed the 'Lower Wooden Shoe' and the 'Upper Wooden Shoe' (Williams et al., 1990; Ellis et al., 2010). However, whole-rock (Fig. 4.22) and mineral chemical data (section 4.17) show that the 'Lower Wooden Shoe' and the 'Upper Wooden Shoe' (herein termed the Little Creek Member) are distinct from one another. In addition, palaeomagnetic mean flow directions (Finn & Coe, unpublished, Fig. 4.8) of each unit are distinguishable. Therefore, the present study is able to demonstrate that the two flow units are actually two distinct eruption-units, and hence the Wooden Shoe Butte Member is redefined as a 45 m-thick eruption-unit overlain by the newly defined Little Creek Member (section 4.11).

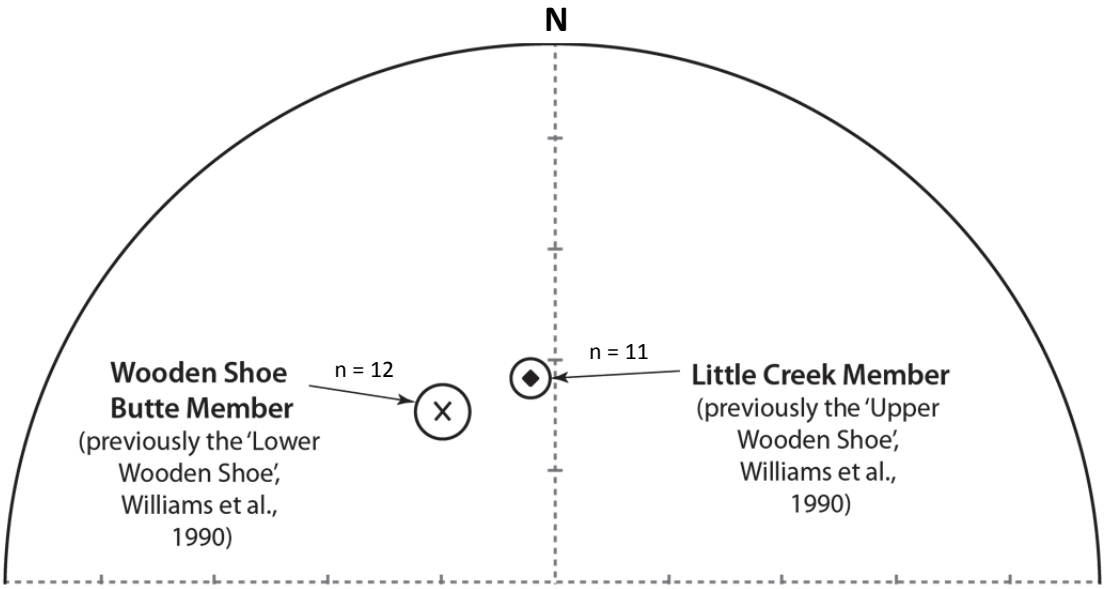

Figure 4.8. Stereonet showing the distinct palaeomagnetic mean flow directions of the Wooden Shoe Butte Member and the Little Creek Member. This supports the interpretation that these two units are individual eruption-units and should not be grouped as in previous studies (Williams et al., 1990; Ellis et al., 2010)

At its type section in Rock Creek (Fig. 4.9 inset) the Wooden Shoe Butte Member overlies a palaeosol in the top of the underlying Deadeye Member (Ellis & Branney, 2010), and is overlain by the Little Creek Member (contact not exposed). It consists of a non-welded, fused, rhyolitic ash-fall tuff and an intensely-welded rhyolitic ignimbrite. The member is easily distinguished from other nearby rhyolites by a characteristic ash-pellet layer in the basal ash-fall tuff, which is observed at all localities throughout the Cassia Mountains (Fig. 4.7d). It is also the youngest member of the Cassia Formation to contain sanidine in its phenocryst assemblage (section 4.17), which is absent from all the overlying members.

4.10.1. Description

The basal 6 m of the member consists of non-welded parallel-bedded ash-fall tuff (Fig. 4.7c) with sparse pumice-fall interbeds (individual pumices up to 10 mm in size). Local cross laminations and ripple laminations are also observed that may suggest small degrees of reworking. The tuff becomes increasingly fused upwards towards the contact with the overlying ignimbrite, which is marked by a gradational colour shift from white (little fusing) to dark grey (highly fused). The fused ash also contains a distinctive 4 cm-thick layer of ash coated pellets (0.5 cm in size), located ~30 cm from the base of the ignimbrite (Fig. 4.7d). The base of the ignimbrite is a 3 m-thick vitrophyre with an estimated crystal content of 10–15 %. This crystal content is consistent throughout the ignimbrite, from base to top, and comprises a mineral assemblage of plagioclase, sanidine, pigeonite, augite, magnetite and accessory apatite and zircon. The vitrophyre is highly perlitic at its base but becomes blockier upwards and is sharply overlain by a ~27 m-thick lithoidal zone. The lower ~12 m of the lithoidal zone are both folded and flow banded and exhibit tight, sub-horizontal, isoclinals folds that are commonly obscured by pervasive sheet jointing (Fig. 4.9). Rheomorphic folding is more evident in the upper ~15 m where upright to overturned, open, antiforms and synforms are dominant. The lithoidal zone is sharply overlain by a 1 m-thick upper vitrophyre that is poorly exposed at the type locality and is better observed in Trapper Creek to the south (Fig. 4.10). Here the vitrophyre is also overlain by ~2 m of diffusely bedded grey ash that develops upwards into a pale orange palaeosol. While the contact with the overlying Little Creek Member is not observed, this capping palaeosol is consistent with the Wooden Shoe Bute Member being a separate eruption-unit.

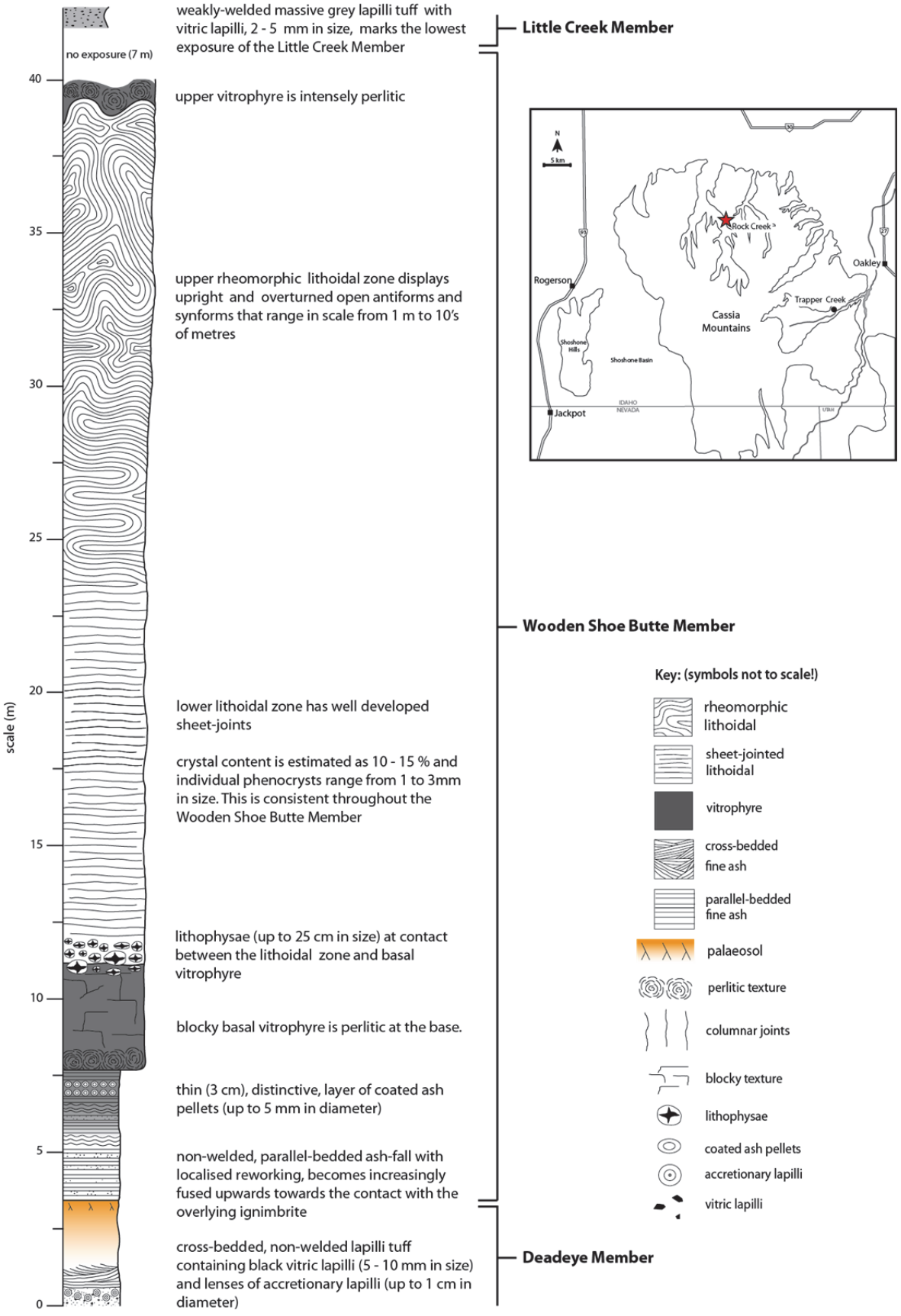

Figure 4.9. Graphic log of the Wooden Shoe Butte Member. Inset shows the type locality (red star) for the member within Rock Creek canyon.

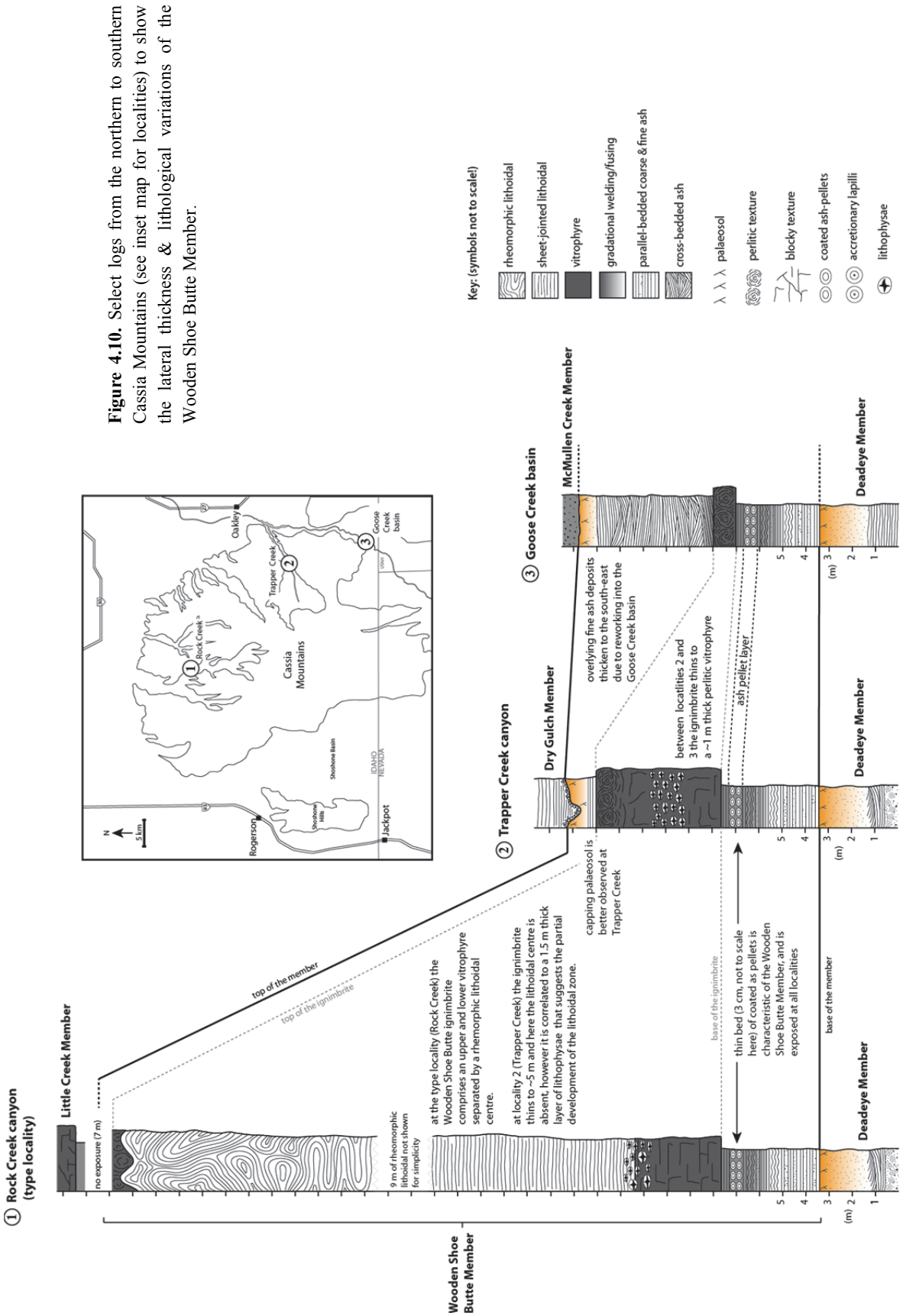

Figure 4.10. Select logs from the northern to southern Cassia Mountains (see inset map for localities) to show the lateral thickness & lithological variations of the Wooden Shoe Butte Member.

4.10.2. Lateral variations

The member is exposed at multiple localities across the entire Cassia Mountains, and generally thins southwards away from the Snake River Plain. Logging of the member at several localities reveals that the basal ash-fall tuff show minimal thickness variations and the distinctive ash-pellet layer is exposed within the upper fused zone at all localities (Fig. 4.10). However, the overlying Wooden Shoe Butte ignimbrite thins significantly southwards. In Trapper Creek it thins to ~5.5 m-thick (Fig. 4.10) and comprises an upper and lower vitrophyre separated by a 1.2 m-thick band of lithophysae, which is likely a correlative of the lithoidal centre better developed further north. The ignimbrite is inferred to approach its distal limit further south in the Goose Creek Basin (Fig. 4.10), where it was previously described as the 'Tuff of Day Canyon' (Hackett et al, 1989). Here it is a 0.9 m-thick perlitic vitrophyre that overlies ~5 m of white ash, containing the distinctive ash pellet layer, and is overlain by ~9 m of cross-stratified ash with a capping palaeosol (Fig. 4.10).

4.10.3. Interpretations

The Wooden Shoe Butte Member is interpreted as a single explosive eruption due to an absence of palaeosols, fallout layers or reworked horizons between the different lithologies, which indicates that there were no significant time gaps during its emplacement. The basal ash-fall tuff was deposited as a result of sustained sub-aerial fallout, and also has suffered some slight reworking post-emplacement as evidenced by localised cross-bedding and ripple laminations. The overlying intensely-welded ignimbrite is interpreted to be the result of a high temperature pyroclastic density current that approached its distal limit in the southern Cassia Mountains (Goose Creek Basin). The ignimbrite is also an example of a simple cooling unit (*sensu* Smith, 1960; Wilson & Hildreth, 2003), with no evidence for any internal cooling breaks from base to top. The overlying parallel-bedded ash is also interpreted to have been deposited due to sub-aerial fallout and may also have been co-ignimbrite. However, the greater thickness of the upper ash in the Goose Creek Basin suggests that it has been heavily reworked into the basin post-emplacement.

4.11. The Little Creek Member

The Little Creek Member is a newly defined member of the Cassia Formation and was previously interpreted as the upper flow unit of the Wooden Shoe Butte Member (Ellis et al., 2010). However, whole-rock chemical data show that the Little Creek Member is distinct from the Wooden Shoe Butte Member (Fig. 4.22). In addition, the Little Creek Member is readily distinguishable from all other Cassia Formation members as it contains unique pyroxenes with the highest MgO concentrations of any other unit (Fig. 4.24a). It also is the oldest member of the Cassia Formation not to contain sanidine. The disappearance of sanidine between the Wooden Shoe Butte and Little Creek Members also marks a unique stratigraphic horizon within the Cassia Formation.

At its type locality in Rock Creek.(Fig. 4.11 inset) it is ~28 m-thick rhyolitic ignimbrite with a complex welding profile that consists of lower and upper intensely-welded zones separated by a less-welded lapilli-tuff containing abundant, non-vesicular, vitric lapilli, 0.5–1 cm in size (Fig. 4.7e). The member overlies the Wooden Shoe Butte Member (contact not seen) and is overlain by the Dry Gulch Member (contact also not seen). Due to its complex welding profile the member has been sub-divided into layers (A-E) in order to facilitate its description.

4.11.1. Description

The lowest exposure of the Little Creek Member is an incipiently-welded, massive, grey tuff containing abundant vitric lapilli, 2–5 mm in size (layer A, Fig. 4.11). Upwards marks a rapid gradational increase in welding and the basal tuff is overlain by a 4 m-thick vitrophyre (layer B, Fig. 4.11). This transition to intensely-welded vitrophyre is also concurrent with the disappearance of the vitric lapilli. The crystal content of Layer B is estimated at 10–15 % (crystals 1–2 mm in size), and this proportion and size range is consistent throughout the Little Creek Member. Layer B is overlain by a 6 m-thick lapilli-tuff containing abundant, non-vesicular vitric lapilli (layer C, Fig. 4.11). From the lower to upper contact, these vitric lapilli first show reverse zoning, with respect to size (2–5 mm at the base to a maximum of 10 mm in the centre), which is followed by normal zoning, with 2–5 mm lapilli at the upper contact (Fig. 4.11). Layer C also exhibits gradational welding, and is most welded towards the upper and lower contacts and is least welded at the centre. This gradational welding is contemporaneous with the size of the vitric lapilli, with the least welding seen where the sizes of the lapilli are at a maximum (~ 10 mm). As welding increases upwards, Layer C grades sharply into an

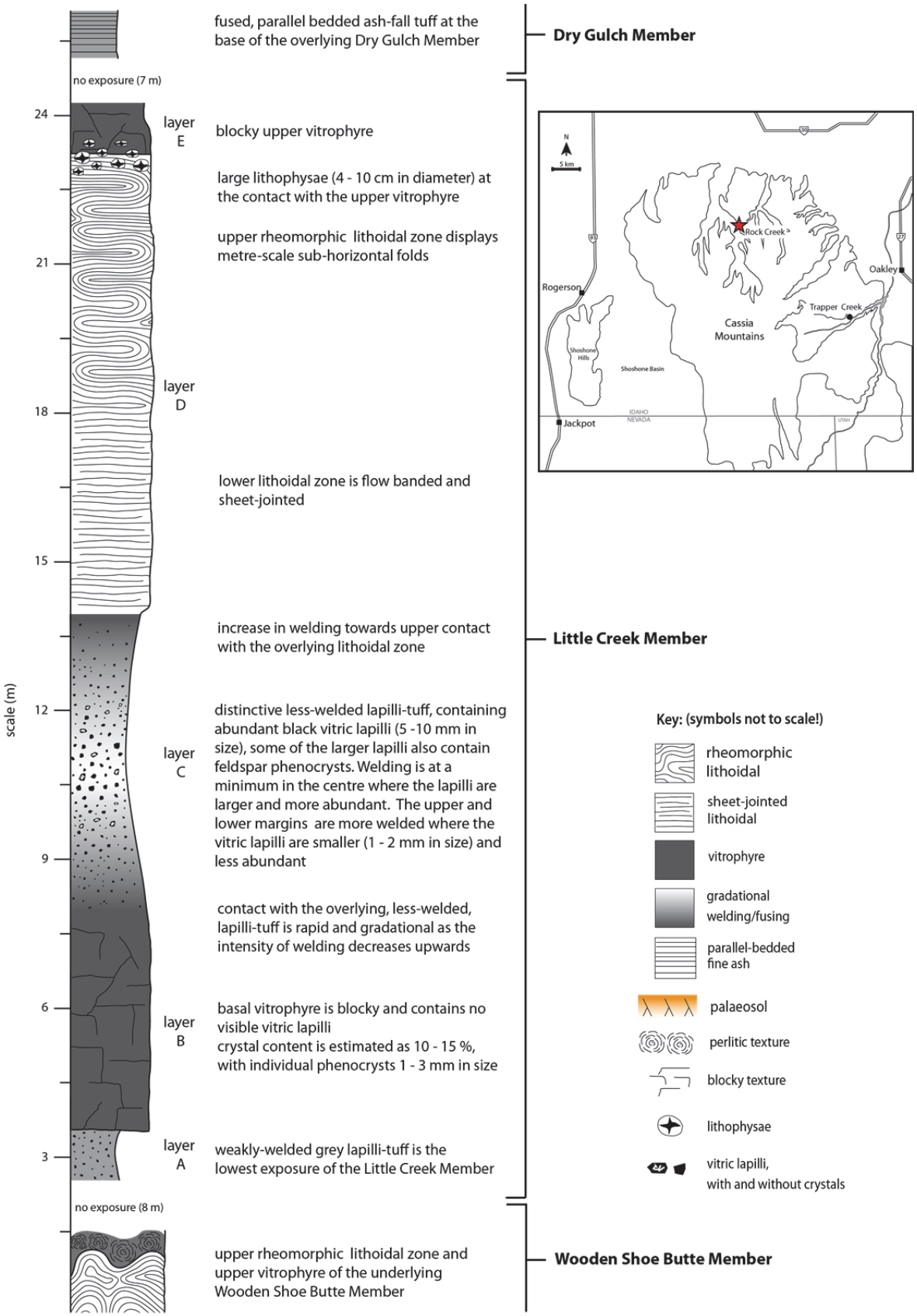

Figure 4.11. Graphic log of the Little Creek Member. Inset map shows the type locality (red star) for the member within Rock Creek canyon.

intensely-welded lithoidal zone (layer D, Fig. 4.11) and the vitric lapilli disappear. The lower ~4 m of layer D is pervasively sheet jointed, which are likely exploiting a sub-horizontal rheomorphic fabric. Rheomorphic folding is more evident in the upper ~5 m of layer D, which exhibits metre-scale recumbent folds. Layer D is sharply overlain by a 1 m-thick upper vitrophyre (layer E, Fig. 4.11) and the contact is marked by abundant lithophysae (4–10 cm in size). The top of the Little Creek Member is not seen, and a ~7 m gap in exposure separates it from the overlying Dry Gulch Member. Therefore a contact is inferred approximately halfway between the two members.

4.11.2. Lateral variations

The Little Creek Member is not as regionally extensive as other members of the Cassia Formation, and is primarily isolated to the northern Cassia Mountains (Williams et al., 1990). At the type section it is ~28 m-thick and it is inferred to thicken northwards towards the Snake River Plain. Reports have suggested that it reaches thicknesses of up to ~60 m (Ellis, 2009) close to the Snake River Plain, however this was not observed during the present study. South of the type section the member is not well exposed, and it is absent from the stratigraphy exposed in Trapper Creek. This suggests that it pinches out somewhere in the central Cassia Mountains, although the precise distal limit remains unknown.

4.11.3. Interpretations

The Little Creek Member is interpreted to record a single explosive eruption due to an absence of palaeosols, fallout layers or reworked horizons between the different lithologies, which indicates that there were no significant time gaps during its emplacement. The complex vertical welding profile indicates that it is a compound cooling-unit (*sensu* Smith, 1960; Wilson & Hildreth, 2003). The two intensely-welded zones (upper and lower) imply emplacement temperatures sufficiently hot to cause intense welding; however the transition from the intensely-welded basal vitrophyre to the less-welded centre indicates a decrease in the emplacement temperature. This is interpreted as the effect of the incorporation of large volumes of cool vitric lapilli that may have acted as a heat sink, lowering the temperature of the density current and the accumulating deposit (e.g., Marti et al., 1991). Although the origin of the vitric lapilli remains unknown this interpretation assumes that the vitric lapilli were accidental in origin, and were entrained into the density current during eruption. It is also observed that as the size and abundance of the vitric lapilli decreases the degree of welding

increases (Fig. 4.11), which supports the interpretation that these lapilli lowered the emplacement temperature of the ignimbrite and prevented intense-welding.

4.12. The Dry Gulch Member

The Dry Gulch Member is a newly defined member of the Cassia Formation, and was previously interpreted as 'Member 1' of the 'Tuff of McMullen Creek' (Wright et al., 2002). However, whole-rock chemical data show that the Dry Gulch Member is distinct from all other members of the Cassia Formation (Fig. 4.22). It is also bound by a palaeosol below and above (Fig. 4.14), and is therefore defined in the present study as an individual ~40 m-thick rhyolitic eruption-unit that is not related to any of the overlying units. At the type locality, within a quarry in the northern Cassia Mountains (Fig. 4.12 inset), it comprises fused, parallel-bedded ash-fall and pumice-fall deposits that are overlain by an intensely-welded rheomorphic ignimbrite (Fig. 4.12). In the northern Cassia Mountains it overlies the Little Creek Member (contact not seen) and is overlain by the Indian Springs Member. In the south (Fig. 4.14) it overlies a palaeosol developed in the top of the underlying Wooden Shoe Butte Member as the Little Creek Member is absent.

4.12.1. Description

The lowest exposure of the Dry Gulch Member is 1.5 m of parallel-bedded, grey, pumice-fall and ash-fall layers (Fig. 4.12) that are fused by the overlying intensely-welded ignimbrite. These ash-fall and pumice-fall layers are typically poorly exposed and are not seen beyond the type area. The base of the overlying ignimbrite is a 2 m-thick vitrophyre that is sharply overlain by a 28 m-thick lithoidal zone that has a distinctive purple-grey colour that aids its identification in the field. The ignimbrite is also relatively crystal poor, in comparison with other members of the Cassia Formation, and crystal content is estimated at 2–3 % comprising a mineral assemblage of plagioclase, pigeonite, augite, magnetite and accessory apatite and zircon. The lower 10 m of the lithoidal zone are pervasively sheet jointed, but flow banding reveals sub-horizontal, isoclinal, rheomorphic folds (Fig. 4.13a). Rheomorphic folds becomes progressively more open upwards, and the upper 18 m of the lithoidal zone are dominated by upright to overturned antiforms and synforms up to 10 m in scale (Fig. 4.12). The lithoidal zone is sharply overlain by a 1–2 m-thick perlitic upper vitrophyre that follows the folding in the upper lithoidal and is locally faulted and auto-brecciated (Fig. 4.13b). The folding also disturbs the overlying massive fine ash, 3 m-thick, which is preserved and fused within synforms in the upper

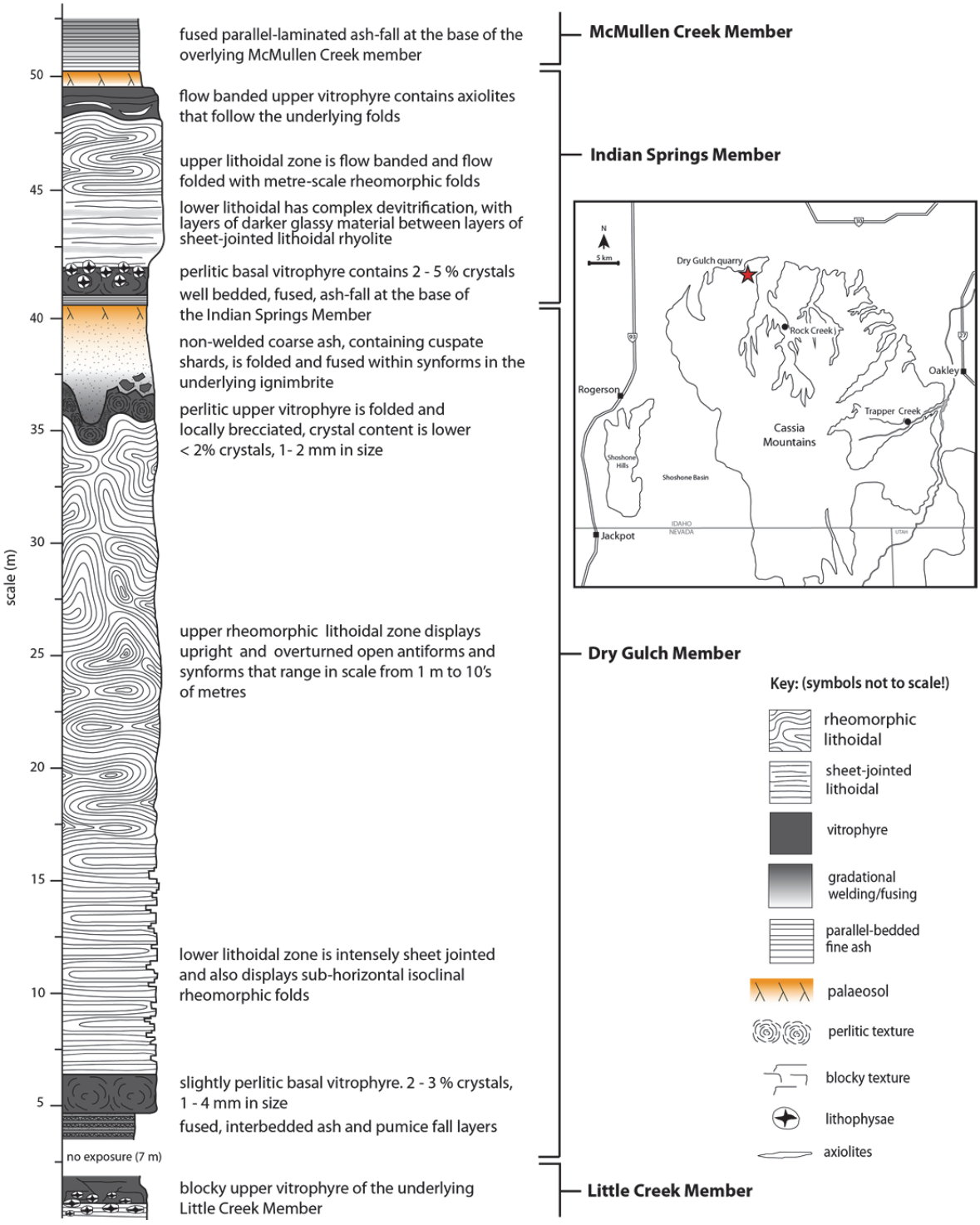

Figure 4.12. Graphic log of the Dry Gulch and Indian Springs members. Inset map shoes the type locality (red star) for both members within the Dry Gulch quarry in the northern Cassia Mountains

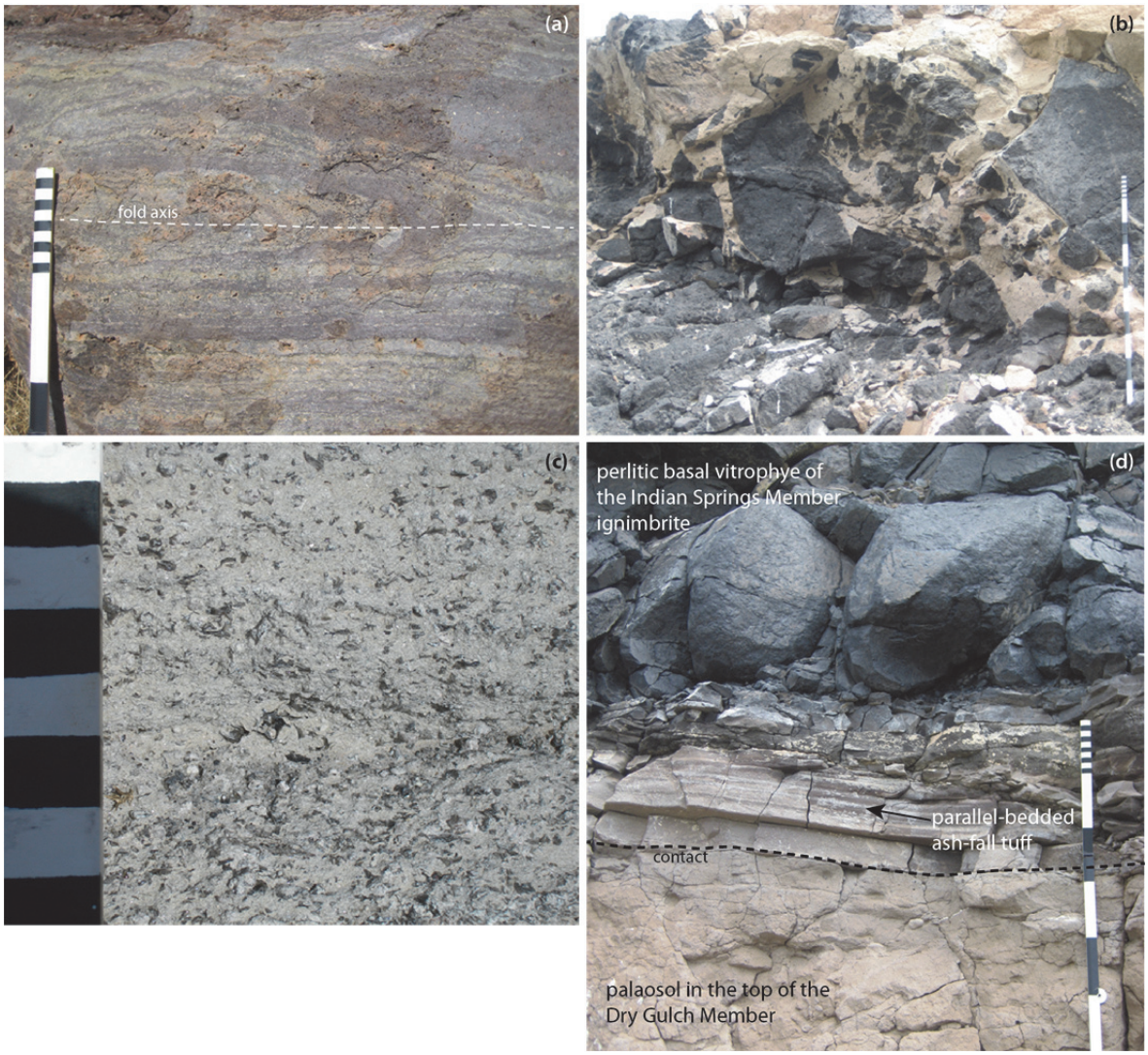

Figure 4.13. (a) isoclinal rheomorphic folds in the lower lithoidal zone of the Dry Gulch Member, also note that the pale-grey/ purple colouration of the flow-banding is characteristic of the member. **(b)** Upper vitrophyric auto-breccia at the top of the Dry Gulch Member, this deformation also disturbs the overlying ash, which is preserved between the vitrophyre clasts. **(c)** Large (5 mm) black cuspate glass shards within the non-welded ash deposit that overlies the Dry Gulch Member ignimbrite. **(d)** Contact between the Dry Gulch Member and the overlying Indian Springs Member. Lowest exposure of the Indian Springs Member is a fused parallel-bedded ash-fall tuff, which is overlain by an intensely-welded ignimbrite.

vitrophyre. The upper ash also contains cuspate vitric shards, 5–6 mm in size (Fig. 4.13c), and develops upwards to a pale orange palaeosol that is sharply overlain by the Indian Springs Member (Fig. 4.13d).

4.12.2. Lateral variations

The Dry Gulch Member is thickest in the northern Cassia Mountains and thins rapidly towards the south. The intensely-welded ignimbrite is exposed ~6 km south of the type locality, in a small quarry in north Rock Creek canyon. Further south along Rock Creek canyon, at the type locality for the Little Creek Member (Fig. 4.11 inset), a ~7 m gap in

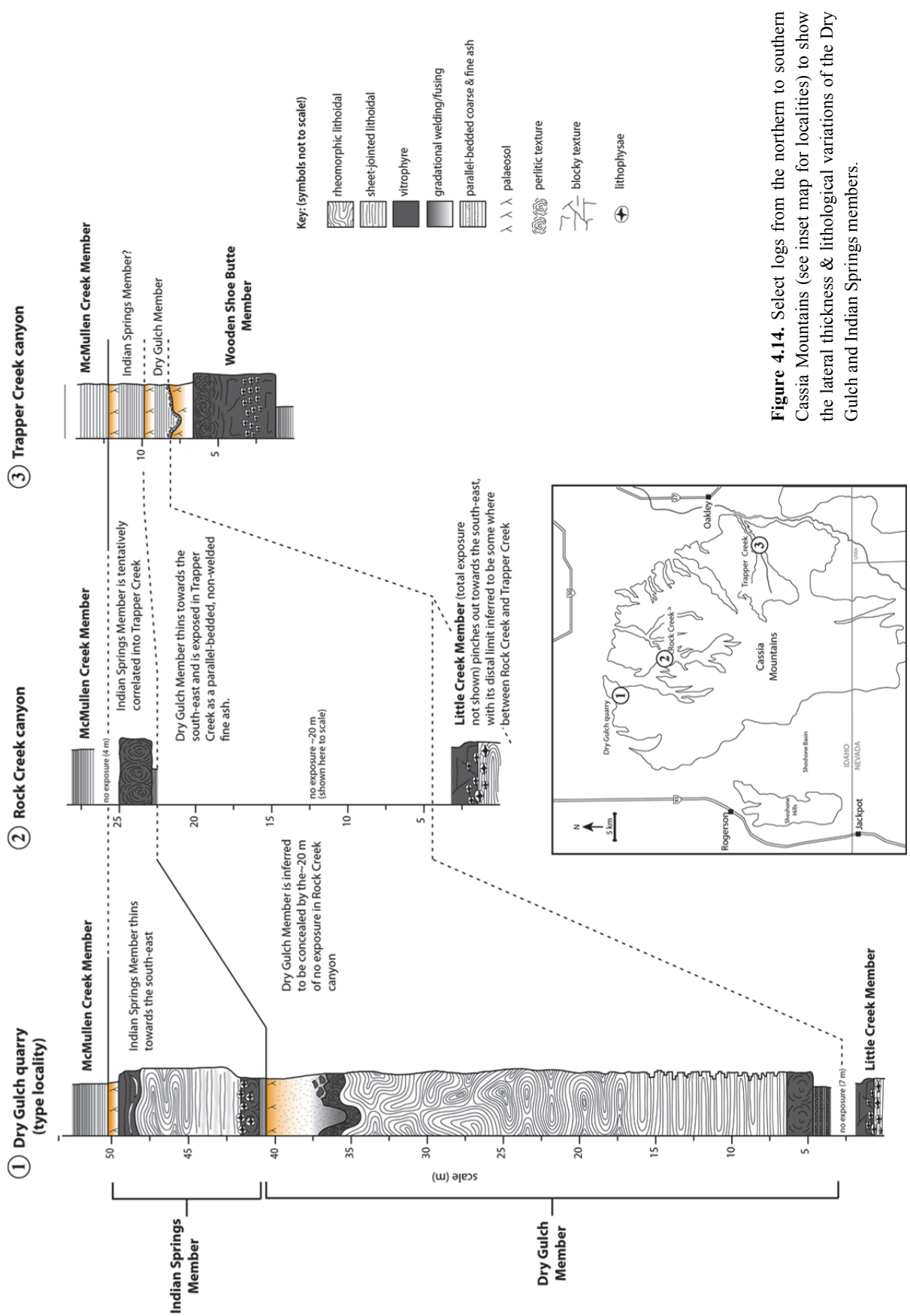

Figure 4.14. Select logs from the northern to southern Cassia Mountains (see inset map for localities) to show the lateral thickness & lithological variations of the Dry Gulch and Indian Springs members.

exposure separates the Little Creek Member from the overlying Indian Springs Member, and is inferred to conceal the entire Dry Gulch Member (Fig. 4.14). In Trapper Creek a 1.5 m-thick, non-welded, aphyric, ash deposit overlies a palaeosol developed at the top of the Wooden Shoe Butte Member, which is chemically indistinguishable from the Dry Gulch Member. This ash deposit is parallel-bedded with an erosional base that includes rip-up clasts of the underlying palaeosol (Fig. 4.14), and is interpreted as a lateral correlative of the Dry Gulch Member. This suggests that as the member thins southwards the degree of welding decreases.

4.12.3. Interpretations

The Dry Gulch Member is interpreted to record a single explosive eruption due to an absence of palaeosols, fallout layers or reworked horizons between the different lithologies, which indicates that there were no significant time gaps during its emplacement. The parallel-bedded pumice and ash layers, at the base of the Dry Gulch Member, are interpreted as the product of sub-aerial fallout. The overlying intensely-welded ignimbrite is interpreted as the product of a high-temperature pyroclastic density current that potentially approached its distal limit somewhere in the region of Trapper Creek. The lack of any internal breaks (i.e., ash-fall layers) also indicates a single emplacement unit and its welding profile is an example of a simple cooling unit (*sensu* Smith, 1960; Wilson & Hildreth, 2003). The overlying fine ash is also interpreted as deposition from sustained sub-aerial fallout and may also have been co-ignimbrite. As it is folded by the underlying ignimbrite it suggests that the ash was depositing while the ignimbrite was still deforming.

4.13. The Indian Springs Member

The Indian Springs Member is a newly defined member of the Cassia Formation and was previously interpreted as 'Member 3' of the 'Tuff of McMullen Creek' (Wright et al., 2002). It is bound by a palaeosol above and below, and therefore the present study redefines it as an individual ~8 m-thick rhyolitic eruption-unit that is not related to the underlying and overlying units. It is the thinnest member of the Cassia Formation and is composed of a parallel-bedded basal ash-fall tuff overlain by an intensely-welded rheomorphic ignimbrite (Fig. 4.12). At its type locality (Dry Gulch quarry, Fig. 4.12 inset) it overlies a palaeosol in the top of the Dry Gulch Member and is overlain by the McMullen Creek Member.

4.13.1. Description

The basal 0.3 m of the member is a pale grey, well-bedded, ash-fall tuff that has been slightly fused by the overlying intensely-welded ignimbrite (Fig. 4.13d). The base of the ignimbrite is a 1 m-thick perlitic vitrophyre with a sharp upper contact with the overlying 5 m-thick lithoidal zone. The lithoidal zone is flow banded and sheet jointed at the base with no observable flow folds, however the flow banding is clearly folded in the upper 3 m (Fig. 4.12). The lower 2 m of the lithoidal zone also displays a complex devitrification pattern with bands of glassier material between the lithoidal rhyolite (Fig. 4.12). The lithoidal zone is sharply overlain by a 2 m-thick upper vitrophyre that follows the rheomorphic folding in the lithoidal zone (Fig. 4.12), and contains folded axiolites and prolate lithophysae that also follow the flow banding. The vitrophyre is overlain by a non-welded, fine grained ash deposit that develops upwards into a tan palaeosol.

4.13.2. Lateral variations

The Indian Springs Member is the thinnest member of the Cassia Formation and is at its thickest (~8 m) in the northern Cassia Mountains and thins rapidly to the south. At the type section if traced laterally ~200 m the central lithoidal zone pinches out and the member is composed entirely of vitrophyre. Further south in Rock Creek canyon the member thins to a 2 m-thick perlitic vitrophyre (Fig. 4.14).

In Trapper Creek a parallel-bedded non-welded ash deposit, 1.5 m-thick, overlies a palaeosol in the top of the non-welded ash thought to be part of the Dry Gulch Member (Fig. 4.14). Due to its stratigraphic position this ash is inferred to be a distal correlative of the Indian Springs Member.

4.13.3. Interpretations

The Indian Springs Member is interpreted to record a single explosive eruption due to an absence of palaeosols, fallout layers or reworked horizons between the different lithologies, which indicates that there were no significant time gaps during its emplacement. The basal 0.3 m of ash is interpreted as an ash-fall tuff and is the result of sustained sub-aerial fallout. The overlying intensely-welded ignimbrite is the result of a high temperature pyroclastic density current that potentially reached its distal limit somewhere in the central Cassia Mountains and may also extend into Trapper Creek. The lack of any internal breaks (i.e., ash-fall layers) within the ignimbrite indicates a single

emplacement unit and its welding profile is typical of a simple cooling unit (*sensu* Smith, 1960; Wilson & Hildreth, 2003).

4.14. The McMullen Creek Member

The McMullen Creek Member is a newly defined member of the Cassia Formation and was previously interpreted as 'Member 4' of the 'Tuff of McMullen Creek' (Wright et al., 2002). As the thickest and most extensive of five ignimbrites (Fig. 4.2), previously thought to comprise the 'Tuff of McMullen Creek' (Wright et al., 2002), the established nomenclature is applied to this unit and it is herein termed the McMullen Creek Member (after Ellis et al., 2010). It is bound by a palaeosol above and below, and therefore the present study redefines it as an individual ~45 m-thick rhyolitic eruption-unit that is not related to its adjacent units. At its type locality (Rock Creek canyon, Fig. 4.15 inset) it overlies a palaeosol in the top of the Indian Springs Member, although this is better exposed at Dry Gulch quarry, and is overlain by the Lincoln Reservoir Member. It consists of a parallel-bedded basal ash-fall tuff overlain by a rhyolitic ignimbrite with a complex welding profile consisting of upper and lower intensely-welded zones separated by a less-welded lapilli-tuff (Fig. 4.15). This welding profile also helps distinguish the member from other adjacent ignimbrites, as only the Little Creek Member shares a similar profile (Fig. 4.11). Due to the complex nature of its vertical profile the McMullen Creek Member has been sub-divided into layers (A-G) to facilitate its description.

4.14.1. Description

The lowest exposure of the member is a pale grey, parallel-laminated, ash-fall tuff (layer A, Fig. 4.15) that has been partially fused by the overlying ignimbrite. The base of the ignimbrite is a 2 m-thick vitrophyre (layer B, Fig. 4.15) that is sharply overlain by a 13 m-thick lithoidal zone (layer C, Fig. 4.15). Both layer B and layer C make up the lower intensely-welded zone, and crystal content is estimated at 10–15 % with a mineral assemblage of plagioclase, pigeonite, augite, magnetite and accessory apatite and zircon. The lower 3 m of layer C are dominated by large (5–30 cm) lithophysal cavities, which become increasingly prolate upwards, and above this layer C is dominated by pervasive sheet jointing. The top of layer C is marked by a distinct 2 m-thick layer (layer D, Fig. 4.15) of abundant lithophysae (2–5 cm in size), which marks an abrupt change upwards from intensely welded tuff to less-welded lapilli-tuff (layer E, Fig. 4.15). Layer E is 10 m-thick

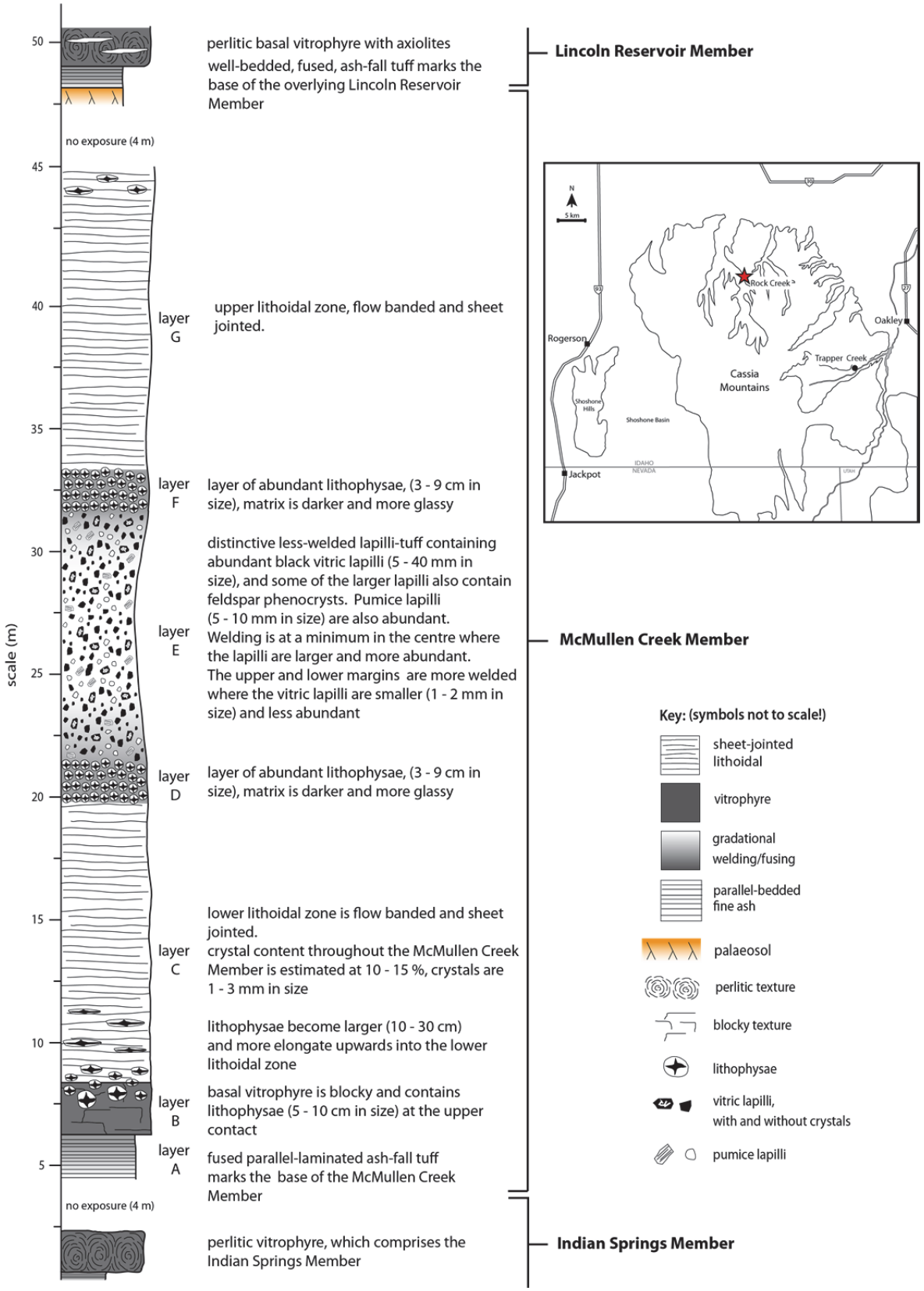

Figure 4.15. Graphic log of the McMullen Creek Member. Inset map shows the type locality (red star) for the member within Rock Creek canyon.

and contains abundant vitric and pumice lapilli. Most lapilli are angular clasts of vitrophyric and lithoidal rhyolite, 0.5–3 cm in size (Fig 4.17b), and the larger contain plagioclase crystals. These lapilli are tentatively interpreted to represent an accidental component (section 4.14.3). Pumice lapilli are rare in Snake River-type ignimbrites (Branney et al, 2008) and in layer E the pumices range from 0.5 to 1 cm in size. The upper and lower margins of layer E are darker in colour and more welded than the centre (Fig. 4.17a). The upper contact of layer E is also marked by a layer (layer F, Fig. 4.15) of abundant lithophysae, ~1.5 m thick, which marks a rapid increase in welding into a 10 m-thick lithoidal zone (layer G, Fig. 4.15). Layer G is pervasively sheet-jointed and contains isolated lithophysae towards the top. A ~4 m gap in exposure separates the top of layer G from a baked palaeosol that underlies the Lincoln Reservoir Member (Fig. 4.15). This gap is inferred to conceal the upper-most parts of the McMullen Creek Member, and the baked palaeosol is inferred to cap the member.

4.14.2. Lateral variations

The McMullen Creek Member is exposed across the entire Cassia Mountains (Williams et al., 1990). In the northern Cassia Mountains the member is ~20 m-thick and thickens southwards towards its type locality in Rock Creek canyon (Fig. 4.16). However, beyond the type section the member thins progressively towards the south. In Trapper Creek it thins to ~30 m and the central lapilli-tuff (layer E) is absent, which suggests that it pinches out somewhere between Rock Creek canyon and Trapper Creek. However, layers of abundant lithophysae are observed within the Trapper Creek exposures and these are interpreted as correlatives of layers D and F (Fig. 4.16). In Trapper Creek the non-welded basal ash-fall tuff (layer A) is ~10 m thick, which may suggest some degree of reworking into a local topographic basin. Here layer A is also overlain by a less-welded, grey, lapilli-tuff, containing small (1–5 mm) vitric lapilli, and also displays cross-bedding. This grey lapilli-tuff is not seen at the type section, however is characteristic of the southern exposures and is also observed in the Goose Creek basin. In the Goose Creek basin the entire member thins to ~10 m-thick (top not seen) and extends into northern Utah (Fig. 4.16). Crystal content also decreases to the south, from 10-15 % at the type locality to < 5 % in the Goose Creek basin.

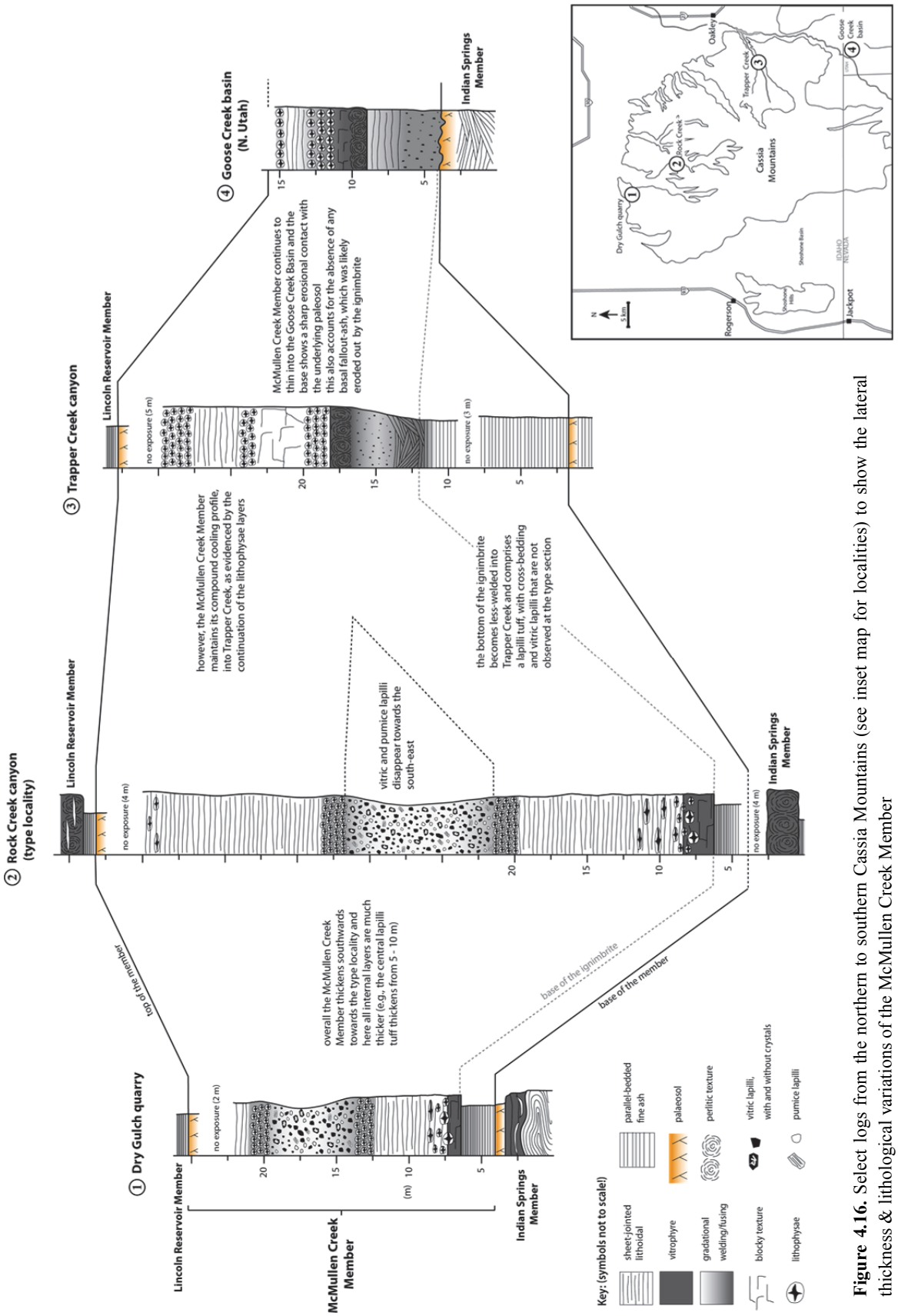

Figure 4.16. Select logs from the northern to southern Cassia Mountains (see inset map for localities) to show the lateral thickness & lithological variations of the McMullen Creek Member

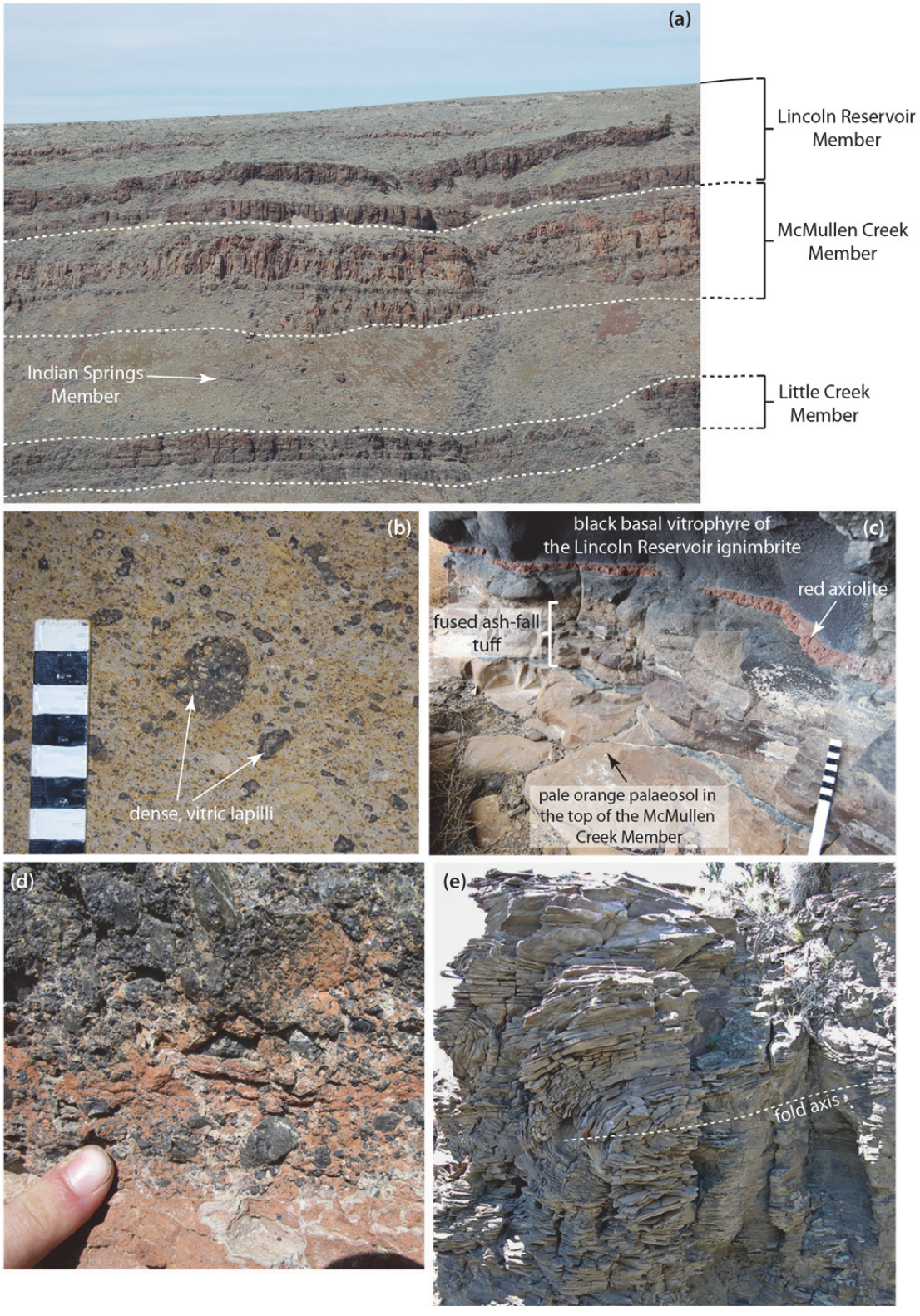

Figure 4.17. (a) Overview of the Rock Creek canyon type section for the Little Creek, McMullen Creek and Lincoln Reservoir members. Note the two darker bands within the McMullen Creek Member, which correspond to layers D and F (section 4.14.2). **(b)** Abundant vitric lapilli within layer E of the McMullen Creek Member. **(c)** Basal contact of the Lincoln Reservoir Member showing the parallel-bedded, fused, ash-fall tuff overlain by an intensely-welded ignimbrite containing distinctive red axiolites. **(d)** Peperitic base of the Lincoln Reservoir Member exposed in the Dry Gulch quarry. **(e)** Rheomorphic folding in the upper lithoidal of the Lincoln Reservoir Member highlighted by abundant sheet joints

4.14.3. Interpretation

The McMullen Creek Member is interpreted as the product of a single explosive eruption due to the the absence of palaeosols, fallout layers or reworked horizons between the different lithologies, which indicates that there were no significant time gaps during its emplacement. The basal ash-fall tuff (layer A) is interpreted to have been deposited from sustained sub-aerial fallout. However, assuming the source region was within the Snake River Plain (after McCurry et al., 1996) a fall deposit would typically thin away from source (Houghton et al., 2000). However, layer A thickens southwards towards Trapper Creek, and may have been thickened by sedimentary reworking.

The complex vertical welding profile exhibited by the overlying ignimbrite indicates that it is a compound cooling-unit (*sensu* Smith 1960; Wilson & Hildreth, 2003). The lower (layers B–D) and upper (layers F–G) intensely-welded zones are interpreted as emplacement from a high-temperature pyroclastic density current, whereas the less-welded lapilli-tuff in the central zone (layer E) likely records a lower emplacement temperature. This is interpreted as the effect of the incorporation of large volumes of cool vitric lapilli that acted as a heat sink and lowered the temperature of the density current and the accumulating deposit and prevented welding (e.g. Marti et al., 1991). This is assuming that the vitric lapilli are an accidental component of the eruption, but this is not fully constrained. However, this hypothesis is supported as the disappearance of these lapilli in the upper and lower parts of the ignimbrite is concurrent with an increase in welding. The cross-bedded lapilli tuff at the base of the ignimbrite, observed in the south, is interpreted as deposition from a fully dilute density current, and the upward transition into the massive intensely-welded facies may record an increase in the concentration of the current as the mass flux of the McMullen Creek eruption was increased with time. It is not clear whether the different lithofacies within the McMullen Creek ignimbrite represent a single or multiple flow-units. However, the ignimbrite is tentatively interpreted here as recording a sustained high-temperature pyroclastic density current with an influx of accidental cool vitric lapilli, which account for the less intense welding in the central lapilli-tuff.

4.15. The Lincoln Reservoir Member

The Lincoln Reservoir Member is a newly defined rhyolitic eruption-unit and is the youngest member of the Cassia Formation. It was previously interpreted as 'Member 5' of the 'Tuff of McMullen Creek' (Wright et al., 2002), however at its type locality (Rock

Creek canyon, Fig. 4.18 inset) it rests on a palaeosol in the top of the McMullen Creek Member (Fig. 4.18), and therefore the present study redefines it as a separate ~32 m-thick eruption-unit. The member comprises a parallel-bedded basal ash-fall tuff overlain by an intensely-welded rheomorphic ignimbrite (Fig. 4.18).

4.15.1. Description

The basal parallel-bedded ash-fall tuff is 0.3 m-thick and is composed of centimetre-scale beds of coarse and fine ash, all of which have been fused by the overlying intensely-welded ignimbrite (Fig. 4.17c). The base of the ignimbrite is a 2 m-thick, slightly perlitic, vitrophyre that contains 3–4 cm-thick devitrified axiolites that extend laterally up to 2 m (Fig. 4.17c). The vitrophyre is sharply overlain by a ~29 m-thick rheomorphic lithoidal zone, which can be sub-divided into two structural domains. This includes a lower 'flat zone' with sub-horizontal recumbent isoclinal folds, and an upper 'steep zone' with upright to overturned open antiforms and synforms (up to 10 m in scale, Fig. 4.17e). The lithoidal zone is sharply overlain by a thin, 1 m-thick, upper vitrophyre that follows the folding in the upper lithoidal zone. The vitrophyre is poorly exposed at the type section and at most other localities of the Lincoln Reservoir Member it is absent.

Crystal content is consistent throughout the member and is estimated at 10–15 %, comprising a mineral assemblage of plagioclase, pigeonite, augite, magnetite and accessory apatite and zircon

4.15.2. Lateral variations

The Lincoln Reservoir Member is exposed across the entire Cassia Mountains (Williams et al., 1990). In the northern Cassia Mountains, in the Dry Gulch quarry, the basal contact is distinctly peperitic and the basal ash-fall tuff is missing (Fig. 4.17d). This suggests that the member was emplaced onto a wet substrate close to the Snake River Plain. However, this basal peperite is not observed at the type section or any other locality to the south. Overall the member thins southwards, and in Trapper Creek it is ~25 m-thick (Fig. 4.19). Further south into the Goose Creek basin the member thins to ~10 m (Fig. 4.19), and here previous descriptions designated it as the 'Upper Goose Creek Tuff' (Hackett et al, 1989). Modern erosion means that the member is not exposed south of the Idaho-Utah border, and therefore its distal limit is unknown. Crystal content also decreases to the south, from 10-15 % at the type locality to <5 % in the Goose Creek basin.

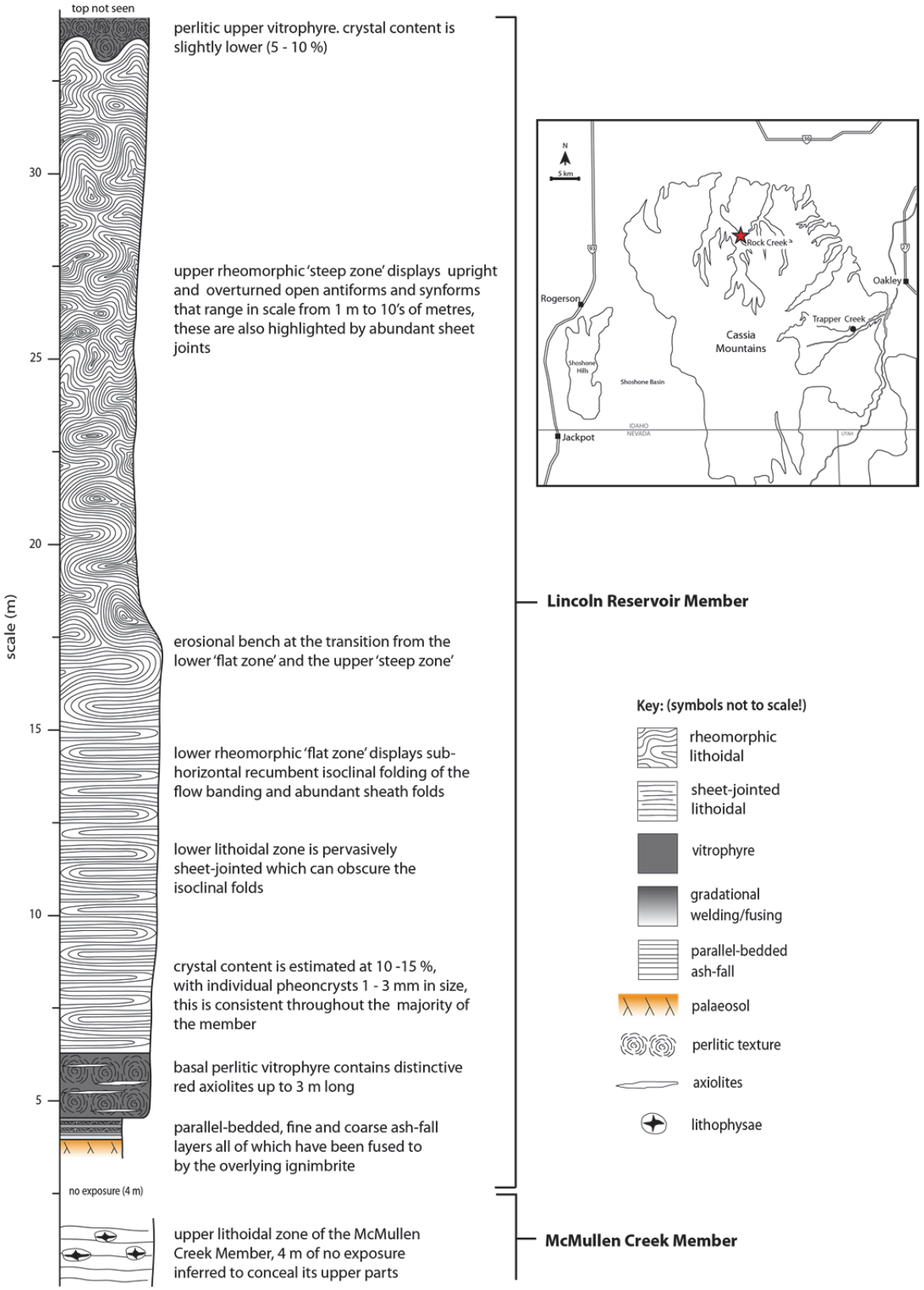

Figure 4.18. Graphic log of the Lincoln Reservoir Member. Inset map shows the type locality (red star) for the member within Rock Creek canyon

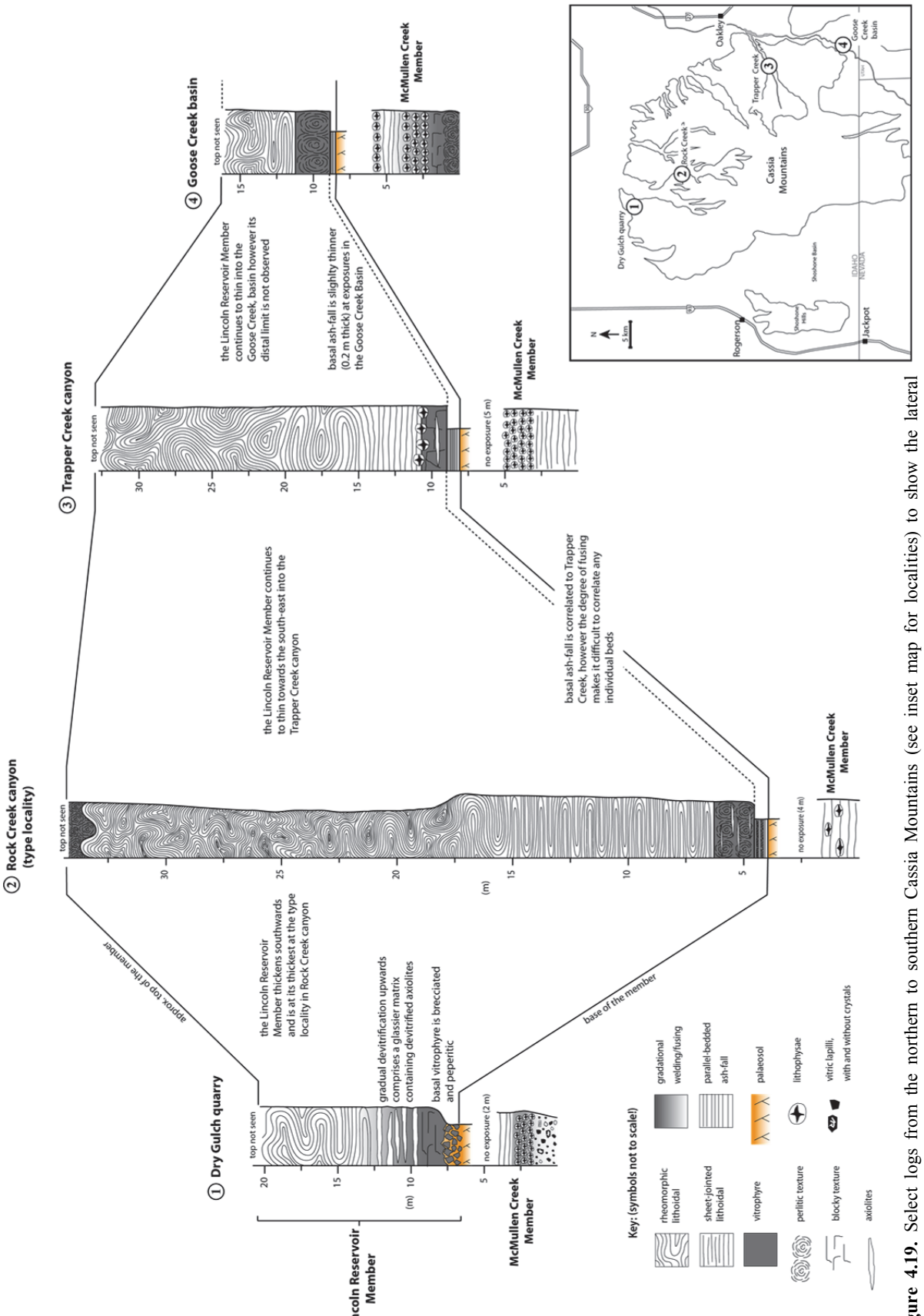

Figure 4.19. Select logs from the northern to southern Cassia Mountains (see inset map for localities) to show the lateral thickness & lithological variations of the Lincoln Reservoir Member

4.15.3. Interpretation

The Lincoln Reservoir Member is interpreted to record a single explosive eruption because an absence of palaeosols, fallout layers or reworked horizons between the different lithologies indicate that there were no significant time gaps during its emplacement. The basal 0.3 m-thick ash-fall tuff is interpreted as the result of sustained sub-aerial fallout; based on the mantling of the substrate, excellent sorting and laterally continuous laminations. The overlying intensely-welded ignimbrite is the result of a single high temperature pyroclastic density current, and the lack of any internal breaks (i.e., ash-fall layers) indicates it is a simple cooling unit (*sensu* Smith, 1960; Wilson & Hildreth, 2003).

4.16. Whole rock chemistry

Whole-rock samples were collected from the Cassia Formation and prepared for X-ray fluorescence (XRF) spectrometry and analysed on a PANalytical PW4400 Axios XRF spectrometer at the University of Leicester (see Appendix B.1). Samples were preferentially collected from the base and top of individual members, at multiple localities, in order characterise the individual eruption-units and assess any vertical or lateral chemical zonation. The limited exposure of the non-welded facies meant that these were not targeted for sampling.

4.16.1. Major elements

The rhyolitic ignimbrites of the Cassia Formation have SiO_2 contents ranging between 68.33–76.15 wt.% and have relatively high concentrations of TiO_2, MgO and Fe_2O_3 (Table C.2), which is consistent with data obtained on other rhyolitic ignimbrites from the central Snake River Plain (e.g., Bonnichson and Citron, 1982; Cathey and Nash, 2004; Wright et al., 2002; Andrews et al., 2008; Ellis et al., 2010; Fig. 4.20a). Alumina Saturation Indices (ASI) for the majority of the members range between 0.91 and 1.00, which suggests most are metaluminous rhyolites (Table C.2). However, slightly higher ASI values (between 1.02 and 1.04) are observed in the Magpie Basin and Dry Gulch Members, which suggests that these members are slightly peraluminous. Loss on ignition (LOI), of all members, is typically <2.5 wt.% (Table C.2) and suggests that post-emplacement alteration was negligible. Major element concentrations are also remarkably consistent within individual members; displaying only subtle vertical variations (e.g., <2 wt.% SiO_2) from base to top at any one locality. However, passing up succession the major element concentrations of

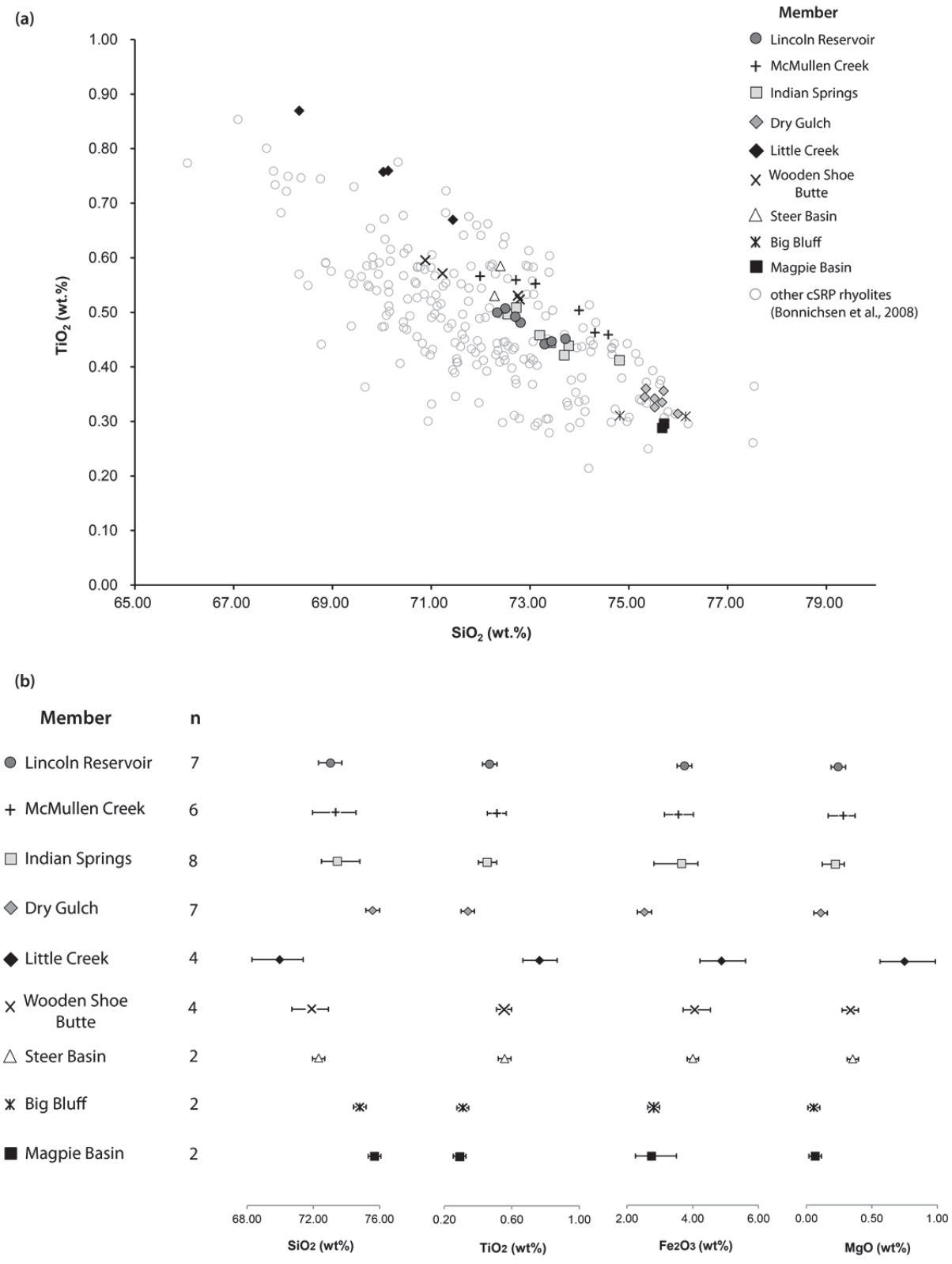

Figure 4.20. (a) SiO_2 vs TiO_2 plot showing the variations between the Cassia Formation members and their similarity to the majority of other cSRP rhyolitic ignimbrites (additional data from Bonnichsen et al., 2008). **(b)** Variations in select major element concentrations with stratigraphic height through the Cassia Formation. Symbols represent the mean concentrations and the black bars represent the range in concentration exhibited by all samples of each member.

ignimbrites show some systematic variations. From the Magpie Basin Member to the Little Creek Member SiO_2 decreases and MgO, TiO_2 and Fe_2O_3 all increase (Fig. 4.20b). This vertical variation is generally consistent with the magmatic system, producing these rhyolites, becoming increasingly more mafic over time (section 4.20). This pattern was also noted by Bonnichsen et al. (2008), who suggest a province wide trend to more mafic compositions in the central Snake River Plain over time. Above the Little Creek Member there is a shift to higher SiO_2 concentrations seen in the overlying Dry Gulch Member and above this the younger Indian Springs, McMullen Creek and Lincoln Reservoir Members show a slight trend towards more mafic compositions. (Fig. 4.20b). This shift to higher SiO_2 concentrations followed by a similar trend towards less-evolved compositions may represent a change in the source region for the younger eruption units, or successive tapping of a different, more-evolved, magma reservoir that underwent a similar petrogenetic history as that which produced the older eruption-units (section 4.20).

4.16.2. Trace elements

Members of the Cassia Formation plot (Fig. 4.21a inset) within the 'within plate granites' field of Pearce et al. (1984) and with high Ga/Al ratios (>3) can be classified as A-type (after Whalen et al., 1987). Totals of high field strength elements (Zr+Nb+Y+Ce) range from 700–996 ppm, which is also within the anorogenic granites range (500-1000 ppm) defined by Eby (1990). Bulk-silicate-Earth-normalised trace element patterns also show that all members of the Cassia formation have broadly similar trace element abundances, with high Rb, Th, U and Pb, and relatively lower Ba, Nb and Sr (Fig. 4.21b). However, the Cassia Formation also shows some significant variations in both compatible and incompatible trace elements between successive members. Both the Magpie Basin and Big Bluff members have much lower Ba and Sr than all other overlying members (Fig. 4.21b), and Sr also increases with height through the Cassia Formation with the highest concentrations in the Little Creek Member. Similar to major element trends (e.g., MgO and TiO_2) the overlying Dry Gulch Member defines an abrupt decrease in Sr, followed by a trend of increasing Sr defined by the younger overlying members (Fig. 4.21b). This variation may be a function of the proportion of feldspar within the whole rock sample; with the lowest Ba and Sr concentrations within the most crystal poor members (Fig. 4.2). However the majority of members have crystal contents of 10–15%, so feldspar proportion in the bulk sample does not solely explain the vertical variation in Sr throughout the Cassia Formation.

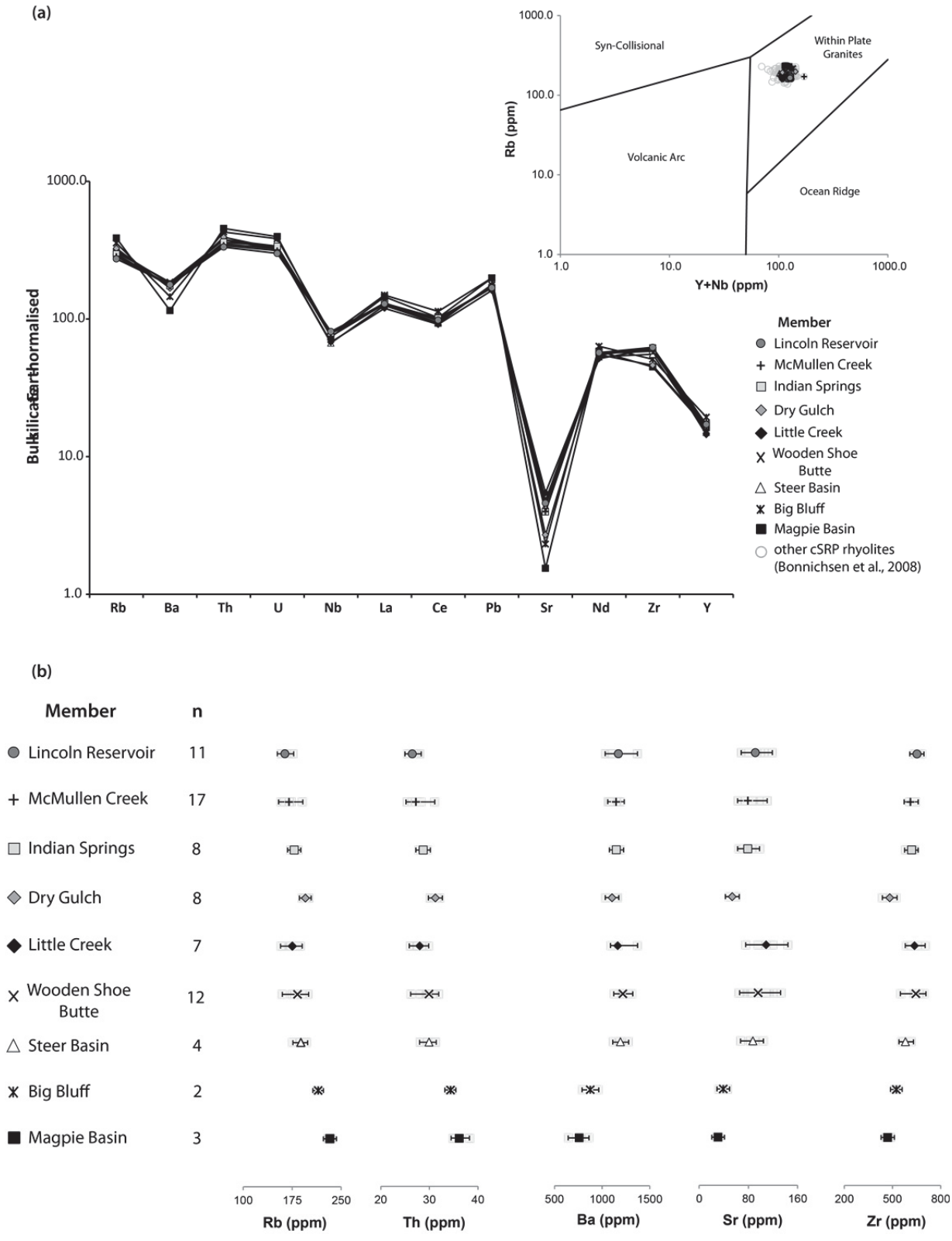

Figure 4.21. (a) Bulk-silicate-Earth (Sun & McDonough, 1995) normalised trace element patterns for all members of the Cassia Formation showing that all have broadly similar trace element abundances. Inset shows all Cassia Formation members plot within the 'Within Plate Granites' field (of Pearce et al., 1984) and all are similar to the majority of other rhyolitic ignimbrites in the cSRP. **(b)** Variations in select trace element concentrations with stratigraphic height through the Cassia Formation. Symbols represent the mean concentrations and the black bars represent the range in concentration exhibited by all samples of each member.

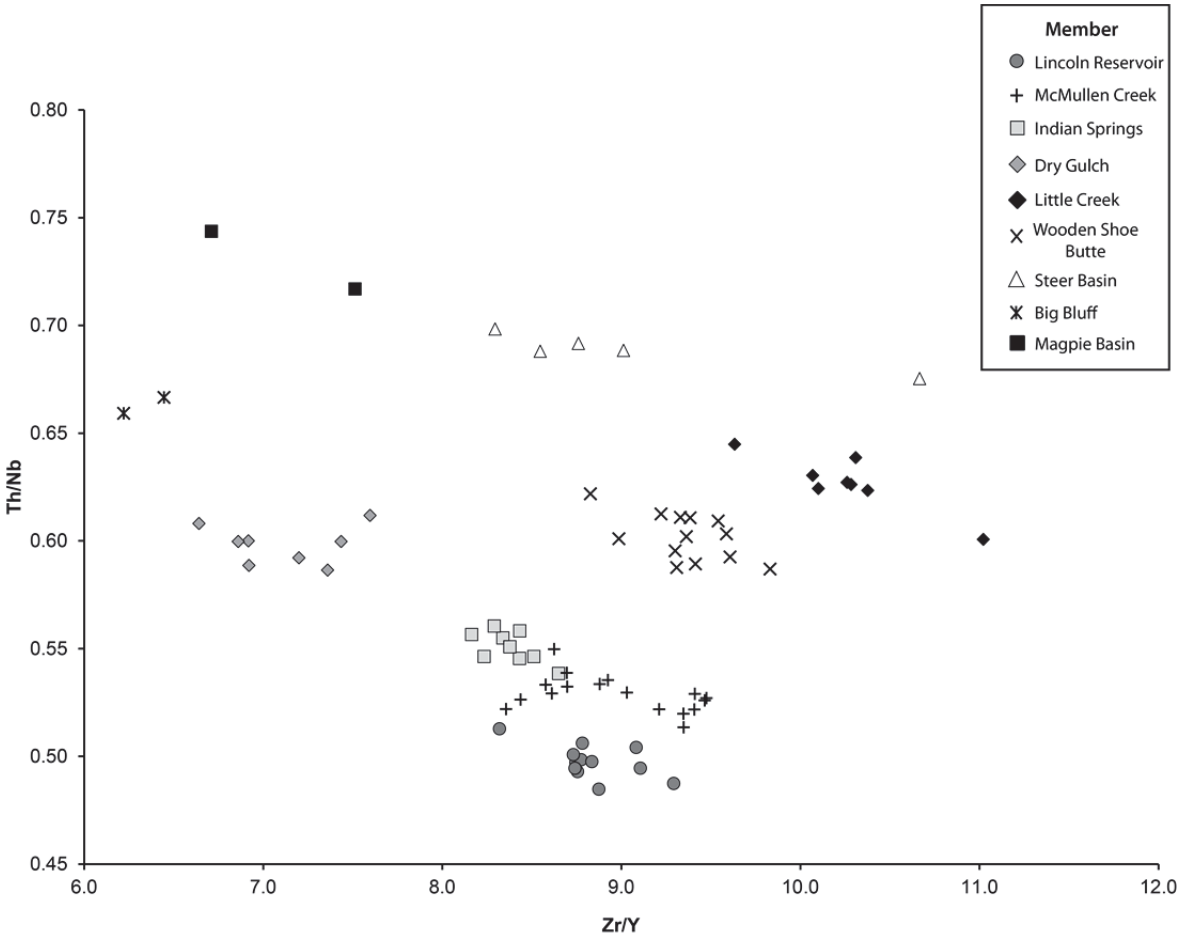

Figure 4.22. Zr/Y vs Th/Nb plot demonstrating how each of the Cassia Formation members defines a unique chemical field, each of which are readily distinguishable from their adjacent members.

Relatively incompatible trace elements, such as Rb, Th and Zr also show systematic variations. Both Rb and Th decrease with stratigraphic height, with a predictable abrupt increase seen in the Dry Gulch Member (Fig. 4.21b). These trends are consistent with a progression towards more mafic compositions over time. However, Zr increases with stratigraphic height (Fig. 4.21b), which is counterintuitive to the magmatic system becoming increasingly more mafic, as Zr concentration would be expected to decrease. Therefore the petrogenetic history of the Cassia Formation rhyolites is likely more complex than a simple time-transgressive progression towards less-evolved compositions (section 4.20).

Despite the bulk chemical similarities between all Cassia Formation members it is possible to distinguish individual members by using the relatively incompatible elements Th, Nb, Zr and Y as discriminators. Zr/Y and Th/Nb ratios define unique chemical fields for each of

the Cassia Formation members (Fig. 4.22) that are readily distinguishable from their underlying and overlying eruption-units. This is therefore a useful method for identifying individual members when field criteria are not sufficient.

4.17. Petrology and mineral chemistry

All members of the Cassia Formation share a broadly similar mineral assemblage comprising feldspars (plagioclase and/or sanidine), pyroxenes (pigeonite and/or augite), Fe-Ti oxides (magnetite and/or ilmenite) and accessory apatite and zircon. The Big Bluff Member is unique as it also contains quartz and rare fayalitic olivine crystals, which are not observed in any other member. Despite the similar mineral assemblage shared by the majority of the Cassia Formation members it is possible to discriminate between individual units by the presence of discrete compositional modes within the most abundant mineral phases, namely the feldspars, Fe-Ti oxides, and in particular the pyroxenes. Therefore data were obtained on these phases by electron microprobe analysis, using a Cameca SX100 electron microprobe at the Open University, Milton Keynes, UK (see Appendix B.2), and each phase is described individually below.

4.17.1. Feldspars

Feldspar is the dominant mineral phase in all members of the Cassia Formation. Feldspar crystals occur as two textural types here termed 'Type 1' and 'Type 2'. Type 1 crystals are euhedral to subhedral laths, 1–3 mm in size, and some contain inclusions of glass (Fig. 4.23b) and/or smaller crystals of pyroxene, Fe-Ti oxides, or apatite. Inclusions of glass are commonly concentrated within the core of Type 1 crystals, similar to the 'cellular feldspars' described by Wright et al (2002) which these authors attribute to rapid growth. Some Type 1 crystals also show weak zoning (Fig. 4.23b), although this is not a common observation and core to rim variation is typically <1% An. However, where zoning is seen the inclusions of glass and/or crystals seem to follow a single zonation ring. Type 1 crystals also occur, in all units, as part of crystal aggregates (up to 3 mm in size) with pyroxene and Fe-Ti oxide crystals.

Type 2 crystals are smaller (0.2–0.5 mm) subhedral crystals, most of which have at least one broken margin and are interpreted as fragments of larger crystals. These crystals show no zoning and are typically isolated within the matrix.

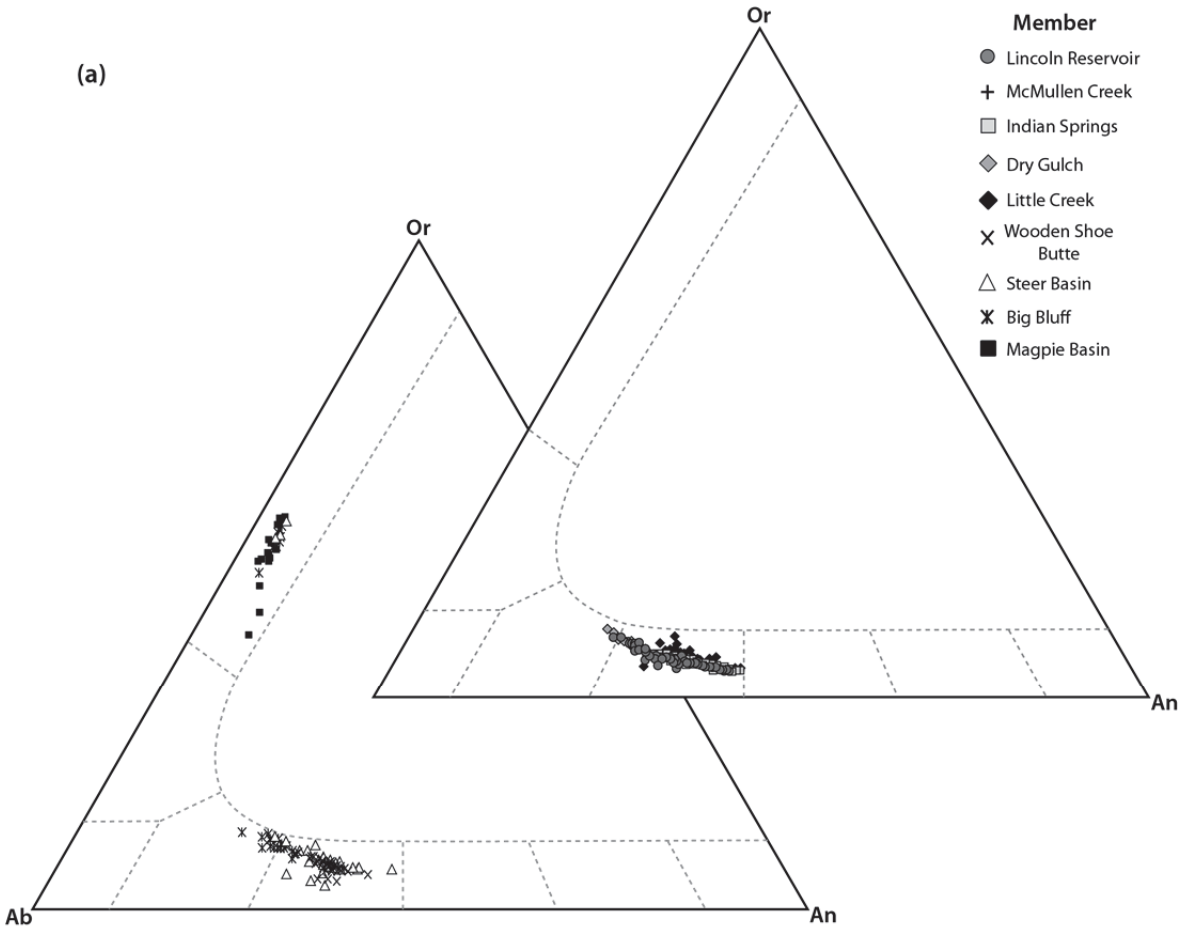

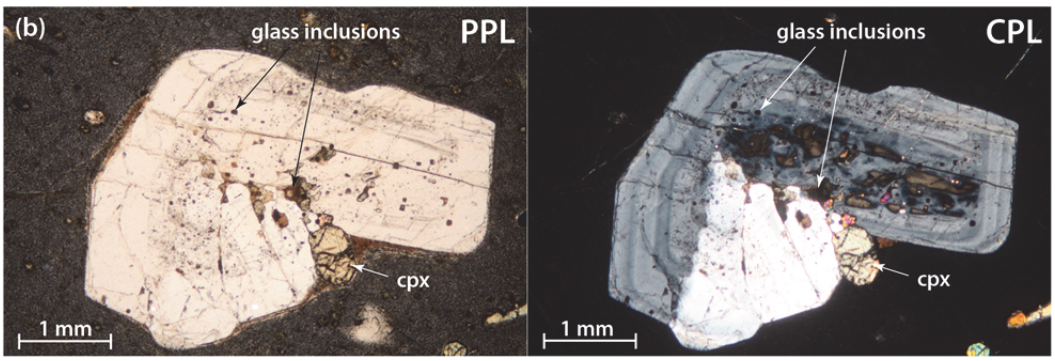

Figure 4.23. (a) Feldspar ternary diagrams showing the dominance of plagioclase (andesine) in all members of the Cassia Formation. Sanidine is also present in the Magpie Basin, Big Bluff, Steer Basin and Wooden Shoe Butte members, but is absent from all overlying members. **(b)** Photomicrographs showing an example of a 'Type 1' feldspar crystal in plane polarised (PPL) and cross polarised (CPL) light. Type 1 crystals contain glass inclusions and or smaller crystals and some also show zoning.

Compositionally, feldspar crystals occur as two types; plagioclase and sanidine. Plagioclase is ubiquitous throughout the entire Cassia Formation (Table C.7) and in the oldest members (e.g., the Magpie Basin and Big Bluff members) is exclusively oligoclase

(An_{21}–An_{29}), whereas andesine (An_{30}–An_{49}) is dominant in all overlying members (Fig. 4.23a). This broad compositional range means that plagioclases are not particularly useful when discriminating between individual members of the Cassia Formation. However, sanidine (Or_{41}–Or_{61}) is present only in the lower members of the Cassia Formation, including the Magpie Basin, Big Bluff, Steer Basin and Wooden Shoe Butte members (Table C.7; Fig. 4.23a). Sanidine disappears somewhere between the Wooden Shoe Butte and Little Creek members, and is also absent from all the overlying members (Fig. 4.23a). Therefore the contact between the Wooden Shoe Butte and Little Creek members marks an important stratigraphic horizon, within the Cassia Formation, above which there is no record of sanidine as a fractionating phase.

4.17.2. Pyroxenes

Pyroxene crystals are subhedral, 0.5–1 mm in size, and have slightly rounded crystal faces. They occur in all members both as single crystals within the matrix, and as crystal aggregates (Fig. 4.24b) with Fe-Ti oxide crystals and/or Type 1 feldspars. Compositionally they occur as two types; Ca-rich augite and Ca-poor pigeonite (Table C.8). Augite and pigeonite are ubiquitous throughout the Cassia Formation, with the exception of the Big Bluff Member, which contains only augite (Fig. 4.24a). It is possible to distinguish between individual members by the FeO and MgO concentrations of both pigeonite and augite crystals. Up succession, from the Magpie Basin Member to the Little Creek Member, MgO concentrations of the pigeonite and augite crystals progressively increase whereas FeO decreases (Fig. 4.24a). This suggests that pyroxenes from successive eruption-units were crystallising from progressively more Mg-rich magmas, which is consistent with the trend towards less evolved compositions seen in the whole-rock chemistry. This is with the exception of the Big Bluff Member, which contains only augite with the lowest MgO concentrations of any other member (Fig. 4.24a). Pigeonite and augite crystals from the Dry Gulch Member have lower MgO and higher FeO concentrations, which is also consistent with the whole-rock data and suggests crystallisation from a more-evolved rhyolite. Pigeonite and augite crystals from the overlying Indian Springs, McMullen Creek, and Lincoln Reservoir members are closely similar (Fig. 4.24a). However, the Lincoln Reservoir Member is distinct as it contains two compositional pairs of pigeonite and augite (Fig. 4.24a).

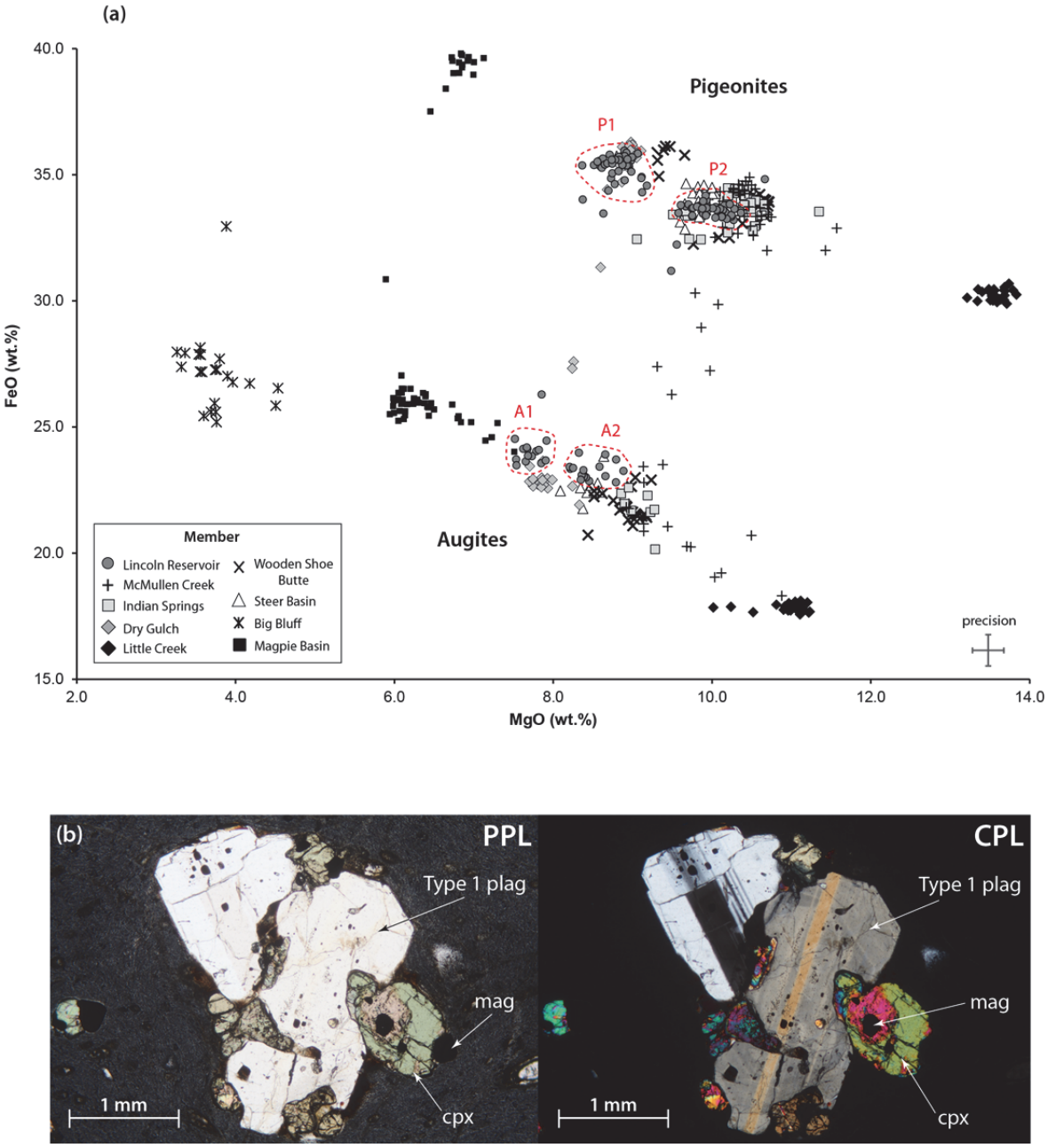

Figure 4.24. (a) Pigeonite and augite compositions from all members of the Cassia Formation. Compositions of both pigeonites and augites generally trend towards higher MgO concentrations up section between the Magpie Basin Member and the Little Creek Member. MgO concentrations in the younger Dry Gulch Member are lower, and pyroxenes in the overlying Indian Springs, McMullen Creek, and Lincoln Reservoir members are broadly similar. The Lincoln Reservoir Member is unique as it contains two modes of pigeonite (P1 and P2) and two modes of augite (A1 and A2). **(b)** Photomicrographs in plane polarised (PPL) and cross polarised (CPL) light.showing an example of a typical Cassia Formation crystal aggregate composed of Type 1 plagioclases (plag) and smaller subhedral crystals of pyroxene (cpx) and magnetite (mag).

Pair 1 includes pigeonites (P1, Fig. 4.24a) with MgO concentrations between 7.84 and 9.43 wt.% (Table C.8), and augites (A1, Fig. 4.24a) with lower MgO concentrations between 7.52 and 7.92 wt.% (Table C.8). Whereas, pair 2 includes pigeonites (P2, Fig. 4.24a) with MgO concentrations between 9.61 and 10.67 wt.% (Table C.8), and augites (A2, Fig. 4.24a) with lower MgO concentrations between 7.82 and 8.88 wt.% (Table C.8). Multiple modes of pyroxene are seen in only one other member, the Wooden Shoe Butte Member, which contains pigeonites similar to P1 and P2, and a single mode of augite similar to A1 (Fig. 4.24a). Multiple pyroxene modes have also been reported for the Steer Basin Member (Ellis et al., 2012a); however these were not observed during the present study. Multiple modes, where present, occur both as single crystals and as part of crystal aggregates, and their presence within a single unit has been attributed to the mixing of compositionally discrete magma batches upon eruption (Ellis et al., 2010; Ellis & Wolff, 2012).

4.17.3. Fe-Ti oxides

Fe-Ti oxide crystals are commonly subhedral to anhedral and small (0.2–0.5 mm), although few reach a maximum of 1 mm. The dominant compositional phase is Ti-rich magnetite (11.07-34.02 wt.% TiO_2), which is ubiquitous throughout the majority of Cassia Formation. The broad compositional range exhibited by the magnetite pheneocrysts (Fig. 4.25) means they are not particularly useful when discriminating between individual members. However, the Big Bluff Member contains solely ilmenite, which is distinct from all other members (Fig. 4.25). Ilmenite is also present in the Magpie Basin, Steer Basin, Dry Gulch, and Indian Springs members, however is much less abundant than magnetite (Fig. 4.25).

4.18. U-Pb geochronology

Age determinations for the Little Creek, Indian Springs and McMullen Creek Members were obtained as part of the present study by U-Pb dating of zircons and analyses were performed at the Edinburgh Ion Microprobe Facility using a CAMECA IMS-1270 ion microprobe (see Appendix B.5). These units were initially targeted in order to gauge a time period for the younger eruption-units that were not previously dated, however a misidentification of units earlier in the study meant that the youngest Lincoln Reservoir Member was not sampled. A total of fifty-eight ion microprobe analyses from these three

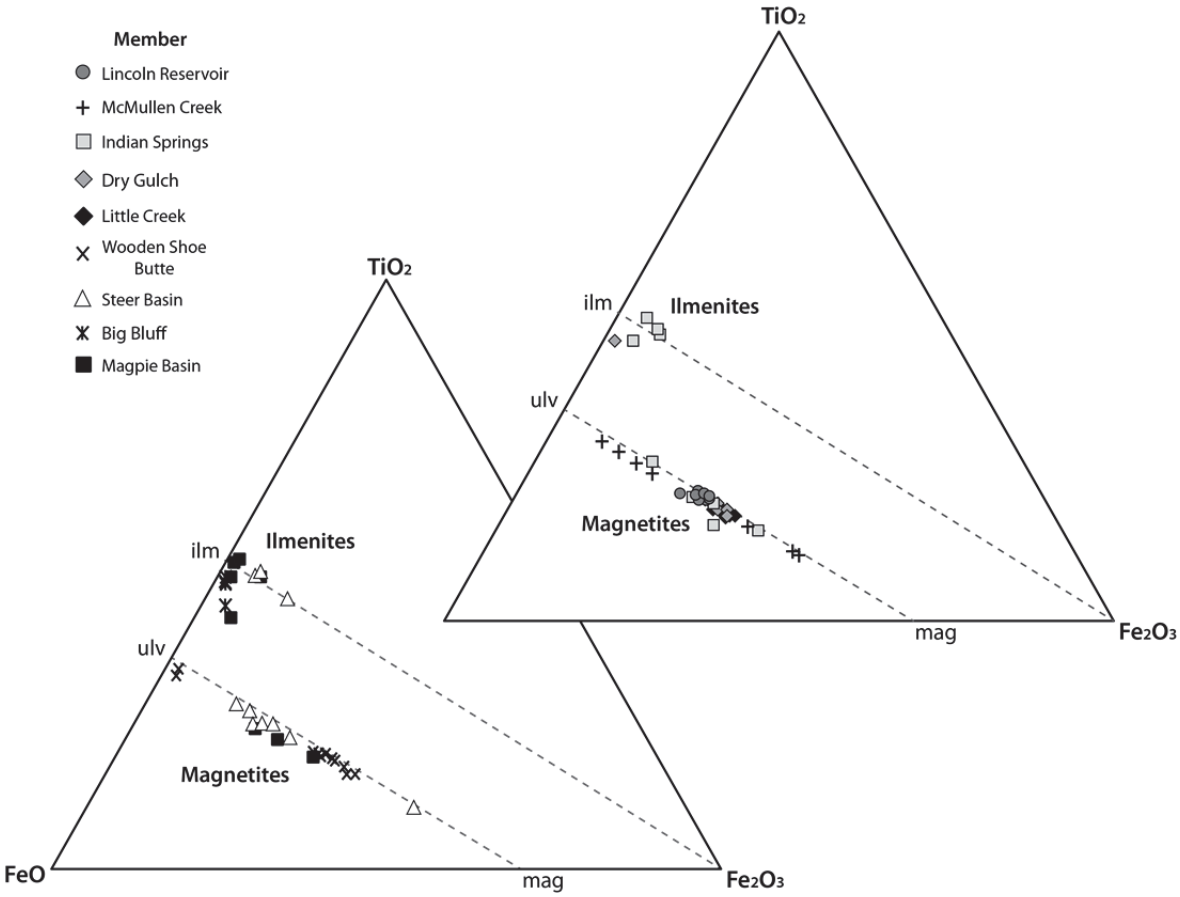

Figure 4.25. Fe-Ti oxide ternary diagrams showing the predominance of magnetite in the majority of the Cassia Formation members. The Big Bluff Member contains solely ilmenite, which is also present in the Magpie Basin, Steer Basin, Dry Gulch, and Indian Springs members, although is much less abundant.

rhyolitic members are presented in Table C.14. Zircons with common lead concentrations >6 ppb ^{204}Pb were not used in age calculations and accompanying U-Pb Concordia diagrams (Fig. 4.26 a–c), and are thus not reported in Table C.14. In general, high Pb concentrations (>20 ppm) are usually observed in xenocrystic zircons with Proterozoic ages but a correlation between U and Th content and zircon age is not observed. Although, statistically meaningful weighted mean ^{206}Pb/^{238}U zircon ages could be derived from the three samples the presence of older zircons derived from subjacent mid-Miocene ignimbrites presumably entrained in the magma chamber or during emplacement cannot be ruled out. However, the resolution of data presented here precludes a more detailed account. Data from the three sampled units are described individually below.

4.18.1. Little Creek Member (sample: RC-11.1-004)

Zircons from the Little Creek Member provide $^{206}Pb/^{238}U$ ages between 9.3 and 11.0 Ma, though two zircon grains are clearly xenocrystic in origin (Table C.14) with $^{206}Pb/^{207}Pb$ ages of ~1456 Ma. Although a statistically meaningful weighted mean $^{206}Pb/^{238}U$ age of 10.3 ± 0.2 Ma (MSWD = 3.1) can be derived for this sample (Fig. 4.26c) the age-probability distribution of these data imply the presence of two age populations at ~10.1 Ma and ~10.6 Ma (Fig. 4.26d). Furthermore, a high precision $^{40}Ar/^{39}Ar$ sanidine age of 10.136 ± 0.005 Ma was obtained on the underlying Wooden Shoe Butte Member (Reichow, unpublished). Although, the U-Pb and argon ages are, within uncertainties, indistinguishable the high-precision argon age from the underlying member provides a maximum age for the Little Creek Member, which consequently has to be younger.

4.18.2. Indian Springs Member (sample: RC-10.1-010)

Analyses of zircons from the stratigraphically younger Indian Springs Member provided a mean weighted $^{206}Pb/^{238}U$ zircon ages of 9.0 ± 0.3 Ma (MSWD = 1.4) (Fig. 4.26b). This age is statistically indistinguishable from that obtained from the overlying McMullen Creek member (section 4.18.3). Three individual grains provided $^{206}Pb/^{238}U$ zircon ages of 32.4 ± 0.4, 34.1 ± 0.4, and 36.6 ± 0.5 Ma. Volcanic rocks of Oligocene age are reported from locations in Nevada and Utah where large volumes are hosted (e.g., Christiansen and McCurry, 2008). However, no similar Oligocene ages were reported from the Snake River Plain so far, and volcanic rocks of the Challis volcanic field widely distributed in the Snake River Plain are considerably older (52–45 Ma; Chetel et al., 2011).

4.18.3. McMullen Creek Member (sample: RC-10.1-006)

$^{206}Pb/^{238}U$ zircon ages for the McMullen Creek Member range between 8.5 and 1414 Ma. However, 22 data points form a cluster of data with a weighted mean $^{206}Pb/^{238}U$ age of 9.0 ± 0.2 Ma (MSWD = 2.3) (Fig. 4.26a), which is considered to represent the crystallisation age of this unit. Core analyses of zircon McM2-19 (Table C.14) also provided two Proterozoic ages of 1459 ± 4 and 1462 ± 12 Ma. Although, the $^{206}Pb/^{238}U$ and $^{206}Pb/^{207}Pb$ ages for analysis McM2-19-1 are not within uncertainty both $^{206}Pb/^{207}Pb$ ages are in agreement and are considered to represent the crystallization age for this zircon. The rim analysis of zircon McM2-19 is clearly younger with a $^{206}Pb/^{238}U$ age of 8.3 ± 0.2 Ma.

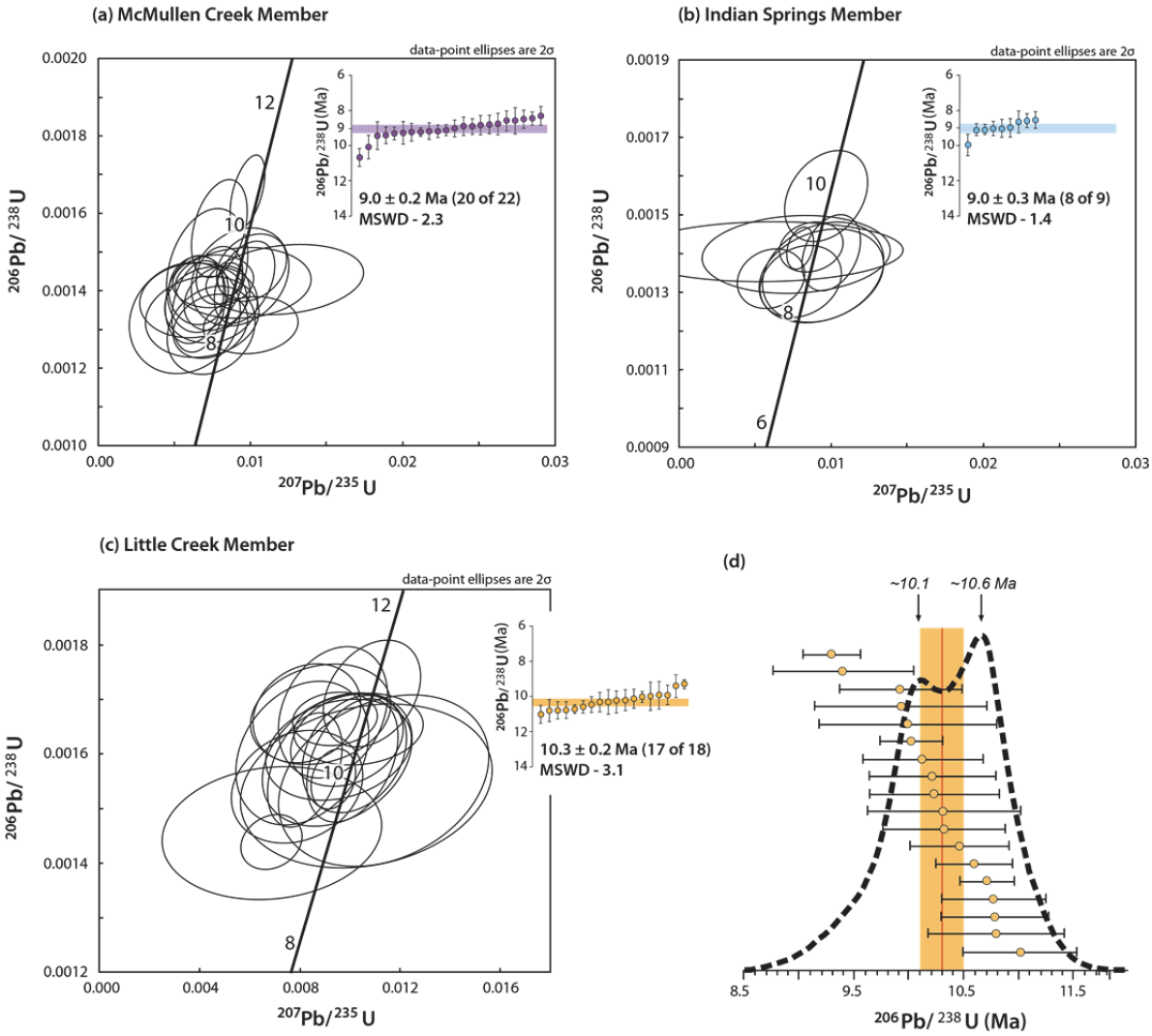

Figure 4.26. Concordia diagrams and weighted average plot for zircon $^{206}Pb/^{238}U$ ages for: **(a)** the McMullen Creek Member, **(b)** the Indian Springs Member, and **(c)** the Little Creek Member. U-Pb zircon analyses were performed by secondary ion mass spectrometry (SIMS) on a Cameca IMS 1270 ion microprobe located at the University of Edinburgh. **(d)** Age-probability distribution plot of the Little Creek Member implying the presence of two age populations at ~10.1 Ma and ~10.6 Ma.

4.19. Periodicity of the Cassia Formation eruptions

In addition to the above mentioned units, $^{40}Ar/^{39}Ar$ age determinations (Reichow, unpublished) have also been obtained for the Magpie Basin, Big Bluff, and Wooden Shoe Butte members (Table 6.1). Age determinations for the Dry Gulch and Lincoln Reservoir members are in progress, and no age determinations exist for the non-welded Niles Gulch, Antelope and Deadeye members. Therefore, published ages have also been combined with new age determinations (Table 6.1) in order to gain a more complete understanding of the periodicity of silicic eruptions recorded by the Cassia Formation. Considering the ages of the oldest Magpie Basin Member and the youngest Lincoln Reservoir Member, the Cassia Formation records a period of Miocene silicic volcanism that lasted for ~2.4 ± 0.04 million

Table 6.1. Compiled age determinations and estimated repose periods between all members of the Cassia Formation.

	Age determinations			
Member	**Present Study**	**Ellis et al., 2012**	**Perkins et al., 1998**	**Repose period (Ma)**
Lincoln Reservoir	-	-	8.95 ± 0.04 Ma[a]	
McMullen Creek	9.0 ± 0.2 Ma[b]	-	-	within ~0.4 - 0.6 Ma
Indian Springs	9.0 ± 0.3 Ma[b]	-	-	
Dry Gulch	-	-	-	1.2 ± 0.4
Little Creek	10.2 ± 0.3 Ma[b]	-	-	
Wooden Shoe Butte	10.136 ± 0.005 Ma[a]	-	10.25 ± 0.06 Ma[a]	within ~0.1 Ma
Deadeye	-	-	-	
Antelope	-	-	-	0.484 ± 0.08
Niles Gulch	-	-	-	
Steer Basin	-	10.62 ± 0.08 Ma[a]		
Big Bluff	10.949 ± 0.010 Ma[a]	10.97 ± 0.07 Ma[a]		0.329 ± 0.08
Magpie Basin	11.341 ± 0.008 Ma[a]	-		0.392 ± 0.013

[a] $^{40}Ar/^{39}Ar$ age, [b] zircon $^{206}Pb/^{238}U$ weighted mean age

years. Averaging this time period over the thirteen individual members results in estimates of periodicity of one explosive eruption every ~180 ka. However, closer examination of the repose periods between the individual members suggests that eruptions in the cSRP may have become more frequent overtime (Table 6.1). For example, the repose period between the Magpie Basin and Big Bluff members is close to 400 ka, whereas the repose period between the Big Bluff and Steer Basin members is closer to 300 ka. Missing age constraints for the Niles Gulch, Antelope, and Deadeye members means that a possible progressive decrease in repose periods cannot be fully constrained. However, ages for the older Steer Basin and younger Wooden Shoe Butte members, bracketing these units, imply they must have been deposited within ~500 ka (Table 6.1). In addition, the ages of the Wooden Shoe Butte and Little Creek members are indistinguishable, which suggests that they must have erupted within a relatively short period of time (within ~100 ka, Table 6.1). This is also the case for the younger Indian Springs, McMullen Creek and Lincoln Reservoir members, and all three likely erupted within ~400–600 ka. However, ages for

the Little Creek and Indian Springs members suggest a much longer period of repose (~1.2 Ma), although there are no age determinations for the Dry Gulch Member in between.

In summary, available ages and calculated repose periods suggest that eruptions may have become more frequent with time as evidenced by the decreasing repose periods between the older members and the indistinguishable ages of the younger units. However, additional age constraints are needed in order to support this hypothesis. In addition, the potentially larger repose period between the Little Creek and Dry Gulch Members may also suggest that the Cassia Formation records two discrete periods of volcanism, although again more age constraints are needed.

4.20. Petrogenetic evolution of the Cassia Formation rhyolites

The present study provides not only a refined and more detailed characterisation of individual eruption-units, but also describes newly identified eruption-units and therefore clarifies the volcanic sequence preserved in the Cassia Formation. These findings are pivotal in order to explore the petrogenetic evolution in this region. Whole-rock chemical data were particularly useful in demonstrating a progressive trend, between individual eruption-units, towards less evolved compositions over time. This is consistent with previous observations (Bonnichsen et al., 2008) of other cSRP rhyolites; however there have been limited attempts to constrain the cause of this trend (Ellis, 2009). By combining new whole-rock and mineral data with new, and published, age determinations for the revised Cassia Formation potential petrogenetic models are explored here in brief, explaining some of the observed whole-rock trends.

It is generally acknowledged that central Snake River Plain (cSRP) rhyolites are the product of crustal melting (e.g., Cathey & Nash, 2004; Nash et al., 2006; Bonnichsen et al., 2008; Boroughs et al., 2012; Ellis et al., 2013) and that the upwelling of mantle-derived basalt provided the thermal energy necessary to achieve this (Leeman et al., 2008). Repeated injections of mantle-derived basalt are thought to ascend through the crust until reaching neutral buoyancy, where they begin to pond likely at mid-crustal depths (Leeman et al., 2008). This is supported by seismic p-wave velocity data that provides evidence of a 10–25 km thick mid-crustal mafic sill complex in the eastern Snake River Plain (Peng & Humphreys, 1998; Shervais et al., 2006; Dueker et al., 2007), and similar voluminous injections of basalt are thought to have driven melting in the cSRP (Bonnichsen et al., 2008; McCurry & Rogers, 2009).

4.20.1. Degree of fractionation and residence time in the magma chamber

Studies have proposed (Wright et al., 2002; McCurry et al., 2009) that rhyolitic partial melts, originating from the mid-crust, ascend to shallow crustal levels where they undergo further fractionation and/or assimilation of surrounding country rocks prior to eruption. In addition, studies of rhyolites in the eastern Snake River Plain (McCurry et al., 2008) have shown they may have been entirely derived from extreme fractional crystallisation of mantle-derived magmas. However, the whole rock trends exhibited by the rhyolites of Cassia Formation are incompatible with those expected of continuous fractional crystallisation alone, and trend towards less-evolved compositions over time (Fig. 4.20b). However, this does not preclude the role fractional crystallisation, and the trends towards less-evolved compositions may reflect differing degrees of fractionation of cSRP silicic magmas due to their residence time in shallower magma chambers. Age determinations for the Magpie Basin Member and the overlying Big Bluff, Steer Basin, Wooden Shoe Butte and Little Creek members suggest that the repose periods between eruptions were becoming progressively shorter overtime (from ~400 ka to ~100 ka, Table 6.1). If the whole-rock compositions of each of these members are assumed to be an approximation of the parent liquids they derived from, then the observed trends in both major and trace element concentrations (Fig. 4.20b and 4.21b) can be accounted for by allowing less time for successive rhyolitic liquids to evolve along the liquid line of descent. The abrupt shift to more evolved compositions seen in the Dry Gulch Member (Fig. 4.20b) suggests a higher degree of fractionation prior to eruption than the older Little Creek Member. Although no formal age exists for the Dry Gulch Member, a comparison of U/Pb ages for the underlying Little Creek Member and overlying Indian Springs Member suggests that it erupted sometime within 1.2 ± 0.4 Ma (Table 6.1). The cause of this potentially longer period of quiescence, compared to those between other eruption-units (e.g., ~0.4 Ma between the Magpie Basin and Big Bluff Members, Table 6.1), is unclear. However, it would explain the more evolved composition of the Dry Gulch Member by allowing more time for the generated melt to fractionate and evolve prior to eruption. Above the Dry Gulch Member, the younger Indian Springs, McMullen Creek and Lincoln Reservoir members define a slight trend back towards less-evolved compositions similar to the older eruption-units. Ages obtained on these three members are indistinguishable (all are ~9.0 Ma old), indicating that these members erupted within ~400–600 ka (Table 6.1). This may explain the slight trend towards less-evolved compositions, by allowing less time for these members to fractionate prior to eruption.

While fractional crystallisation may have played a role in the evolution of the Cassia Formation rhyolites (e.g., Wright et al., 2002), Nd-isotope data have shown that cSRP rhyolites require both a crustal and mantle-derived component during their generation (Wright et al., 2002; Nash et al., 2006; Bonnichsen et al., 2008; McCurry & Rodgers, 2009; Boroughs et al., 2012). In addition, the $^{143}Nd/^{144}Nd$ ratios of cSRP rhyolites, including the Cassia Formation, progressively increase overtime (Ellis et al., 2013), which cannot be explained by simple fractionation.

4.20.2. Evolution of the source region

Previous petrogenetic models indicate that the $^{144}Nd/^{143}Nd$ ratios of cSRP rhyolites are consistent with mixing between mantle and crustal components, however estimates of the total mantle contribution vary from 10–60% (Nash et al., 2006; McCurry & Rogers, 2009) to 80% (Wright et al., 2002) depending on different model parameters. This mix of crustal and mantle-derived material is thought to be due to repeated injections of basaltic material into the crust (Hildreth et al., 1991), and the associated thermal pulse is thought to be the driving mechanism for generating voluminous partial melts (Leeman et al., 2008). The mantle-derived and crustal-derived materials are thought to undergo MASH-like mixing (after Hildreth & Moorbath, 1988, Fig. 4.27a) in the mid-crust, and this subsequently generates an isotopically hybridised source region (McCurry et al., 2009). It has also been suggested that with continued injection of basalt, and periodic extraction of partial melts from the crust, the residual crust becomes increasingly mafic and more refractory overtime (Leeman et al., 2008). Therefore successive batches of melt extracted from this hybrid mixing zone would have an increased mantle-derived contribution (Fig. 4.27b), which is supported by the increasing $^{143}Nd/^{144}Nd$ ratios in cSRP rhyolites (Ellis et al., 2013). This is therefore a possible model for explaining the progression towards less evolved compositions seen throughout the Cassia Formation. For example, the older Magpie Basin Member may be representative of the earliest silica-rich melt to be extracted from the source region (Fig. 4.27a), whereas the progressively more mafic overlying members (i.e., the Big Bluff – Little Creek members) are indicative of later melt batches extracted as the source region became increasingly hybridised with mantle-derived basalts (Fig. 4.27b). The significantly higher SiO_2 concentration seen in the Dry Gulch Member may suggest a shift in the source region to an area of the crust that was more fertile and less hybridised by the intrusion of basalt. However, the progressively more mafic compositions seen in the

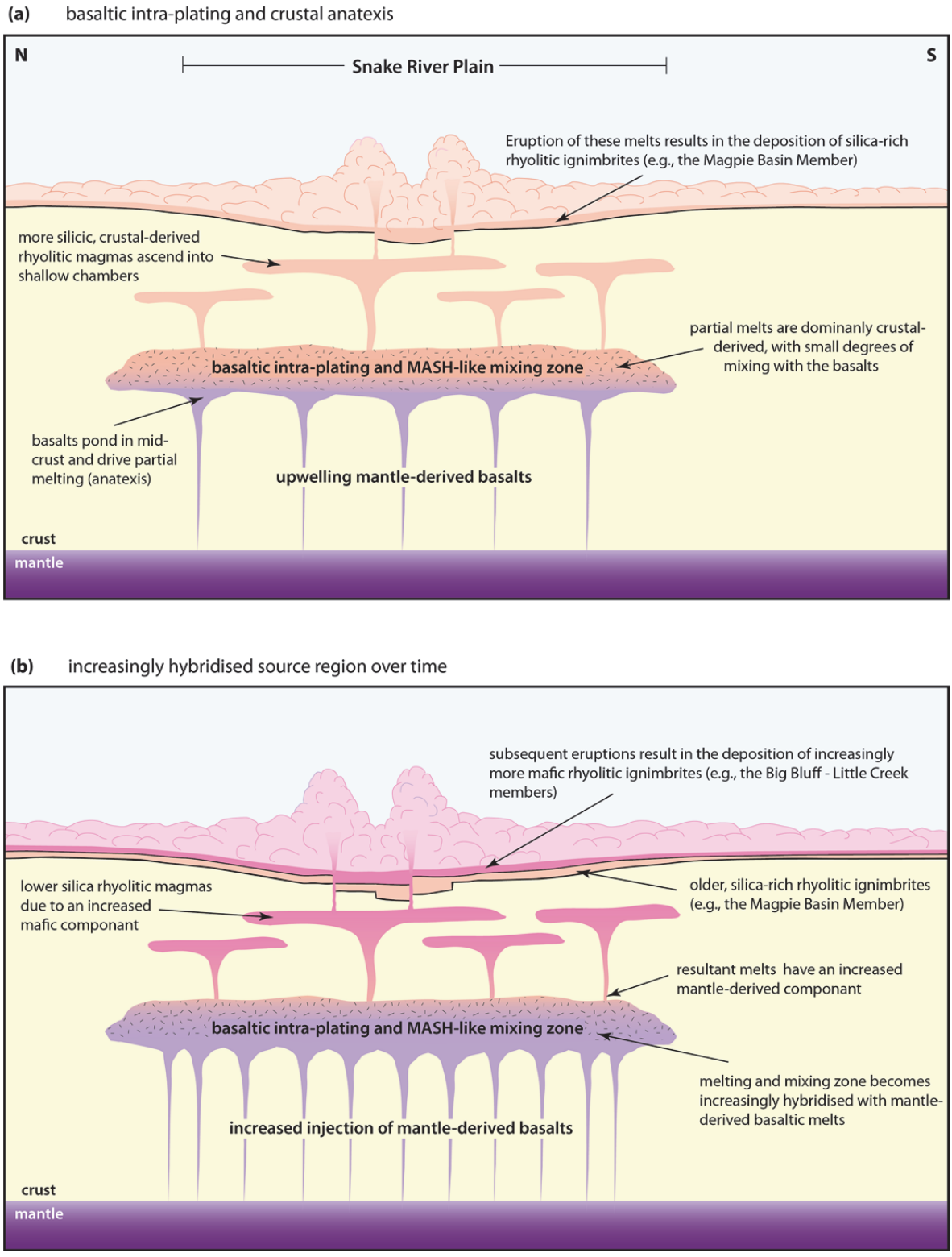

Figure 4.27. Schematic diagrams (not to scale) illustrating a model of progressive hybridisation of a mid-crustal source region to produce progressively less-evolved rhyolitic ignimbrites (e.g., the Cassia Formation). **(a)** Upwelling mantle-derived basaltic partial melts pond in the mid crust and generate a MASH-like melting and mixing zone (Hildreth & Moorbath, 1988). This produces crustal-derived rhyolitic melts that upwell into shallower magma chambers, and are later erupted as silica-rich ignimbrites (e.g., the Magpie Basin Member). **(b)** As the injection of mantle-derived basalts increases the mid-crustal source region becomes increasingly hybridised with the basaltic melts. Therefore subsequent rhyolitic melt batches extracted from this source region have an increased mantle-component, and these erupt as ignimbrites with progressively less-evolved compositions (e.g., the Big Bluff - Little Creek members).

overlying members (i.e., Indian Springs Member – Lincoln Reservoir Member, Fig. 4.20b) suggest a return towards an increasingly hybridised source region overtime.

While modifying the source region with the injection of basalt is capable of explaining the Cassia Formations trends in major element concentrations (e.g., decreasing SiO_2 and increasing TiO_2 and Fe_2O_3) it fails to explain all trends seen in the relatively incompatible trace elements. Although decreasing Rb and Th contents with stratigraphic height (Fig. 4.21b) are consistent with the magmatic system becoming less-evolved, an observed increase in Zr is inconsistent with this interpretation. Zirconium concentrations for bulk continental crust are between 123 – 175 ppm (Rudnick & Gao, 2003) and the composition of mantle-derived basalts, in the cSRP, has been assumed as either the average of the Columbia River Basalts (Zr = 174 ppm; Boroughs et al., 2012) or the approximate composition of the later erupted basalt lavas (Wright et al., 2002; Nash et al., 2006; McCurry & Rodgers, 2009), for example the Basalt of McHann (Zr = 85 ppm, Oakley & Link, 2006). Assuming either basalt composition to be representative, the addition and mixing of more mantle-derived basalt into crustal melts would result in progressively diluted Zr concentrations. Therefore simple mixing between mafic and silicic melts cannot account for the progressively increasing Zr concentrations seen throughout the Cassia Formation.

4.20.3. Injection and mixing of more-mafic liquids into shallow silicic magma chambers

All previous models suggest that the increased addition of a mantle-derived component, as seen in the $^{144}Nd/^{143}Nd$ ratios, occurs within a mid-crustal melting and mixing zone (Hildreth et al., 1991, Leeman et al., 2008; McCurry & Rogers, 2009; Fig. 4.27a). However, the following section presents a new model wherein mixing between mantle-derived material and rhyolitic melts occurs within shallower upper-crustal magma chambers due to the upwelling and injection of more mafic mantle-derived melts.

The initial model parameters (Table.C.15) were set assuming that the composition of average Columbia River Basalts are representative of mantle-derived basalt (after Boroughs et al., 2012), and that the composition of the silica-rich Magpie Basin Member is representative of a typical evolved cSRP rhyolitic liquid that was ponded in a shallower magma chamber (Fig. 4.29a). With these parameters set simple mixing calculations were performed between these two end members using the following formula:

$$C_M = (X * C_x) + (1\text{-}X) * C_p$$

Where: C_M – concentration in the mix

X – proportion of mixing component

C_x – concentration in mixing component

C_p – concentration in parent liquid

Resultant mixing lines (Fig. 4.28) reveal that mixing between Columbia River Basalts and the Magpie Basin Member cannot account for all the chemical trends exhibited by the overlying members of the Cassia Formation. For example, mixing between these two end-members demonstrates a rapid increase in Mg and Fe, whereas Zr decreases. This is inconsistent with the observed data trends throughout the Cassia Formation. This suggests that if mantle-derived mafic liquids were mixing into shallow rhyolitic magma chambers they must have been more evolved than average Columbia River Basalts; with lower Mg and Fe concentrations and higher Zr concentrations. It is therefore proposed that these more evolved liquids likely fractionated from mid-crustal basalts (Fig. 4.29a), as studies have suggested that mantle-derived magmas pond in the mid-crust due to their higher density (Leeman et al., 2008; McCurry & Rogers, 2009). These fractionated melts would then be less dense and rise buoyantly to the top of the basaltic reservoir (Fig. 4.29a). The accumulating fractionated melts would then ascend buoyantly through the crust and subsequently be injected and mixed into shallower silicic magma chambers (Fig. 4.29b). This would result in the contamination of the pre-existing rhyolitic melt within the chamber, generating progressively less-evolved compositions that would be reflected in the erupted ignimbrites (Fig. 4.29c).

By assuming model parameters that best fit the major and trace element trends of the Cassia Formation, extrapolated mixing lines indicated mixing between the Magpie Basin Member and a liquid with the following approximate composition: Mg = ~5500 ppm; Fe = ~55000 ppm; Rb = ~100 ppm; Sr = ~ 200 ppm; Zr = ~850 ppm. Continuing the assumption that average Columbia River Basalts are an approximation of the mantle-derived basalts beneath the cSRP, fractionation of these basalts was modelled in order to determine whether this approximate evolved liquid composition was achievable. Fractionation was modelled assuming Rayleigh fractional crystallisation given by:

$$C_1 = F^{(D-1)} * C_0$$

Where: C_1 – concentration in the liquid

C_0 – initial concentration in liquid

D – bulk partition coefficient

F – fraction of liquid remaining

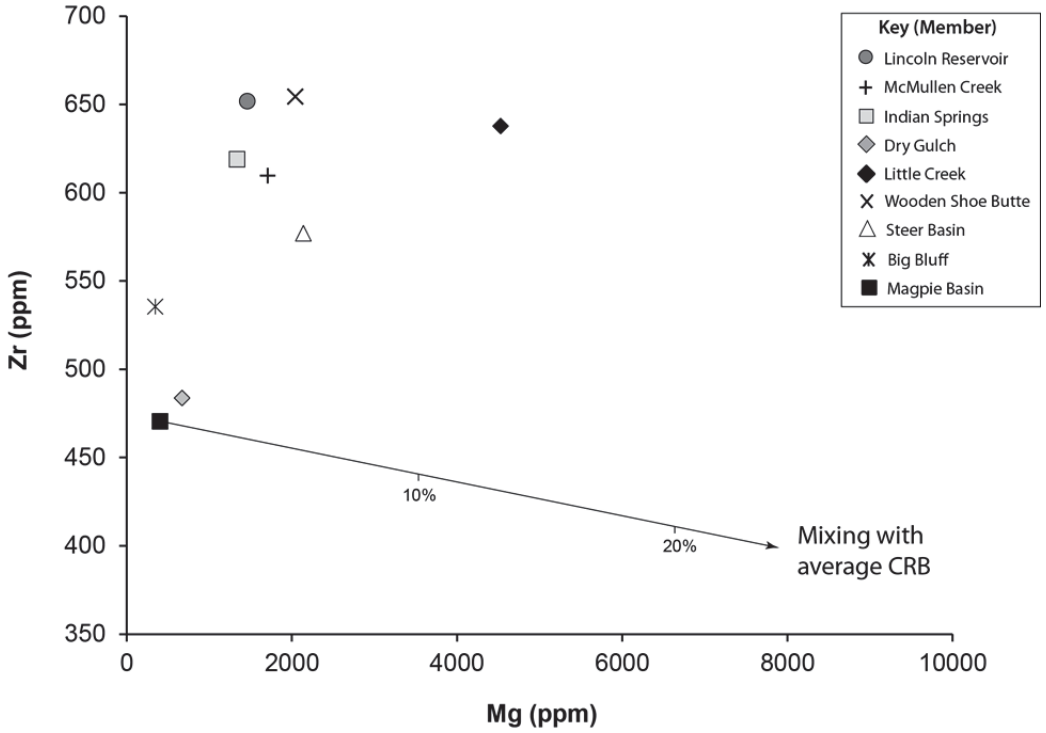

Figure 4.28. Mg (ppm) versus Zr (ppm) plot showing the results of mixing between the Magpie Basin Member and average Columbia River Basalt (CRB). Mixing between these two end-members cannot account for the geochemical trends exhibited by the Cassia Formation.

Previous studies have shown that melts 'trapped' in the crust undergo strong polybaric fractionation of plagioclase, clinopyroxene and olivine (e.g., Putirka et al., 2003; Whitaker et al., 2007). Therefore for the purpose of model calculations presented here a fractionating mineral assemblage of plagioclase, clinopyroxene and olivine was also assumed in the proportions of 50:25:25%, respectively (see Table C.16). The results from the model calculations show that similar concentrations of Mg, Fe, Rb, Sr and Zr, to the required more-evolved liquid, are achieved after 80% fractionation of average Columbia River Basalt (Table C.16). Similar degrees of fractionation have also been suggested for the generation of post-hotspot silicic lavas in the eastern Snake River Plain (~77 % fractionation of basaltic trachyandesite, McCurry et al., 2008).

Simple mixing between this more-evolved liquid (L_2) and the Magpie Basin Member (Table C.15) show that a total addition of ~40 % of L_2 can account for most of the observed trends in Fe, Mg, Rb, Sr and Zr, from the Magpie Basin Member to the Little Creek Member (Fig. 4.30 a–d). This is assuming that the Magpie Basin, Big Bluff, Steer Basin, Wooden Shoe Butte and Little members were all erupted from a single magma chamber that was periodically contaminated by the injection of L_2. However, the Little Creek Member has more elevated Mg concentrations than those expected from extrapolated mixing lines (Fig. 4.30b). This may highlight the limitations of using ignimbrite whole-rock composition as an approximation of the liquid compositions, and the elevated Mg may be due to the abundant high-Mg pyroxenes present in the Little Creek Member. However, further work is needed to constrain this.

The sudden deviation from projected mixing trends exhibited by the younger Dry Gulch Member (e.g., higher Rb, and lower Mg, Fe, Sr and Zr, Fig. 4.30 a–d) suggests that it was erupted from a more-evolved magma chamber, isolated from the chamber that produced the older eruption-units. Simple mixing calculations (Table C.15) show that the continuing trend towards less-evolved compositions seen in the overlying Indian Springs, McMullen Creek and Lincoln Reservoir members is consistent with the injection and mixing of L_2 into the 'Dry Gulch magma chamber', and the whole-rock composition of the youngest Lincoln Reservoir Member is mostly consistent with ~30 % addition of L_2 (Fig. 4.30 a–d). However, assuming that the Dry Gulch Member represents the parental magma for these younger units, the three overlying members do lie off of the projected Zr mixing line (Fig. 4.30d). This again may be due to the limitations of assuming that ignimbrite whole-rock compositions are representative of the parent melts, and the increased Zr concentrations may be due to differing proportions of accessory zircon crystals in these members, which is not well constrained.

Recent oxygen isotope data (Reichow, unpublished data), obtained on zircons from cSRP ignimbrites, show that $\delta^{18}O$ values progressively increases over time (Fig. 4.31). Rhyolites of the cSRP have characteristic low $\delta^{18}O$ values (from −1.2 to 4.8 ‰, previously obtained on feldspar and quartz crystals, Boroughs et al., 2005), and it has been concluded that $\delta^{18}O$ values show no correlation with major and trace elements and radiogenic isotopes (Boroughs et al., 2012). However, these new zircon $\delta^{18}O$ values are positively correlated with progressively increasing $^{144}Nd/^{143}Nd$ ratios over time (Ellis et al., 2013). This is supportive of the model proposed above, and may suggest progressive mixing between

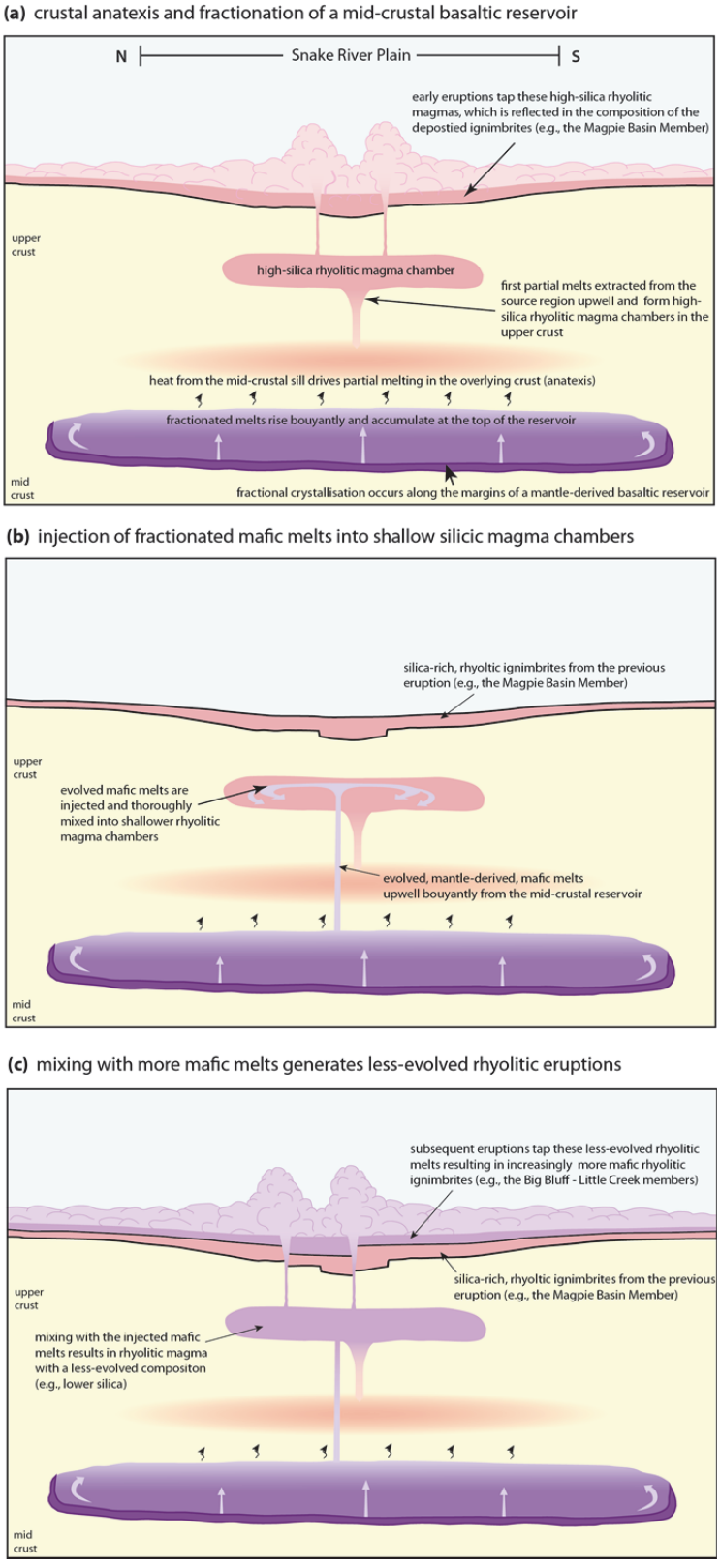

Figure 4.29. Schematic diagrams (not to scale) illustrating a model of fractionation of mid-crustal basaltic melts and their subsequent injection and mixing into shallower rhyolitic magma chambers. **(a)** Thermal energy from ponded mantle-derived basalts drives melting in the overlying crust (anatexis) and produces rhyolitic melts that rise into shallower magma chambers, and are later erupted as silica-rich ignimbrites (e.g., the Magpie Basin Member). **(b)** Fractionation of the basalts produces more-evolved mafic liquids that ascend buoyantly and are injected and mixed into pre-existing rhyolitic magma chambers. **(c)** Mixing between the evolved mafic liquids and the rhyolitic magmas results in progressively less-evolved rhyolitic magmas and this is reflected in the compositions of the erupted ignimbrites (e.g., the geochemical trend exhibited by the Big Bluff – Little Creek Members).

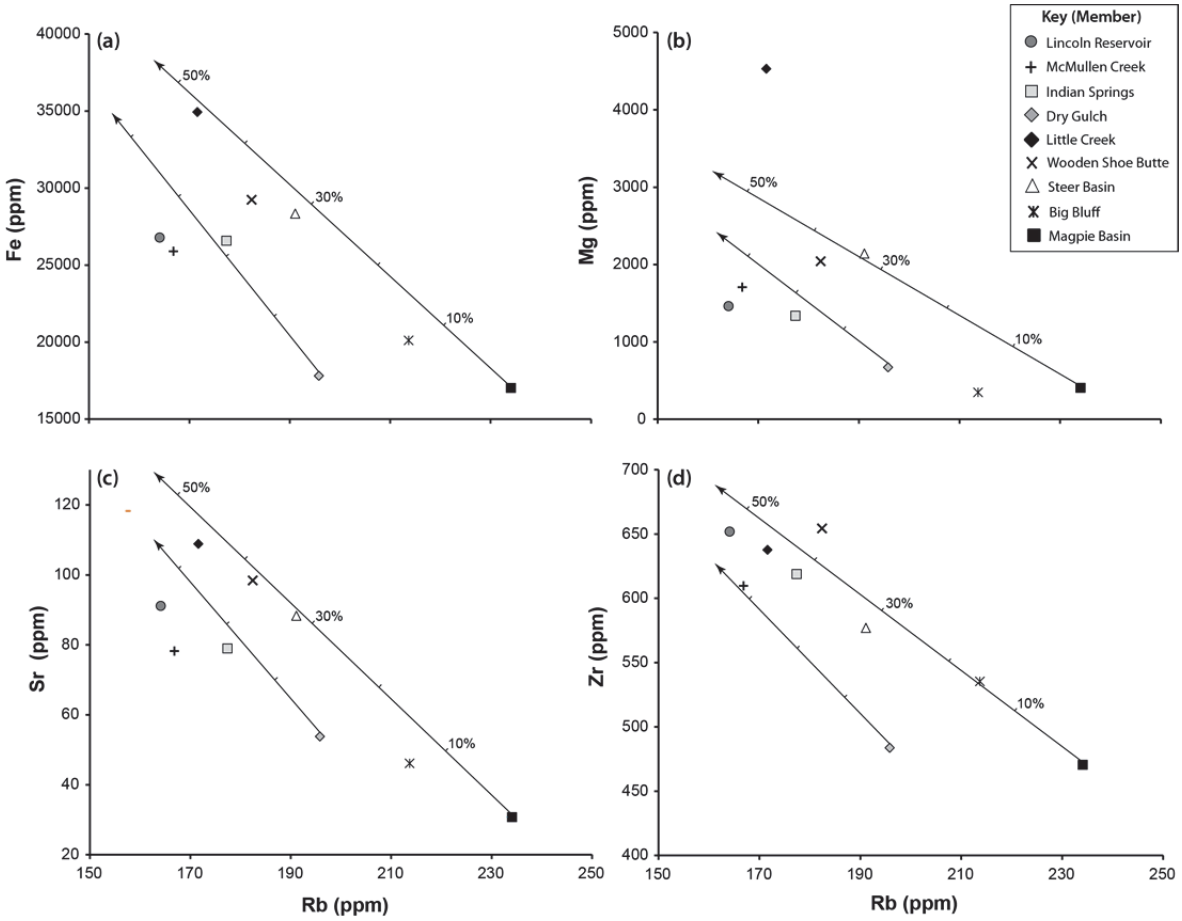

Figure 4.30. Select major elements (Fe and Mg) and trace elements (Sr and Zr) versus Rb indicating the results of simple mixing between the more-mafic liquid (L_2) and parental rhyolitic magmas represented by the Magpie Basin and Dry Gulch Members. Tick marks along mixing lines mark 10 % mixing increments.

cSRP rhyolitic magmas, and liquids with mantle-derived $\delta^{18}O$ values (~5.3 ‰, Valley et al., 1998).

In summary, a model of injection of more-evolved mafic liquids (L_2) into shallower rhyolitic magma chambers, presented here, is capable of explaining the majority of major and trace element trends exhibited by the Cassia Formation. In addition, it is also proposed that the two distinct geochemical trends (i.e., between the Magpie Basin and Little Creek Members, and between the Dry Gulch and Lincoln Reservoir Members) suggests that L_2 was likely injected into two separate magma chambers. However, the deviation of some members from projected mixing lines suggests that the model may be too simplistic, and further investigation is needed in order fully constrain the petrogenetic evolution of the Cassia Formation rhyolites.

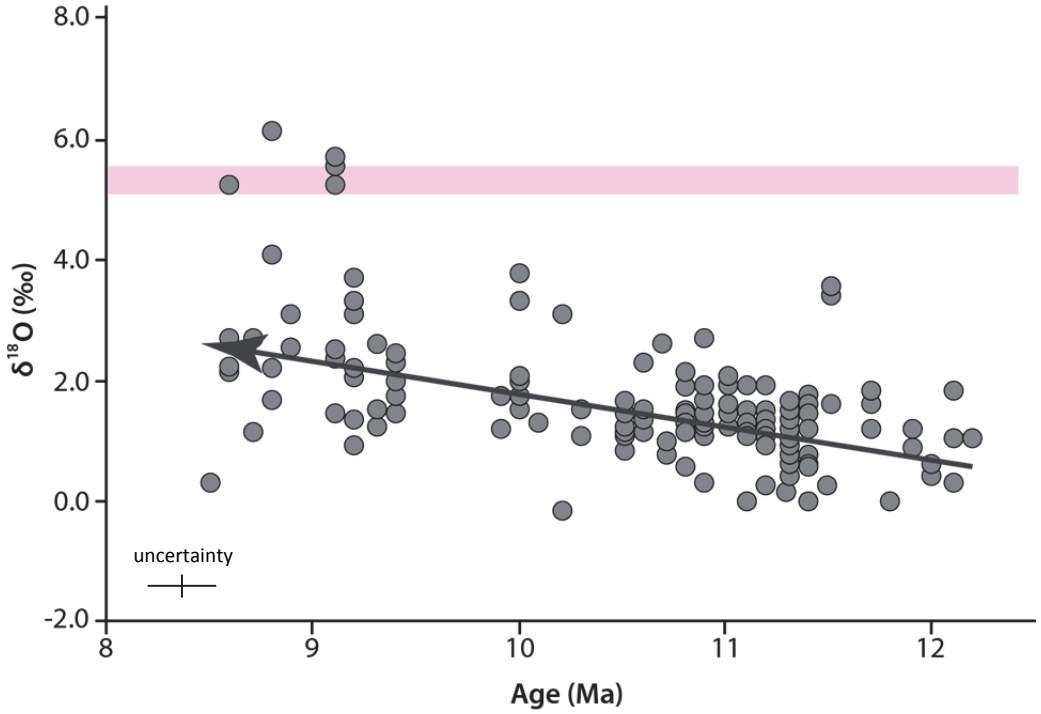

Figure 4.31. Oxygen isotope data (Reichow, unpublished) from zircons from several rhyolitic ignimbrites in the cSRP. Data shows that $\delta^{18}O$ values increase slightly overtime, which supports the model that mantle-derived liquids with higher (~5.3 ‰, pink bar, Valley et al., 1998) $\delta^{18}O$ values were mixing with low $\delta^{18}O$ Snake River-type rhyolitic magmas.

4.21. Conclusions

The Cassia Formation provides a well-exposed window into the evolution of silicic explosive volcanism originating from the cSRP, between ~11–9 Ma. An investigation of the silicic pyroclastic succession has yielded the following conclusions (1–6):

(1) The volcanic succession in the Cassia Mountains comprises 13 individual eruption-units, each of which records a single explosive rhyolitic eruption. This is five more than was defined in previous accounts (e.g., Williams et al., 1990; Ellis et al., 2010). Each eruption-unit constitutes a member of the re-defined Cassia Formation.

(2) Individual members can be distinguished from one another using a combination of physical field characteristics, whole-rock and mineral chemistry, and some palaeomagnetic and geochronology data.

(3) Eruptions from the cSRP may have become more frequent with time from ~11–9 Ma with repose periods decreasing from ~400 ka to ~100 ka, which are now recorded as palaeosols. However, additional high-precision age determinations (work in progress, see Chapter 7) are required in order to constrain this further.

(4) The rhyolite whole-rock geochemistry of the Cassia Formation reveals two geochemical trends from more-evolved high-silica (~76 wt %) rhyolites towards less-evolved compositions. These trends are observed between the Magpie Basin and Little Creek Members, and between the Dry Gulch and Lincoln Reservoir Members.

(5) The two compositional trends in (4) are inferred to have resulted from the injection of more-mafic liquids into shallower rhyolitic magma chambers, which was then followed by mixing between these two liquids. The more-mafic melts are thought to have been generated by extreme fractionation of mantle-derived basalts ponded within the mid-crust resulting in lower Fe and Mg concentrations and elevated Zr concentrations.

5. Drilling a rhyolitic caldera fill: proximal volcanic succession revealed by the HOTSPOT deep drill hole, Kimberly, Idaho.

5.1. Introduction

The Yellowstone–Snake River volcanic province is a series of time-transgressive bimodal (rhyolite–basalt) volcanics that extend ~600 km from northern Nevada, across southern Idaho to the Yellowstone volcanic field in Wyoming, USA (Fig. 5.1a). It is well known that the Yellowstone volcanic field has produced several large explosive eruptions over the past two million years. This includes the Huckleberry Ridge Tuff (2.2 Ma, 2210 km^3), the Mesa Falls Tuff (1.3 Ma, 280 km^3), and the Lava Creek Tuff (0.6 Ma, 1000 km^3) (Christiansen, 2001; Lanphere et al., 2002; Ellis et al., 2012b). Each of these eruptions produced large overlapping calderas with the eruption of the Lava Creek Tuff producing the 70 km-diameter Yellowstone caldera seen today (Christiansen, 2001). This overlapping of calderas is an example of a nested caldera complex (e.g. similar to the San Juan volcanic field, Steven & Lipman, 1976), and a similar nested caldera complex has also been identified in the Yellowstone-Snake River volcanic province as part of the older (~6.6 Ma) Heise volcanic field (Morgan and McIntosh, 2005, Fig. 5.1a). However, there is currently no documented evidence for calderas in the central Snake River Plain (cSRP).

Recently, three large volume ignimbrite eruption-units have been identified in the cSRP, and are termed 'Cougar Point Tuff XI' (~350 km^3)'; 'Cougar Point Tuff XIII' (~1,000 km^3); and the 'Steer Basin Tuff' (~350 km^3) (Ellis et al., 2012a). Cougar Point Tuff XIII is comparable in size to the Lava Creek Tuff of the Yellowstone volcanic field (Ellis et al., 2012a). Total dense rock equivalent (DRE) eruption volumes, for these three eruption-units, were estimated as twice that of the measured outflow volumes (Ellis et al., 2012a) assuming associated intra-caldera fill to be equal to the outflow volumes (after Lipman, 1984). While this assumption has been shown to be reasonable (e.g., the Younger Toba Tuff, Rose & Chesner, 1987; and the Oruanui eruption, Wilson, 2001) an accurate determination of intra-caldera fill volumes in the cSRP remains a challenge as any evidence for calderas is obscured by late Miocene-Pliocene voluminous basaltic lavas, which overlie the older rhyolites (Bonnichsen et al., 2008).

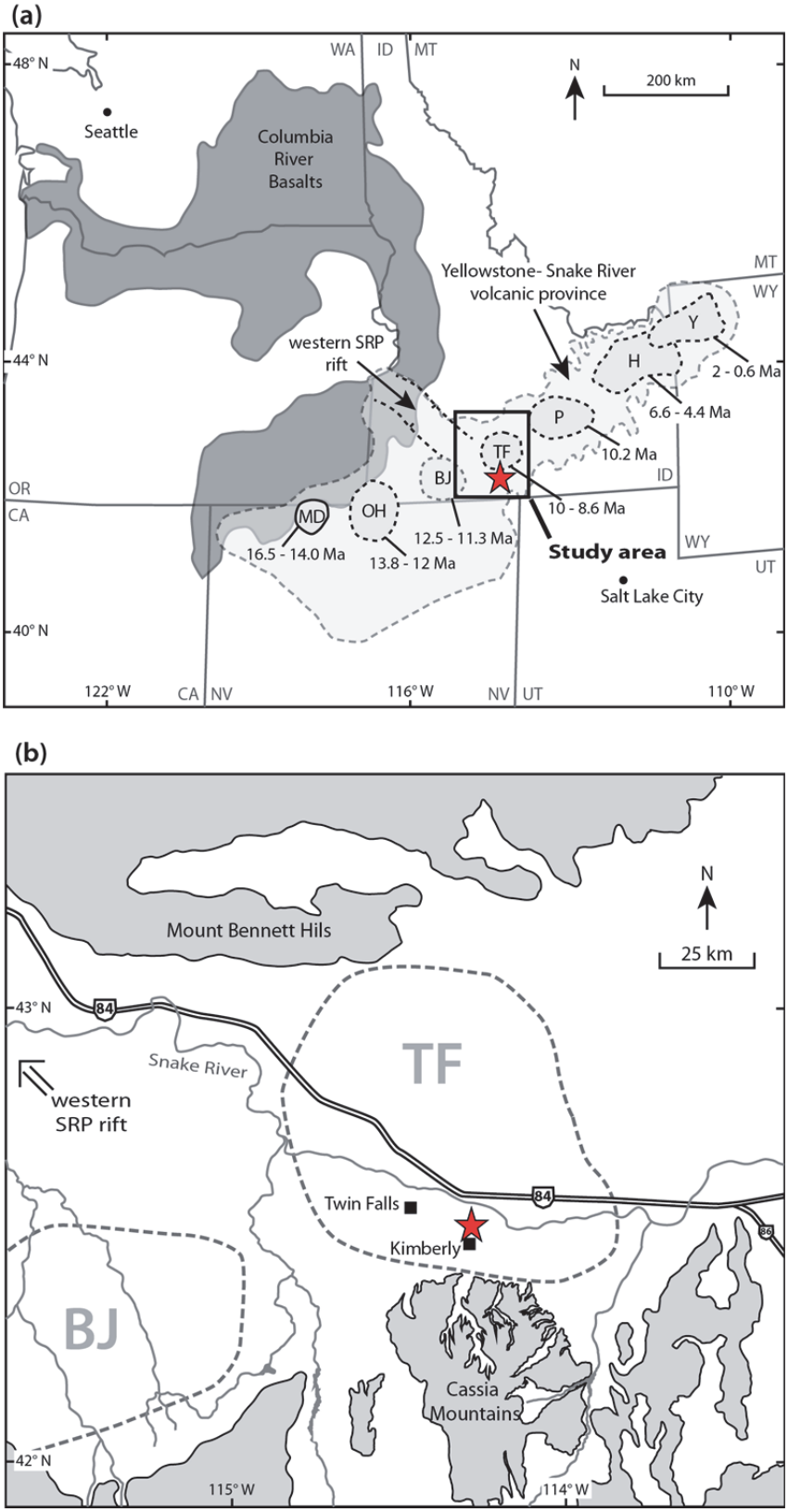

Figure 5.1. (a) The Yellowstone-Snake River bimodal volcanic province showing the study area of the present study (black square) and the locations of all proposed volcanic centres. Volcanics centres are termed: MD, McDermitt; OH, Owyhee-Humbolt; BJ, Bruneau-Jarbidge; TF, Twin Falls; P, Picabo; H, Heise; and Y, Yellowstone, after Bonnichsen et al (1989) and Morgan & McIntosh (2005). **(b)** Simplified location map of the study area of the present study showing the location of the Kimberly borehole (red star) and place names mentioned in the text.

The 1.9 km deep Kimberly borehole, located 1 km N. of Kimberly, southern Idaho, USA (Fig. 5.1b) was drilled in 2012 as part of Project HOTSPOT (Shervias, et al., 2013), which seeks to understand volcanism in the Yellowstone-Snake River volcanic province including magma generation and eruption history. The Kimberly bore-hole penetrates surficial basalt lavas and deep into the underlying rhyolites on the southern margin of the cSRP. It is positioned north of the Cassia Mountains (Fig. 5.1b), where several intensely-welded rhyolitic ignimbrites are exposed that are thought to have originated from the postulated Twin Falls eruptive centre within the cSRP (McCurry et al., 1996; Wright et al., 2002). The Kimberly borehole therefore provides a unique window into proximal deposits on the southern margin of this tentative eruptive centre and potentially reveals intra-caldera ignimbrites associated with nearby outflow ignimbrites.

The following chapter presents the first description and interpretation of the proximal mid-Miocene volcanic succession recovered by the Kimberly borehole, with the primary focus on the Kimberly rhyolites, and explores whether this succession represents an intra-caldera sequence. In addition the individual rhyolites, identified in the Kimberly core, are compared to known rhyolitic outflow sheets exposed on the margins of the cSRP in order to establish any potential correlations.

5.2. The formation of calderas and intra-caldera fill facies

Calderas are topographic depressions, more or less circular in form, which are widely acknowledged to form during large-explosive eruptions due to the collapse of the magma chamber roof as the chamber empties (e.g., Spera and Crisp, 1981; Lipman, 1984, 1997; Christiansen, 2001). However there are disparate opinions about when caldera collapse occurs during large explosive eruptions. Many have concluded that collapse ensues only after enough magma erupts to remove support for the roof and allow it to collapse into the emptying magma chamber (e.g., Lipman, 1997; Christiansen, 2005; Best et al., 2013). In this case, collapse occurs syn-eruption and the development of a caldera results in late erupted products (e.g., ignimbrites and/or lavas) being largely confined within the caldera. In contrast to this model, others propose that in some cases caldera collapse may occur during the onset of volcanism and therefore the majority of the eruptive products will be confined to the caldera (Willcock et al., 2013). In either scenario calderas commonly preserve thick intra-caldera facies of

ponded ignimbrites and/or lavas, which make up a significant proportion of the total eruptive volume during any one explosive-eruptive event. For example, it has been suggested that the volume of intra-caldera ignimbrite is approximately equal to that of any outflow ignimbrite (Lipman, 1984), and a number of subsequent studies have shown that intra-caldera volume may even be larger than the outflow volume (e.g., Bishop Tuff, Hildreth and Wilson 2007; Bandelier Tuff, Self 2010). It is therefore important to identify and correlate intra-caldera ignimbrites to their equivalent outflow sheets in order to gain a more accurate estimation of total eruptive volume for a single eruption. Typical intra-caldera fill sequences (Lipman, 1984) include thick (0.2–2 km) massive welded ignimbrites, mesobreccias (blocks < 10 m in size) and megabreccias (blocks 10 m - 1 km in size) formed due to the collapse of the caldera collar and volcano-tectonic faulting (e.g., Scarfell Caldera, UK, Branney & Kokelaar, 1994), hydrothermal alteration, silicic lava domes, and lake sediments.

5.3. The volcanic succession of the Kimberly borehole

Based on core-descriptions, whole-rock and mineral chemical data and geochronology data the present study identifies three distinct rhyolitic eruption-units separated by intercalated sediments and basalt lavas (Fig. 5.2). These three rhyolitic units are herein termed, from stratigraphically oldest to youngest, Kimberly Rhyolite 1, Kimberly Rhyolite 2 and Kimberly Rhyolite 3. Each is described individually below.

5.3.1. Kimberly Rhyolite 1

Kimberly Rhyolite 1 is 1340 m-thick but could be substantially thicker as its base was not recovered by the borehole. Its top is located at 610 m depth and it is overlain by non-welded, parallel-laminated, white sediments that separate it from the stratigraphically younger Kimberly Rhyolite 2. It has a 1308 m-thick, pale grey, lithoidal zone that contains sparse vitric lapilli, 1–3 mm in size (Fig. 5.3d). These vitric lapilli are not seen in the overlying rhyolites and are therefore a unique characteristic of Kimberly Rhyolite 1. The lithoidal zone also has a very pronounced foliation, the angle of which varies with height through the eruption-unit and implies rheomorphic folding in the upper lithoidal zone. In the lower 1190 m the foliation is primarily low angle or sub-horizontal, however in the upper 118 m the angle of the foliation alternates between low and high upwards towards the contact with the upper vitrophyre (Fig. 5.3c).

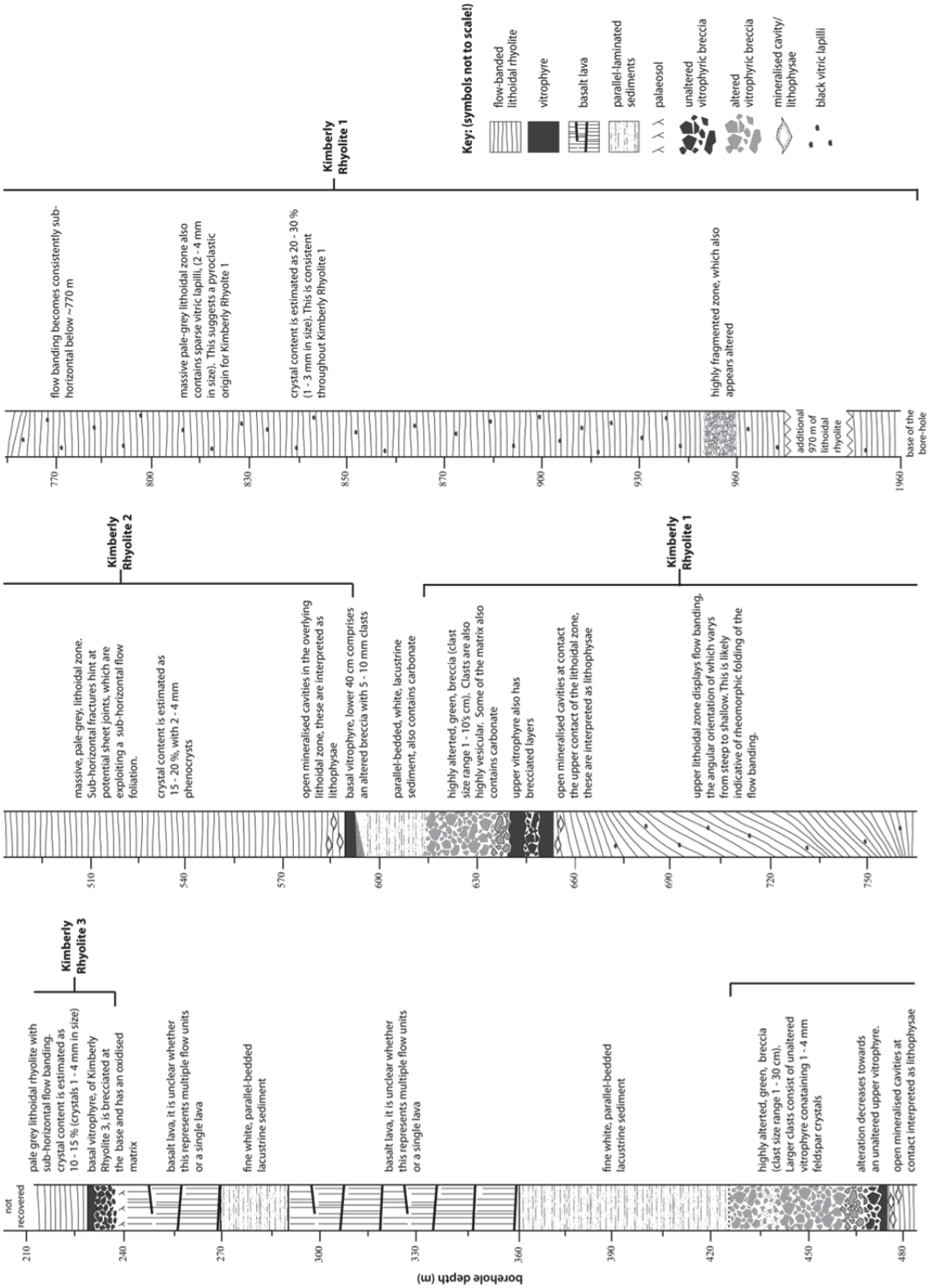

Figure 5.2. Graphic log of the Kimberly borehole succession showing the characteristic physical features of Kimberly Rhyolites 1 – 3.

Petrographic observations reveal that this foliation is in fact well-developed flow banding (better observed in the upper vitrophyre), which wraps around the present phenocrysts (Fig. 5.3e). Crystal content is estimated at 20–30 % (crystals 1–4 mm in size), with a mineral assemblage of plagioclase, pigeonite, augite, magnetite and rare quartz (section 5.5). This crystal content and assemblage is consistent throughout Kimberly Rhyolite 1 from base to top. The top of the thick lithoidal zone is in sharp contact with the overlying upper vitrophyre. This contact is also marked by open, mineralised, cavities (2–4 cm in size) that are elongate along the flow banding (Fig. 5.2). These are likely lithophysae, which are common at the contact between glassy and devitrified zones in the majority of Snake River (SR)-type rhyolites (Branney et al., 2008). The upper vitrophyre is dominantly auto-brecciated, however the lower 14 m are more coherent with only small layers of brecciation. These breccia layers consist of angular clasts of dark grey vitrophyre (2–5 cm in size) in an oxidised, orange, matrix. Above the more coherent zone the overlying 28 m consist of clast-supported auto-breccia with angular clasts, 1 cm to >10 cm in size, that are highly vesicular and green in colour due to hydrothermal alteration (Fig. 5.3b). Vesiculation in upper vitrophyric auto-breccias has also been recorded in other cSRP rhyolites (e.g., the Grey's Landing ignimbrite, Andrews et al., 2008). The matrix between the clasts shares a similar pale green colour, due to hydrothermal alteration (Fig. 5.3a), and some of the matrix also contains carbonate. The upper auto-breccia is overlain by 18 m of parallel-laminated white sediment (see section 5.3.4).

5.3.2. Kimberly Rhyolite 2

Kimberly Rhyolite 2 is 169 m-thick, with its base located at 595 m depth and its top at 426 m depth. The rhyolite sharply overlies 18 m of parallel laminated sediments that separate it from the underlying Kimberley Rhyolite. The basal vitrophyre of Kimberly Rhyolite 2 is 6 m thick, and the lower 0.4 m is brecciated and hydrothermally altered (Fig. 5.4e). This alteration can also be observed in bands, 1–2 cm-thick, within the vitrophyre that are concentrated around fractures. Where unaltered, the vitrophyre is dark grey and contains 15–20 % crystals, 1–4 mm in size. This crystal content is consistent throughout Kimberly Rhyolite 2 and comprises a mineral assemblage of plagioclase, anorthoclase, sanidine, pigeonite, augite, magnetite and quartz (section

Figure 5.3. (a) Upper hydrothermally altered green auto-breccia towards the top of Kimberly Rhyolite 1. **(b)** Some of the larger clasts in the upper auto-breccia are highly vesicular. **(c)** Flow-banding in the upper lithoidal zone of Kimberly Rhyolite 1 varies from shallow to steep angles, which implies the upper lithoidal zone displays rheomorphic folding. **(d)** Sparse vitric lapilli (~5 mm in size) within the lithoidal zone of Kimberly Rhyolite 1. **(e)** Photomicrograph showing how the flow-banding in the upper vitrophyre of Kimberly Rhyolite 1 wraps around phenocrysts of plagioclase (plag), pyroxene (cpx), and magnetite (mag).

5.5). The presence of anorthoclase is characteristic of Kimberly Rhyolite 2 and helps to distinguish it from Kimberly Rhyolite 1 and 3. In addition, the quartz crystals are heavily resorbed (Fig. 5.4f), which is also a distinct characteristic of Kimberly Rhyolite 2. The basal vitrophyre of Kimberly Rhyolite 2 is sharply overlain by a 119 m-thick lithoidal zone, and the contact is marked by open mineralised cavities (4–5 cm in size) that may be lithophysae similar to those seen in Kimberly Rhyolite 1 (Fig. 5.2). The

pale-grey lithoidal zone has abundant sub-horizontal fractures throughout that are likely exploiting the pervasive sub-horizontal flow banding better observed in the basal and upper vitrophyre. The contact with the overlying upper vitrophyre is sharp and is also marked by lithophysae within the top of the lithoidal zone (Fig. 5.2). The lower 1.5 m of the upper vitrophyre is dark grey and above this a clast supported auto-breccia, 2 m-thick, composed of angular vitrophyre clasts (2–10 cm in size) within a red oxidised matrix (Fig. 5.2). Upwards, the auto-breccia is hydrothermally altered and above ~467 m depth clasts that are between 2 and 5 cm in size are devitrified, and the surrounding matrix is green in colour. Clasts larger than 5 cm have dark grey vitrophyric cores, but have pale grey devitrified rims (Fig. 5.4d). Hydrothermal alteration continues to increase upwards and is most intense between 435 m and 438 m depth, where a 3 m-thick layer is entirely altered to green clay (Fig. 5.4c). Above this layer the auto-breccia is less-intensely altered, and continues for a further 9 m and is overlain by parallel-laminated white sediments.

5.3.3. Kimberly Rhyolite 3

Only the basal 30 m of Kimberly Rhyolite 3 were recovered by the Kimberly core, however interpretation of data obtained through in-situ wireline logging suggests it is ~120 m thick (Shervais et al., 2013), with its base located at 236 m depth. The rhyolite overlies a baked palaeosol developed in the top of underlying basalt lavas and is subsequently overlain by later basaltic lavas (contact not recovered, Shervais et al., 2013). The basal vitrophyre of Kimberly Rhyolite 3 is 8 m thick (Fig. 5.2), the lower 5 m of which are brecciated with angular clasts of vitrophyre (1–8 cm in size) within a red oxidised matrix (Fig. 5.4a). It is possible that the oxidised matrix is in fact an invasion of the underlying palaeosol forming a peperite, however this has yet to be confirmed. The vitrophyre is sharply overlain by a >22 m thick, massive, lithoidal zone (top not recovered) that displays sub-horizontal fractures that follow the flow banding. Crystal content throughout Kimberly Rhyolite 3 is estimated at 10–15 %, comprising a mineral assemblage of plagioclase, sanidine, pigeonite, augite, magnetite and trace amounts of quartz (section 5.5).

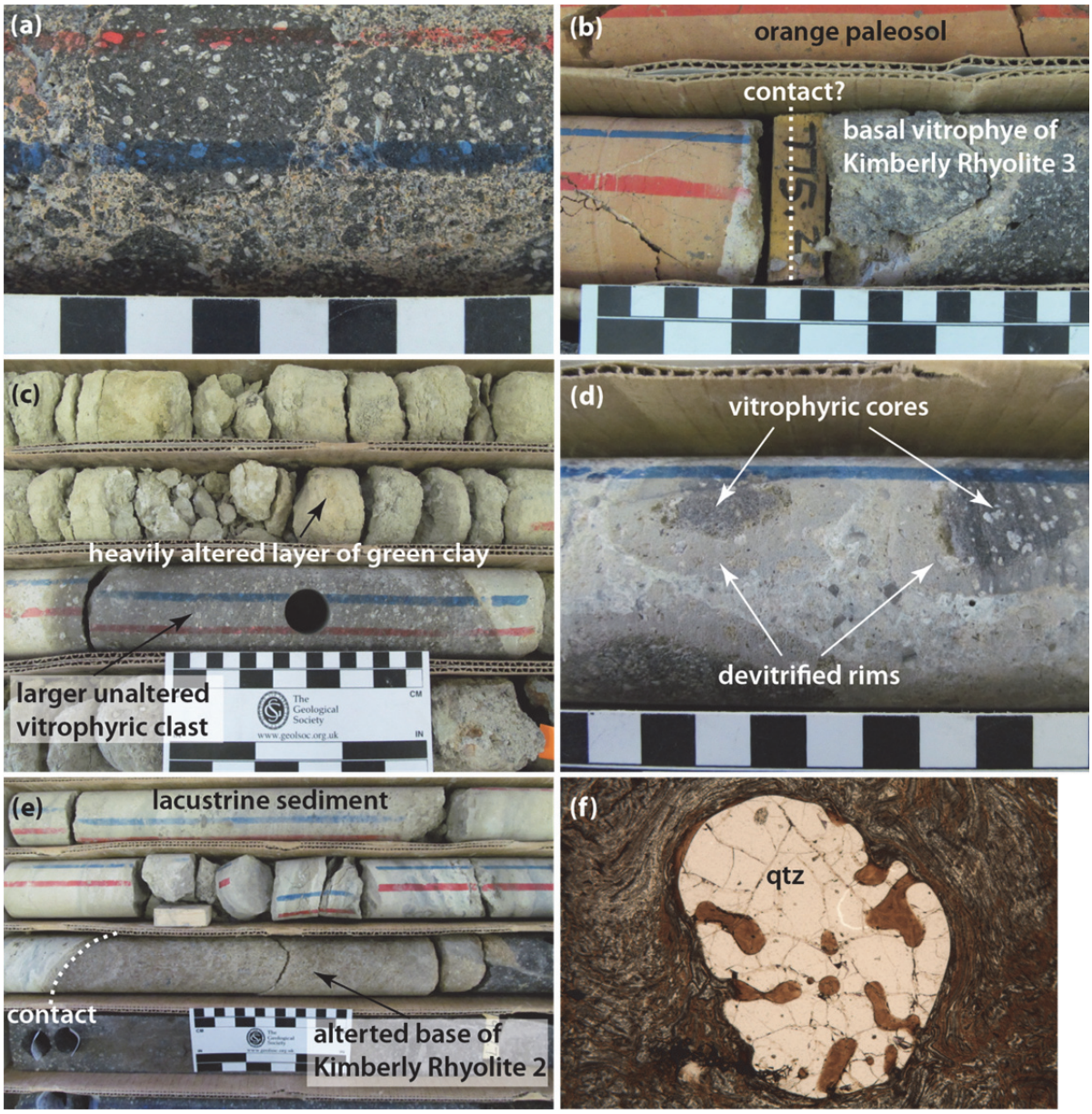

Figure 5.4. (a) Auto-breccia at the base of Kimberly Rhyolite 1. **(b)** Basal contact of Kimberly Rhyolite 3, which overlies an orange palaeosol in the top of the underlying basalt lavas. **(c)** Example of the larger unaltered vitrophyric clasts in the upper auto-breccia of Kimberly Rhyolite 2. Also shown is the highly altered layer of green clay between 435 and 438 m depth. **(d)** Clasts larger than 5 cm, in the Kimberly Rhyolite 2 upper auto-breccia, have dark grey vitrophyric cores and devitrified rims. **(e)** Basal contact of Kimberly Rhyolite 2 with the underlying parallel-laminated lacustrine sediments. Lower 40 cm of Kimberly Rhyolite 2 are brecciated and altered. **(f)** Distinctive resorbed quartz (qtz) crystal, which are characteristic of Kimberly Rhyolite 2. The matrix is flow-banded and wraps around the phenocryst.

5.3.4. Intercalated basalt lavas and parallel-laminated sediments

Two basaltic zones are exposed in the Kimberly core: one 34 m-thick (between 236–270 m depth) and the other 70 m-thick (between 290–360 m depth), and these occur stratigraphically between Kimberly Rhyolite 2 and Kimberly Rhyolite 3 (Fig. 5.2). These basalts were not formally described as part of this study and it is unclear whether

these basalts represent single lavas or are composed of several flows. A further ~120 m of basalt forms the capping unit of the Kimberly succession (Shervais et al., 2013), however this was not recovered by the Kimberly core but is well exposed in the Snake River canyon ~5 km north of the Kimberly borehole.

There are also three sediment packages recovered by the Kimberly borehole. The first is 18 m-thick and separates Kimberly Rhyolite 1 from the overlying Kimberly Rhyolite 2 (Fig. 5.2). The other two are 64 and 23 m-thick and are intercalated with basaltic lavas between Kimberly Rhyolites 2 and 3 (Fig. 5.2). Each of these sediment layers consist of millimetre-scale laminations of grey mudstone, fine sandstone and white, non-welded, volcanic ash (Shervais et al., 2013). The sediment layer above Kimberly Rhyolite 1 also contains carbonate that may suggest a calcareous cement or the later introduction of carbonate during hydrothermal alteration of the upper auto-breccia of Kimberly Rhyolite 1.

5.4. Whole-rock chemistry

Whole-rock samples obtained for this study were collected from the three rhyolitic units in the Kimberly core, in order to allow chemical classification and discrimination between the three units. Four samples were collected from the base and top of Kimberly Rhyolites 1 and 2 in order to assess any vertical chemical zonation, however only the base of Kimberly Rhyolite 3 was recovered for sampling. All samples were prepared for X-ray fluorescence (XRF) spectrometry and analysed on a PW4400 Axios XRF spectrometer at the University of Leicester (see Appendix B.1).

5.4.1. Results

Kimberly Rhyolites 1–3 are all metalumnious, with Alumina Saturation Indices (ASI) of 0.79–0.97 (Table C.3). Data of all three rhyolites plot (Fig. 5.5a) within the 'within plate granites' field defined by Pearce et al. (1984) and with high Ga/Al ratios (>3) can be classified as A-type (after Whalen et al., 1987).

Kimberly Rhyolites 1 and 3 are both low silica rhyolites (68.0–69.6 wt.% SiO_2) with relatively high concentrations of TiO_2, MgO, CaO and Fe_2O_3 (Fig. 5.5b). In contrast, Kimberly Rhyolite 2 is much more evolved than the other two rhyolites, and has significantly higher SiO_2 (~74 wt.%) and lower TiO_2 and Fe_2O_3 (Fig. 5.5b). Internally, Kimberly Rhyolites 1–3 are chemically homogeneous, and do not exhibit any

significant vertical chemical variations. For example variation in SiO_2, from base to top, in the 1340 m thick Kimberly Rhyolite 1 is <2 wt.%, and in Kimberly Rhyolites 2 and 3 is <1 wt.% (Fig. 5.5b).

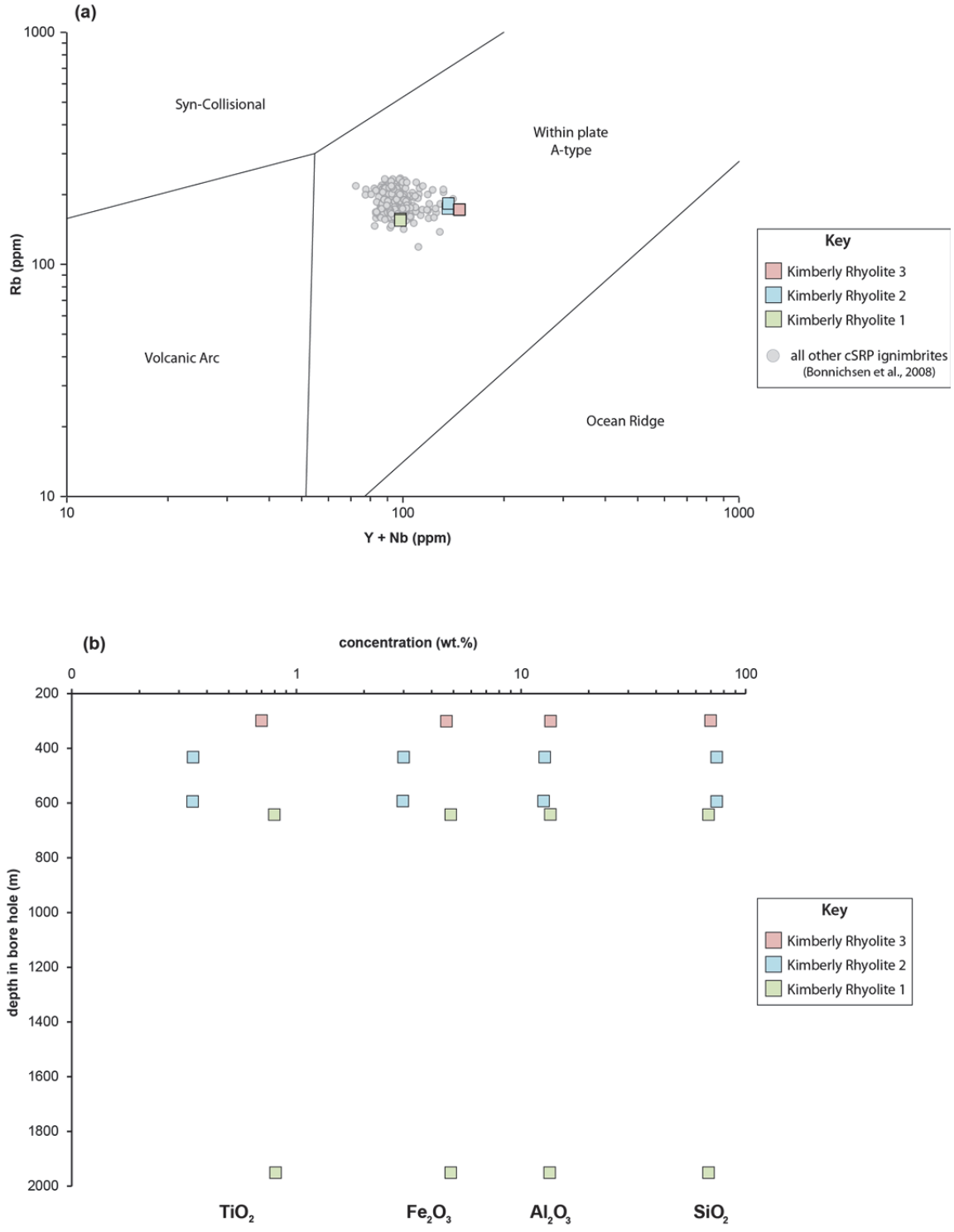

Figure 5.5. (a) Each of the Kimberly rhyolites plot within the 'Within Plate Granites' field of Pearce et al. (1984), which is consistent with all other cSRP ignimbrites. **(b)** Select major element concentrations plotted against borehole depth showing the distinguishable, but internally consistent compositions of each of the Kimberly rhyolites. The major elements TiO_2 and Fe_2O_3 are particularly useful to discriminate between the Kimberly Rhyolites 1, 2 and 3.

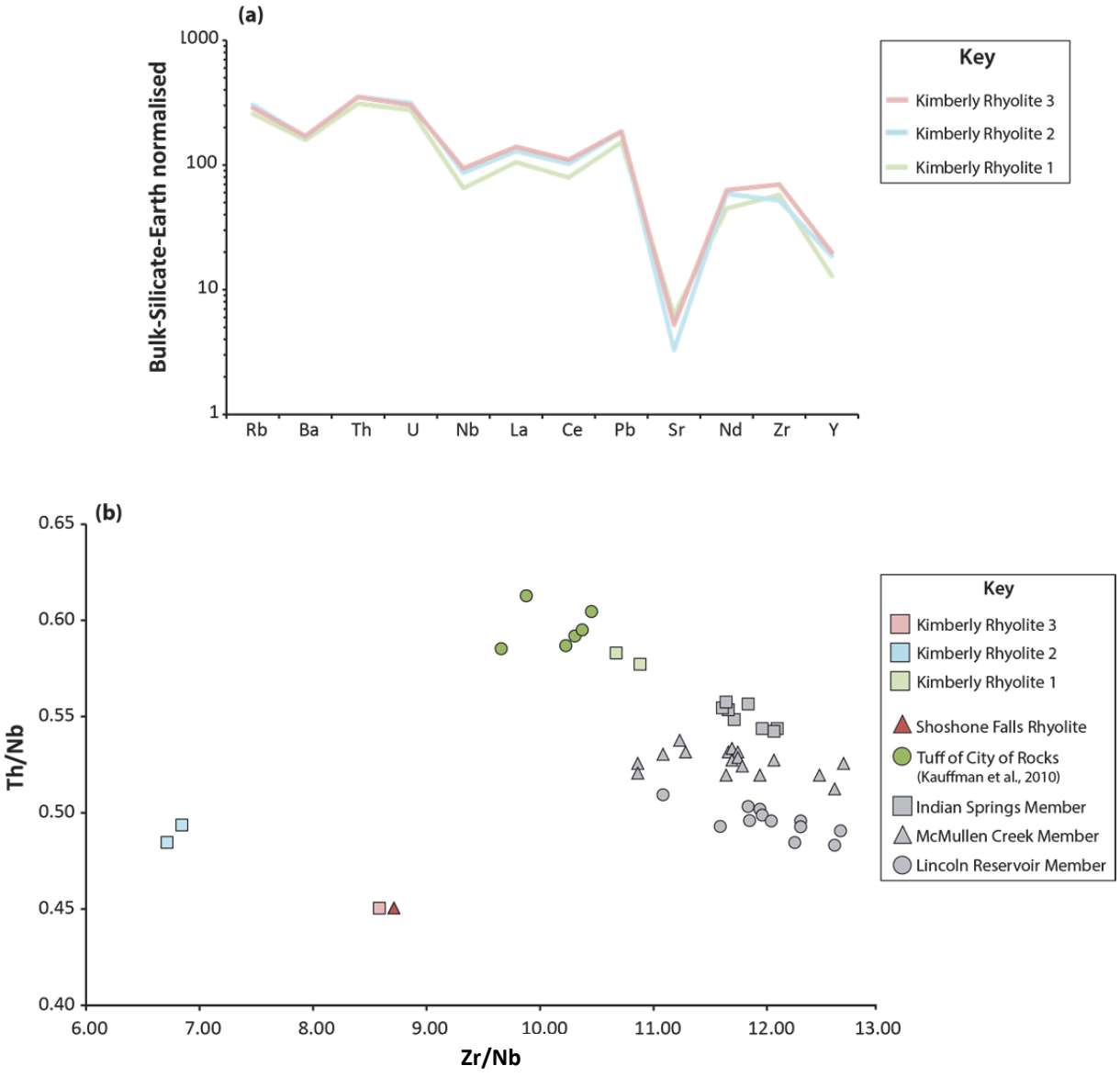

Figure 5.6. (a) Bulk-silicate-Earth (Sun & McDonough, 1995) normalised trace element patterns for each of the Kimberly rhyolites showing that all have broadly similar trace element abundances. **(b)** Zr/Nb versus Th/Nb plot demonstrating how each of the Kimberly rhyolites has a unique chemical composition. The composition of Kimberly Rhyolite 1 is also closely similar to the composition of the Tuff of the City of Rocks, which is supportive evidence of a correlation between them. In addition, data from Kimberly Rhyolite 3 and the Shoshone Falls Rhyolite lava are closely similar, therefore Kimberly Rhyolite 3 is proposed, in the present study, to be a lateral correlative of this lava.

Bulk-silicate Earth normalised trace element patterns (Fig. 5.6a) demonstrate that all rhyolites of the Kimberly bore-hole have broadly similar trace element abundances, with high Rb, Th, U and Pb, and relatively low abundances of Ba, Nb and Sr. However, despite these similarities it is possible to distinguish the individual Kimberly rhyolites based on the relative abundance of individual trace elements. For example, Kimberly Rhyolite 1 has lower abundances of Nb, La, Ce, Pb and Nd than both Kimberly

Rhyolite 2 and Kimberly Rhyolite 3 (Fig. 5.6a). In addition, each of the rhyolites is further distinguished when the relatively incompatible elements Th, Nb, and Zr are used as discriminators, and data from each unit define unique chemical fields with respect to their Zr/Nb and Th/Nb ratios (Fig. 5.6b).

In summary, both major and trace element data support the division of the Kimberly rhyolites into three eruption-units and allows clear distinction between them.

5.5. Petrology and mineral chemistry

Crystal content of the Kimberly rhyolitic succession decreases upwards from 20–30 % in Kimberly Rhyolite 1 to 10–15 % in Kimberly Rhyolites 3. All of the Kimberly rhyolites have broadly similar mineral assemblages that are dominated by feldspars, pyroxenes and magnetite. In addition, Kimberley 2 contains abundant quartz crystals (1–2 mm in size), which are also present in Kimberly Rhyolites 1 and 3 but are far less abundant. The quartz crystals in Kimberly Rhyolite 2 are heavily resorbed (Fig. 5.4f) and these are a characteristic feature of the unit.

Despite their similarities, the individual Kimberly rhyolites can be distinguished by the presence of discrete compositional modes within the most abundant mineral phases (feldspar and pyroxene). Chemical analyses of feldspar and pyroxene crystals were performed on a Cameca SX100 electron microprobe at the Open University, Milton Keynes, UK (see Appendix B.2), and the resultant data for these phases are described separately below.

5.5.1. Feldspars

Feldspar crystals in all three rhyolitic units are Type 1 euhedral crystals, and range in size from 1–3 mm. Compositions of all feldspar crystals, for each of the Kimberly rhyolites, are summarised in Table C.9. Plagioclase is ubiquitous in all of the Kimberly rhyolites (Fig. 5.7), however the compositions differ between the three units. Kimberly Rhyolite 1 contains solely andesine (An_{39}–An_{43}), whereas Kimberly Rhyolite 2 contains solely oligoclase (An_{33}–An_{27}). Plagioclase compositions in Kimberly Rhyolite 3 have a much larger range from andesine through to oligoclase (An_{33}–An_{38}), which are indistinguishable from those of Kimberly Rhyolite 1 and 2.

Kimberly Rhyolite 2 is unique as it is the only unit within the bore-hole to contain abundant anorthoclase (An_{12}–An_{15}, Fig. 5.7), and also contains abundant sanidine (An_3–An_5, Or_{40}–Or_{52}). Kimberly Rhyolite 3 also contains sanidine although only two crystals were analysed (Fig. 5.7).

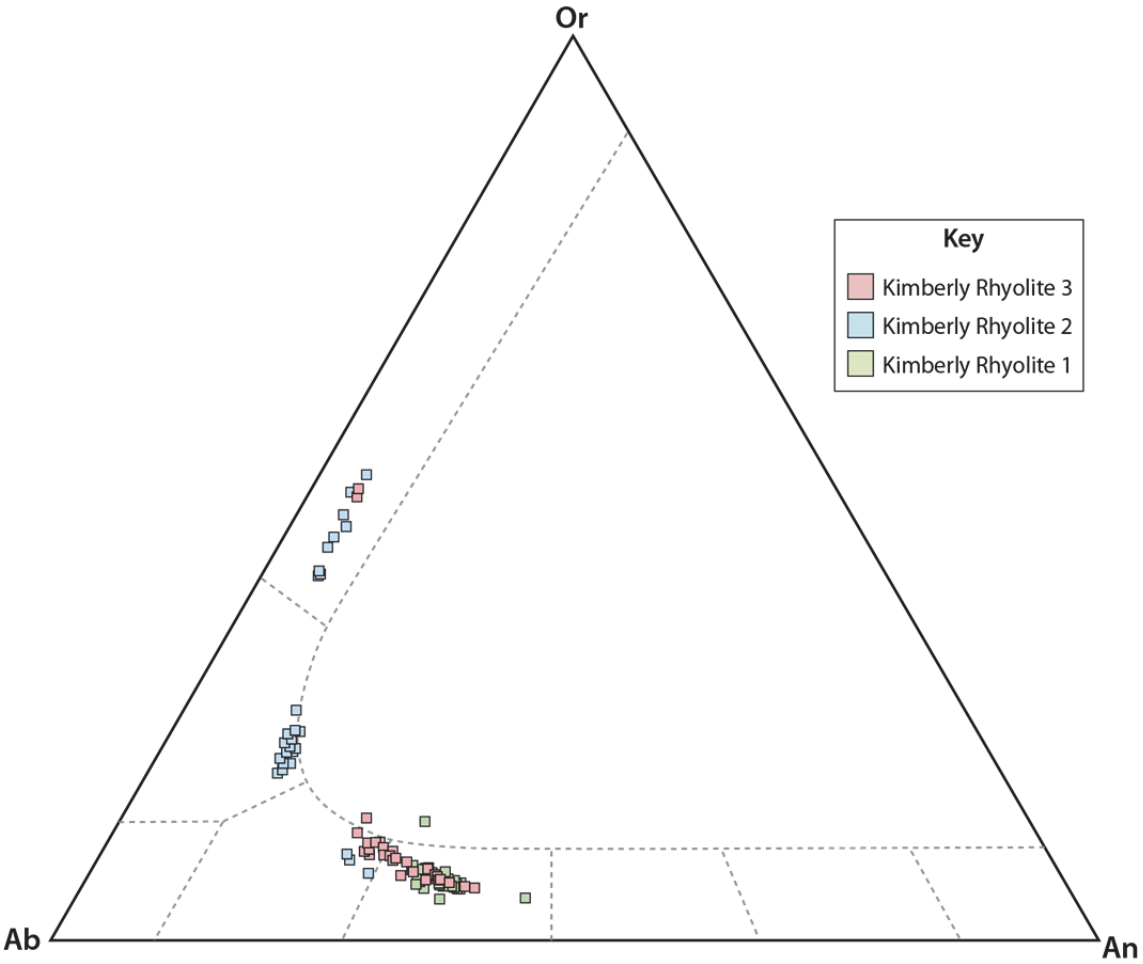

Figure 5.7. Feldspar ternary diagram showing the different feldspar compositions within each of the Kimberly rhyolites. Kimberly Rhyolite 1 contains solely plagioclase (andesine). Kimberly Rhyolite 2 also contains plagioclase (oligoclase), and is unique as it also contains abundant anorthoclase and sanidine. Kimberly Rhyolite 3 contains a range of plagioclase compositions that are similar to both of the underlying rhyolites, and also contains sanidine.

5.5.2. Pyroxenes

Pyroxene crystals, in each of the rhyolites, are typically subhedral and small (up to 1 mm in size) with slightly rounded crystal faces. Compositionally they occur as two types: Ca-rich augite and Ca-poor pigeonite (Table C.10). Both augite and pigeonite are ubiquitous throughout Kimberly Rhyolites 1–3. The pyroxenes of Kimberly Rhyolites 1 and 3 have high MgO concentrations (10.62 – 16.82 wt.%) that are among the highest

of any rhyolitic unit in the cSRP (Fig. 5.8). The pyroxenes of Kimberly Rhyolite 2 have much lower MgO concentrations, consistent with a more evolved whole-rock composition, and pigeonite is also less abundant than the other Kimberly rhyolites.

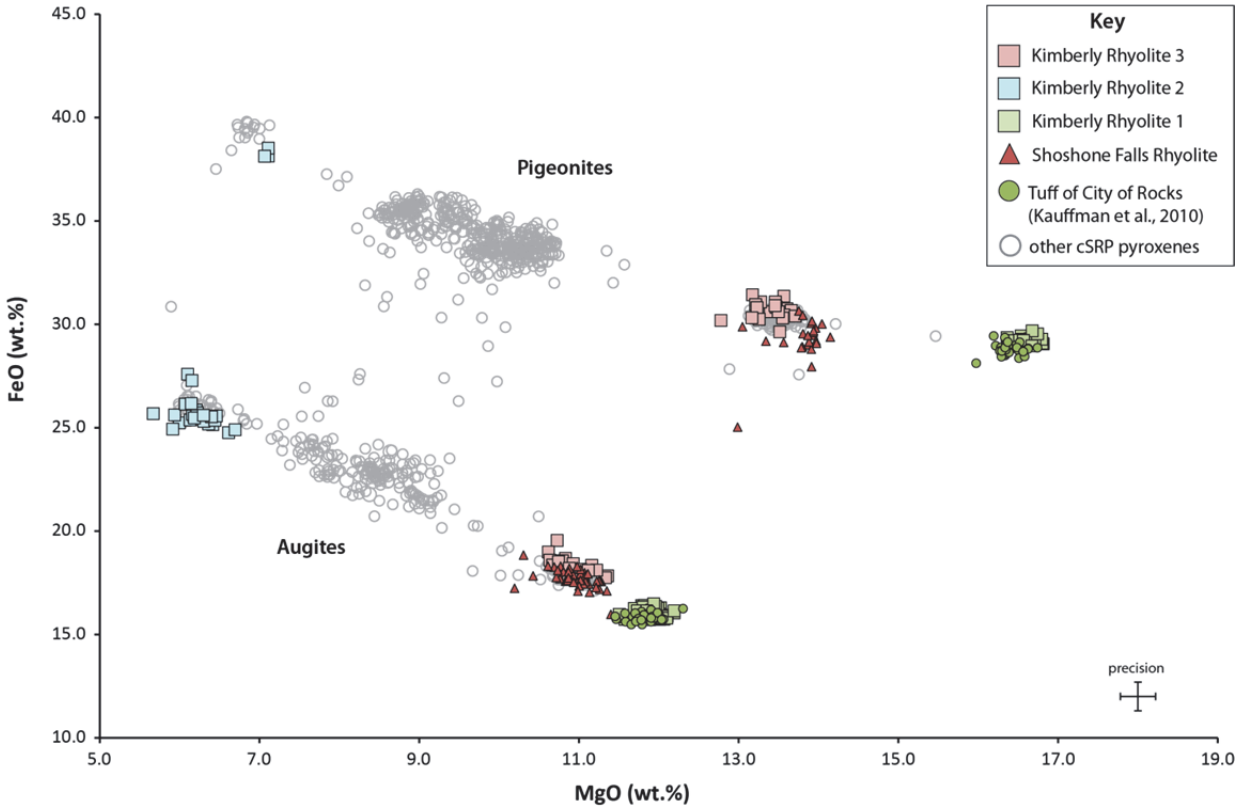

Figure 5.8. MgO versus FeO plot showing pigeonite and augite compositions of Kimberly Rhyolites 1, 2 and 3. The pyroxenes from each of the rhyolites are distinct from each other with respect to their MgO concentrations. Kimberly Rhyolite 2 contains pyroxenes with low MgO concentrations, which is consistent with crystallisation from a more-evolved silicic melt. Pyroxenes from Kimberly Rhyolites 1 and 3 have high MgO concentrations that are among the highest concentrations of all other cSRP pyroxenes. In addition, pyroxenes from the Tuff of the City of Rocks are indistinguishable from those of Kimberly Rhyolite 1, which supports a correlation between them. The pyroxenes of the Shoshone Falls Rhyolite lava are closely similar to Kimberly Rhyolite 3, which also suggests that these two units are correlatives of one another.

5.6. Interpretation of the Kimberly bore-hole succession

A combination of core observations and whole-rock and mineral chemistry suggests that the Kimberly borehole succession comprises three distinct rhyolitic eruption-units separated by non-welded, laminated, sediments and basaltic lavas.

Kimberly Rhyolite 1 is interpreted as an intensely-welded ignimbrite, and the absence of any internal palaeosols, fallout layers or reworked horizons suggests it may be a single emplacement unit with no significant repose periods during its deposition. Although primary shard characteristics are obscured by the development of flow

banding, the presence of angular non-vesicular vitric lapilli are indicative of a pyroclastic origin and are also observed in other Snake River-type ignimbrites (e.g., the Little Creek Member of the Cassia Formation, southern Idaho, Chapter 4.11).

Kimberly Rhyolites 2 and 3 are tentatively interpreted as rhyolite lavas as they both have well-developed flow-banding and lack any convincing pyroclastic features (such as glass shards, fragmented crystals, or entrained pyroclasts). In addition, both rhyolites have basal auto-breccias, which have been invoked as diagnostic criteria for distinguishing between Snake-River-type lavas and ignimbrites (e.g., auto-breccias at the base of Snake River-type rhyolitic lavas are particularly common, whereas auto-breccias at the base of Snake River-type ignimbrites are rare, Branney et al., 2008). The Kimberly borehole provides only a small window into these deposits, therefore it is stressed that the interpretation of Kimberly Rhyolites 2 and 3 as lavas is tentative. However Kimberly Rhyolite 3 is also proposed to be a correlative of the Shoshone Falls Rhyolite, which is the youngest rhyolitic lava exposed in the Snake River canyon (section 5.8).

The three sediment packages, overlying Kimberly Rhyolites 1 and 2, are interpreted as lacustrine sediments as they consist of millimetre-scale laminations of mudstone, sandstone and fine volcanic ash (Shervais et al., 2013).

The entire Kimberly succession is interpreted here to represent an intra-caldera fill sequence. The large thickness (>1.3 km) of Kimberly Rhyolite 1 is indicative of a caldera-fill ignimbrite (Lipman, 1984), which have been identified in many other intra-caldera sequences both globally and within the Yellowstone–Snake River volcanic province (e.g., Doherty et al., 1979; Branney & Kokelaar, 1994; McCurry & Rogers, 2009; Chesner, 2012). The upper auto-breccias of Kimberly Rhyolites 1 and 2 are also pervasively hydrothermally altered, which is common in caldera complexes (e.g., the Long Valley caldera, USA, Flexser, 1991; the Tejeda caldera, Gran Canaria, Donoghue et al., 2008). However, lithic mesobreccias, that typify calderas elsewhere (e.g., Branney & Kokelaar, 1994; Troll et al., 2000; Ferguson et al., 2012), are not seen. It is inferred that caldera collapse mesobreccias may be preserved closer to the margins of the proposed caldera, and may not have encountered by the Kimberly borehole due to its position (Fig. 5.10). The intercalated lacustrine sediments are also indicative of caldera-fill sequences (Lipman, 1984) and were likely deposited from a caldera-lake

environment (similar to Crater Lake, USA, Williams, 1942) that developed in periods of quiescence between rhyolitic and basaltic eruptions.

5.7. Geochronology

Age determinations were obtained for each of the Kimberly rhyolites utilising $^{40}Ar/^{39}Ar$ geochronology, and laser fusion experiments on individual feldspars were conducted by Dan Barfod at the NERC Argon Isotope Facility at the Scottish Universities Environmental Research Centre (SUERC), East Kilbride, UK (see Appendix B.4).

Laser fusion experiments on single plagioclases from base (sample: A2-6400-6411) and top (sample: A2-2102-2106) of Kimberly Rhyolite 1 provided weighted mean ages of 8.8 ± 1.5 Ma (MSWD=1.47) and 9.5 ± 0.9 Ma (MSWD = 1.18), respectively (Fig. 5.9). The observed complex age distribution in experiment A2-6400-6411 suggests the presence of multiple feldspar populations. Some ages older than the weighted mean age of this sample suggest derivation from subjacent mid-Miocene ignimbrites, presumably entrained in the magma chamber or during emplacement. An older (~28 Ma) xenocrystic grain is clearly identified in sample A2-2102-2106 (Table C.13). However, age data with low radiogenic yield also provided younger ages implying the presence of argon loss. Although a statistically meaningful age for sample A2-6400-6411 was obtained, the age derived from the stratigraphically higher sample A2-2102-2106 is considered to be more reliable.

Laser fusion experiments on the base (sample: A2-1945-1953) and top (sample: A2-1419-1424) of Kimberly Rhyolite 2, which contains sanidine feldspar, provided two statistically indistinguishable weighted mean ages of 8.0 ± 0.3 Ma (MSWD=1.21) and 7.70 ± 0.17 Ma (MSWD = 1.24), respectively (Fig. 5.9). The latter, more precise age is considered here to represent the best estimate of the crystallization age.

The stratigraphically highest sample A2-751-754 obtained from Kimberly Rhyolite 3 provided a more complex age distribution (Fig. 5.9). However, by rejecting age data with low radiogenic yields and xenocrystic grains the best age for this sample is represented by a weighted mean age of 7.9 ± 1.4 Ma (MSDW = 1.49). This age is statistically indistinguishable from that obtained on Kimberly Rhyolite 2 due to the larger uncertainty. However, based on detailed core-descriptions Kimberly Rhyolite 3 is known to overlie Kimberly Rhyolite 2 and is therefore younger.

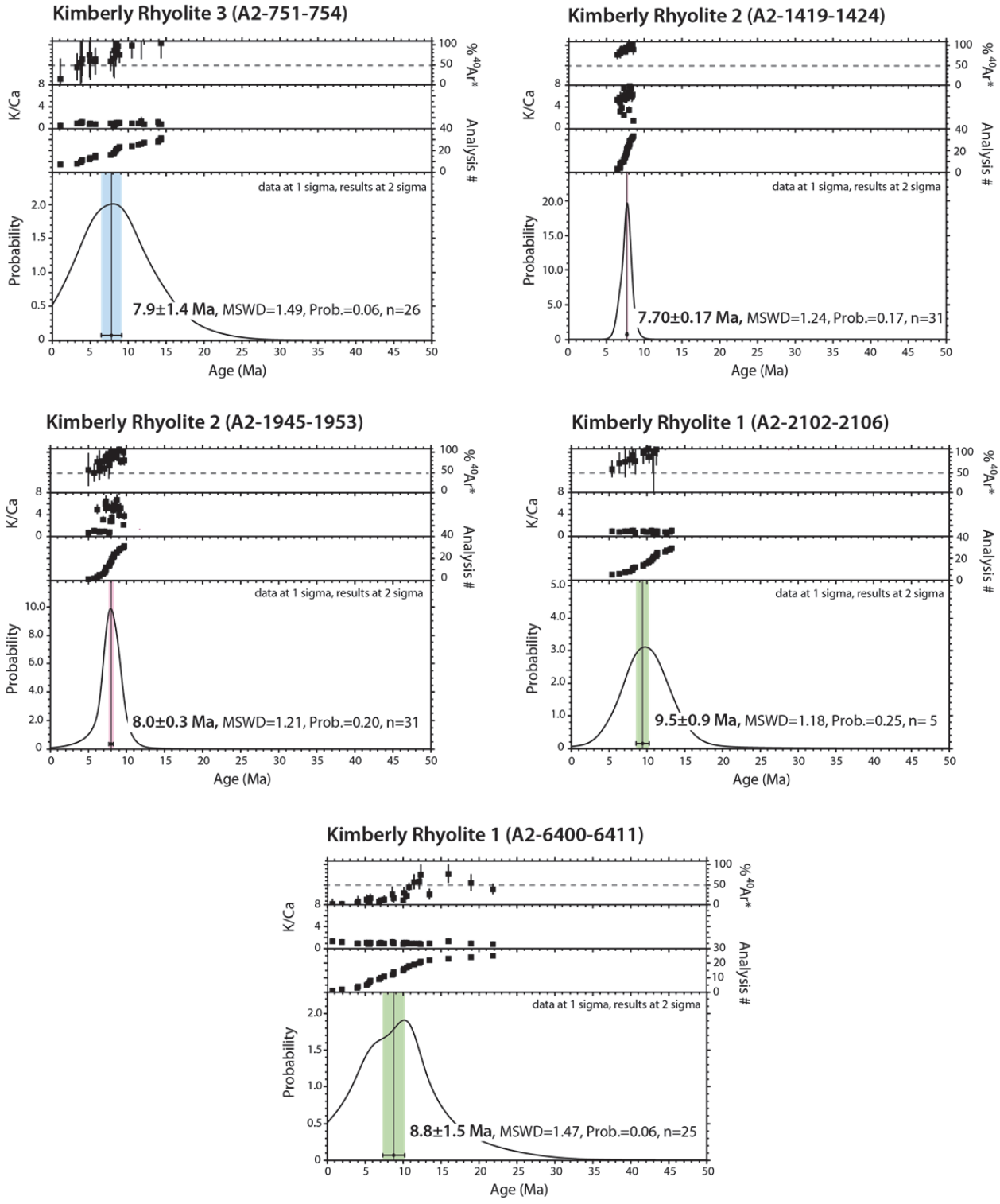

Figure 5.9. $^{40}Ar/^{39}Ar$ single crystal feldspar age probability distributions, along with K/Ca ratios and $^{40}Ar^*$ percentage from representative samples from Kimberly Rhyolites 1, 2 and 3. Coloured bars indicate weighted mean ages with 2-sigma analytical uncertainties.

5.8. Comparisons of the Kimberly rhyolites to known rhyolites of the central Snake River Plain

The proximity of the Kimberly borehole to the Cassia Mountains (Fig. 5.1 and 5.10) south of the Snake River Plain, suggests that Kimberly Rhyolite 1 may be an intra-caldera fill of one of the younger outflow ignimbrites exposed in this region. However, a comparison of whole-rock chemical data from Kimberly Rhyolite 1 with data from the three youngest members of the Cassia Formation (the Indian Springs, McMullen Creek and Lincoln Reservoir members, Chapter 4) show that Kimberly Rhyolite 1 is chemically distinct from these members (Fig. 5.6b). In addition, a comparison of their respective pyroxene compositions again shows that Kimberly Rhyolite 1 is distinct as it contains pyroxenes with much higher MgO concentrations (Fig. 5.8). Therefore, a correlation between Kimberly Rhyolite 1 and any of these three rhyolitic eruption-units is precluded. However, the youngest Lincoln Reservoir Member is proposed to correlate to the 'Tuff of Gwin Springs' exposed in the northern cSRP (see Chapter 6), which in turn is overlain by the intensely-welded 'Tuff of the City of Rocks' (Tcort, Oakley & Link, 2006). Therefore, a potential correlation between Kimberly Rhyolite 1 and the younger Tcort was also tested. A comparison of whole-rock data for each of these units demonstrates that they both have similar Zr/Nb and Th/Nb ratios (Fig. 5.6b). Tcort also contains high-Mg pyroxenes that are indistinguishable from those of Kimberly Rhyolite 1 (Fig. 5.8). In addition, a K-Ar age of 9.15±0.13 Ma is reported for Tcort (Honjo et al., 1986), which is indistinguishable from the $^{40}Ar/^{39}Ar$ plagioclase age of Kimberly Rhyolite 1 (9.5 ± 0.9 Ma). Therefore, Tcort is proposed, in the present study, to be a lateral outflow correlative of the Kimberly Rhyolite 1 intra-caldera ignimbrite. This is proposed on the basis of their similar stratigraphic position, indistinguishable whole-rock and mineral chemistries (particularly their unique high-Mg pyroxenes), and comparable age determinations.

Hitherto, no correlative is proposed for Kimberly Rhyolite 2 as no rhyolite lava is exposed that has a similar stratigraphic position. The only rhyolite lava exposed in close proximity to the Kimberly bore-hole is the Shoshone Falls Rhyolite lava (Bonnichsen et al., 2008; Othberg et al., 2012), which is exposed in the Snake River canyon, north of the bore-hole (Fig. 5.10). The Shoshone Falls Rhyolite lava directly underlies younger surficial basalt lavas (Othberg et al., 2012) and is therefore at a similar stratigraphic horizon to Kimberly Rhyolite 3.

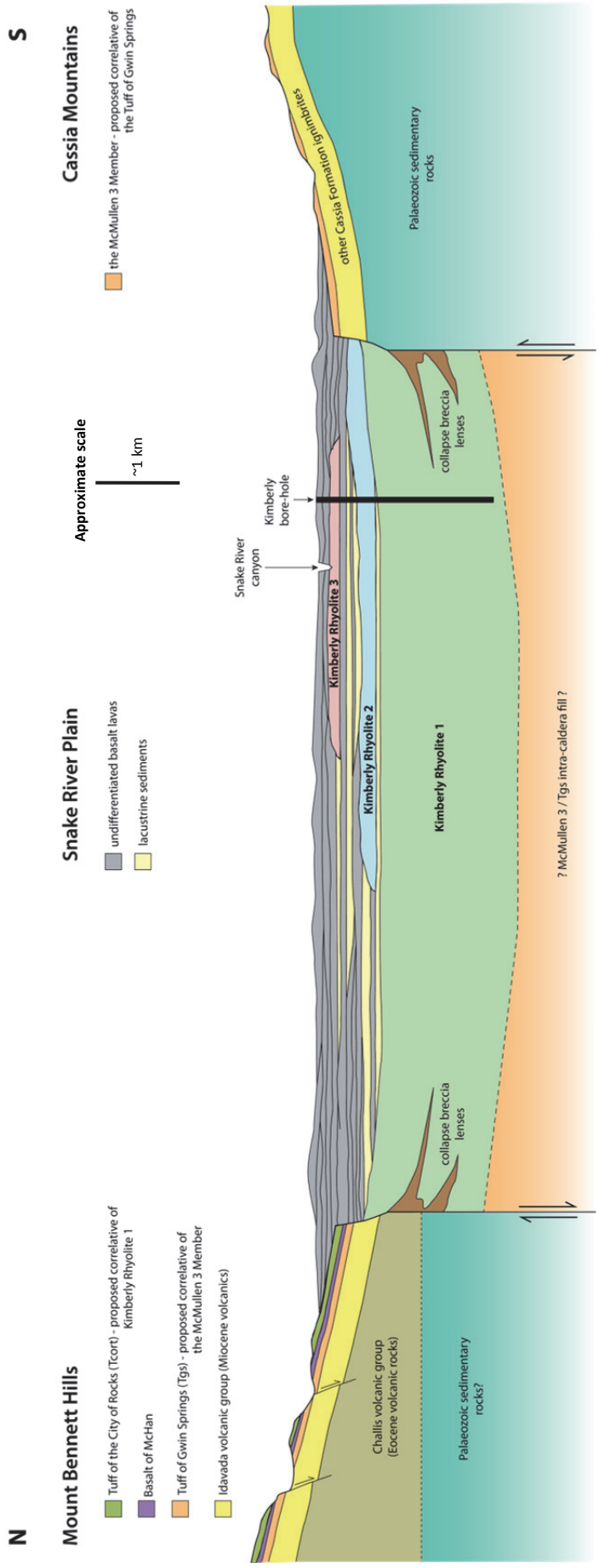

Figure 5.10. Speculative cross-section (not to scale) through the Snake River Plain and into the Mount Bennett Hills to the north and the Cassia Mountains to the south. The 1.3 km-thick Kimberly Rhyolite 1 is interpreted as an intra-caldera ignimbrite, and the Tuff of the City of Rocks in the Mount Bennett Hills is proposed to be its outflow ignimbrite equivalent. Kimberly Rhyolites 2 and 3 are tentatively interpreted to be Snake River-type rhyolitic lavas, and Kimberly Rhyolite 3 is proposed to be a lateral extension and correlative of the 6.53±0.04 Ma Shoshone Falls Rhyolite lava. Hitherto, no correlative is proposed for Kimberley Rhyolite 2.

Whole-rock chemical data obtained from Kimberly Rhyolite 3 and the Shoshone Falls Rhyolite are indistinguishable (Fig. 5.6b), and both units contain closely similar high-Mg pyroxenes (Fig. 5.8). In addition, a whole-rock $^{40}Ar/^{39}Ar$ age of 6.53±0.04 Ma (Othberg et al., 2012) is reported for the Shoshone Falls Rhyolite, which is indistinguishable from the $^{40}Ar/^{39}Ar$ age obtained for Kimberly Rhyolite 3 (7.9 ± 1.4 Ma), although the error on this age is much larger. Therefore, Kimberly Rhyolite 3 is proposed, in the present study, to be a lateral extension and correlative of the Shoshone Falls Rhyolite lava on the basis of their similar stratigraphic position, indistinguishable whole-rock and mineral chemistries and comparable age determinations.

5.9. Volumes estimates for intra-caldera ignimbrites in the cSRP

To date there has been no reported evidence for calderas, and associated intra-caldera fill sequences, in the cSRP. However, their presence has been inferred by recent studies (Ellis et al., 2012a) in order to estimate eruption volumes for three newly defined large explosive eruptions (e.g., the ~350 km^3 'Cougar Point Tuff XI'; the ~350 km^3 'Steer Basin Tuff' and the ~1,000 km^3 'Cougar Point Tuff XIII'). Dense rock equivalent (DRE) volumes for these three tuffs were estimated by calculating the volume of the correlated outflow ignimbrites, exposed in the southern cSRP, and doubling this value to account for equal volumes of intra-caldera ignimbrites (Ellis et al., 2012a). This method has become common practice where accurate determinations of intracaldera volumes are not possible (Lipman, 1984).

As evidenced by Kimberly Rhyolite 1, intra-caldera ignimbrites in the cSRP may be as much as 1.3 km-thick. If individual calderas in the cSRP are assumed to be comparable in area to those observed in the Yellowstone volcanic field (e.g., ~3000 km^2, Christiansen et al., 2001), and using the thickness of Kimberly Rhyolite 1 as a proxy, then intra-caldera volumes for individual cSRP eruption-units could be as large as ~3000 km^3 (DRE). However, estimates of individual ignimbrite outflow volumes, in the cSRP, range from ~177 km^3 to ~500 km^3 (Ellis et al., 2012a). This would therefore suggest that a considerable proportion of erupted tephra, during each cSRP super-eruption, is confined within the resultant caldera. This has also been suggested for the Atana ignimbrite in northern Chile where ~66% of the total volume is preserved as intra-caldera fill (Lindsay et al., 2001); and for the Vilama ignimbrite where ~83% of its total volume is preserved within the Vilama caldera on the Andean plateau (Soler et al.,

2007). However, further investigation would be required in order to confirm this hypothesis for cSRP super-eruptions.

5.10. Conclusions

The Kimberly bore-hole provides a unique window into proximal deposits located on the southern margin of the proposed Twin Falls eruptive-centre, and exposes the first evidence for a caldera in the cSRP. Detailed characterisation of the volcanic succession, in particular the rhyolites, exposed in the drill core has led to the following four conclusions:

(1) The Kimberly drill core exposes three distinct rhyolitic eruption-units, here termed Kimberly Rhyolite 1, Kimberly Rhyolite 2, and Kimberly Rhyolite 3.

(2) Kimberly Rhyolite 1 is interpreted as an intra-caldera ignimbrite, which is proposed to correlate to the 'Tuff of the City of Rocks' outflow sheet exposed in the northern cSRP.

(3) Kimberly Rhyolite 2 and 3 are tentatively interpreted as rhyolite lavas, and Kimberly Rhyolite 3 is proposed to be a lateral correlative of the Shoshone Falls Rhyolite.

(4) The large thickness of Kimberly Rhyolite 1 suggests that cSRP intra-caldera fill volumes may be significantly larger than their equivalent outflow sheets; however additional investigation is needed to confirm this hypothesis.

6. Correlation of three widespread ignimbrites in the central Snake River Plain, Idaho, USA, and the identification of two new super-eruptions.

6.1. Introduction

The Yellowstone–Snake River Plain volcanic province comprises extensive Miocene-Recent rhyolite ignimbrites overlain by basalt lavas in a 150 km wide, elongate region that extends ~600 km from northern Nevada, across southern Idaho, towards the Yellowstone volcanic field in Wyoming, USA (Fig. 6.1a). The Yellowstone volcanic field has famously experienced some very large explosive eruptions (e.g. the 2160 km^3 Huckleberry Ridge Tuff, Christiansen, 2001; Ellis et al., 2012b) in the last 2 million years, but rather less well-known is that previous eruptions from further west, along the central Snake River Plain (cSRP) may have been as voluminous, more numerous, and hotter (the mid-Miocene ignimbrite 'flare-up' of Nash et al., 2006 and Bonnichsen et al., 2008). However, this has yet to be confirmed. One problem has been that detailed studies of the volcanism have tended to interpret local volcanic successions (Williams et al., 1990, 1991; Wright et al., 2002; Bonnichsen et al., 2008; Andrews et al., 2008; Ellis et al., 2010), and only very few individual pyroclastic units have been traced regionally (Ellis et al., 2012a) in order to assess their scale and impact. The reason for the scarcity of good regional correlations is because the ignimbrites in southern Idaho are numerous and monotonous, often with similar appearance and chemistry, making robust correlations challenging. Thus, the number of very large explosive eruptions that occurred along the Yellowstone hotspot-track in the Mid–Miocene (~12–8 Ma) remains unknown.

Rhyolitic units in the cSRP have been divided into 13 'composition and time groups' ('CAT groups') based on broadly similar chemical composition and age (Bonnichsen et al., 2008). Each CAT group contains up to eight individual rhyolitic units, but it is not known how many eruptions are represented by each CAT group. Within older (11.4–10.6 Ma) successions, three large-volume eruption-units (Cougar Point Tuff XIII, ~1000 km^3; Steer Basin Tuff and Cougar Point Tuff XI, ~350 km^3) have recently been proposed in the south cSRP (Ellis et al., 2012a), but, hitherto, no correlations have been made within the younger (~10.5–8 Ma) pyroclastic successions.

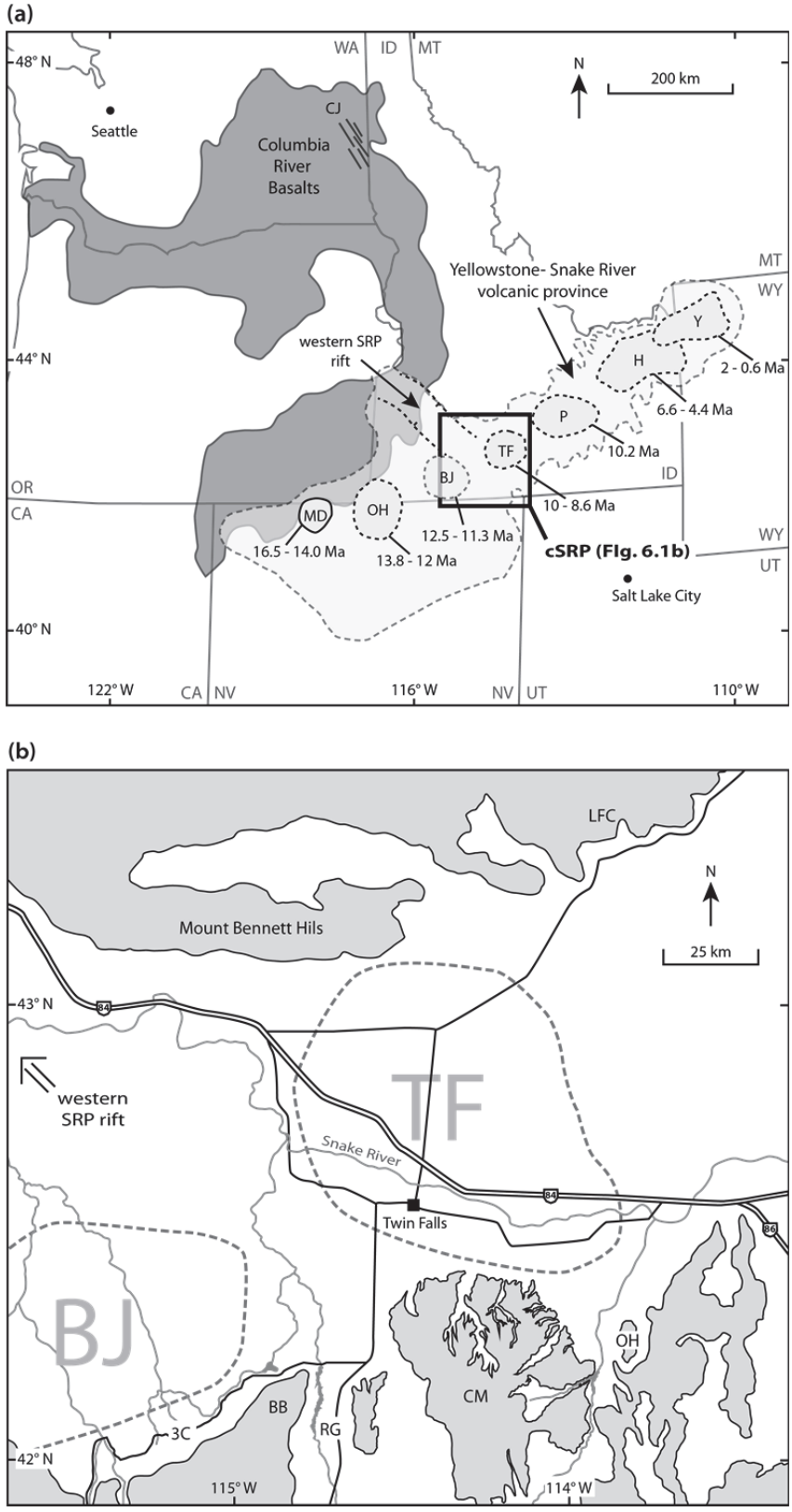

Figure 6.1. (a) The Yellowstone-Snake River bimodal volcanic province showing the central Snake River Plain (cSRP) and the locations of all proposed volcanic centres. Volcanics centres are termed: MD, McDermitt; OH, Owyhee-Humbolt; BJ, Bruneau-Jarbidge; TF, Twin Falls; P, Picabo; H, Heise; and Y, Yellowstone, after Bonnichsen et al. (1989) and Morgan & McIntosh (2005). Dark grey area shows the extent of the Columbia River Basalts that erupted along the Chief Joseph (CJ) dyke swarm (Camp et al., 2003). **(b)** Simplified location map of the study area of the present study showing the locations of all place names mentioned in the text, including: 3C, Three Creek road; BB, Browns Bench massif; RG, Rogerson Graben; CM, Cassia Mountains; OH, Oakley Hills; and LFC, Little Fish Creek canyon.

This chapter presents evidence for the correlation of three newly defined, regionally widespread ignimbrite sheets; herein termed the 'Brown's View ignimbrite', the 'McMullen Creek ignimbrite', and the 'Grey's Landing ignimbrite'. Previously these ignimbrites had only been recognised locally (Andrews et al., 2008; Ellis et al., 2010). Their regional extent has been established by correlating between individual eruption-units described within younger (~10.5–8 Ma) local successions across the south side of the cSRP. In addition, data from the north-side of the cSRP (provided by colleagues, Reichow, unpublished data) have allowed the extension of these correlations, for the first time, across the Snake River Plain to the north.

Each of the locally described volcanic successions includes several intensely-welded, Snake River–type (Branney et al., 2008) ignimbrite sheets, and associated non-welded ash-deposits. Limited exposure of the non-welded ash-deposits precludes their use for correlation, and attention was given to the better exposed ignimbrites. However, the similar features of many of the Snake River-type ignimbrites make them notoriously difficult to correlate by conventional field-based methods (see Chapter 2). Therefore correlations have been achieved by combining detailed physical field characterisation, with whole-rock and mineral chemistry and palaeomagnetic and geochronology data. Only by using all techniques in combination could robust correlations be established, in this study, which allows the regional extent and volume of widespread outflow ignimbrite sheets to be estimated. Critically, these new correlations provide much needed constraints on the volumes and masses of explosive eruptions in the cSRP, during the proposed ignimbrite 'flare up' (Nash et al., 2006).

6.2. The Brown's View Ignimbrite

The Brown's View ignimbrite was previously thought to be a localised eruption-unit of the Rogerson Formation, recognised within the Rogerson Graben (Fig. 6.1b; Andrews et al., 2008; see also Chapter 3). The present study, however, compares its physical and chemical features with those of other localised eruption-units in the cSRP to propose that it is a considerably more widespread ignimbrite sheet. Three individual eruption-units are proposed to correlate together, namely: (1) the Brown's View ignimbrite (Andrews et al., 2008); (2) a welded ignimbrite formerly called 'Browns Bench 11' exposed to the west on the Browns Bench massif (Fig. 6.1b; Bonnichsen et al., 2008); and (3) the Little Creek ignimbrite of the Cassia Formation (see Chapter 4) in the Cassia Mountains south of Twin

Falls, Idaho (Fig. 6.1b). All three units were grouped within CAT group 10A of Bonnichsen et al. (2008), and each is described briefly below (1–3).

(1) The Brown's View ignimbrite is a >4 m-thick rhyolitic ignimbrite sheet (top not seen) exposed within the N-S-trending Rogerson Graben, south of Twin Falls, Idaho (Fig. 6.1b). It is the third of five members of the Rogerson Formation (Chapter 3) and hitherto has not been recognised beyond the graben. At its reference section (GR: N42°04'04.8" /W114°45'44.5") it overlies a palaeosol in the Rabbit Springs Member, and it is overlain by the non-welded Backwaters Member (Fig. 6.2; Andrews et al., 2008). It is a compound cooling unit with a 1 m-thick basal vitrophyre and a 2 m-thick upper vitrophyre separated by a less-welded lapilli-tuff, 1 m-thick, that contains abundant angular, non-vesicular, vitric lapilli 0.5–1 cm in size (Fig. 6.2).

(2) The 'Browns Bench 11' ignimbrite (Bonnichsen et al., 2008) outcrops in several small mesas on the Browns Bench massif above the Browns Bench escarpment, Idaho (Fig. 6.1b). At the reference section (GR: N42°08'17.0" / W114°48'38.0") it is >4 m-thick (upper and lower contacts not seen) and overlies 'Browns Bench 10' (Bonnichsen et al., 2008). 'Browns Bench 11' is a compound cooling unit with a 1 m-thick lower vitrophyre and a 2 m-thick upper vitrophyre separated by a less-welded lapilli-tuff, 1 m-thick, that contains abundant angular, non-vesicular, vitric lapilli, 0.5–1 cm in size (Fig. 6.2). Modern erosion has left two topographic benches, each exposing vitrophyric tuff, designated as 'Browns Bench 11' and 'Browns Bench 12' by Bonnichsen et al. (2008). However, further examination revealed no evidence (e.g., intervening palaeosol, sediment or ashfall layer that record a significant period of repose) for the presence of more than one eruption-unit. Therefore, 'Browns Bench 11' was redefined as the uppermost (capping) eruption-unit of the Browns Bench stratigraphy, and the term 'Browns Bench 12' was dropped (Reichow et al., unpublished).

(3) The Little Creek ignimbrite is a >30 m-thick (upper and lower contacts not seen) rhyolitic ignimbrite that is well-exposed at a type section in Rock Creek canyon, Cassia Mountains, Idaho (Fig. 6.1b). It is the ninth of thirteen members of the Cassia Formation (see Chapter 4) and hitherto was not recognised beyond the northern Cassia Mountains, where it overlies the Wooden Shoe Butte Member and is overlain by the Dry Gulch Member (Fig. 6.2). It is a compound cooling unit with upper and lower intensely-welded zones separated by a less-welded lapilli-tuff, 6 m-thick, that contains abundant angular,

non-vesicular, vitric lapilli, 0.5 – 1 cm in size (Fig. 6.2). The lower intensely-welded zone is a 4 m-thick basal vitrophyre and the upper intensely-welded zone is a 10 m-thick lithoidal zone overlain by a 1 m-thick vitrophyre (Fig. 6.2).

6.2.1. Similar physical characteristics

The Brown's View, 'Browns Bench 11' and Little Creek ignimbrites share three physical characteristics, which are not shared by most other cSRP ignimbrites. (1) All three are compound cooling-units, and exhibit a complex welding profile that consists of upper and lower intensely welded zones separated by a less-welded centre (Fig. 6.2). (2) The central zones of all three contain abundant vitric lapilli, 0.5–1 cm in size, supported within a less-welded lapilli-tuff. Similar vitric lapilli occur in other Snake River-type ignimbrites (e.g., 'Jackpot 6', Andrews et al., 2008; Branney et al., 2008); however they are rare within the enclosing ignimbrites of all three local successions. For example, in the Cassia Formation, only three of nine ignimbrites (including the Little Creek ignimbrite) contain abundant vitric lapilli (see Chapter 4); and within the Rogerson Formation (Chapter 3) and the Browns Bench stratigraphy, the Brown's View ignimbrite and 'Browns Bench 11' are the only eruption-units that contain abundant vitric lapilli. (3) In all three ignimbrites, the vitric lapilli are observed only within the central less-welded zones, and do not extend into the overlying and underlying intensely-welded zones. Only two other ignimbrites in the cSRP, exhibit this vertical lithological profile (the McMullen Creek ignimbrite in the Cassia Formation, and the 'Tuff of Idavada Old', Reichow, pers. comm.) and both of these are much younger than the three ignimbrites being correlated. Therefore the characteristic pyroclastic lithofacies, welding characteristics, and vertical profiles of the three ignimbrites are supportive of a correlation and can be used to help distinguish them from other adjacent Mid-Miocene ignimbrites in the field. There are, however, some differences in the field characteristics of the three ignimbrites that warrant consideration. The Brown's View and 'Browns Bench 11' ignimbrites are closely similar, being relatively thin (>4 m) with upper and lower vitrophyres and central lapilli-tuffs of similar thicknesses (Fig. 6.2). However, the Little Creek ignimbrite is thicker (>30 m) than the other two ignimbrites, with thicker upper and lower intensely-welded zones and central lapilli-tuff (Fig. 6.2). In particular, the upper intensely-welded zone of the Little Creek ignimbrite comprises a 10 m-thick devitrified lithoidal zone with rheomorphic folds and is overlain by a 1 m-thick vitrophyre (Fig. 6.2). Devitrification and rheomorphism is not observed in the Brown's View and 'Browns Bench 11' ignimbrites, although these

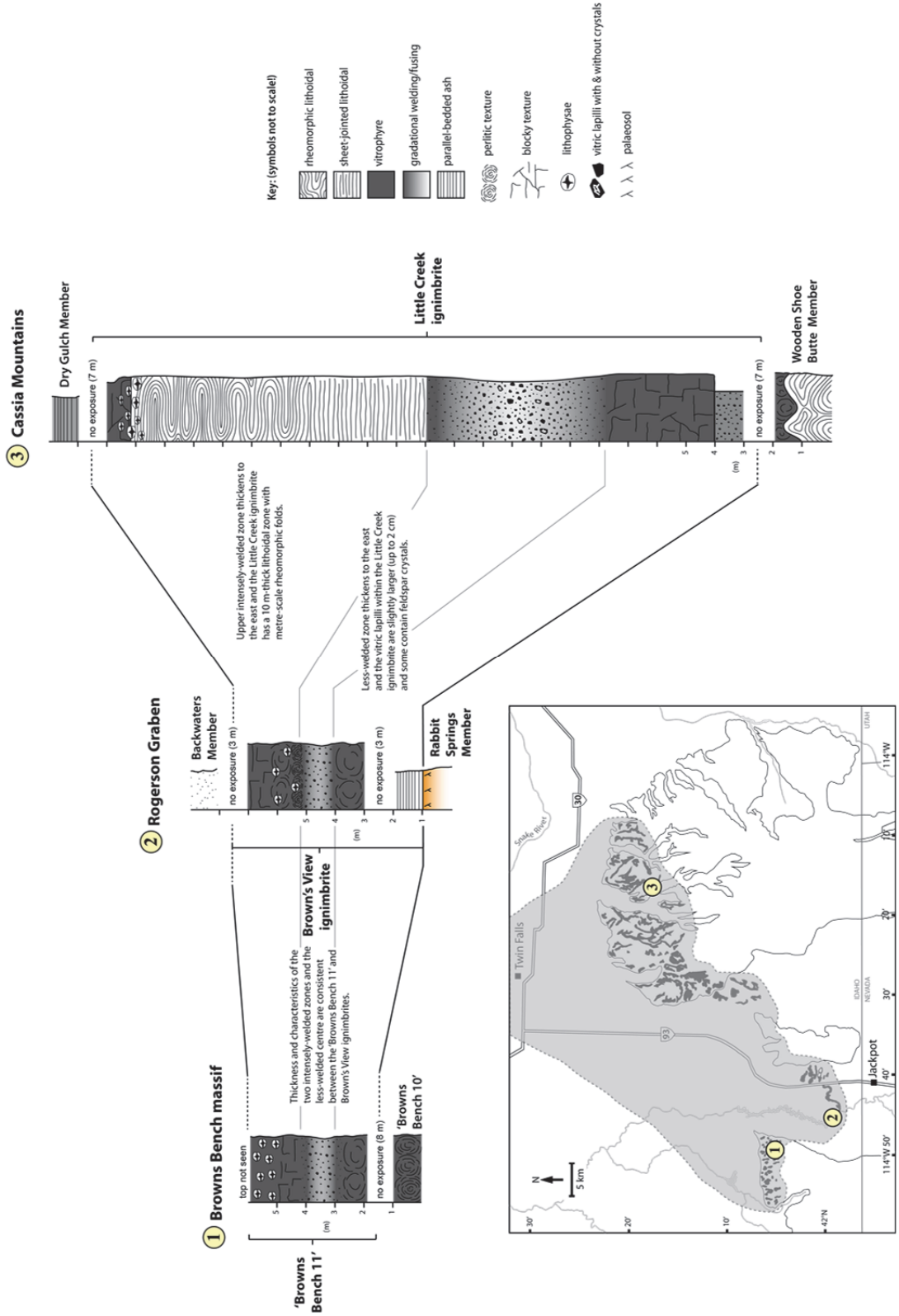

Figure 6.2. Select logs from the type sections (see inset map for locations) of the 'Browns Bench 11,' Brown's View, and Little Creek ignimbrites, showing the characteristic vertical profile of upper and lower intensely-welded zones separated by a less-welded lapilli-tuff containing abundant vitric lapilli (0.5–1 cm in size) . Inset map shows the outcrop patterns of each of the three units and the geographic distribution (grey area) of the widespread 'Brown's View Ignimbrite' (~2700 km^2).

differences are readily ascribed to an increase in thickness, such as commonly results in ignimbrites from infill of basinal topography (e.g., the Rattlesnake Tuff, Oregon,USA, Streck & Grunder, 1995). These differences do not preclude a correlation, however must be kept in mind when using field characteristics to correlate.

6.2.2. Similar whole-rock chemistry

Whole-rock samples of the Brown's View, 'Browns Bench 11' and Little Creek ignimbrites, from several localities within their localised areas, were prepared for X-ray fluorescence (XRF) spectrometry and analysed on a PANalytical PW4400 Axios XRF spectrometer at the University of Leicester (see Appendix B.1). Samples were preferentially collected from the base and top of each ignimbrite in order to assess any vertical or lateral chemical zonation. This methodology is consistent between all correlations described in this chapter.

Chemical zonation has been demonstrated in many medium to large volume ignimbrites in other volcanic fields, for example the Zaragoza ignimbrite, central Mexico (Carrasco-Nuñez and Branney, 2005), the Bishops Tuff, USA (Hildreth & Wilson, 2007), and the Sgurr of Eigg pitchstone, Scotland (Brown & Bell, 2013). Subtle zonation has also been suggested for some ignimbrites in the cSRP, such as the Cougar Point Tuffs (Cathey & Nash, 2004). Chemical heterogeneity in ignimbrites may limit the effectiveness of whole-rock data when establishing correlations (Hildreth & Mahood, 1985), but chemical zoning in large-volume rhyolitic ignimbrites is commonly less marked than it is in medium-volume ignimbrites.

The whole-rock compositions of the Brown's View, 'Browns Bench 11' and Little Creek ignimbrites are remarkably consistent and unique chemical fields have been distinguished that are supportive of their correlation (Fig. 6.4).

All three ignimbrites are relatively low-silica (70.13–72.03 wt.% SiO_2) rhyolites (Table C.1, C.2, and C.4) and all contain 0.52–0.76 wt.% TiO_2, a criterion for inclusion within CAT group 10A of Bonnichsen et al. (2008). Alumina Saturation Indices (ASI) range between 0.87 and 0.99 (Table C.1, C.2, and C.4) indicating all three are metaluminous, which is consistent with the majority of cSRP ignimbrites (Bonnichsen et al., 2008). Vertical compositional zonation within each ignimbrite is also minimal, with ≤2 wt.% SiO_2 variation from base to top (Table C.1, C.2, and C.4).

Bulk-silicate-Earth-normalised trace element patterns for each of the three units are closely similar, and show high Rb, Th, U and Pb with relatively lower abundances of Ba, Nb and Sr (Fig. 6.3). This pattern is broadly similar to other cSRP ignimbrites (Fig. 6.3) but with differences in the magnitude of some of the negative anomalies. For example, Ba is less depleted than all underlying older ignimbrites (Fig. 6.3). The depletion of Ba may be due to the fractionation of sanidine, and this is consistent with the lack of sanidine in the Brown's View, Browns Bench 11 and Little Creek ignimbrites, which may suggest that sanidine stopped fractionating sometime prior to their eruption.

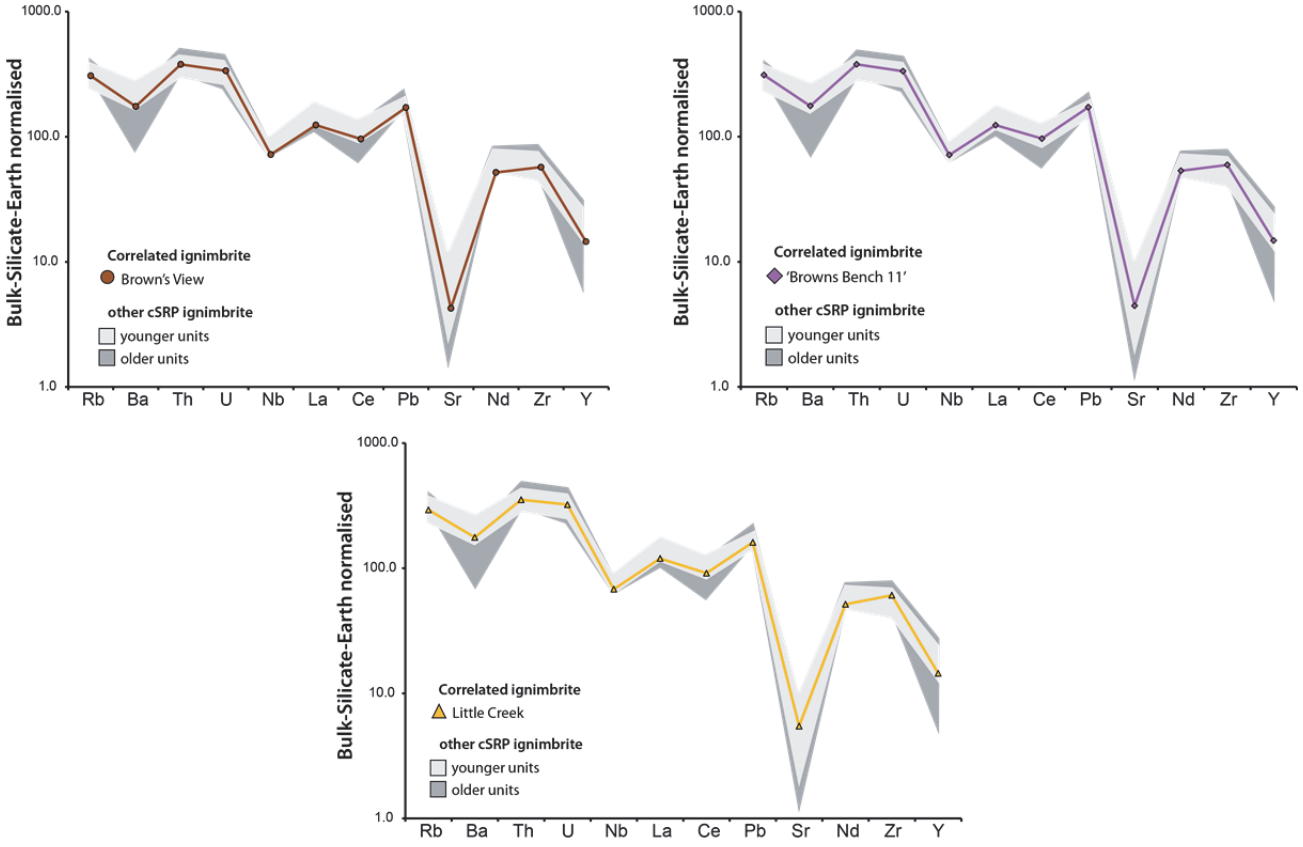

Figure 6.3. Bulk-silicate-Earth (Sun & McDonough, 1995) normalised trace element patterns for the Brown's View, 'Browns Bench 11', and Little Creek ignimbrites. Each of the three ignimbrites have indistinguishable trace element patterns that are also broadly similar to the majority of other cSRP ignimbrites. However, the three ignimbrites have significantly higher Ba abundances than all underlying older ignimbrites, which may be due to the lack of sanidine as a phenocryst phase (Fig. 3.5).

Despite overall similarities with other cSRP ignimbrites it is possible to distinguish the Brown's View, 'Browns Bench 11' and Little Creek ignimbrites by using the relatively incompatible elements Th, Nb, Zr and Y as discriminators. Zr/Y and Th/Nb ratios define chemical fields for each of the ignimbrites that are distinct from the adjacent eruption-

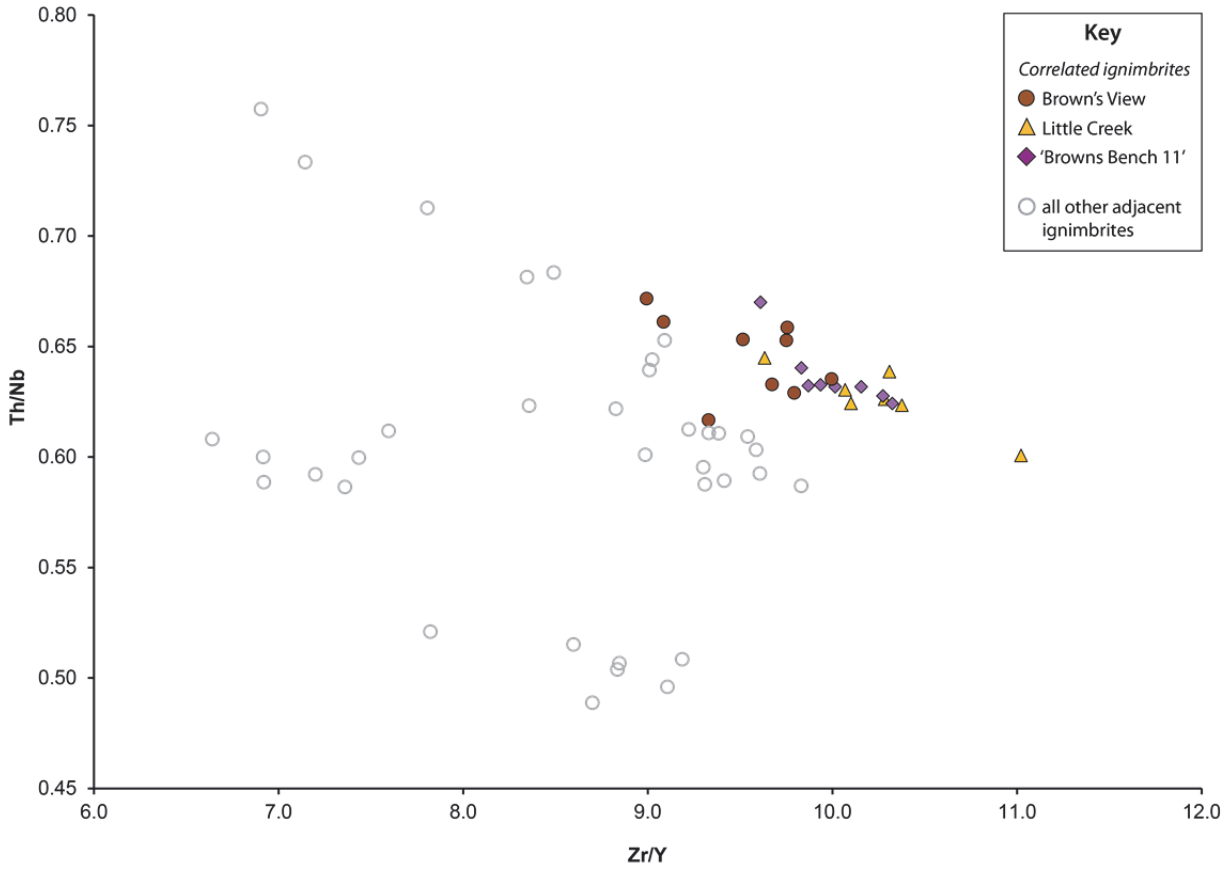

Figure 6.4. Zr/Y versus Th/Nb plot demonstrating how the Brown's View, Little Creek, and 'Browns Bench 11' ignimbrites have closely similar whole-rock compositions, and define a unique chemical field that is distinct from all other adjacent ignimbrites.

units within their respective successions (Fig. 6.4). More importantly these chemical fields are consistent between the three ignimbrites and this provides good supporting evidence for a correlation between them.

6.2.3. Similarities in petrology and mineral chemistry

Crystal content, in each of the ignimbrites, is estimated as 10-15 % and comprises an anhydrous mineral assemblage of plagioclase, pigeonite, augite, magnetite and accessory apatite and zircon with plagioclase, pigeonite, and augite being the most abundant. This crystal content and assemblage is common in most cSRP ignimbrites (Ellis et al., 2013), but the Brown's View, 'Browns Bench 11' and Little Creek ignimbrites all lack sanidine (Fig. 6.5). This is significant because sanidine is present in all underlying eruption-units in all three successions (Fig. 6.5). Thus, in each of the three successions, the targeted ignimbrite records a change in the mineral assemblage that marks a regional stratigraphic horizon above which there is no record of sanidine as a fractionating phase.

Compositions of plagioclase, pigeonite and augite crystals were obtained on 30 micron polished thin sections and analysed using a Cameca SX100 electron microprobe at the Open University, Milton Keynes (see Appendix B.2).

Plagioclase crystals in all three units range in size from 0.5 to 3 mm. The largest (2–3 mm) are mostly euhedral and some contain inclusions of glass and/or smaller crystals of pyroxenes, magnetite, or apatite. The smaller plagioclase crystals (0.5–1 mm) are subhedral to euhedral, with at least one broken margin, and are interpreted as crystal fragments. These crystal sizes and textures are similar to many other cSRP ignimbrites (Wright et al., 2002; Ellis et al., 2012a) and are not unique to this correlation. Plagioclase crystals, in each of the three units, are dominantly andesine (Fig. 6.5) with a limited

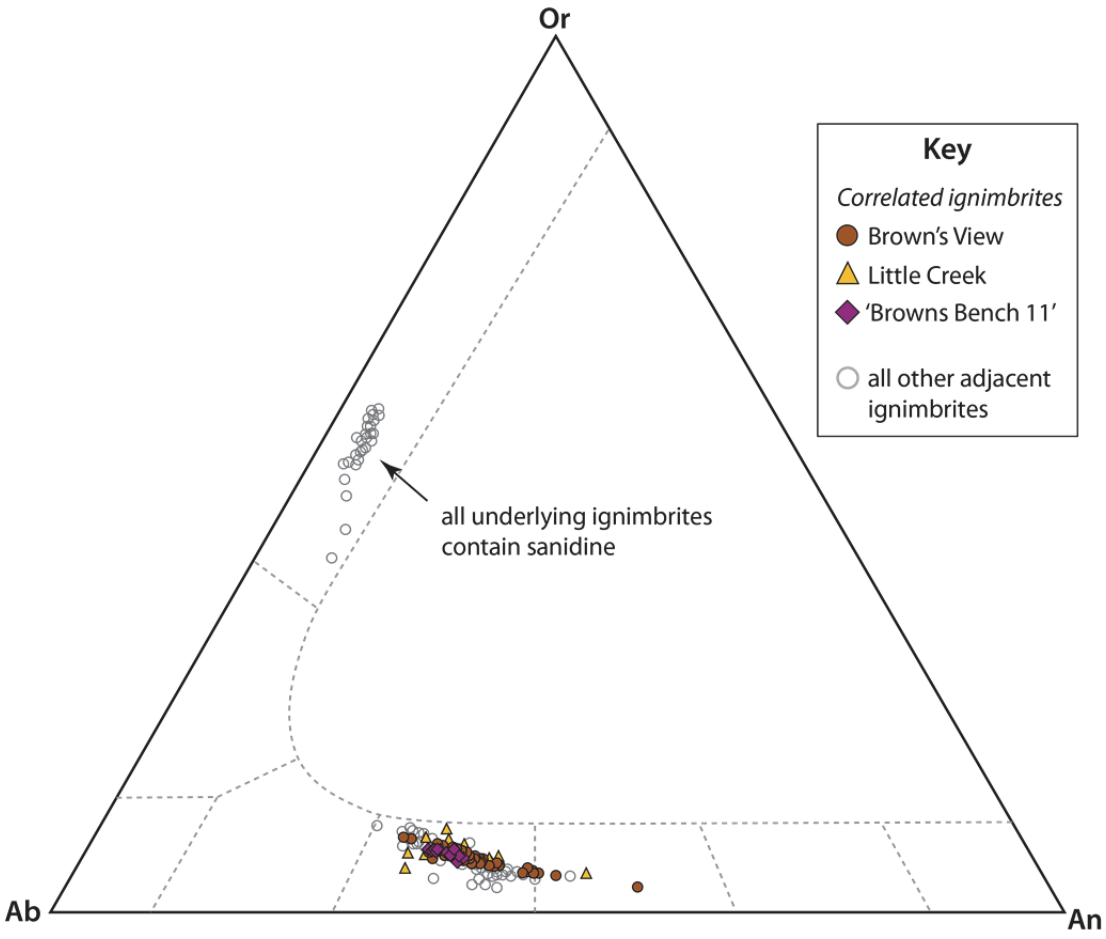

Figure 6.5. Feldspar ternary diagram showing the indistinguishable plagioclase (andesine) compositions of the Brown's View, Little Creek and 'Browns Bench 11' ignimbrites. These are also indistinguishable from all other adjacent ignimbrites. However, all underlying members contain sanidine. Therefore, each of the correlated ignimbrites marks a distinct horizon in the phenocryst assemblage, within their respective successions, where sanidine disappears.

compositional range (An_{31}–An_{57}, Table C.5, C.7, and C.11) and negligible zoning (typical core to rim variation is <1% An). These compositions are consistent with all other cSRP eruption units (Fig. 6.5) and so is not a useful correlation criterion.

The pyroxenes, in contrast, are useful for correlation. The pyroxene crystals in all three ignimbrites are subhedral, 0.5 to 1 mm in size, and define two compositional modes; one of pigeonite and one of augite (Fig. 6.6, Table C.6, C.8, and C.12). In addition, they have the highest MgO concentrations of any other cSRP ignimbrite (Fig. 6.6). These unique pyroxenes are therefore excellent supporting evidence for a correlation and are also a defining characteristic of this proposed widespread ignimbrite sheet.

Pyroxenes from the Brown's View and Little Creek ignimbrites were also analysed by LA-ICP-MS at Idaho State University, USA (see Appendix B.3) during a pilot study to determine the usefulness of pyroxene trace element data in distinguishing between individual ignimbrites. Results show that the trace elements Y, V and Sc are useful discriminatory elements. Pyroxenes of the Brown's View and Little Creek ignimbrites are indistinguishable, and generally have higher V/Y ratios than those of the Grey's Landing and Lincoln Reservoir ignimbrites (Fig. 6.14b, see also section 6.4.3). This constitutes additional supporting evidence for a correlation between the Brown's View and Little Creek ignimbrites, and work is planned on the pyroxenes of 'Browns Bench 11' to help correlate it with the these ignimbrites.

6.2.4. Similar palaeomagnetic polarity and mean flow direction

A total of 12 drill-cores (10 cm in length) were taken from each of the three ignimbrites in order to determine their palaeomagnetic polarity and their mean palaeomagnetic flow directions. Cores were analysed and subsequent data were provided by collaborators D.Finn and R.Coe working at the University of California, Santa Cruz, USA (Appendix B.6). In addition, mean palaeomagnetic flow directions, for each of the ignimbrites, were tilt corrected by measuring the present dip and strike of each unit, and rotating their respective sections back to horizontal (Finn, pers. comm.).

The Brown's View, 'Browns Bench 11' and Little Creek ignimbrites all exhibit a normal magnetic polarity (Fig. 6.15a). While this is supporting evidence for a correlation, this polarity is common among many cSRP ignimbrites and is therefore not a unique characteristic. Tilt-corrected mean palaeomagnetic flow directions, for each of the ignimbrites, are indistinguishable and show a steep inclination to the north

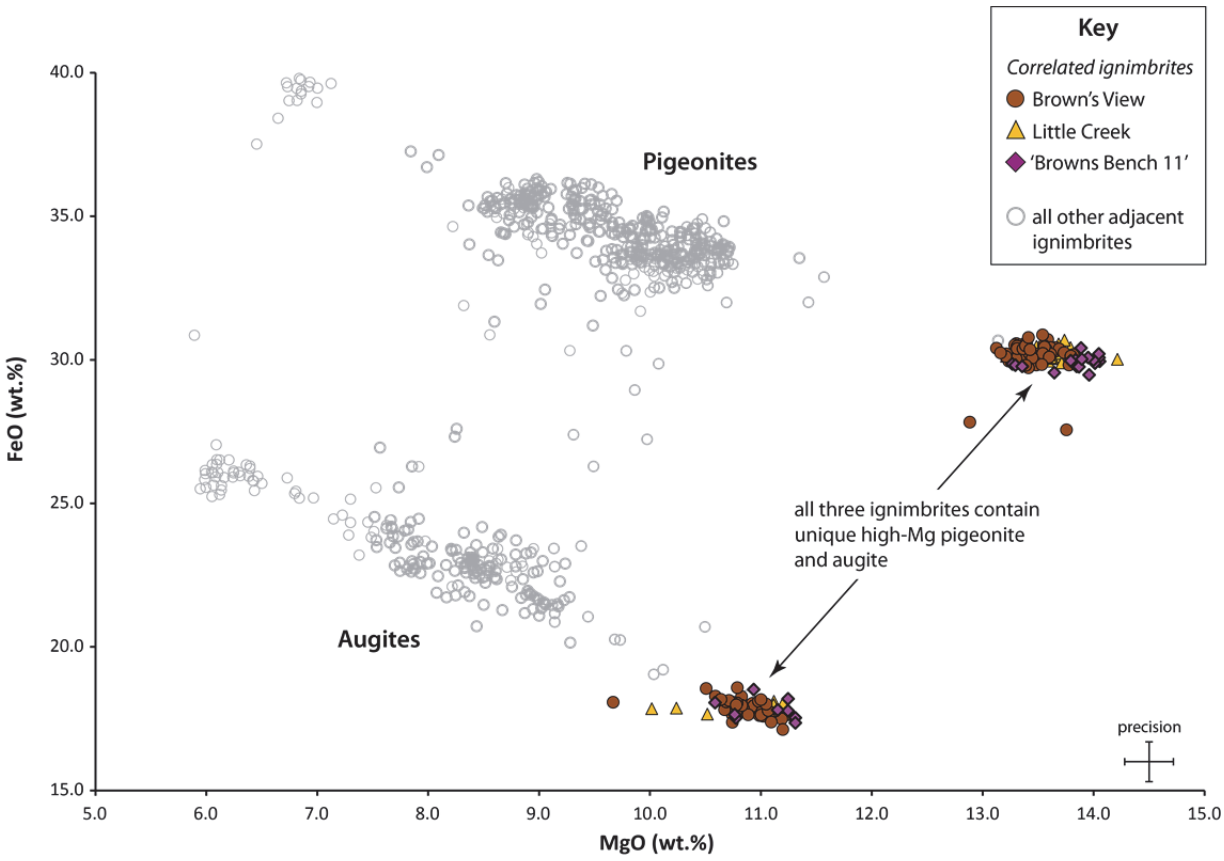

Figure 6.6. MgO versus FeO plot demonstrating the unique high-Mg pyroxenes in the Brown's View, Little Creek and 'Browns Bench 11' ignimbrites. These pyroxenes are characteristic of all three ignimbrites, and are excellent supporting evidence for a correlation between them.

(Finn & Coe, unpublished, Fig. 6.15a). However, this direction is indistinguishable from other cSRP rhyolitic ignimbrites (e.g., the McMullen Creek and Grey's Landing ignimbrites). Therefore, while palaeomagnetic polarity and mean flow directions are supportive of a correlation they are not a characteristic criterion.

6.2.5. Geochronology

Zircons from the Little Creek ignimbrite provide a statistically meaningful weighted mean $^{206}Pb/^{238}U$ age of 10.3 ± 0.2 Ma (MSWD = 3.1). A high precision $^{40}Ar/^{39}Ar$ sanidine age of 10.136 ± 0.005 Ma (Reichow, unpublished) was also obtained on the underlying Wooden Shoe Butte ignimbrite, and provides a maximum age of the Little Creek ignimbrite. Age determinations on the Brown's View and 'Browns Bench 11' ignimbrites are in progress. These two ignimbrites are grouped within CAT group 10A of Bonnichsen et al. (2008), and together with their stratigraphic position infer eruption ages between ~10.0 and 9.5 Ma, which is the age range given for CAT group 10A (Bonnichsen

et al., 2008). In addition, published (Bonnichsen et al., 2008) sanidine argon ages on the Rabbit Springs (10.49 ± 0.13 Ma) and Browns Bench 9 (10.34 ± 0.09 Ma) ignimbrites underlying the Brown's View and 'Browns Bench 11' ignimbrites, respectively, provide minimum ages and places them at a similar stratigraphic horizon to the Little Creek ignimbrite. Although, presented data provide strong support for a correlation additional geochronology data are required to further consolidate this hypothesis.

6.2.6. Summary: the extensive 'Brown's View ignimbrite; a useful stratigraphic marker in the southern CSRP

A correlation between the Brown's View ignimbrite of Rogerson Graben, the Little Creek ignimbrite of the Cassia Formation further east, and the 'Browns Bench 11' ignimbrite on the Browns Bench massif to the west (Fig. 6.2) is inferred on the basis of the following six criteria listed below:

(1) All three units occupy the same stratigraphic position according to available radiometric dates.

(2) All three units contain distinctive high-Mg pyroxenes, which are not seen in any other cSRP ignimbrite.

(3) All three units are the oldest rhyolitic unit, within their respective successions, to contain no sanidine.

(4) All three units have rather unusual welding profiles in which a central less-welded zone is enclosed between two intensely-welded zones. This type of welding profile is shared in the cSRP only by the McMullen Creek ignimbrite and the Tuff of Idavada Old.

(5) Each of the three units contains abundant, angular, black vitric lapilli within a central layer of less-welded lapilli-tuff. These lapilli are absent from other (upper and lower) parts of each unit. This characteristic distribution is rare elsewhere in the cSRP.

(6) The three units have consistent whole-rock chemistry, in terms of their Zr/Y and Th/Nb ratios, and define a unique chemical field that is distinct from all other subjacent and superjacent ignimbrites in all three successions.

The above evidence, in combination, provides a robust correlation and infers the existence of a widespread ignimbrite sheet, here termed 'The Brown's View Ignimbrite'. Rock Creek canyon in the Cassia Mountains (GR: N42°20'25.1"/W114°16'58.8") is

designated as the type area for this extensive unit. At this location the ignimbrite is thickest, and well-exposed, and best exhibits the compound cooling profile and abundant vitric lapilli. The ignimbrite is inferred to have been emplaced during a single large explosive eruption on the basis of the absence of evidence for repose periods within the unit, at all sites. The complex welding profile is inferred to record the progress of a sustained explosive eruption in which large volumes of cool vitric lapilli may have been entrained, during the eruption, which lowered the emplacement temperature and hindered welding in the central lapilli-tuff. This is assuming that the vitric lapilli are an accidental component of the eruption, but this is not fully constrained. However, this hypothesis is supported as the disappearance of these lapilli in the upper and lower parts of the ignimbrite is concurrent with an increase in welding.

The original distribution of the ignimbrite (Fig. 6.2 inset) is estimated using the outcrop patterns of each of the three correlated ignimbrites, mindful that the original ignimbrite terminations are unlikely to exactly mirror the present-day outcrop pattern. Outcrop patterns were determined by a combination of field mapping (this study) and published geological maps (Mytton et al., 1990; Wlliams et al., 1990, 1991, 1999). Other geological factors such as thickness variations and inferred basin topographies were also considered and the original distribution is reasonably extended to inferred topographic barriers, assumed to have been present during the Brown's View eruption. The source location for the eruption is taken to have been the nearest point in the central axis of the Snake River Plain (as in previous interpretations e.g., McCurry et al. 1996), and this proximal area is also included within the estimated geographic distribution of the ignimbrite (Fig. 6.2 inset). On this basis, the geographic distribution for the Brown's View Ignimbrite is estimated to be ~2700 km^2 (Table 6.1). This estimate is taken as a minimum, because its distal limits have not been located.

The Brown's View Ignimbrite is less extensive and less voluminous when compared with other cSRP ignimbrites (see section 6.5). However, the very distinctive nature of its characteristic features, particularly the high-Mg pyroxenes and lack of sanidine, make it a regionally important stratigraphic marker in the southern cSRP.

6.3. The McMullen Creek Ignimbrite

The McMullen Creek ignimbrite was previously thought to be a localised eruption-unit of the Cassia Formation, recognised in the Cassia Mountains, Idaho (Wright et al., 2002;

Ellis et al., 2010; see also Chapter 4.14). While it is extensive within the Cassia Mountains it has not been recognised outside of this localised area (Wright et al., 2002). The present study, however, compares its physical and chemical features with those of other localised eruption-units in the cSRP to propose that it is a considerably more widespread ignimbrite sheet. As with the correlation of the Brown's View Ignimbrite, a multi-technique approach was used in order to present a roust correlation between three localised eruption-units, namely: (1) the McMullen Creek ignimbrite of the Cassia Formation in the Cassia Mountains (Fig. 6.1b); (2) 'Oakley Hills 1', a newly defined intensely-welded ignimbrite east of Oakley, Idaho (Fig.6.1b); and (3) the 'Tuff of Idavada Old (Tivo, Michalek, 2009), exposed in the Little Fish Creek canyon north of Carey, Idaho (Fig.6.1b).

The McMullen Creek ignimbrite has been grouped as part of CAT group 12B of Bonnichsen et al. (2008), which includes a total of six individual ignimbrites. The 'Oakley Hills 1' and Tivo ignimbrites are not assigned a Cat group, however whole-rock chemistry (Kauffman et al., 2010; Reichow, unpublished) and palaeomagnetic data (Finn & Coe, unpublished) suggests they are consistent with the ignimbrites of CAT group 12B (sections 6.3.2 and 6.3.4).

For the purpose of this study each of the McMullen Creek, 'Oakley Hills 1' and Tivo ignimbrites are described in terms of their physical field characteristics, whole-rock and mineral chemistry and palaeomagnetic data in order to establish a correlation between them. This is also the first proposed correlation that extends across the Snake River Plain to the north, and data from the Tivo ignimbrite was provided by colleagues (Reichow, unpublished) working on the north-side of the cSRP. Each individual ignimbrite of this proposed correlation is described briefly below (1–3).

(1) The McMullen Creek ignimbrite is a ~45 m-thick rhyolitic ignimbrite that is well-exposed at a type section in Rock Creek canyon, Cassia Mountains, Idaho (Fig. 6.1b). It is the twelfth of thirteen members of the Cassia Formation (see Chapter 4) and overlies a poorly exposed ash-fall tuff, which in turn overlies a palaeosol in the top of the Indian Springs Member. The ignimbrite is subsequently overlain by the Lincoln Reservoir Member (Fig. 6.7). The McMullen Creek ignimbrite is a compound cooling unit with upper and lower intensely welded zones (15 m and 20 m-thick) separated by a 10 m-thick centre containing abundant vitric and pumice lapilli, supported within a less-welded

lapilli tuff (Fig. 6.7). Most lapilli are angular clasts of vitrophyric and lithoidal rhyolite, 0.5–3 cm in size, and the larger also contain plagioclase crystals (Fig. 6.8b). Pumice lapilli are rare in Snake River-type ignimbrites (Branney et al, 2008) and here range in size from 0.5 to 1 cm. Welding increases towards the margins of the central lapilli-tuff and the contacts with the upper and lower intensely-welded zones are marked by 2 m-thick layers of abundant lithophysae (2–5 cm in size), which are characteristic of the McMullen Creek ignimbrite (Fig. 6.7).

The lower intensely-welded zone consists of a 2 m-thick basal vitrophyre, overlain by a 13 m thick lithoidal zone with abundant sheet-joints. This is similar to the upper intensely welded zone, which is composed of lithoidal rhyolite that is sheet-jointed throughout (Fig. 6.7).

(2) 'Oakley Hills 1' is a newly described intensely-welded ignimbrite exposed in the Oakley Hills, a small fault escarpment east of Oakley, Idaho (Fig. 6.1b), and is overlain by 'Oakley Hills 2' (Fig. 6.7). It is ~15 m-thick, but is likely much thicker as upper and lower contacts are not seen. It is composed of lithoidal rhyolite with abundant sheet-joints towards the base and metre-scale rheomorphic folds towards the top (Fig. 6.7). It also contains abundant lithophysae, 5–10 cm in size, towards base of the exposure.

(3) The Tuff of Idavada-old (Tivo, Michalek, 2009) is located in the Little Fish Creek canyon, north of the town of Carey (Fig. 6.1b). Here it unconformably overlies members of the Challis volcanic group (Chetel et al., 2011) and is overlain by the 'Tuff of Idavada medial' (contact not seen, Michalek, 2009). The ignimbrite is ~60 m-thick (Fig. 6.7; Reichow, unpublished), although has been reported to be locally up to 200 m thick (Michalak, 2009). It is a compound cooling unit with upper and lower intensely-welded zones separated by a less-welded lapilli-tuff containing abundant angular, non-vesicular, vitric lapilli, 1–3 cm in size (Fig. 6.8a). Pumice lapilli are also reported to be present within the central lapilli-tuff (Michalek, 2009), but were not observed in the present study. The lower intensely-welded zone comprises a 2 m-thick basal vitrophyre overlain by an 18 m-thick, sheet-jointed, lithoidal zone that contains several layers of lithophysae that may suggests several cooling breaks (e.g., similar to the Jackpot Member, Andrews et al., 2008). The lithoidal zone is sharply overlain by the central, 15 m-thick, less-welded lapilli-tuff and the contact is marked by a 1 m-thick layer of lithophysae. The base of the lapilli-tuff displays low-angle cross-bedding but the majority is massive (Fig. 6.8a). The

top of the lapilli-tuff is marked by a 1 m thick layer of lithophysae, which is overlain by a 23 m-thick lithoidal zone and a 2 m-thick upper vitrophyre (Fig. 6.7).

6.3.1. Similar physical characteristics

The McMullen Creek and Tivo ignimbrites share five physical characteristics, which are not shared by most other cSRP ignimbrites. (1) Both are compound cooling-units, and exhibit a complex welding profile that consists of upper and lower intensely welded zones separated by a less-welded centre (Fig. 6.7). (2) The central zones of each ignimbrite contain abundant vitric lapilli, 0.5–3 cm in size, supported within a less-welded lapilli-tuff (Fig. 6.8 a–b). Similar vitric lapilli occur in other Snake River-type ignimbrites (e.g., 'Jackpot 6', Andrews et al., 2008; Branney et al., 2008); however they are rare within the enclosing ignimbrites in each of their local successions. As mention in the previous correlation (section 6.2), in the Cassia Formation only three of nine ignimbrites (including the McMullen Creek ignimbrite) contain abundant vitric lapilli (see Chapter 4); and no vitric lapilli have been observed in the ignimbrites that enclose Tivo (Reichow, unpublished). (3) The central lapilli-tuffs of both ignimbrites also contain pumice lapilli, which are very rare in most cSRP ignimbrites (Branney et al., 2008), and are not seen in any other ignimbrite within their respective successions. (4) In both ignimbrites, the pumice and vitric lapilli are observed only within the central less-welded zones, and do not extend into the overlying and underlying intensely-welded zones. This is particularly unique, as this vertical lithological profile is only also exhibited by the Brown's View Ignimbrite (section 6.2.1). (5) Both ignimbrites have layers of abundant lithophysae that mark the upper and lower contacts of the central less-welded zone. This defines two darker colour bands either side of the paler central zones (Fig. 6.7), and this is not seen in any other cSRP ignimbrite.

The 'Oakley Hills 1' ignimbrite does not share the above characteristics, which is potentially problematic for establishing a correlation to the other two ignimbrites. The 'Oakley Hills 1' ignimbrite overlies a ~15 m gap in exposure, and due to the abundant lithophysae at its base (Fig. 6.7) it is inferred that this gap conceals the lower parts of the 'Oakley Hills 1' ignimbrite and may also conceal a less-welded lapilli-tuff. However, this remains a hypothesis, and the limited exposure means that a correlation to the other two ignimbrites is proposed on the basis of whole-rock chemistry (section 6.3.2) and palaeomagnetic data (Finn & Coe, unpublished; section 6.3.4)

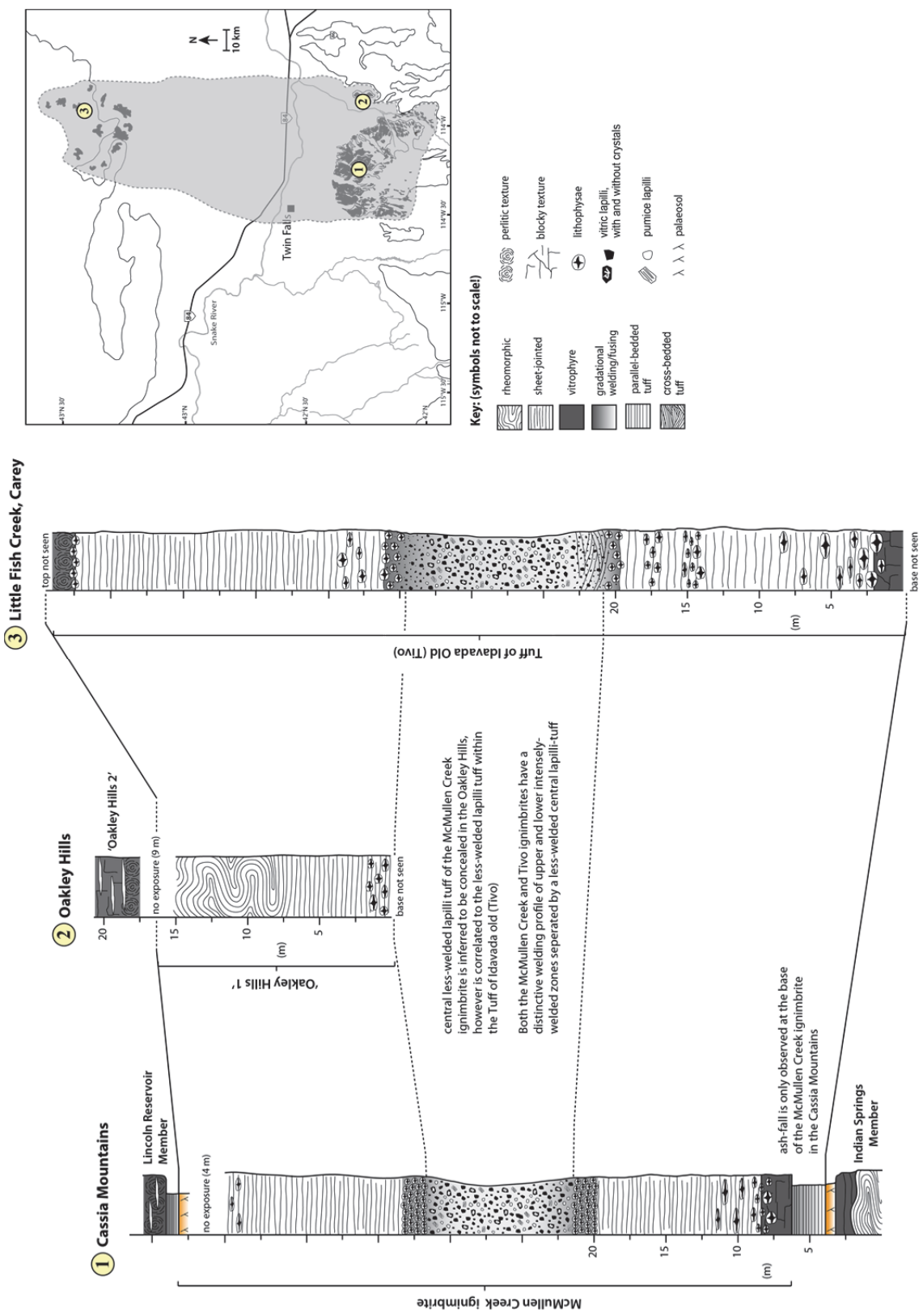

Figure 6.7. Select logs from the type sections (see inset map for locations) of the McMullen Creek, 'Oakley Hills 1', and Tivo ignimbrites, showing the characteristic vertical profile of upper and lower intensely-welded zones separated by a less-welded lapilli-tuff containing abundant vitric and pumice lapilli (0.5–3 cm in size) . Inset map shows the outcrop patterns of each of the three units and the estimated geographic distribution (grey area) of the widespread 'McMullen Creek Ignimbrite' (~12,000 km^2).

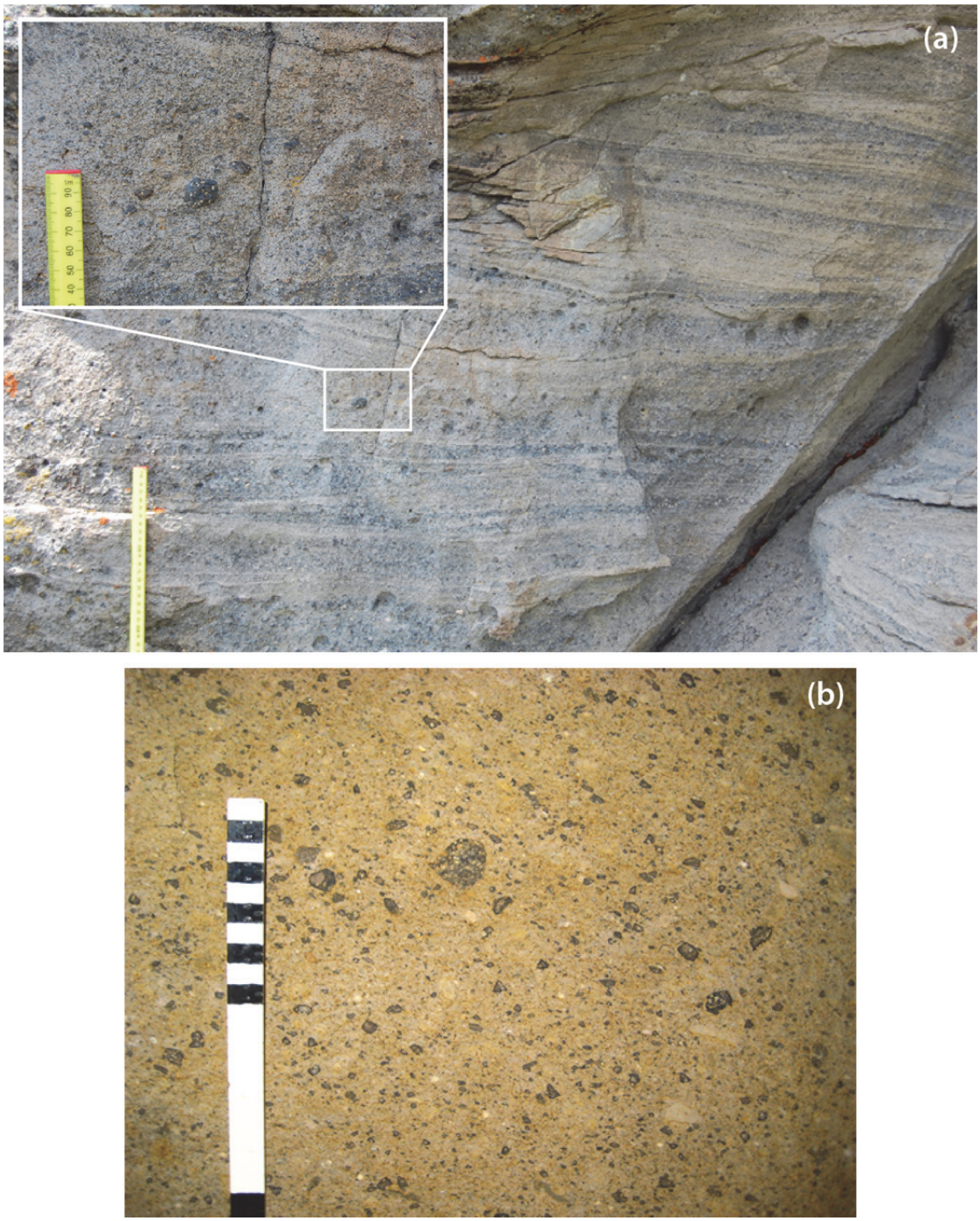

Figure 6.8. (a) Central lapilli-tuff of the 'Tuff of Idavada old (Tivo). The lower ~2m of this lapilli-tuff show low-angle cross-bedding, which may indicate that the pyroclastic density current was fully dilute during deposition. Inset photo shows a magnification of the abundant vitric lapilli, which are characteristic of the unit. **(b)** Abundant vitric lapilli are also present in the characteristic central lapilli-tuff of the McMullen Creek ignimbrite. This is therefore strong supporting evidence for a correlation between this ignimbrite and the Tivo ignimbrite.

6.3.2. Similarities in whole-rock chemistry

The McMullen Creek, 'Oakley Hills 1' and Tivo (Reichow, unpublished data) ignimbrites are all metaluminous (ASI 0.84 – 1.00 Table C.2, and C.4), and have closely similar SiO_2 concentrations (71.54–74.59 wt%.; Table C.2, and C.4). In addition, their TiO_2

concentrations (0.46–0.57 wt.%; Table C.2, and C.4) are within the range defined for CAT group 12B (0.41–0.60 wt.% TiO_2, Bonnichsen et al., 2008). Each of the ignimbrites also display minimal vertical zonation, and variation in SiO_2 is <2 wt.% from base to top.

Bulk-silicate-Earth-normalised trace element patterns for each of the three units are closely similar, with high abundances of Rb, Th, U and Pb, and relative lower abundances of Ba, Nb and Sr (Fig. 6.9). This pattern is broadly similar to other cSRP ignimbrites (Fig. 6.9); however Ba is less depleted than all underlying older ignimbrites (Fig. 6.9). As sanidine is not present as a phenocryst phase in all three ignimbrites (section 6.3.3), the lower depletion of Ba may suggest sanidine was not fractionating. This is consistent with the stratigraphic position of the ignimbrites, as the McMullen Creek ignimbrite in particular is known to be younger than the phenocryst marker horizon defined by the widespread Brown's View Ignimbrite.

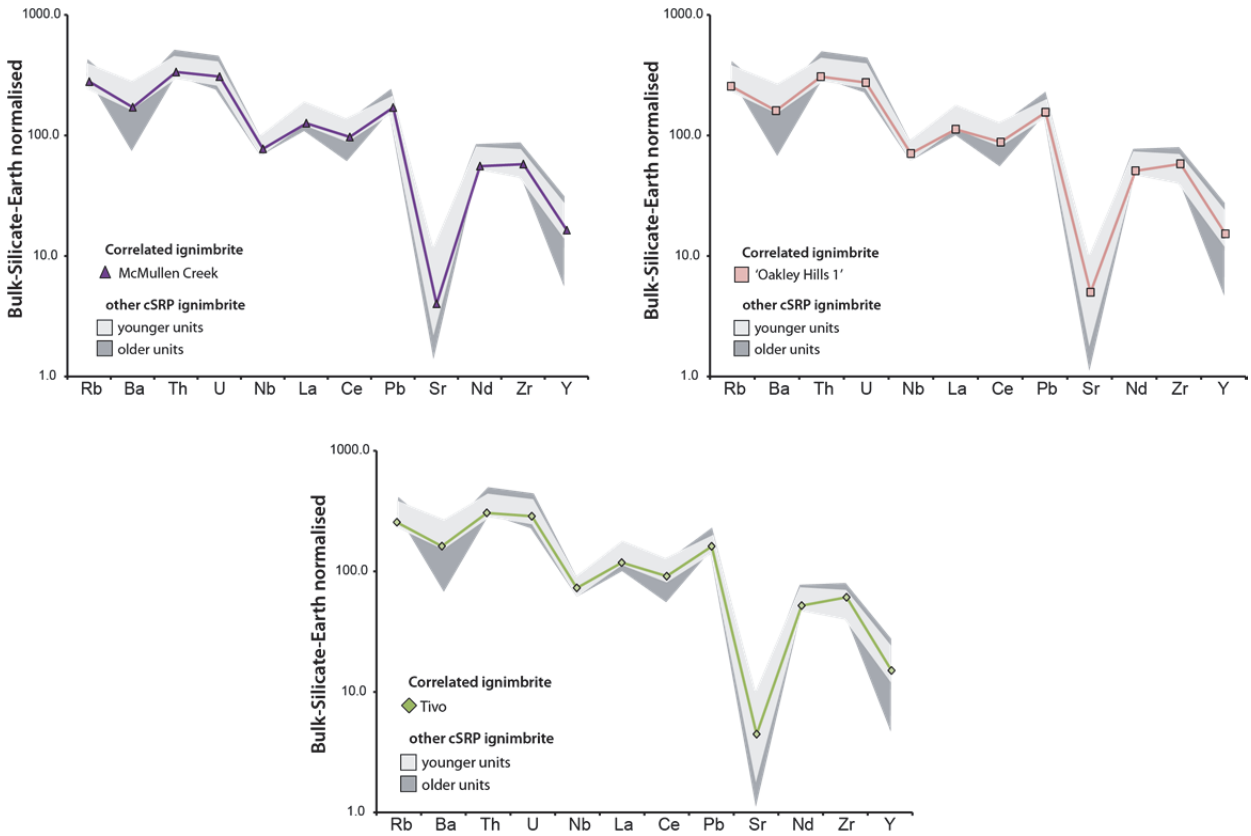

Figure 6.9. Bulk-silicate-Earth (Sun & McDonough, 1995) normalised trace element patterns for the McMullen Creek, 'Oakley Hills 1' and Tivo ignimbrites. Each of the three ignimbrites have indistinguishable trace element patterns that are also broadly similar to the majority of other cSRP ignimbrites. However, the three ignimbrites have significantly higher Ba abundances than all underlying older ignimbrites, which may be due to the lack of sanidine as a phenocryst phase. Therefore each of the ignimbrites is inferred to be above the phenocryst marker horizon defined by the Brown's View Ignimbrite.

Despite overall similarities with other cSRP ignimbrites it is possible to distinguish the three targeted ignimbrites by using the relatively incompatible elements Th, Nb, Zr and Y as discriminators. Zr/Y and Th/Nb ratios of each of the three ignimbrites are closely similar and are therefore supportive of a correlation (Fig. 6.10). In addition, the overlying ignimbrites within each of their respective succession are correlatives of the widespread Grey's Landing Ignimbrite (section 6.4). This adds further validity to the proposed correlation between the McMullen Creek, 'Oakley Hills 1' and Tivo ignimbrites by confirming that each of the ignimbrites are at an identical stratigraphic horizon.

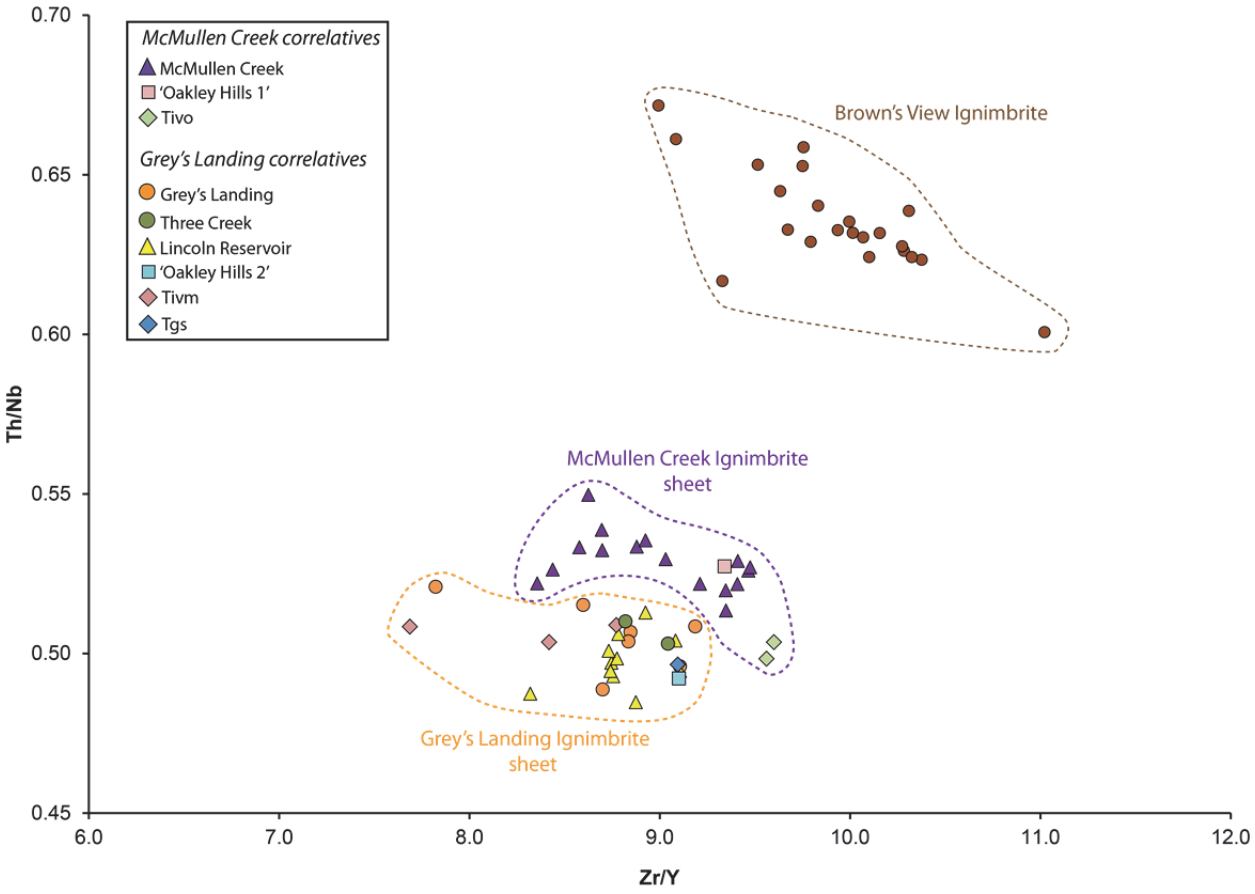

Figure 6.10. Zr/Y versus Th/Nb plot demonstrating the closely similar compositions of the correlated ignimbrites of the widespread McMullen Creek Ignimbrite and the widespread Grey's Landing Ignimbrite. Moreover, all individual units that compose each correlation are stratigraphically adjacent to one another within their respective successions. Therefore both correlations support each other based on the stratigraphic positions of each of their respective correlated units.

6.3.3. Similarities in petrology and mineral chemistry

Crystal content, in each of the ignimbrites, is estimated as 10–15 % and comprises an anhydrous mineral assemblage of plagioclase, pigeonite, augite, magnetite and accessory apatite and zircon, with plagioclase, pigeonite, and augite being the most abundant.

Similar to the previous correlation, this crystal content and mineral assemblage is common in most cSRP ignimbrites (Ellis et al., 2013), and not unique to this correlation. Sanidine is also absent from the assemblage. This is expected of the McMullen Creek ignimbrite as it is above the phenocryst marker horizon defined by the Brown's View Ignimbrite (section 6.2.3). The stratigraphic positions of the 'Oakley Hills 1' and Tivo ignimbrites, in relation to the Brown's View ignimbrite, are not fully determined. However, these units also lack sanidine and are therefore inferred to be stratigraphically above the Brown's View Ignimbrite marker horizon.

Compositions of plagioclase, pigeonite and augite crystals were only obtained for the McMullen Creek and Tivo ignimbrites, due to time constraints, and future work is planned for analysing the phenocrysts of the 'Oakley Hills 1' ignimbrite.

Plagioclase crystals in the McMullen Creek and Tivo (Reichow unpublished, data) ignimbrites are texturally similar to those of the Brown's View Ignimbrite, and include larger (2–3 mm) euhedral crystals and smaller (0.5–1 mm) subhedral crystals. All are andesine with a restricted compositional range (An_{32}–An_{47}, not shown, Table C.7, and C.11) and negligible zoning with typical core to rim variation of <1% An. These compositions are indistinguishable from those of the Brown's View Ignimbrite and all other cSRP eruption-units, and are therefore not useful correlation criteria.

Pyroxene crystals in these two units are subhedral, between 0.5 to 1 mm in size, and define two compositional modes: one of pigeonite and one of augite (Fig. 6.11, Table C.8, and C.12). Pigeonite crystals define a relatively narrow compositional range (between 9.86 and 11.57 wt.% MgO), whereas the augite crystals define a slightly larger range (between 8.92 and 10.88 wt.% MgO). Pyroxenes from the McMullen Creek ignimbrite also show a degree of scatter between these two compositional modes (Fig. 6.11). This may be due to micro-exsolution lamellae, the compositions of which were subsequently homogenised during analysis. Pyroxenes from the McMullen Creek ignimbrite are also indistinguishable from those of the underlying units (Fig. 6.11). This demonstrates that while pyroxene compositions of the McMullen Creek and Tivo ignimbrites are supportive of a correlation, they are not a unique correlation characteristic. However, further support is provided for this correlation by the unique pyroxenes in each of the overlying units, which define four compositional modes (Fig. 6.11) and are a characteristic feature of the widespread Grey's Landing Ignimbrite (section 6.4.3). Therefore, the more robust

correlation defined between these directly overlying units adds validity to a correlation between the underlying McMullen Creek and Tivo ignimbrites.

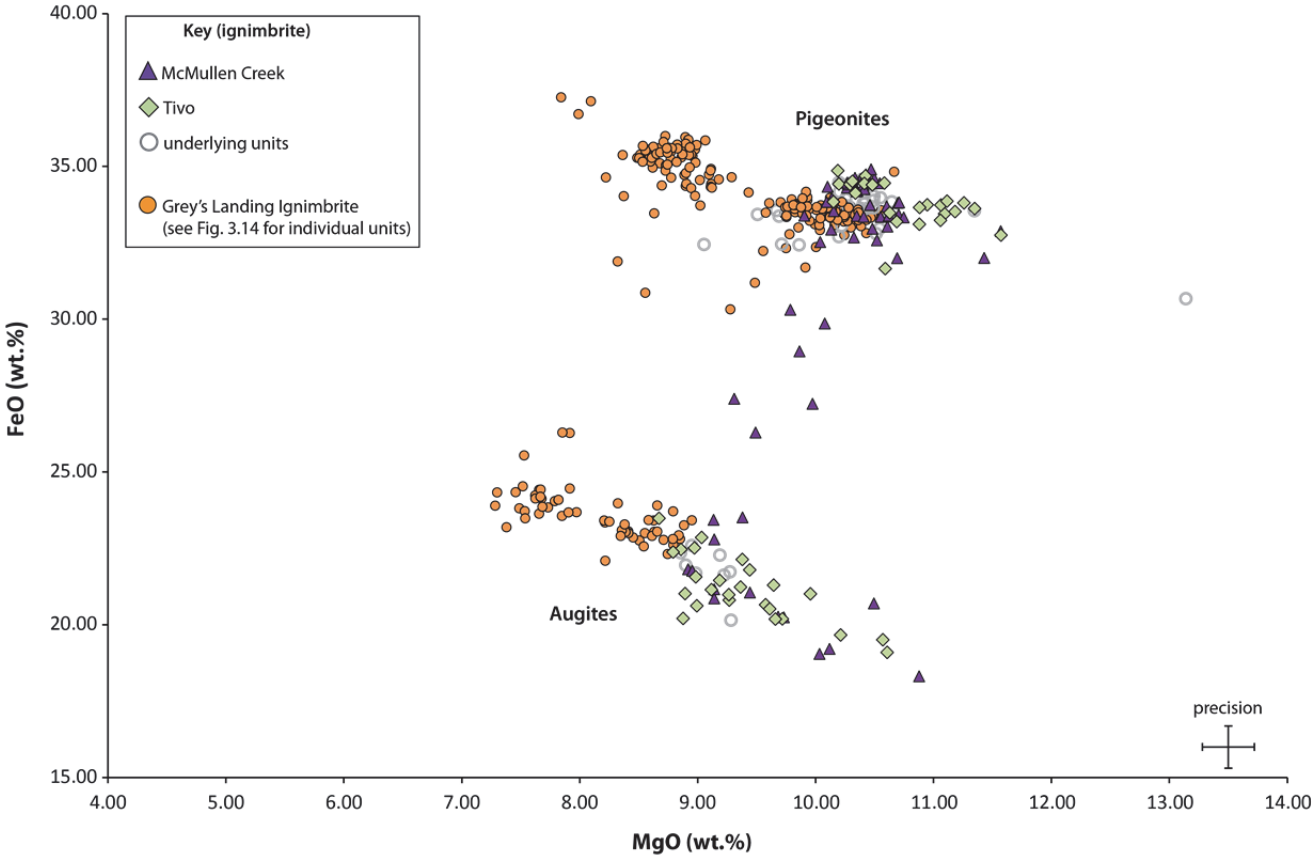

Figure 6.11. MgO versus FeO plot demonstrating the closely similar pigeonite and augite compositions in the McMullen Creek and Tivo ignimbrites. These compositions are similar to those of the underlying units, however are distinct from the overlying widespread Grey's Landing Ignimbrite sheet, which contains multiple pyroxene modes (see also Fig. 6.14).

6.3.4. Similar palaeomagnetic polarity and mean flow directions

A total of 12 drill-cores (10 cm in length) were taken from each of the McMullen Creek, 'Oakley Hills 1' and Tivo ignimbrites in order to determine their palaeomagnetic polarity and their mean palaeomagnetic flow directions.

All three ignimbrites exhibit a normal magnetic polarity (Fig. 6.15b). This is consistent with ignimbrites of CAT group 12B (Bonnichsen et al., 2008). While this is supporting evidence for a correlation, this polarity is common among many cSRP ignimbrites and is therefore not a unique characteristic. However, tilt-corrected mean palaeomagnetic flow directions, for each of the ignimbrites, are indistinguishable and show a steep inclination to the north (Finn & Coe, unpublished, Fig. 6.15b). These flow directions are similar to

the Brown's View Ignimbrite, however are distinct from the overlying units that define the Grey's Landing Ignimbrite (Fig. 6.15b). In summary, while the mean flow directions of the McMullen Creek, 'Oakley Hills 1' and Tivo ignimbrites are readily distinguishable from the overlying units, their similarity to the Brown's View Ignimbrite means that they cannot be used as an isolated correlation criteria, and must be used in combination with the other analytical methods described above in order to provide a robust correlation.

6.3.5. Geochronology

An $^{40}Ar/^{39}Ar$ plagioclase age of 9.0±0.1 Ma (Reichow, unpublished) was obtained on the McMullen Creek ignimbrite, and also a U-Pb age (9.0 ± 0.2 Ma), both of which are indistinguishable. In addition, a published (Michalek, 2009) $^{40}Ar/^{39}Ar$ plagioclase age of 9.21 ± 0.18 Ma for the Tivo ignimbrite is also indistinguishable from the ages of the McMullen Creek ignimbrite. Hitherto, no age determination exists for the 'Oakley Hills 1' ignimbrite; however its inclusion within CAT group 12B suggests that it erupted between ~9.0 and 7.5 Ma (Bonnichsen et al., 2008).

In summary, all dates suggest that all three ignimbrites occupy a similar stratigraphic horizon, and are therefore supportive of a correlation. However, it is clear that additional geochronology data are required to further consolidate this hypothesis.

6.3.6. Summary: the 'McMullen Creek Ignimbrite', an extensive ignimbrite sheet across the cSRP

A correlation between the McMullen Creek and 'Oakley Hills 1' ignimbrites in the southern cSRP, and across to the Tivo ignimbrite in the northern cSRP (Fig. 6.7) is not the strongest correlation proposed by the present study. However, by combining physical field characterisation, stratigraphic position, whole-rock and mineral chemistry, palaeomagnetic data, and limited geochronology data a correlation between these ignimbrites is inferred on the basis of the following seven criteria listed below:

(1) All three units occupy the same stratigraphic position according to available radiometric dates, this is further supported by the more robust correlation defined by the overlying units (the Grey's Landing Ignimbrite, section 6.4)

(2) The McMullen Creek and Tivo ignimbrites have rather unusual welding profiles in which a central less-welded zone is enclosed between two intensely welded zones, and a

similar profile is inferred for the 'Oakley Hills 1' ignimbrite. This type of welding profile is distinct and is shared in the cSRP only by the Brown's View ignimbrite. Therefore, this distinct vertical profile is one of the strongest lines of evidence supporting this correlation.

(3) The McMullen Creek and Tivo contains abundant, angular lapilli of dense vitrophyre and also pumice lapilli within a central layer of less-welded lapilli-tuff. However, these lapilli are absent from other (upper and lower) parts of each unit, and this characteristic distribution is rare (particularly the presence of pumice lapilli) elsewhere in the cSRP. Similar to (2) this field characteristic is excellent supporting evidence of a correlation.

(5) The three units have closely similar whole-rock chemistry, in terms of their Zr/Y and Th/Nb ratios, and define a unique chemical field that is distinct from other adjacent ignimbrites in all three successions.

(6) Each of the three units contains closely similar pyroxene compositions, which are distinct from their overlying units but are similar to the Indian Springs eruption-unit that underlies the McMullen Creek ignimbrite.

(7) The three-units have indistinguishable palaeomagnetic mean flow directions that are distinct from the overlying units.

Therefore, the three units are inferred to be part of a widespread ignimbrite sheet, hereby termed 'The McMullen Creek Ignimbrite'. Rock Creek canyon in the Cassia Mountains (GR: N42°20'30.8"/ W114°16'58.4") is designated as the type area for this extensive unit. At this location the ignimbrite is well-exposed, and best exhibits the compound cooling profile and abundant vitric and pumice lapilli at its centre. The ignimbrite is inferred to have been emplaced during a single large explosive eruption on the basis of the absence of evidence for repose periods within the unit, at all sites. The complex welding profile is inferred to record the progress of a sustained explosive eruption in which large volumes of cool vitric lapilli were entrained, during the eruption, which lowered the emplacement temperature and hindered welding in the central lapilli-tuff. This is assuming that the vitric lapilli are an accidental component of the eruption, but this is not fully constrained. However, this hypothesis is supported as the disappearance of these lapilli in the upper and lower parts of the ignimbrite is concurrent with an increase in welding, similar to the Brown's View ignimbrite.

The original distribution of the ignimbrite (Fig. 6.7 inset) is estimated using the outcrop patterns of each of the three correlated ignimbrites, mindful that the original ignimbrite terminations are unlikely to exactly mirror the present-day outcrop pattern. Outcrop patterns were determined by a combination of field mapping (this study) and published geological maps (Mytton et al., 1990; Wlliams et al., 1990, 1991, 1999; Michalek, 2009). Other geological factors such as thickness variations and inferred basin topographies were also considered and the original distribution is reasonably extended to inferred topographic barriers, assumed to have been present during the McMullen Creek eruption. On this basis, the geographic distribution for the McMullen Creek Ignimbrite is estimated to be ~12000 km^2 (Table 6.1), including the area within the SRP assumed to be the source region (after McCurry et al., 1996). This estimate is taken as a minimum, because its distal limits have not been located.

The McMullen Creek Ignimbrite is one of the most extensive and voluminous (Table 6.1) ignimbrites in the cSRP, and may record one of the largest super-eruptions of the Yellowstone-Snake River volcanic province (section 6.6). In addition, this correlation is one of the first proposed to extend across the Snake River Plain to ignimbrites exposed in the north.

6.4. The Grey's Landing Ignimbrite

The Grey's Landing ignimbrite was previously thought (Andrews et al., 2008) to be a localised eruption-unit of the Rogerson Formation, recognised within the Rogerson Graben (Fig. 6.1b; see also Chapter 3.7). The present study, however, compares its physical and chemical features with those of other localised eruption-units in the cSRP to propose that it is a considerably more widespread ignimbrite sheet, and may be one of the largest eruption-units in the cSRP. By utilising a similar methodology to the previous correlations a robust correlation is presented here between six localised ignimbrite eruption-units, namely: (1) the Grey's Landing ignimbrite (Andrews et al., 2008); (2) the Three Creek ignimbrite (Bonnichsen et al., 2008), located along Three Creek Road in southern Idaho (Fig. 6.1b); (3) the Lincoln Reservoir ignimbrite (Chapter 4.15) of the Cassia Formation in the Cassia Mountains (Fig. 6.1b); (4) 'Oakley Hills 2', a newly described intensely-welded ignimbrite east of Oakley, Idaho (Fig. 6.1b); (5) the 'Tuff of Gwin Springs' (Tgs, Smith, 1966; Oakley & Link, 2006), exposed in the Mount Bennett

Hills to the north (Fig. 6.1b); and (6) the 'Tuff of Idavada-Medial' (Tivm, Michalek, 2009), exposed in the Little Fish Creek canyon north of Carey, Idaho (Fig. 6.1b).

The Grey's Landing, Three Creek and Lincoln Reservoir ignimbrites are grouped within CAT group 12B of Bonnichsen et al. (2008) however, Tgs is grouped within CAT group 10A (Bonnichsen et al., 2008). However, whole-rock chemistry (Kauffman et al., 2010; Reichow, unpublished) and palaeomagnetic data (Finn & Coe, unpublished) suggests Tgs is similar to ignimbrites of CAT group 12B (sections 6.4.2 and 6.4.4), and should be reclassified to this group. Tivm has not been assigned a CAT group, although whole-rock chemistry and palaeomagnetic data (Reichow, unpublished; Finn & Coe, unpublished) suggests it should be grouped within CAT group 12B (of Bonnichsen et al., 2008)

For the purpose of this study each ignimbrite is described in terms of their physical field characteristics, whole-rock and mineral chemistry and palaeomagnetic data in order to establish a correlation between them. Data from Tgs and Tivm were provided by colleagues (Reichow, unpublished) working on the north-side of the cSRP. Each individual ignimbrite of the proposed correlation is described briefly below (1–6).

(1) The Grey's Landing ignimbrite (Andrews et al., 2008; Chapter 3.7) is the youngest eruption-unit of the Rogerson Formation and is well exposed within the Rogerson Graben (Fig. 6.1b). At the reference section (GR: N42°07'58.9"/W114°43'45.4") it overlies a 0.3 m-thick parallel-bedded, fused, ash-fall deposit which in turn overlies a palaeosol developed in the top of the underlying Backwaters Member (Fig. 6.12; Andrews et al., 2008). The Grey's Landing ignimbrite is ~60 m-thick with a 2 m-thick basal vitrophyre that contains distinctive red axiolites that extend laterally up to 3 m (Fig. 6.13d). The vitrophyre is sharply overlain by a 57 m-thick lithoidal zone with sub-horizontal rheomorphic isoclinal folds and sheath folds towards the base (typically obscured by sheet-jointing, Fig. 6.12), and upright to overturned open antiforms and synforms, up to 10 m in scale, towards the top (Fig. 6.12). The lithoidal zone is overlain by a 1 m-thick perlitic vitrophyre, which also follows the underlying folds (Fig. 6.12).

(2) The Three Creek ignimbrite (Bonnichsen et al., 2008) is a localised unit best exposed along Three Creek Road, west of the Rogerson Graben (Fig. 6.1b). Here it is ~10 m thick (top not seen, Fig. 6.12), although it thickens northwards, and overlies a parallel-

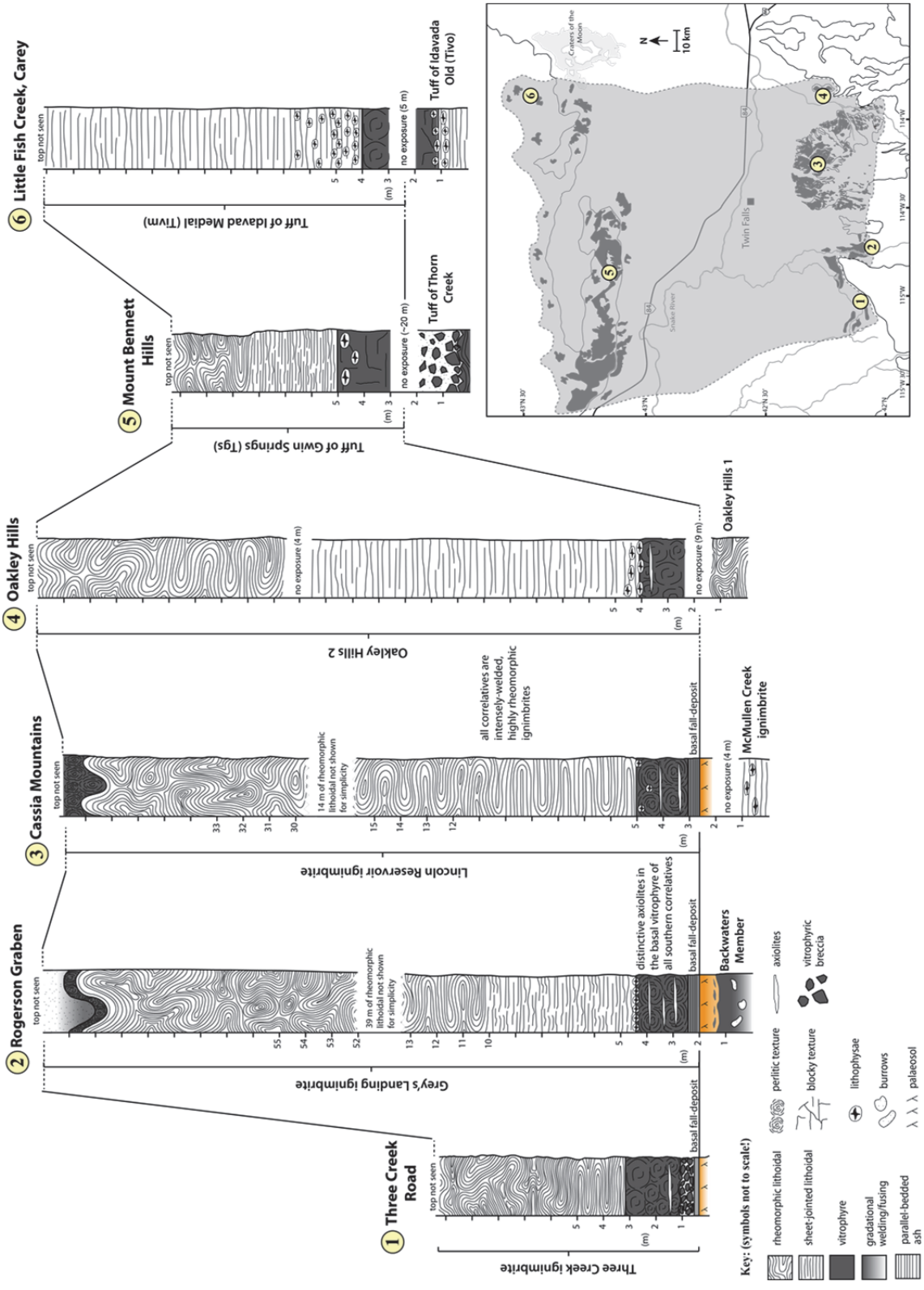

Figure 6.12. Select logs from the type sections (see inset map for locations) of the Three Creek, Grey's Landing, Lincoln Reservoir, 'Oakley Hills 2', Tgs, and Tivm ignimbrites. All are intensely-welded rheomorphic ignimbrites that are prosed to correlate as part of a single widespread ignimbrite sheet. Inset map shows the outcrop patterns of each of the six units and the estimated geographic distribution (grey area) of the widespread 'Grey's Landing Ignimbrite' (~18,000 km^2).

bedded ash-fall deposit, 0.3 m-thick, which in turn overlies a palaeosol possibly developed in the top of Cougar Point Tuff XIII (Bonnichsen, 1982a). The basal vitrophyre (2 m-thick) of the ignimbrite is locally brecciated and forms a peperite with the underlying fine ash (Fig. 6.13a). Earlier investigations interpreted this as an auto-breccia at the base of a Snake River-Type rhyolitic lava (Bonnichsen, 1982a). However, due to the laterally inconsistent occurrence of the breccia the unit was subsequently redefined as a lava-like Snake River-type ignimbrite (Bonnichsen et al., 2008). The basal vitrophyre also contains distinctive red axiolites that extend laterally up to 2 m. The overlying lithoidal zone is ~8 m-thick and exhibits sub-horizontal isoclinal rheomorphic folds towards the base, and open metre-scale antiforms and synforms towards the top (Fig. 6.12).

(3) The Lincoln Reservoir ignimbrite (Chapter 4.15) is ~38 m-thick and is the youngest eruption-unit of the Cassia Formation, located within the Cassia Mountains (Fig. 6.1b). It overlies a fused 0.3 m-thick parallel-bedded ashfall deposit, which in turn sits on a palaeosol developed in the top of the underlying McMullen Creek Ignimbrite (Fig. 6.12). The Lincoln Reservoir ignimbrite has a 2 m-thick basal vitrophyre that contains red axiolites, which extend laterally up to 2 m (Fig. 6.13c). The vitrophyre is sharply overlain by a lithoidal zone, ~35 m-thick, with sub-horizontal isoclinal rheomorphic folds towards the base, and open antiforms and synforms, up to 10 m in scale, towards the top (Fig. 6.12). The lithoidal zone is sharply overlain by a 1 m-thick perlitic vitrophyre (Fig. 6.12), which is poorly exposed.

(4) 'Oakley Hills 2' is a newly described intensely-welded ignimbrite exposed in the Oakley Hills, a small fault escarpment east of Oakley, Idaho (Fig. 6.1b), and overlies 'Oakley Hills 1' (Fig. 6.12). It is >30 m thick (base and top not seen) with a slightly perlitic basal vitrophyre (3 m-thick) containing red axiolites, and a 26 m-thick lithoidal zone with abundant sheet-joints towards the base and metre-scale rheomorphic folds towards the top (Fig. 6.12). The lithoidal zone is overlain by a 1 m thick vitrophyre (Fig. 6.12), although this is poorly exposed.

(5) The 'Tuff of Gwin Spring's (Tgs, Smith, 1966; Oakley & Link, 2006) is located in the Mount Bennett Hills (Fig. 6.1b), where it overlies the Tuff of Thorn Creek and is overlain by the Tuff of the City of Rocks (Oakley & Link, 2006). It is an ~8 m thick intensely-welded rheomorphic ignimbrite (base at top not seen, Reichow, unpublished, Fig. 6.12).

It has been reported to be up to 60 m-thick (Oakley & Link, 2006), although this was not observed in the present study. The ignimbrite is composed of a blocky basal vitrophyre, 2 m-thick, overlain by a 6 m-thick lithoidal zone with abundant sheet-joints in the lower 3 m and metre-scale rheomorphic folds towards the top (Fig.6.12; Reichow, unpublished).

(6) The 'Tuff of Idavada-medial' (Tivm) is located in the Little Fish Creek canyon, north of Carey, Idaho (Fig. 6.1b), where it overlies the 'Tuff of Idavada-Old' (contact not seen, Michalek, 2009). It is a ~13 m-thick intensely-welded ignimbrite (base and top not seen, Fig. 6.12; Reichow, unpublished), although it has been reported to be up to 60 m-thick (Michalek, 2009). The ignimbrite comprises a poorly exposed basal vitrophyre, ~1 m-thick, which is overlain by a ~12 m- thick lithoidal zone with abundant sheet-joints (Fig. 6.12). The lower ~1 m of the lithoidal zone also contains abundant lithophysae and is highly vesicular, with rounded vesicles up to 1 cm in size (Reichow, unpublished).

6.4.1. Similar physical characteristics

All six of the ignimbrites are intensely-welded with rheomorphic folds throughout that are commonly obscured by abundant sheet-jointing.

On the south side of the cSRP, the Three Creek, Grey's Landing and Lincoln Reservoir ignimbrites overlie parallel-bedded ash-fall deposits (0.3 m-thick), all of which are fused to vitrophyre by the overlying ignimbrite (Fig. 6.12). This fusing makes it impossible to correlate any individual ash beds between localities; however the presence of a fused ash-fall deposit beneath these three ignimbrites is supportive of a correlation, but is not a unique criterion. The basal vitrophyres, of these three ignimbrites, also contain distinctive red axiolites (Fig. 6.12; 6.13 c & d), and similar axiolites are also observed within the basal vitrophyre of the 'Oakley Hills 2' ignimbrite (Fig. 6.12). Devitrification features typically have limited effectiveness when establishing field correlations, as they tend to vary laterally within a single ignimbrite (e.g., devitrification within the Brown's View Ignimbrite, see section 6.2.1). However, these red axiolites are characteristic of the Grey's Landing, Three Creek, Lincoln Reservoir and Oakley Hills 2 ignimbrites and are not observed in any other ignimbrite within their respective successions. Therefore, they are unique to these four ignimbrites and are good supporting evidence for a correlation between them.

On the north side of the cSRP, Tgs and Tivm are similar intensely-welded rheomorphic ignimbrites to those on the south side (Reichow, unpublished). However, the

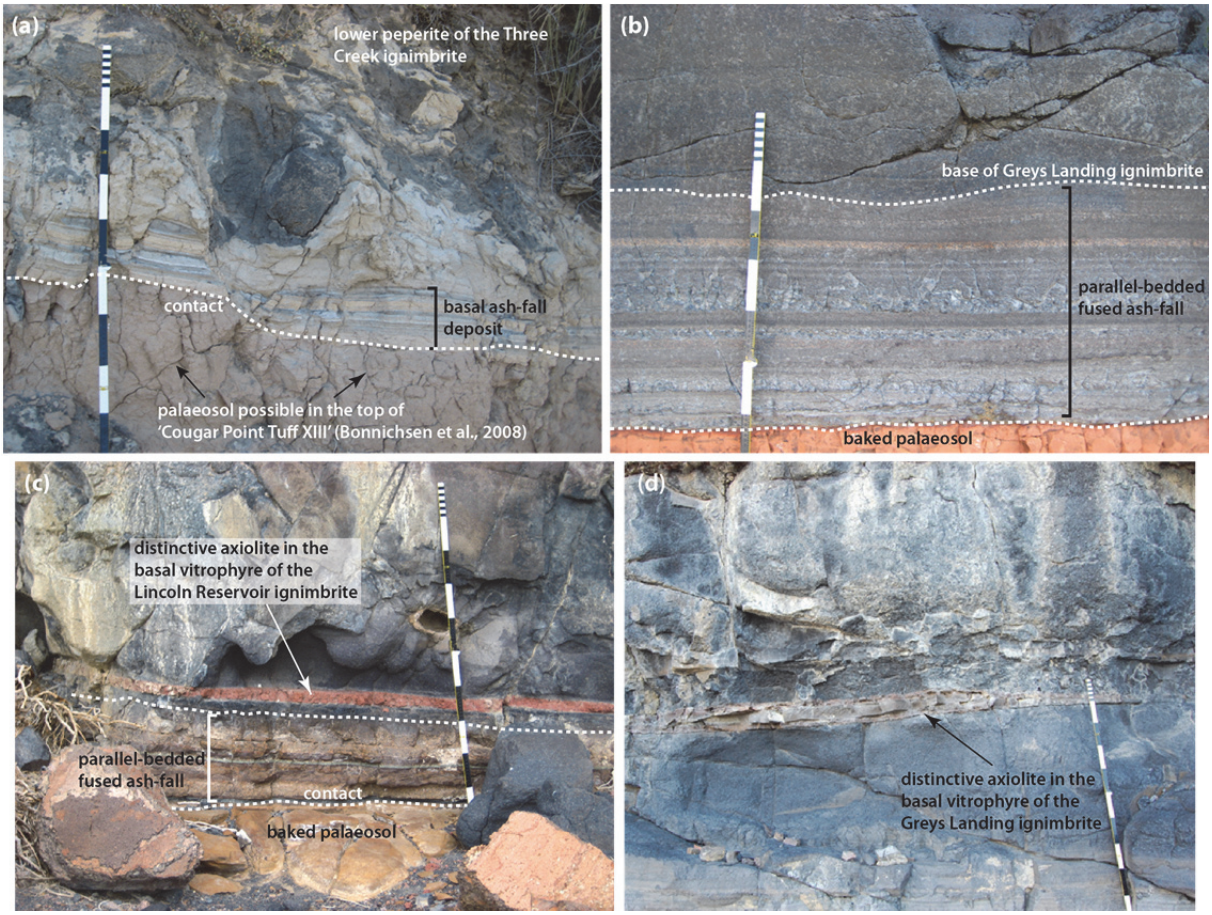

Figure 6.13. (a) Ash-fall deposit beneath the Three Creek ignimbrite is disturbed by the overlying peperite. **(b)** Parallel-bedded highly fused ash-fall deposit beneath the Grey's Landing ignimbrite. **(c)** Ashfall deposit beneath the Lincoln Reservoir ignimbrite is well-fused and likely correlates with the ashfall beneath the Grey's Landing ignimbrite. Overlying basal vitrophyre of the Lincoln Reservoir ignimbrite contains distinctive red axiolites. **(d)** Similar axiolites are also observed in the base of the Grey's Landing ignimbrite.

characteristic red axiolites and underlying ashfall deposits, seen in the south, are not observed (Fig. 6.12). This highlights the limitations of the field criteria, and a correlation to these north side ignimbrites is proposed based on additional criteria (e.g., whole-rock and mineral chemistry and palaeomagnetic data, sections 6.4.2–6.4.4).

6.4.2. Similar whole-rock chemistry

The whole-rock compositions of all six ignimbrites are remarkably consistent and unique chemical fields have been distinguished that are supportive of their correlation (Fig. 6.10).

The Grey's Landing, Three Creek, Lincoln Reservoir, 'Oakley Hills 2', Tgs and Tivm (Reichow, upublished data) ignimbrites all have similar SiO_2 (72.34–74.59 wt%.; Table C.1, C.2, C.4) and TiO_2 (0.42–0.51 wt.%; Table C.1, C.2, and C.4) concentrations. Their TiO_2 concentrations are within the range defined for CAT group 12B (0.41–0.60 wt.%

TiO_2, Bonnichsen et al., 2008), and therefore all are assigned to this group. All six ignimbrites are metaluminous, with ASI between 0.80–0.98 (Table C.1, C.2, and C.4), and compositional zonation is also minimal with vertical variations in SiO_2, in all units, of ≤2 wt % from base to top. This is consistent with the majority of cSRP ignimbrites.

Bulk-silicate-Earth-normalised trace element patterns for each of the six units are closely similar, with high abundances of Rb, Th, U and Pb, and relative lower abundances of Ba, Nb and Sr. These pattern are also closely similar to those of the McMullen Creek Ignimbrite (Fig. 6.9), and therefore are not shown. As observed in the McMullen Creek Ignimbrite, Ba in all six ignimbrites is less depleted than all underlying older ignimbrites. As sanidine is not present as a phenocryst phase (section 6.4.3) in all six ignimbrites, the lower depletion of Ba may suggest sanidine was not fractionating. This is consistent with the stratigraphic position of the ignimbrites, as the Grey's Landing and Lincoln Reservoir ignimbrites in particular are known to be younger than the phenocryst marker horizon defined by the Brown's View Ignimbrite.

Despite overall similarities with other cSRP ignimbrites it is possible to distinguish the six targeted ignimbrites by using the relatively incompatible elements Th, Nb, Zr and Y as discriminators. Zr/Y and Th/Nb ratios define chemical fields for each of the ignimbrites that are distinct from the adjacent units within their respective successions (Fig. 6.10). More importantly these chemical fields are consistent between all six of the ignimbrites and this provides good supporting evidence for a correlation between them. All underlying units are also correlatives of the widespread McMullen Creek Ignimbrite (section 6.3).

6.4.3. Similarities in petrology and mineral chemistry

Crystal content, in each of the ignimbrites, is estimated as 10–15 % and comprises an anhydrous mineral assemblage of plagioclase, pigeonite, augite, magnetite and accessory apatite and zircon, with plagioclase, pigeonite, and augite being the most abundant. This crystal content and mineral assemblage is common it most cSRP ignimbrites (Ellis et al., 2013), and not unique to this correlation. Sanidine is absent from the assemblage. This is expected of the Grey's Landing and Lincoln Reservoir ignimbrites, as both are known to overlie the marker horizon defined by the Brown's View Ignimbrite. The stratigraphic positions of the Three Creek, 'Oakley Hills 2', Tgs and Tivm ignimbrites in relation to the

Brown's View Ignimbrite are not fully determined. However, due to the lack of sanidine in these units they are inferred to also overlie the same phenocryst marker horizon.

Plagioclase crystals in all six units are textural similar to those of the previous correlations and range in size from 0.5–3 mm. All are andesine with a restricted compositional range (An31–An49; Table C.5, C.7, and C.11) and negligible zoning (typical core to rim variation is <1% An). These compositions are consistent with all other cSRP eruption units and so are not useful correlation criteria.

Pyroxenes are much more useful for correlation, and pyroxene crystals in all six ignimbrites are subhedral, between 0.5 to 1 mm in size. Pyroxenes from the Grey's Landing, Lincoln Reservoir, 'Oakley Hills 2', Tgs and Tivm ignimbrites define four compositional modes: two of pigeonite and two of augite (Fig. 6.14a). 'Pigeonite mode 1' (P1, Fig. 6.14a) is defined as crystals with MgO concentrations between 8.22 and 9.29 wt.% (Table C.6, C.8, and C.12), and 'pigeonite population 2' (P2, Fig. 6.14a) is defined as crystals with higher MgO concentrations between 9.61 and 10.56 wt.% (Table C.6, C.8, and C.12). In addition, 'Augite population 1' (A1, Fig. 6.14a) is defined as crystals with MgO concentrations between 7.28 and 7.97 wt.% (Table C.6, C.8, and C.12), and 'augite population 2' (A2, Fig. 6.14a) is defined as crystals with higher MgO concentrations between 8.22 and 8.95 wt.% (Table C.6, C.8, and C.12). Pyroxenes from the Grey's Landing and Lincoln Reservoir ignimbrites were also analysed by LA-ICP-MS at Idaho State University, USA during a pilot study to determine the usefulness of pyroxene trace element data in distinguishing between individual ignimbrites. Results show that ratios of the trace elements Y, V and Sc obtained can also distinguish between the different pigeonite and augite modes (Fig. 6.14b). Sc/Y and V/Y ratios also demonstrate that the compositional modes are distinct from the pyroxenes of other cSRP ignimbrites (e.g., the Brown's View Ignimbrite, Fig. 6.14b). This constitutes additional supporting evidence for a correlation between the Grey's Landing and Lincoln Reservoir ignimbrites. Future work is also planned for analysing the trace element concentrations of pyroxenes for other cSRP ignimbrites. This may help to further consolidate correlations presented here and also test the possibility for others.

The Three Creek ignimbrite differs slightly from the other five ignimbrites. It contains the P1, P2 and A2 compositional modes; however no A1 crystals were recorded. While this is inconsistent with the other five ignimbrites it likely reflects a sampling issue, as less

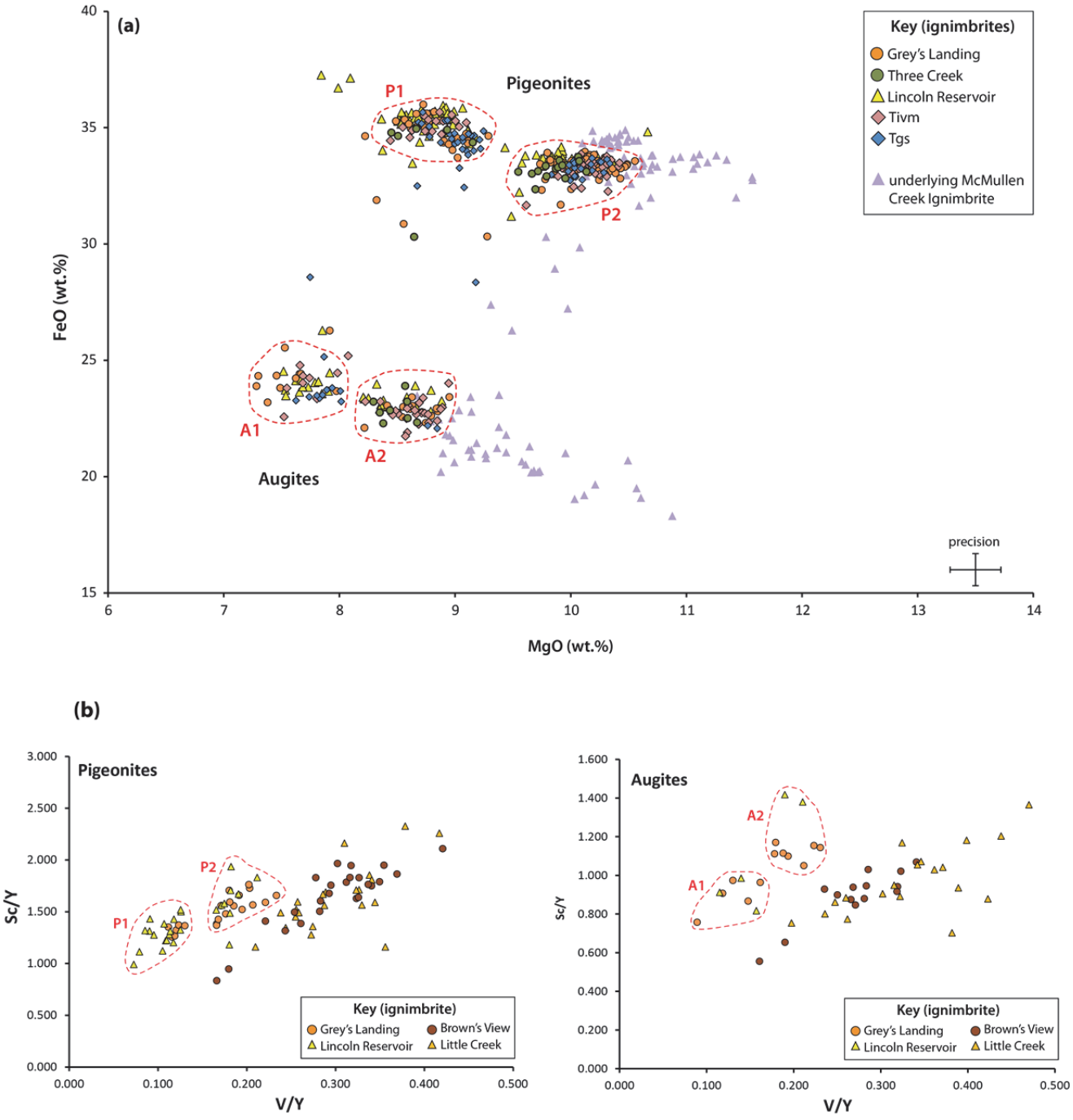

Figure 6.14 (a) MgO versus FeO plot demonstrating the closely similar pigeonite and augite compositions in the Grey's Landing, Lincoln Reservoir, Three Creek, Tivm, and Tgs ignimbrites. These ignimbrites are unique as they contain two modes of pigeonite (P1 and P2) and two modes of augite (A1 and A2). **(b)** V/Y versus Sc/Y plots demonstrating how the unique pigeonite and augite modes can be distinguished using trace element data (determined by LA-ICP-MS). These modes are also distinct from those of the Brown's View and Little Creek ignimbrites, both of which are correlatives of the widespread 'Brown's View Ignimbrite' (section 6.2).

augite crystals were analysed from the Three Creek ignimbrite. Therefore the lack of A1 crystals and does not necessarily preclude its correlation to the other five ignimbrites.

Despite these differences the presence of multiple compositional modes, in all six units, is unique as no other cSRP ignimbrites above the Brown's View Ignimbrite marker (i.e. those that lack sanidine) contain multiple modes of pyroxene. Therefore these four compositional modes are excellent supporting evidence for a correlation, and are also a defining characteristic of this proposed widespread ignimbrite sheet.

6.4.4. Similar palaeomagnetic polarity and mean flow direction

A total of 12 drill-cores (10 cm in length) were taken from each of the six units in order to determine their palaeomagnetic polarity and their mean palaeomagnetic flow directions and were analysed, along with the previous correlations, at the University of California, Santa Cruz, USA.

All six ignimbrites exhibit a normal magnetic polarity (Fig. 6.15b), which again is typical of many other cSRP rhyolites. However, tilt-corrected mean palaeomagnetic flow directions, for each of the ignimbrites, are indistinguishable and show a steep inclination to the NNW (Finn & Coe, unpublished, Fig. 6.15b). Moreover, these mean flow directions are readily distinguishable from all other adjacent ignimbrites and are therefore good supporting evidence for a correlation.

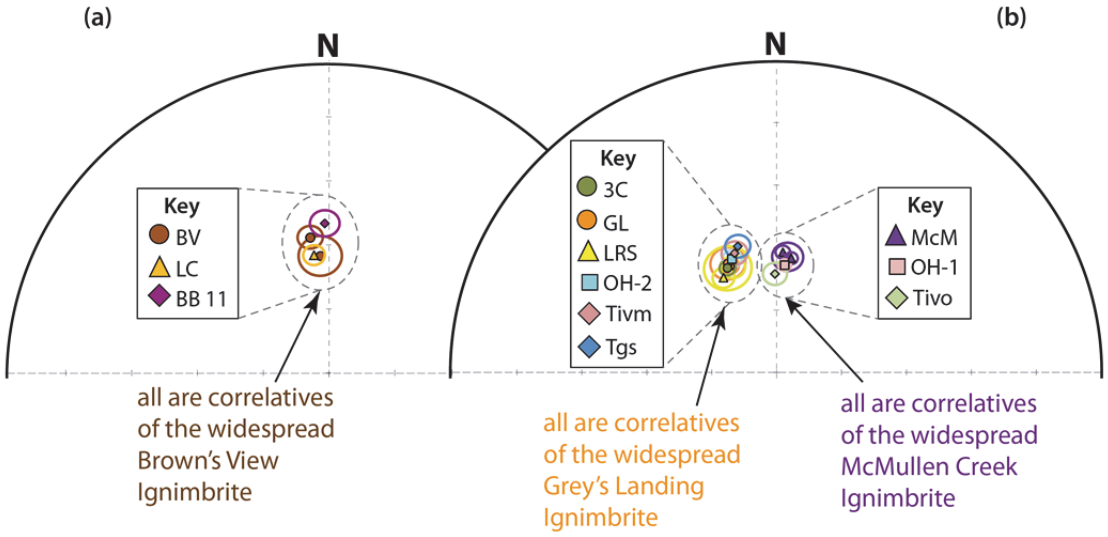

Figure 6.15. Stereonets showing the indistinguishable palaeomagnetic mean flow directions (Finn & Coe, unpublished) between all correlatives of **(a)** the widespread Brown's View Ignimbrite and **(b)** the widespread Grey's Landing and McMullen Creek ignimbrites. Directions of the Brown's View and McMullen Creek ignimbrite correlatives are similar and show a steep inclination to the north. Correlatives of the Grey's Landing Ignimbrite are distinct as they have steep inclinations to the NNW. Unit abbreviations are: BV, Brown's View; LC, Little Creek, BB11, 'Browns Bench 11; 3C, Three Creek; GL, Grey's Landing; LRS,; Lincoln Reservoir; OH-1, 'Oakley Hills 1'; OH-2, 'Oakley Hills 2'; Tivo, 'Tuff of Idavada old'; Tivm, 'Tuff of Idavada medial; Tgs, 'Tuff of Gwin Springs.

6.4.5. Geochronology

An $^{40}Ar/^{39}Ar$ plagioclase age of 9.1±0.1 Ma (Reichow, unpublished) was obtained on the Tgs ignimbrite, and age determinations on the other five ignimbrites of this correlation are still in progress. However, a maximum age is provided for the Lincoln Reservoir ignimbrite based on an $^{40}Ar/^{39}Ar$ plagioclase age of 9.0±0.1 Ma (Reichow, unpublished) for the underlying McMullen Creek Ignimbrite. In addition, a published (Michalek, 2009) $^{40}Ar/^{39}Ar$ plagioclase age of 8.39±0.59 Ma for the Tivm ignimbrite is similar to the Tgs and Lincoln Reservoir ignimbrites. Hitherto, there are no formal age determinations for the Three Creek or Grey's Landing ignimbrites; however their inclusion with CAT group 12B suggests they erupted between ~9.0 and 7.5 Ma (Bonnichsen et al., 2008).

All dates presented suggest that all six ignimbrites occupy a similar stratigraphic horizon, and are therefore supportive of a correlation between them. However, these are also indistinguishable from the underlying McMullen Creek Ignimbrite, therefore additional geochronology data are required to further consolidate this proposed correlation.

6.4.6. The 'Grey's Landing ignimbrite', an extensive ignimbrite sheet across the cSRP

A correlation between the Grey's Landing, Three Creek, Lincoln Reservoir, 'Oakley Hills 2' ignimbrites in the southern cSRP, and the Tgs and Tivm ignimbrites in the northern cSRP (Fig. 6.12) is inferred on the basis of the following five criteria listed below:

(1) All three units occupy the same stratigraphic position according to available radiometric dates, although more data is need to consolidate this hypothesis.

(2) All three units exhibit indistinguishable palaeomagnetic directions, and are readily distinguishable from other adjacent ignimbrites.

(3) All units contain multiple discrete modes of pyroxenes, including two of pigeonite and two of augite. This is particularly distinctive as no other cSRP ignimbrite, above the Brown's View Ignimbrite marker, contains multiple modes of pyroxene.

(4) All six units have consistent whole-rock chemistry, in terms of their Zr/Y and Th/Nb ratios, and define a unique chemical field that is distinct from all other subjacent and superjacent ignimbrites in each of their respective successions.

(5) A correlation between the southern units is supported by the presence of an underlying fused ashfall tuff, and the presence of distinctive red axiolites in the overlying basal

vitrophyre. However, these are not observed in the northern units, and are therefore not the most useful correlation criteria.

The above evidence, in combination, provides a robust correlation and infers the existence of a widespread ignimbrite sheet, here termed 'The Grey's Landing Ignimbrite'. The Grey's Landing recreation site in the Rogerson Graben (GR: N42°08'02.8"/W114°43'46.9") is designated as the type area for this extensive unit, as here the ignimbrite is thickest, and best exposed. The ignimbrite is inferred to have been emplaced during a single large explosive eruption due to the absence of evidence for repose periods within the unit, at all sites. It is also inferred to have been deposited from a high temperature (850–1000°C, Andrews et al., 2008) pyroclastic density current, and intense-welding of the ignimbrite occurred during deposition and rheomorphic deformation continued post-emplacement with the development of rheomorphic folds (Andrews & Branney, 2011).

The original distribution of the ignimbrite (Fig. 6.12 inset) is estimated using the outcrop patterns of each of the six correlated ignimbrites, mindful that the original ignimbrite terminations are unlikely to exactly mirror the present-day outcrop pattern. Outcrop patterns were determined by a combination of field mapping (this study) and published geological maps (Mytton et al., 1990; Wlliams et al., 1990, 1991, 1999; Oakley & Link, 2006; Andrews et al., 2008; Michalek, 2009). It is important to note that the north side of the cSRP is relatively understudied, and older geological maps (e.g., Worl et al., 1991) do not distinguish between individual Miocene eruption-units, which are grouped as part of the 'Idavada volcanic group' of Malde & Powers, 1962. However, due to the locations of known outcrops of the Tgs and Tivm ignimbrites (Oakley & Link, 2006; Michalek, 2009), the outcrop patterns of undivided Idavada volcanics (Worl et al., 1991) are also included in the original distribution (Fig. 6.12 inset). In addition, other geological factors such as thickness variations and inferred basin topographies were also considered and the original distribution is reasonably extended to inferred topographic barriers, assumed to have been present during the Grey's Landing eruption. On this basis, the geographic distribution for the Grey's Landing ignimbrite is estimated to be ~18000 km^2 (Table 6.1). This estimate is taken as a minimum, because its distal limits have not been located.

The Grey's Landing Ignimbrite is one of the most extensive and voluminous (Table 6.1) ignimbrites in the cSRP, and may record one of the largest super-eruptions of the Yellowstone-Snake River volcanic province (see section 6.6).

6.5. Estimated eruption volumes

Large caldera-forming eruptions are associated with three main types of deposit. These are; outflow ignimbrite sheets; intra-caldera ignimbrite fill; and widespread ashfall deposits (Mason et al., 2004). It is rare that the volumes of all three components can be estimated; therefore assessments of erupted volumes are prone to a number of potentially significant sources of error or omission. However, in order to calculate a reasonable estimate of the total erupted volume for any one eruption it is important to consider each of these three components. Estimates of these components for each of the Brown's View, McMullen Creek and Grey's Landing ignimbrites are presented in the following sections.

6.5.1. Estimating bulk outflow volumes

Estimates of the bulk volume of outflow ignimbrites have been determined in other volcanic fields by using the known geographic distribution, for an individual ignimbrite, and multiplying this by an average thickness (e.g., the Kneeling Nun Tuff, Elston et al., 1975; and the Bishop Tuff, Bailey, 1976). A similar method has also been used to calculate outflow volumes for three recently defined super-eruptions from the cSRP (e.g., the ~350 km^3 'Cougar Point Tuff XI'; the ~350 km^3 'Steer Basin Tuff' and the ~1,000 km^3 'Cougar Point Tuff XIII', Ellis et al., 2012a). Ignimbrites commonly exhibit lateral thickness variations due to pre-existing topography (e.g., thickening within valleys and thinning over topographic highs) and thinning away from source (Branney & Kokelaar, 2002). Therefore averaging the thickness of a single ignimbrite across multiple localities is considered reasonable as it gives a much better approximation of the thickness of the entire ignimbrite sheet. This method was therefore utilised in estimating the outflow volumes for each of the Brown's View, McMullen Creek and Grey's Landing ignimbrites. Average thickness for each of these three ignimbrite sheets were calculated using both measured thickness (taken from multiple localities, during field reconnaissance, with increasing distance away from the SRP) and published thickness from the geological maps (e.g., Williams et al., 1990; Oakley & Link, 2006; Andrews et al., 2008; Michalek, 2009) when field reconnaissance data was insufficient. This resulted in average thicknesses for each of the Brown's View, McMullen Creek and Grey's

Landing ignimbrites of 0.015 km, 0.05 km and 0.04 km, respectively. Applying these thicknesses to the estimated geographic distributions of each ignimbrite results in bulk outflow volumes of 41 km^3 for the for the Brown's View ignimbrite; 600 km^3 for the McMullen Creek ignimbrite; and 720 km^3 for the Grey's Landing ignimbrite (Table. 6.1).

6.5.2. Dense rock equivalent (DRE) outflow volumes

Super-eruptions are defined as eruptions that yield >450 km^3 of silicic magma (Sparks et al. 2005; Self, 2006). However, bulk eruption volumes do not consider the density of the deposits, and individual ignimbrites can have significant density variations (e.g., non-welded tuffs may have a density of 600–800 kg m^{-3}, while welded tuffs may have densities >2,000 kg m^{-3}, Mason et al., 2004). Therefore in order to classify the size of large explosive eruptions it is necessary to convert bulk eruption volumes into dense rock equivalent (DRE) volumes using the following calculation:

DRE = bulk volume x bulk density / magma density

For the Brown's View, McMullen Creek, and Grey's Landing ignimbrites bulk densities varied from 2340 kg m^{-3} (for intensely-welded facies) to 2330 kg m^{-3} (for less-welded facies, e.g., the less-welded centres of the Brown's View and McMullen Creek ignimbrites). Magma density was assumed to be equivalent to water-free silicic magma (2380 kg m^{-3}, Ochs & Lange, 1999).

For the intensely-welded Grey's Landing ignimbrite a DRE outflow volume (708 km^3) was calculated assuming a density of 2340 kg m^{-3} throughout the deposit. However for the Brown's View and McMullen Creek ignimbrites the less-welded centres compose ~20 % of the total outflow volume. Therefore 80 % of the bulk outflow volume was converted to DRE using a bulk density of 2340 kg m^{-3} and 20 % was converted using a bulk density of 2330 kg m^{-3}, and the sum of these two components equal the total DRE outflow volume (40 km^3 and 589 km^3, respectively).

6.5.3. Volume estimates including caldera fills and widespread ash falls

Studies have suggested that intra-caldera fill (I) DRE volumes are approximately equal to outflow deposit (O) DRE volumes (Lipman, 1984). In addition, earlier studies (Sparks & Walker, 1977) also showed that outflow deposit volumes are approximately equal to widespread ash-fall volumes (A). These assumptions double (with the inclusion of I) or triple (including both I and A) estimates of the DRE outflow volume, and both are shown

Table 6.1. Geographic distribution, average thickness, and volume estimates for each of the widespread Grey's Landing, McMullen Creek, and Brown's View ignimbrites. Also included are volume estimates for additional large explosive silicic eruptions from the cSRP, Heise and Yellowstone volcani fields

Ignimbrite Name	Geographic distribution (km^2)	Average thickness (km)	Bulk volume (km^3)*	Deposit density (kg m^{-3})	DRE# volume (km^3)	Erupted Mass (kg)	Magnitude	Age (Ma)	Error	Reference
central Snake River Plain (cSRP)										
The Greys Landing ignimbrite	18,000	0.040	1440	2340[a]	1416	$3.4x10^{15}$	**8.5**	9.0	0.1	This study
The McMullen Creek ignimbrite	12,000	0.050	1200	2340[a] & 2330[b]	1179	$2.8x10^{15}$	**8.4**	9.0	0.1	This study
The Browns View ignimbrite	2,700	0.015	82	2340[a] & 2330[b]	81	$1.9x10^{14}$	**7.3**	10.2	0.3	This study
Steer Basin Tuff	3,221	0.055	354	2340[a]	348	$8.3x10^{14}$	**7.9**	10.62	0.12	Ellis et al., 2012
Cougar Point Tuff XIII	6,719	0.075	1000	2340[a]	983	$2.5x10^{15}$	**8.4**	10.95	0.06	Ellis et al., 2012
Cougar Point Tuff XI	2,773	0.065	360	2340[a]	354	$8.4x10^{14}$	**7.9**	11.38	0.08	Ellis et al., 2012
Heise volcanic field										
Kilgore Tuff	12,000	0.075	1800	2200[c]	1664	$4.0x10^{15}$	**8.6**	4.50	0.05	Morgan & McIntosh, 2005
Conant Creek Tuff	3,000	0.05	300	2200[c]	277	$6.6x10^{14}$	**7.8**	5.58	0.13	Morgan & McIntosh, 2005
Walcott Tuff	7,500	0.05	750	2200[c]	693	$1.7x10^{15}$	**8.2**	6.35	0.04	Morgan & McIntosh, 2005
Blacktail Creek Tuff	8000	0.075	1200	2200[c]	1109	$2.6x10^{15}$	**8.4**	6.70	0.03	Morgan & McIntosh, 2005
Yellowstone volcanic field										
Lava Creek Tuff	7,300	0.14	1000	2200[c]	924	$2.2x10^{15}$	**8.3**	0.645	0.002	Christiansen, 2001; Lanphere et al., 2002
Mesa Falls Tuff	2,700	0.10	280	2200[c]	259	$6.2x10^{14}$	**7.8**	1.297	0.004	Christiansen, 2001; Lanphere et al., 2002
Huckleberry Ridge Tuff	15,400	0.14	2210	2200[c]	2043	$4.9x10^{15}$	**8.7**	2.078	0.004	Christiansen, 2001; Lanphere et al., 2002

*Bulk volume = outflow + inferred caldera fill; # Dense Rock Equivelent; [a] density of intensely-welded facies (this study); [b] density of less-welded facies (this study); [c] density from Mason et al., 2004

to be valid when considering the volumes of the Younger Toba Tuff (I:O:A= 1000:1000:800 km^3, Rose & Chesner, 1987), and the Oruanui eruption (I:O:A= 420:320:430 km^3, Wilson, 2001).

Recent studies in the cSRP (e.g., the Kimberly bore-hole, Chapter 5) indicate that intra-caldera fill volumes, in the cSRP, may be considerably larger than their equivalent outflow volumes (up to 3000 km^3, assuming a caldera size similar to the Yellowstone volcanic field, see Chapter 5.9). However, in order to allow comparison with other large explosive eruptions from Yellowstone-Snake River volcanic province (Christiansen, 2001; Morgan & McIntosh, 2005; Ellis et al., 2012a) the assumptions of Lipman (1984) are maintained, and intra-caldera fill DRE volumes for the Brown's View, McMullen Creek and Grey's Landing ignimbrites are assumed to be equal to the calculated outflow volumes (Table 6.1). In addition, eruption volumes calculated for Cougar Point Tuff XI, the Steer Basin Tuff, and Cougar Point Tuff XIII do not include widespread ashfall deposits (Ellis et al., 2012a), and final estimates considered only equal proportions of outflow and intra-caldera fill deposits. Widespread ashfall deposits were also omitted from volume estimates of other large explosive eruptions from the younger Heise (Morgan & McIntosh, 2005) and Yellowstone (Christiansen, 2001) volcanic fields, which also consider only the outflow and intra-caldera fill deposits. Therefore, widespread ashes were also omitted from final volume estimates for the Brown's View, McMullen Creek and Grey's Landing ignimbrites. As a result final erupted DRE volumes are estimated as 81 km^3 for the Brown's View Ignimbrite, 1179 km^3 for the McMullen Creek Ignimbrite, and 1416 km^3 for the Grey's Landing Ignimbrite (Table 6.1).

6.6. Comparisons with other large explosive eruptions from the Yellowstone-Snake River volcanic province

Prior to recent studies in the cSRP (e.g., this study; Ellis et al., 2012a) large volume ignimbrite eruptions were better known from the younger Heise and Yellowstone volcanic fields in the eastern SRP (Fig. 6.1a). The Heise volcanic field records four large-volume silicic eruptions (Morgan & McIntosh, 2005; Table 6.1) as expressed by the ~6.7 Ma, ~1100 km^3 (DRE, converted assuming a bulk deposit density of 2200 kg m^{-3}, after Mason et al., 2004), Blacktail Creek Tuff; the ~6.4 Ma, ~700 km^3 (DRE), Walcott Creek Tuff; the ~5.6 Ma, ~300 km^3 (DRE), Conant Creek Tuff; and the ~4.5 Ma, ~1660 km^3 (DRE), Kilgore Tuff. The Yellowstone volcanic field has produced three large-

volume eruptions (Christiansen, 2001; Table 6.1) including the ~2.1 Ma Huckleberry Ridge Tuff (~2040 km^3 DRE, revised volume after Ellis et al., 2012b); the ~1.3 Ma Mesa Falls Tuff (~260 km^3 DRE); and the ~0.6 Ma Lava Creek Tuff (~920 km^3 DRE).

The DRE volume of the Brown's View ignimbrite is much smaller in comparison to eruptions from the Heise and Yellowstone volcanic fields; although it does define a useful stratigraphic marker in the southern cSRP. However, the McMullen Creek and Grey's Landing ignimbrites record two explosive silicic eruptions with DRE volumes that are comparable, if not larger, than eruptions from the eastern volcanic fields. In order to facilitate comparisons between the McMullen Creek and Grey's Landing ignimbrites and others from the cSRP (e.g., Cougar Point Tuff XI, Cougar Point Tuff XII and the Steer Basin Tuff, Ellis et al., 2012a) and the eastern SRP; the size of each eruption was classified on the magnitude scale (Table 6.1) using the following equation:

Magnitude (M) = Log_{10}(m) – 7.0; where (m) is the erupted mass in kg (Pyle, 2000).

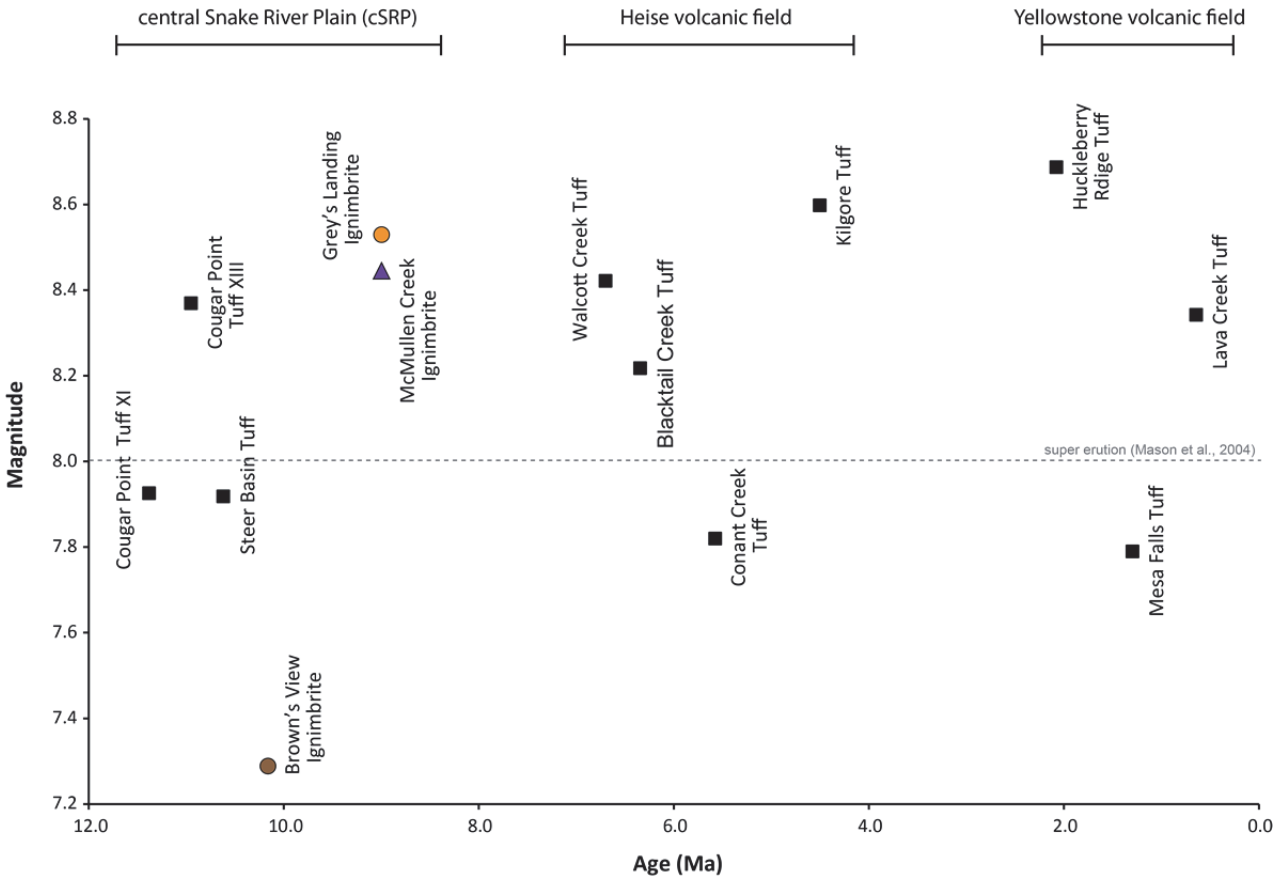

Figure 6.16. Comparison of magnitudes of large rhyolitic explosive eruptions from the central Snake River Plain (cSRP), and the Heise and Yellowstone volcanic fields. Also shown is the minimum magnitude (magnitude 8) for classification as a super-eruption (Mason et al., 2004). The Grey's Landing and McMullen Creek ignimbrites defined by the present study are the largest super-eruptions of the cSRP and are among the largest of the entire Yellowstone-Snake River volcanic province, with only the Kilgore and Huckleberry Ridge tuffs being larger.

Super eruptions are defined on the magnitude scale as eruptions larger than magnitude-8 (Mason et al., 2004). On this scale rhyolitic ignimbrites in the cSRP record three super-eruptions, and these are Cougar Point Tuff XIII (Ellis et al., 2012a), and the McMullen Creek and Grey's Landing ignimbrites (Fig. 6.16). This is comparable to the Heise volcanic field (three super-eruptions) and slightly higher than the Yellowstone volcanic field (two super-eruptions, Fig. 6.16). The McMullen Creek and Grey's Landing ignimbrites, in particular, record two super-eruptions with magnitudes of 8.4 and 8.5, respectively (Table 6.1). These are the largest super-eruptions recorded in the cSRP and are among the largest super eruptions of the entire Yellowstone-Snake River volcanic province; with only the Kilgore (magnitude-8.6) and Huckleberry Ridge (magnitude-8.7) tuffs recording larger eruptions (Fig. 6.16).

6.7. Estimating eruption frequency in the central Snake River Plain (cSRP)

Previous estimates of overall eruption frequency, in the cSRP, range from 10-20 eruptions/Myr, which is thought to coincide with an ignimbrite flare-up between ~12–8 Ma (Nash et al., 2006; Bonnichsen et al., 2008). These estimates were based on the total number of ignimbrite eruption-units (~42), identified in the cSRP, and averaged over this ~4 million year period. The ignimbrite total was calculated by Nash et al., 2006 as the sum of individual eruption-units identified within localised successions in the cSRP. However, the recent definition of the widespread Cougar Point XI, Cougar Point XIII and Steer Basin Tuffs has reduced the number of eruptions in the cSRP by six (Ellis et al., 2012a). In addition the three correlations, defined by the present study, have reduced the number of eruptions by a further seven (Fig. 6.17a). Therefore the total number of eruptions recorded in the cSRP to date is reduced to 29. This results in an estimate of eruption frequency in the cSRP of ~7.5 eruptions/Myr (Fig. 6.17b), during the ~12–8 Ma ignimbrite flare-up, which is significantly lower than previous estimates (Nash et al., 2006). Although the number of eruptions is reduced by correlating several units, the sizes of individual eruptions are increased as a result of this study and consequently increases the number of super-eruptions recorded in the cSRP. In summary the identification of the Grey's Landing and McMullen Creek super-eruptions (present study), and the Cougar Point Tuff XIII super-eruption (Ellis et al., 2012a) brings the total number of super-eruptions recorded in the cSRP to three. Averaging this number over the time period of the ignimbrite flare-up results in an estimated cSRP super-eruption frequency of one every 700–800 ka. This frequency should be considered tentative, and additional

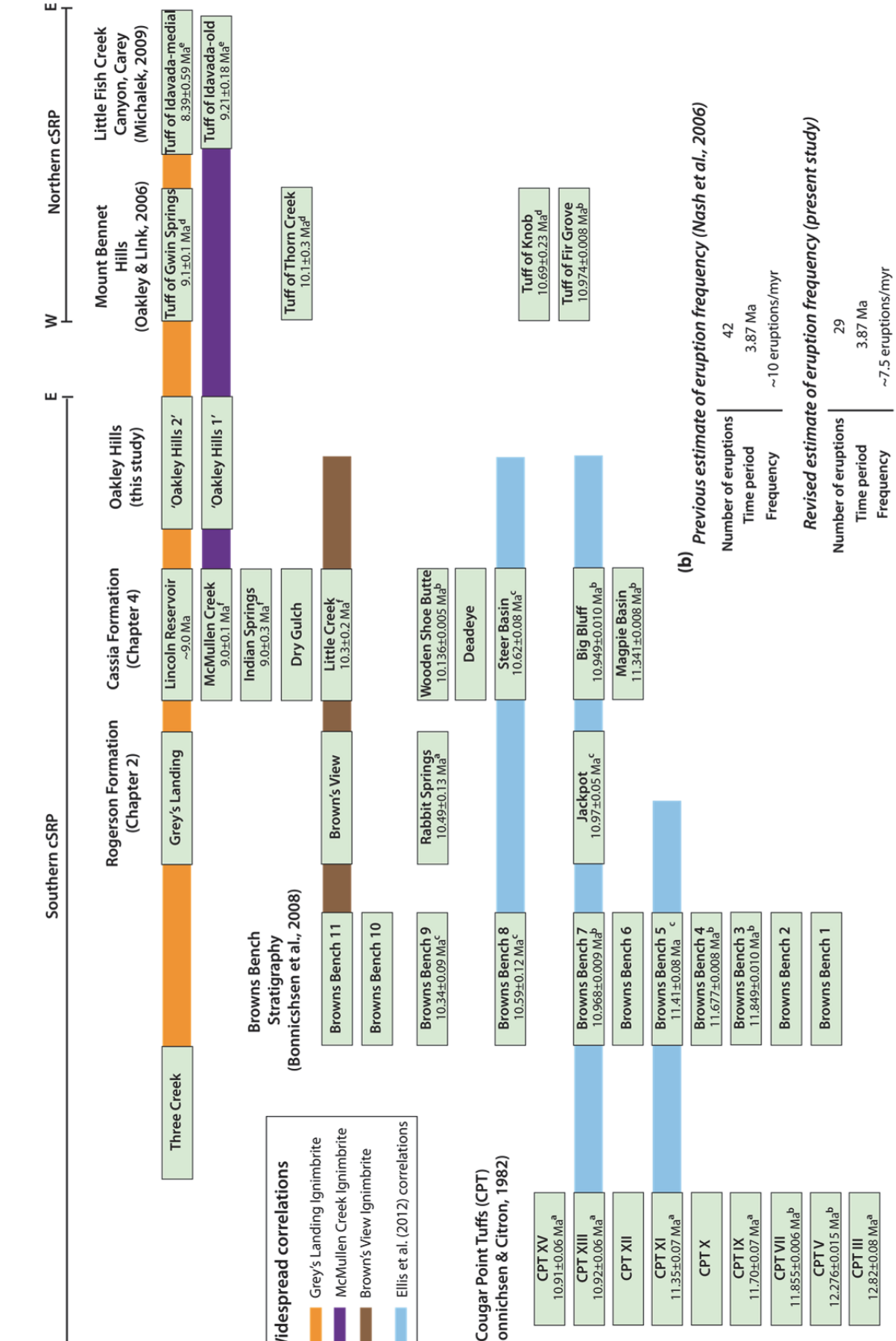

Figure 6.17. (a) Correlation panel showing all known rhyolitic ignimbrites from the central Snake River Plain (cSRP) and the widespread correlations of the Grey's Landing, McMullen Creek, and Brown's View Ignimbrites. These correlations along with those proposed by Ellis et al. (2012a) reduce the total number of eruption-units from 40 to 29. Age determinations: [a]^{40}Ar/^{39}Ar , Bonnichsen et al., 2008; [b]^{40}Ar/^{39}Ar, Reichow, unpublished; [c]^{40}Ar/^{39}Ar, Ellis et al., 2012a; [d]^{40}Ar/^{39}Ar, Oakley & Link, 2006; [e]^{40}Ar/^{39}Ar, Michalek, 2009; [f]U/Pb zircon, present study. (b) Table showing a comparison between the previous estimate of eruption frequency in the cSRP, and the revised estimate after considering all proposed correlations.

geochronology data are required to further constrain the occurrence of cSRP super-eruptions. In addition, the record of super-eruptions within the cSRP is still incomplete as many other eruption-units are recorded, and other potential correlatives are proposed (e.g., The Steer Basin Tuff and Cougar Point Tuff XV, Ellis et al., 2012a) that are yet to be confirmed.

6.8. Conclusions

The three correlations proposed in this chapter serve to further refine the regional mid-Miocene rhyolitic volcanic stratigraphy in the central Snake River Plain, and reduces the total number of known eruptions from ~42 (Nash et al., 2006) to 29. To summarise, the present study highlights the following five conclusions:

(1) Despite their broad similarities, correlation between SR-type ignimbrites in the cSRP is possible by combining multiple techniques including; detailed physical field characterisation, whole-rock and mineral chemistry, and palaeomagnetic and geochronology data.

(2) Robust correlations have been established that propose the existence of three newly defined widespread ignimbrite sheets. These are the Brown's View Ignimbrite (81 km^3), the McMullen Creek Ignimbrite (1179 km^3), and the Grey's Landing Ignimbrite (1416 km^3).

(3) The Brown's View Ignimbrite defines a regionally important stratigraphic marker in the southern cSRP, due to its unique high-Mg pyroxenes, and is also the first record of the disappearance of sanidine as a phenocryst phase.

(4) The McMullen Creek and Grey's Landing ignimbrites are the first correlations to be extended across the cSRP to the north. In addition, they record the largest super-eruptions in the cSRP, and are among the largest super-eruptions of the entire Yellowstone –Snake River volcanic province.

(5) The identification of McMullen Creek and Grey's Landing ignimbrites increases the number of super-eruptions, recorded in the cSRP, from one to three. Therefore a preliminary estimate of super eruption frequency in the cSRP is one super-eruption every 700–800 ka.

7. Summary and future research

The central Snake River (cSRP) ignimbrite 'flare up' (Nash et al., 2006; Bonnichsen et al., 2008) was thought to mark an increase in Yellowstone hot-spot volcanic activity during the mid-Miocene, between ~12–8 Ma. The frequency of large explosive eruptions during this period was estimated to be 10–20 eruptions/Ma (Nash et al., 2006), which is significantly higher than the estimated eruption frequency at the Yellowstone volcanic field (1–2 eruption/Ma). The larger frequency estimate was based on the total number of ignimbrite eruption-units (~42), identified within localised successions in the cSRP, and averaged over the ~4 million year period (Nash et al., 2006). However, by combining detailed fieldwork with whole-rock and mineral chemistry, palaeomagnetic data, and geochronology data the present study has revealed that silicic eruptions from the cSRP were less numerous than previously thought. In the Rogerson Graben the revised Rogerson Formation (Chapter 3) comprises five eruption-units, which is two less than previous interpretations (Andrews et al., 2008). However, in the Cassia Mountains ~20 km further east the revised Cassia Formation (Chapter 4) comprises 13 eruption-units, five more than previously recognised (Williams et al., 1990; Ellis et al., 2010). The revisions made to both of these localised successions were achieved only by using all the above analytical methods in combination. Individual eruption-units were identified and characterised based on the combined evidence of unique vertical welding profiles (e.g., the McMullen Creek ignimbrite, Chapter 4.14), distinct whole-rock chemical fields (in particular those defined by Zr/Y and Th/Nb ratios), unique mineral compositional modes (particularly MgO concentration in pyroxenes), distinguishable palaeomagnetic mean flow directions, and new and published $^{40}Ar/^{39}Ar$ age determinations combined with U-Pb zircon ages. By characterising and 'finger-printing' individual ignimbrites in this way, comparisons between ignimbrites of the Rogerson and Cassia Formations and other localised ignimbrites in the southern cSRP have been made in order to establish regionally widespread correlations. In addition, comparisons to ignimbrites described across the cSRP to the north (Reichow, unpublished data) has allowed the identification of three new widespread outflow ignimbrite sheets. These are designated as: (1) the Brown's View Ignimbrite (10.3±0.2 Ma; 2700 km^2; 40 km^3 DRE); (2) the McMullen Creek Ignimbrite (9.0 ±0.1 Ma; 12,000 km^2; 589 km^3 DRE); and (3) the Grey's Landing Ignimbrite (~9.0 Ma; 18,000 km^2; 708 km^3 DRE). A new deep-drill hole near Kimberly, Idaho also has revealed three rhyolitic eruption-units: the stratigraphically oldest and

thickest (1.3 km-thick) of these, here named Kimberly Rhyolite 1, is inferred to be an intra-caldera ignimbrite (Chapter 5). Its recognition supports the idea that the large Snake River ignimbrite eruptions were caldera-forming, and that a significant proportion of the total erupted volume for any one cSRP ignimbrite may reside within the caldera, which are concealed under younger basalt lavas. This also is consistent with the very thick ignimbrites reported from INEL-1 borehole (Dohety et al., 1979), the only other borehole in the Snake River Plain sufficiently deep to penetrate the proximal ignimbrite succession. This underscores that the usual practice of considering a caldera-fill component in eruption volume and magnitude estimates is reasonable in the Snake River Plain as it is on other volcanic fields. On this basis, estimates of the volumes of the Brown's View, McMullen Creek and Grey's Landing ignimbrite eruptions (including a caldera fill) are 81 km^3, 1179 km^3, and 1416 km^3, respectively. Using standard techniques to calculate eruption magnitude the McMullen Creek (magnitude–8.4), and Grey's Landing (magnitude–8.5) eruptions were the largest super-eruptions within the cSRP, which are also among the largest of the entire Yellowstone–Snake River volcanic province. In addition, the identification of these three widespread ignimbrite sheets, alongside the Cougar Point Tuff XI, Cougar Point Tuff XIII, and the Steer Basin Tuff described recently (Ellis et al., 2012a), has effectively reduced the total number of known large explosive eruptions in the cSRP from 42 (Nash et al., 2006; Bonnichsen et al., 2008) to 29. Therefore, mid-Miocene rhyolitic explosive eruptions in the Snake River Plain were less numerous, but significantly larger in magnitude than was previously thought.

These findings provide a significant advance in our understanding of the regional stratigraphy of the cSRP, and in the scale of the silicic volcanism that it records. The present study also offers several opportunities for further research. In particular, several other localised rhyolitic eruption-units have yet to be correlated across the cSRP. Correlations between the Steer Basin Tuff and Cougar Point Tuff XV in the southern cSRP, and between Cougar Point Tuff XI in the south and the Tuff of Fir Grove in the north have been proposed (Ellis et al., 2012a) and it seems likely that the application of the multi-technique approach to correlating, as described in the present study, may serve to identify additional records or super-eruptions in the cSRP. In addition, more high-precision geochronology data are required, not only to support potential correlations but also to gain a better understanding of the frequency of large explosive silicic eruptions in the cSRP. Work is in progress (Reichow, unpublished) on obtaining high-precision U-Pb ages by utilising TIMS analysis of zircons, which is particularly useful for the younger

(~10–8 Ma) ignimbrites because these do not contain sanidine, which is required for the highest-precision $^{40}Ar/^{39}Ar$ geochronology. The recognition of further widespread ignimbrite sheets by such correlation combined with geochronology data would further resolve the cSRP regional stratigraphy, as well as provide much better constraints on eruption volumes, the volcanic history, and the petrogenetic evolution of the province. Although the mixing model outlined in Chapter 4 can account for most of the time-progressive trends towards less-evolved whole-rock compositions, the deviation of some eruption-units from extrapolated mixing lines (e.g., Fig. 4.30 a–d) highlights the simplicity and limitations of the model. Considering the role of replenishment, tapping, and fractionation (RTF) processes (of O'Hara & Matthews, 1981) in the evolution of voluminous rhyolitic magmatism in the cSRP may refine and develop our understanding of the petrogenesis.

From a physical volcanological standpoint, some of the correlations (e.g., the Brown's View and McMullen Creek ignimbrites) presented here have been supported by the presence of distinctive angular black, vitric lapilli within several of the correlated ignimbrites. The origin of these enigmatic vitric fragments may be revealed by LA-ICP-MS analysis of trace elements from the matrix glass and the lapilli: similar compositions of the matrix glass and vitric lapilli within a single ignimbrite may indicate that both are juvenile, whereas differences in trace-element signatures may indicate that the vitric lapilli are an accidental component entrained from conduits or substrate during the eruptions. Either way, further the understanding of these vitric lapilli may serve to facilitate additional correlations and also develop our understanding of Snake-River (SR)-type volcanism (Branney et al., 2008).

Finally, a future goal is to understand the overall magmatic mass flux and thermal flux in the Snake River Plain-Yellowstone volcanic province, and how these changed with time as the site of rhyolitic volcanism migrated eastwards. Together with a better understanding of the frequency of super-eruptions, this would represent a significant improvement in our appreciation of the workings and significance of large-scale intra-plate silicic volcanism.

Appendix A

Sample List

Unit	Sample Number	Lithology	Locality	Grid Reference
Cassia Formation				
Lincoln Reservoir Member	MCM3-12.1-001	upper vitrophyre	Rock Creek	N42°20'34.3'' / W114°17'00.9''
	RC-10.1-007	top vitrophyre	Rock Creek	N42°20' 36.0'' / W114°16' 56.0''
	UTC-12.2-001	upper lithoidal	Trapper Creek	N42°10'45.8'' / W113°58'35.0''
	DG-11.1-002	vitrophyre	Dry Gulch quarry	N42°24'59.6'' / W114°19'18.0''
	RC-10.1-008	basal vitrophyre	Rock Creek	N42°20'32.0'' / W114°16'59.4''
	RC-11.1-003	basal vitrophyre	Rock Creek	N42°20'32.0'' / W114°16'59.4''
	MCM3-12.1-002	basal vitrophyre	Rock Creek	N42°20'31.8'' / W114°16'58.6''
	ERC-12.1-004	basal vitrophyre	Rams Horn Ridge	N42°22'29.9'' / W114°10'38.4''
	TC-12.1-012	basal vitrophyre	North Trapper Creek	N42°10'44.3'' / W113°57'50.0''
	GC-12.2-005	basal vitrophyre	Goose Creek basin	N42°04'36.7'' / W113°55'37.0''
	GC-12.2-009	basal vitrophyre	Goose Creek basin	N42°01'42.1'' / W113°58'40.9''
McMullen Creek Member	BCW-12.2-006	upper orange ash	Big Cottonwood Creek	N42°16'59.0'' / W114°01'22.2''
	TC-12.1-005	upper orange ash	South Trapper Creek	N42°10'04.1'' / W114°00'15.9''
	BCW-12.2-005	upper vitrophyre	Big Cottonwood Creek	N42°16'59.0'' / W114°01'22.2''
	HG-11.2-001	upper vitrophyre	Hoppers Gulch road	N42°19'25.0'' / W114°29'07.9''
	RC-10.1-009	upper lithoidal	Rock Creek	N42°20'30.3'' / W114°16'56.8''
	DG-11.1-001	basal vitrophyre	Dry Gulch quarry	N42°24'55.0'' / W114°19'17.0''
	CW-11.2-001	basal vitrophyre	Cottonwood Creek	N42°21'08.0'' / W114°25'52.5''
	HG-11.2-002	basal vitrophyre	Hoppers Gulch road	N42°19'21.4'' / W114°29'06.1''
	RC-10.1-005	basal vitrophyre	Rock Creek	N42°20'30.3'' / W114°16'59.3''
	TC-12.1-004	basal vitrophyre	South Trapper Creek	N42°10'00.9'' / W114°00'14.4''
	TC-12.1-011	basal vitrophyre	North Trapper Creek	N42°10'43.0'' / W113°57'48.5''
	GC-12.2-004	basal vitrophyre	Goose Creek basin	N42°04'36.07'' / W113°55'38.7''
	GC-12.2-008	basal vitrophyre	Goose Creek basin	N42°01'42.1'' / W113°58'40.3''
	BCW-12.2-004	basal vitrophyre	Big Cottonwood Creek	N42°16'52.9'' / W114°01'28.3''
	GC-12.2-003	lower grey ash	Goose Creek basin	N42°04'36.07'' / W113°55'38.7''
	GC-12.2-007	lower grey ash	Goose Creek basin	N42°01'42.1'' / W113°58'40.3''
	GC-12.2-010	lower grey ash	Goose Creek basin	N41°57'45.8'' / W114°00'44.9''
Indian Springs Member	Q2-11.1-001	vitrophyre	Quarry 2	N42°23'57.7'' / W114°22'01.0''
	Q2-11.1-002	vitrophyre	Quarry 2	N42°23'54.4'' / W114°22'04.7''
	DG-11.1-003	vitrophyre	Dry Gulch quarry	N42°24'56.9'' / W114°19'37.6''
	RC-10.1-010	vitrophyre	Rock Creek	N42°20'39.8'' / W114°17'15.6''
	RC-10.2-001	vitrophyre	Rock Creek	N42°20'39.8'' / W114°17'15.6''
	CW-11.2-002	vitrophyre	Cottonwood Creek	N42°21'02.5'' / W114°25'54.9''
	HG-11.2-003	vitrophyre	Hoppers Gulch road	N42°19'26.3'' / W114°29'11.8''
	IS-11.1-001	basal vitrophyre	Indian Springs road	N42°23'53.6'' / W114°20'35.8''
	RC-10.2-002	fused tuff	Rock Creek	N42°20'39.8'' / W114°17'15.6''
Dry Gulch Member	DG-11.1-004	upper vitrophyre	Dry Gulch quarry	N42°24'56.9'' / W114°19'37.6''
	Q2-11.1-003	upper vitrophyre	Quarry 2	N42°23'53.8'' / W114°22'03.7''
	CW-11.2-003	purple lithoidal	Cottonwood Creek	N42°21'12.1'' / W114°25'59.7''
	HG-11.2-004	purple lithoidal	Hoppers Gulch road	N42°19'15.5'' / W114°29'03.1''
	NRC-11.2-001	purple lithoidal	North Rock Creek	N42°23'50.7'' / W114°17'42.3''
	NRC-11.2-003	purple lithoidal	North Rock Creek	N42°24'03.4'' / W114°17'48.0''
	SIS-12.1-004	purple lithoidal	Indian Springs road	N42°21'25.7'' / W114°21'45.1''
	Q2-11.1-004	purple lithoidal	Quarry 2	N42°23'53.0'' / W114°22'06.4''
Little Creek Member	UWS-12.1-002	upper vitrophyre	Rock Creek	N42°20'26.1'' / W114°16'59.0''
	RC-11.1-002	upper vitrophyre	Rock Creek	N42°20'23.6'' / W114°16'48.9''
	ERC-12.1-002	vitrophyre	Rams Horn Ridge	N42°22'30.1'' / W114°10'44.4''
	NRC-11.2-002	basal vitrophyre	North Rock Creek	N42°23'49.0'' / W114°17'48.2''
	RC-11.1-001	basal vitrophyre	Rock Creek	N42°20'22.5'' / W114°16'48.9''
	RC-11.1-004	basal vitrophyre	Rock Creek	N42°20'.24.8'' / W114°16'55.3''
	UWS-12.1-001	basal vitrophyre	Rock Creek	N42°20'25.1'' / W114°16'58.8''
Wooden Shoe Butte Member	RC-11.1-006	upper vitrophyre	South Rock Creek	N42°15'21.0'' / W114°16'24.1''
	TC-12.1-008	upper vitrophyre	North Trapper Creek	N42°10'39.4'' / W113°57'50.6''
	TC-12.1-003	upper vitrophyre	South Trapper Creek	N42°09'58.6'' / W114°00'15.2''
	GC-12.2-006	vitrophyre	Goose Creek basin	N42°01'41.8'' / W113°58'39.6''
	GC-12.2-001	vitrophyre	Goose Creek basin	N42°04'51.1'' / W113°55'43.4''
	RC-10.1-003	hackly plated	Rock Creek	N42°20'18.66'' / W114°16'53.9''
	ERC-12.1-001	basal vitrophyre	Rams Horn Ridge	N42°22'29.5'' / W114°10'46.7''
	RC-11.1-005	basal vitrophyre	South Rock Creek	N42°15'11.9'' / W114°16'01.3''
	RC-10.1-002	basal vitrophyre	Rock Creek	N42°20'17.3'' / W114°16'53.3''
	BCW-12.2-003	basal vitrophyre	Big Cottonwood Creek	N42°16'57.4'' / W114°01'28.3''
	TC-12.1-007	basal vitrophyre	North Trapper Creek	N42°10'39.1'' / W113°57'50.2''
	TC-12.1-002	basal vitrophyre	South Trapper Creek	N42°09'57.4'' / W114°00'13.0''

Unit	Sample Number	Lithology	Locality	Grid Reference
Cassia Formation				
Steer Basin Member	SIS-12.1-001	upper vitrophyre	South Indian springs Road	N42°21'20.8" / W114°22'00.3"
	RC-10.1-001	upper lithoidal	Rock Creek	N42°19'40.8" / W114°16'24.8"
	RC-10.1-004	vitrophyre	Rock Creek	N42°19'40.0" / W114°16'24.9"
	BCW-12.2-001	basal vitrophyre	Big Cottonwood Creek	N42°17'03.5" / W114°01'33.9"
Big Bluff Member	RC-11.1-008	upper vitrophyre	South Rock Creek	N42°15'06.5" / W114°15'55.0"
	RC-10.1-011	vitrophyre	Rock Creek	N42°18'39.2" / W114°15'34.0"
Magpie Basin Member	RC-10.2-005	top perl. vitrophyre	South Rock Creek	N42°15'01.7" / W114°15'49.8"
	RC-10.2-004	basal perl. vitrophyre	South Rock Creek	N42°15'01.7" / W114°15'49.2"
	RC-10.2-006	fused tuff	South Rock Creek	N42°15'01.7" / W114°15'49.8"
Rogerson Formation				
Greys Landing Member	RG-09-001A	top unit	E. of Highway 93	N42°05'12.3" / W114°39'12.3"
	RG-09-001B	top unit	E. of Highway 93	N42°05'12.3" / W114°39'12.3"
	GL-12.2-002	upper lithoidal	Backwaters Rec. Site	N42°03'40.9" / W114°44'32.0"
	GL-12.2-004	upper lithoidal	Greys Landing Rec. Site	N42°07'57.7" / W114°43'43.1"
	BU-11.1-001	vitrophyre	E. of Highway 93	N42°05'13.5" / W114°39'11.6"
	GL-12.2-001	basal vitrophyre	Backwaters Rec. Site	N42°03'40.4" / W114°44'32.6"
	GL-12.2-003	basal vitrophyre	Greys Landing Rec. Site	N42°07'57.7" / W114°43'43.1"
Browns View Member	RG-09-010	upper vitrophyre	Backwaters Rec. site	N42°03'34.1" / W114°44'34.2"
	RG-12.1-004	upper vitrophyre	Backwaters Rec. site	N42°03'34.1" / W114°44'34.2"
	SSp-11.1-001	upper vitrophyre	E. of Highway 93	N42°05'09.4" / W114°39'11.1"
	GL-12.1-001	vitrophyre	E. of Highway 93	N42°05'04.5" / W114°39'26.9"
	RG-09-002	central lapilli-tuff	E. of Highway 93	N42°05'09.4" / W114°39'11.1"
	RG-09-003	central lapilli-tuff	E. of Highway 93	N42°05'09.4" / W114°39'11.1"
	SSp-11.1-002	central lapilli-tuff	E. of Highway 93	N42°05'09.4" / W114°39'11.1"
	RG-09-011	basal vitrophyre	Backwaters Rec. site	N42°03'33.8" / W114°44'34.2"
	RG-12.1-003	basal vitrophyre	Backwaters Rec. site	N42°03'33.8" / W114°44'34.2"
Rabbit Springs Member	RG-09-012	upper vitrophyre	Backwaters Rec. site	N42°03'30.7" / W114°44'44.1"
	RG-12.1-002	upper vitrophyre	Backwaters Rec. site	N42°03'31.5" / W114°44'50.8"
	RG-12.1-001	basal vitrophyre	Backwaters Rec. site	N42°03'30.4" / W114°44'51.5"
	RG-09-013	basal vitrophyre	Backwaters Rec. site	N42°03'29.5" / W114°44'44.0"
	RS-12.1-001	basal vitrophyre	E. of Highway 93	N42°05'01.2" / W114°39'25.1"
	RG-10.1-005	xstal rich vitroph.	Backwaters Rec. site	N42°03'23.8' / W114°45'23.3"
Jackpot Member	JP-10.1-005	upper vitrophyre	Sweetwater Lane	N41°57'19.4" / W114°40'37.8"
	JP-10.1-001	massive	Salmon Falls Creek rest area	N41°56'34.9" / W114°41'19.1"
	RG-10.2-002	lithoidal	Backwaters Rec. Site	N42°03'27.0" / W114°44'47.2"
	JP-10.1-002	hackly plated	Salmon Falls Creek rest area	N41°56'34.9" / W114°41'19.1"
	JP-10.1-003	hackly plated	Salmon Falls Creek rest area	N41°56'34.9" / W114°41'19.1"
	JP-10.1-004	massive	Salmon Falls Creek rest area	N41°56'34.9" / W114°41'19.1"
Additional eruption-units				
Browns Bench 11'	SWC-12.2-006	upper lithoidal	W. Browns Bench massif	N42°09'44.4" / W114°56'46.8"
	SWC-12.2-002	vitrophyre w/chips	W. Browns Bench massif	N42°09'17.7" / W114°56'43.3"
	RG-10.2-003	vitrophyre	Browns Bench massif	N42°08'17.0" / W114°48'38.0"
	NBB-11.2-002	vitrophyre	Browns Bench massif	N42°09'43.6" / W114°50'34.5"
	UBB-12.1-001	vitrophyre	Browns Bench massif	N42°08'17.3" / W114°48'32.6"
	UBB-12.1-002	vitrophyre	Browns Bench massif	N42°08'16.3" / W114°48'40.2"
	SWC-12.2-001	basal vitrophyre	W. Browns Bench massif	N42°09'17.7" / W114°56'43.3"
	SWC-12.2-005	basal vitrophyre	W. Browns Bench massif	N42°09'45.5" / W114°56'43.3"
'Oakley Hills 1'	OH-12.1-001	lower lithoidal	Oakley Hills	N42°16'49.0" / W113°50'20.5"
'Oakley Hills 2'	OH-12.1-003	upper lithoidal	Oakley Hills	N42°16'50.8" / W113°50'15.8"
	OH-12.1-002	basal vitrophyre	Oakley Hills	N42°16'50.1" / W113°50'18.1"
Three Creek ignimbrite	3C-10.2-002	lithoidal	Three Creek Road	N42°04'20.5" / W115°09'47.9"
	3C-10.2-001	basal vitrophyre	Three Creek Road	N42°04'20.5" / W115°09'47.9"
Shoshone Falls Rhyolite	SHO-12.2-001	lithoidal	Snake River canyon	N42°35'20.3" / W114°21'41.0"

Unit	Sample Number	Lithology	Depth in bore-hole (m)	Grid Reference
Kimberly Rhyolite 1	A2-2102-2106	upper vitrophyre	640.7 - 641.9	N42°32'56.9" / W114°22'30.1"
	A2-6400-6411	lower lithoidal	1950.7 - 1954.1	N42°32'56.9" / W114°22'30.1"
Kimberly Rhyolite 2	A2-1419-1424	upper vitrophyre	432.5 - 434.0	N42°32'56.9" / W114°22'30.1"
	A2-1945-1953.2	basal vitrophyre	592.8 - 595.3	N42°32'56.9" / W114°22'30.1"
Kimberly Rhyolite 3	A2-751.6-754	basal vitrophyre	229.1 - 229.8	N42°32'56.9" / W114°22'30.1"

Appendix B
Analytical Methods

B.1. X-ray fluorescence (XRF) spectroscopy

Individual samples were prepared for X-ray fluorescence (XRF) spectroscopy analysis in the same manner at the University of Leicester, UK.

B.1.1. Sample preparation and analysis.

Samples were split by hand into 3–5 cm fragments and weathered surfaces were removed. These fragments were then placed in a fly-press and crushed by hand to gravel-sized (1–2 mm) chips. These chips were then prepared for analysis in an agate planetary mill set at 280 RPM for 15 minutes in order to achieve a fine powder.

For major element analysis ~5g of fine powder was placed in ceramic crucibles oven dried overnight at 110°C. Powders were then weighed and subsequently ignited at 950°C for 2 hours. After cooling, ignited powders were then reweighed and loss on ignition (LOI) determined by the following formula.

$$\mathrm{LOI} = \frac{100 * [(\mathrm{crucible} + \mathrm{sample})_{before} - (\mathrm{crucible} + \mathrm{sample})_{after}]}{(\mathrm{crucible} + \mathrm{sample})_{after}}$$

Fusion beads (glass discs) were then prepared for major element analysis by combining 0.6 g of ignited powder with 3g of flux (20% lithium tetraborate and 80 % lithium metaborate). The sample-flux mixture was then heated to ~1200°C for about 10 min on a Spartan gas burner, in order to melt and homogenise the mixture. The molten sample/flux mixture was poured into a Pt/Al casting plate, rapidly air cooled, before being tapped out and labelled.

For trace element analysis 7 g of non-ignited fine powder was combined with Mowiol 88 adhesive fluid and pressed into pellets at 10 tonnes per square inch.

Both major (wt.%) and trace (ppm) element data were determined on a PANalytical PW4400 Axios XRF spectrometer at the University of Leicester.

B.1.1. Reference material.

A variety of international reference materials were analysed with each batch of samples, in order to assess the precision of the XRF data. These are listed in Table B.1 (major) and B.2 (traces).

Table B.1. Major element (wt.%) results for international reference materials.

Batch ID	Reference Material	SiO_2 (wt%)	TiO_2 (wt%)	Al_2O_3 (wt%)	Fe_2O_3 (wt%)	MnO (wt%)	MgO (wt%)	Na_2O (wt%)	K_2O (wt%)	P_2O5 (wt%)	SO_3 (wt%)
AFUS401	BH-1	68.84	0.41	14.38	5.72	0.13	2.65	3.69	0.90	0.06	0.01
AFUS406	BH-1	68.74	0.41	14.43	5.72	0.13	2.67	3.72	0.91	0.07	0.07
AFUS407	BH-1	68.62	0.41	14.48	5.72	0.13	2.70	3.76	0.91	0.08	0.14
AFUS410	BH-1	68.70	0.42	14.29	5.84	0.13	2.72	3.82	0.93	0.07	0.10
AFUS414	BH-1	68.44	0.41	14.43	5.73	0.13	2.65	3.73	0.93	0.07	0.08
AFUS416	BH-1	69.46	0.41	14.57	5.76	0.13	2.70	3.81	0.92	0.07	0.08
AFUS418	BH-1	69.43	0.41	14.60	5.76	0.13	2.71	3.82	0.91	0.07	0.07
AFUS421	BH-1	69.43	0.41	14.61	5.76	0.13	2.70	3.81	0.92	0.07	0.07
AFUS428	BH-1	68.72	0.40	14.41	5.70	0.13	2.66	3.77	0.91	0.07	0.05
	Average	*68.93*	*0.41*	*14.47*	*5.75*	*0.13*	*2.68*	*3.77*	*0.92*	*0.07*	*0.08*
	StDv	*0.40*	*0.00*	*0.11*	*0.04*	*0.00*	*0.03*	*0.05*	*0.01*	*0.00*	*0.04*
	% StDv	*0.57*	*1.19*	*0.75*	*0.73*	*0.88*	*1.06*	*1.28*	*1.04*	*5.31*	*47.08*
AFUS401	WS-1	51.56	2.51	13.88	13.45	0.18	5.32	2.82	1.32	0.30	0.02
AFUS406	WS-1	51.45	2.50	13.86	13.43	0.18	5.29	2.83	1.31	0.30	0.01
AFUS407	WS-1	51.52	2.51	13.90	13.44	0.18	5.32	2.86	1.32	0.30	0.09
AFUS410	WS-1	51.49	2.57	13.73	13.76	0.18	5.39	2.89	1.35	0.30	0.08
AFUS414	WS-1	51.15	2.50	13.86	13.51	0.18	5.23	2.78	1.34	0.30	0.05
AFUS416	WS-1	51.96	2.53	14.06	13.56	0.18	5.36	2.86	1.33	0.30	0.06
AFUS418	WS-1	51.87	2.52	14.02	13.56	0.18	5.36	2.85	1.33	0.30	0.05
AFUS421	WS-1	51.99	2.52	14.04	13.56	0.18	5.33	2.86	1.34	0.31	0.05
AFUS428	WS-1	51.31	2.50	13.86	13.42	0.18	5.29	2.82	1.32	0.31	0.04
	Average	*51.59*	*2.52*	*13.91*	*13.52*	*0.18*	*5.32*	*2.84*	*1.33*	*0.30*	*0.05*
	StDv	*0.29*	*0.02*	*0.11*	*0.11*	*0.00*	*0.05*	*0.03*	*0.01*	*0.00*	*0.03*
	% StDv	*0.57*	*0.86*	*0.78*	*0.79*	*0.97*	*0.88*	*1.11*	*0.98*	*1.53*	*50.20*
AFUS401	BCS375	67.47	0.38	20.12	0.12	0.01	0.01	10.53	0.75	0.02	0.01
AFUS406	BCS375	67.47	0.38	20.14	0.11	0.01	0.03	10.53	0.75	0.02	0.02
AFUS407	BCS375	67.36	0.38	20.09	0.12	0.01	0.07	10.45	0.77	0.02	0.09
AFUS410	BCS375	67.41	0.39	19.92	0.11	0.01	0.07	10.66	0.78	0.03	0.07
AFUS414	BCS375	67.07	0.37	20.09	0.10	0.00	0.02	10.42	0.77	0.02	0.04
AFUS416	BCS375	68.14	0.38	20.41	0.11	0.01	0.05	10.62	0.76	0.03	0.05
AFUS418	BCS375	68.08	0.38	20.38	0.11	0.01	0.05	10.60	0.76	0.03	0.05
AFUS421	BCS375	68.15	0.38	20.39	0.11	0.01	0.05	10.62	0.76	0.03	0.05
AFUS428	BCS375	67.43	0.38	20.22	0.11	0.00	0.05	10.53	0.76	0.03	0.04
	Average	*67.62*	*0.38*	*20.20*	*0.11*	*0.01*	*0.04*	*10.55*	*0.76*	*0.02*	*0.05*
	StDv	*0.40*	*0.00*	*0.17*	*0.00*	*0.00*	*0.02*	*0.08*	*0.01*	*0.00*	*0.02*
	% StDv	*0.59*	*1.27*	*0.82*	*4.29*	*13.55*	*43.46*	*0.76*	*1.03*	*16.11*	*49.91*
AFUS401	MRG-1	39.57	3.87	8.51	18.06	0.17	13.69	0.72	0.20	0.06	0.15
AFUS406	MRG-1	39.70	3.85	8.56	17.99	0.17	13.58	0.77	0.22	0.06	0.14
AFUS407	MRG-1	39.71	3.87	8.54	18.04	0.17	13.58	0.79	0.21	0.06	0.16
AFUS410	MRG-1	39.64	3.95	8.44	18.50	0.18	13.85	0.78	0.21	0.06	0.16
AFUS414	MRG-1	39.31	3.85	8.47	18.16	0.17	13.52	0.72	0.21	0.05	0.15
AFUS416	MRG-1	39.98	3.91	8.64	18.23	0.17	13.77	0.78	0.20	0.06	0.16
AFUS418	MRG-1	39.91	3.90	8.60	18.22	0.17	13.75	0.78	0.20	0.06	0.16
AFUS421	MRG-1	39.99	3.89	8.60	18.22	0.17	13.78	0.78	0.20	0.06	0.16
AFUS428	MRG-1	39.47	3.85	8.51	18.02	0.17	13.59	0.75	0.20	0.06	0.15
	Average	*39.70*	*3.88*	*8.54*	*18.16*	*0.17*	*13.68*	*0.76*	*0.21*	*0.06*	*0.16*
	StDv	*0.23*	*0.04*	*0.07*	*0.16*	*0.00*	*0.12*	*0.03*	*0.01*	*0.00*	*0.01*
	% StDv	*0.58*	*0.91*	*0.78*	*0.87*	*0.93*	*0.84*	*3.41*	*3.19*	*5.36*	*4.32*
AFUS410	BCS372/1	20.12	0.27	5.22	3.48	0.07	1.39	0.11	0.76	0.08	2.83
AFUS416	BCS372/1	20.32	0.27	5.36	3.43	0.07	1.38	0.11	0.75	0.08	2.82
AFUS418	BCS372/1	20.30	0.27	5.36	3.43	0.07	1.38	0.11	0.75	0.08	2.85
AFUS421	BCS372/1	20.37	0.27	5.35	3.43	0.07	1.38	0.11	0.75	0.08	2.87
AFUS428	BCS372/1	20.18	0.26	5.29	3.40	0.07	1.36	0.11	0.74	0.08	2.77
	Average	*20.26*	*0.27*	*5.32*	*3.44*	*0.07*	*1.38*	*0.11*	*0.75*	*0.08*	*2.83*
	StDv	*0.10*	*0.00*	*0.06*	*0.03*	*0.00*	*0.01*	*0.00*	*0.01*	*0.00*	*0.04*
	% StDv	*0.52*	*1.52*	*1.14*	*0.85*	*1.76*	*1.02*	*2.10*	*0.82*	*0.68*	*1.29*

Table B.2. Trace element (ppm) results for international reference materials.

Batch ID	Reference Material	Ga (ppm)	Zn (ppm)	Cu (ppm)	Ni (ppm)	Cr (ppm)	V (ppm)	Sc (ppm)	Ba (ppm)	La (ppm)	Ce (ppm)	Nd (ppm)	Rb (ppm)	Sr (ppm)	Y (ppm)	Zr (ppm)	Nb (ppm)	Th (ppm)
AXRHT495	NIM-G	28.0	53.9	21.8	7.1	11.4	0.3	1.4	110.9	111.1	204.9	79.0	318.4	12.6	144.1	285.4	55.7	51.7
AXRHT504	NIM-G	27.8	53.0	22.6	6.7	12.2	1.7	0.3	99.9	110.1	205.1	77.2	318.8	13.1	144.6	285.4	55.8	51.4
AXRHT514	NIM-G	27.5	51.6	16.7	6.8	12.3	2.8	0.3	103.1	110.5	207.1	77.3	319.1	13.3	144.2	284.1	55.6	51.0
AXRHT517	NIM-G	27.7	52.3	16.3	6.4	13.8	0.1	0.9	107.0	111.6	204.7	77.0	319.3	13.0	143.8	284.3	55.8	51.2
AXRHT523	NIM-G	28.0	54.1	16.2	7.0	11.0	0.4	1.0	105.1	109.2	204.0	78.2	318.4	13.1	144.0	283.7	55.5	51.3
AXRHT526	NIM-G	27.2	53.3	16.1	6.8	13.7	-0.4	1.1	103.2	110.1	201.4	75.9	319.0	13.3	144.1	284.0	55.6	50.6
AXRHT529	NIM-G	27.9	54.4	16.8	7.5	14.3	1.5	1.2	109.3	111.7	203.9	77.4	318.4	13.6	144.0	284.8	55.5	51.9
AXRHT549	NIM-G	27.0	54.3	16.8	6.7	14.1	0.7	2.2	105.3	108.6	205.0	77.2	319.1	13.4	144.1	283.7	55.4	52.0
AXRHT552	NIM-G	28.2	53.4	16.7	6.3	13.2	1.0	-0.1	107.3	109.7	202.9	78.8	318.3	13.8	144.0	283.8	55.3	51.9
	Average	*27.72*	*53.37*	*17.80*	*6.80*	*12.88*	*0.90*	*0.94*	*105.69*	*110.29*	*204.32*	*77.56*	*318.75*	*13.24*	*144.10*	*284.36*	*55.57*	*51.43*
	StDv	*0.39*	*0.94*	*2.53*	*0.36*	*1.19*	*0.97*	*0.70*	*3.38*	*1.03*	*1.59*	*0.97*	*0.37*	*0.37*	*0.23*	*0.69*	*0.15*	*0.46*
	% StDv	*1.41*	*1.77*	*14.24*	*5.31*	*9.27*	*107.73*	*74.62*	*3.20*	*0.94*	*0.78*	*1.25*	*0.12*	*2.77*	*0.16*	*0.24*	*0.27*	*0.90*
AXRHT495	MRG-1	17.6	215.9	145.3	195.0	462.3	550.1	58.2	51.7	7.6	31.3	19.8	8.4	274.0	14.7	111.6	21.2	0.9
AXRHT504	MRG-1	17.9	213.9	143.9	195.6	455.6	547.7	56.8	50.5	8.6	34.3	18.5	8.5	273.2	14.7	112.1	21.5	0.3
AXRHT514	MRG-1	17.3	209.4	140.3	196.5	462.7	550.0	57.9	51.9	9.3	30.6	19.0	9.1	274.0	14.3	111.7	21.6	0.6
AXRHT517	MRG-1	17.7	214.9	139.3	196.1	461.8	549.5	58.0	51.5	6.7	33.2	20.5	8.9	274.9	14.3	112.3	21.5	-0.1
AXRHT523	MRG-1	17.9	216.4	138.6	196.8	463.0	549.5	57.4	51.9	8.6	34.6	18.2	8.7	274.1	14.3	111.7	21.5	0.6
AXRHT526	MRG-1	17.9	216.3	138.7	196.3	460.4	548.4	57.7	54.7	9.1	32.8	18.7	8.9	273.1	14.3	111.8	21.4	1.2
AXRHT529	MRG-1	18.5	215.2	139.4	196.5	457.3	548.9	57.3	51.5	9.8	32.7	15.1	8.8	274.4	14.3	112.2	21.2	0.5
AXRHT549	MRG-1	18.7	219.6	139.3	196.4	458.0	550.2	56.8	54.1	7.0	27.2	15.9	8.8	274.0	14.2	111.7	21.3	0.7
AXRHT552	MRG-1	17.7	218.6	139.9	195.3	425.9	534.9	52.7	49.6	6.8	28.9	16.2	8.5	273.7	14.1	112.2	21.8	0.3
	Average	*17.91*	*215.60*	*140.52*	*196.06*	*456.32*	*547.70*	*56.98*	*51.94*	*8.17*	*31.73*	*17.99*	*8.73*	*273.93*	*14.36*	*111.94*	*21.45*	*0.54*
	StDv	*0.44*	*2.92*	*2.39*	*0.60*	*11.72*	*4.87*	*1.69*	*1.59*	*1.14*	*2.47*	*1.86*	*0.22*	*0.55*	*0.21*	*0.27*	*0.19*	*0.37*
	% StDv	*2.44*	*1.35*	*1.70*	*0.31*	*2.57*	*0.89*	*2.96*	*3.06*	*13.98*	*7.80*	*10.36*	*2.51*	*0.20*	*1.44*	*0.24*	*0.90*	*68.18*
AXRHT495	BE-N	16.3	116.1	82.8	273.7	338.9	233.5	27.3	1109.9	82.1	154.9	67.7	44.8	1373.8	29.7	267.4	112.7	10.42
AXRHT504	BE-N	17.2	117.9	79.2	273.5	346.4	233.6	25.3	1120.9	83.4	149.6	64.3	44.5	1374.9	29.9	268.7	112.9	10.43
AXRHT514	BE-N	17.0	115.5	75.8	275.3	339.8	231.4	25.9	1102.1	81.8	152.4	66.8	44.6	1376.3	29.8	269.8	112.9	10.38
AXRHT517	BE-N	16.8	115.9	77.7	276.2	340.0	234.5	26.4	1121.9	79.7	152.8	68.5	44.6	1375.7	29.9	268.7	112.6	10.41
AXRHT523	BE-N	16.7	118.3	77.6	274.0	339.8	233.3	25.5	1112.9	79.3	152.3	65.4	44.1	1375.0	30.1	268.1	112.8	10.44
AXRHT526	BE-N	17.1	119.2	77.0	274.8	340.4	231.9	27.4	1110.8	83.7	158.2	70.1	44.5	1375.7	29.9	268.1	113.3	10.38
AXRHT529	BE-N	15.9	117.6	78.0	272.5	340.9	233.3	25.1	1118.6	80.6	152.6	66.5	44.4	1376.0	29.8	268.8	112.6	10.40
AXRHT549	BE-N	17.7	119.8	77.7	275.4	340.9	232.8	26.1	1122.5	81.3	149.9	65.3	44.2	1375.7	29.8	267.7	113.1	10.39
AXRHT552	BE-N	16.7	117.7	77.1	276.1	345.2	244.9	24.8	1161.8	85.3	159.3	68.0	44.5	1376.7	29.6	268.4	112.9	10.40
	Average	*16.82*	*117.56*	*78.09*	*274.62*	*341.37*	*234.35*	*25.98*	*1120.15*	*81.91*	*153.55*	*66.97*	*44.47*	*1375.54*	*29.83*	*268.42*	*112.87*	*10.41*
	StDv	*0.51*	*1.46*	*1.98*	*1.26*	*2.62*	*4.06*	*0.93*	*17.01*	*1.97*	*3.35*	*1.83*	*0.22*	*0.88*	*0.15*	*0.71*	*0.24*	*0.02*
	% StDv	*3.06*	*1.24*	*2.54*	*0.46*	*0.77*	*1.73*	*3.58*	*1.52*	*2.41*	*2.18*	*2.73*	*0.49*	*0.06*	*0.50*	*0.26*	*0.21*	*0.21*
AXRHT495	JR-3	37.3	193.9	11.2	7.4	-1.3	0.5	0.9	52.5	156.7	309.1	103.9	472.5	9.7	174.3	1670.9	572.2	113.6
AXRHT504	JR-3	37.4	192.9	11.3	5.9	-1.2	0.7	0.9	54.8	157.8	308.5	106.0	471.4	10.3	173.9	1673.0	572.8	113.6
AXRHT514	JR-3	37.9	189.9	5.6	5.9	-0.4	1.6	-0.1	58.2	157.5	309.4	104.1	471.6	11.0	174.1	1673.3	573.1	113.6
AXRHT517	JR-3	37.6	190.7	4.9	6.0	-1.6	0.8	1.2	53.2	158.2	310.6	105.1	471.4	10.8	174.3	1672.6	573.1	113.7
AXRHT523	JR-3	37.8	194.3	4.8	6.4	-1.1	2.0	2.0	53.0	157.6	309.1	104.9	471.5	10.5	174.5	1671.9	573.0	113.7
AXRHT526	JR-3	37.3	194.3	4.5	6.9	-1.9	2.0	-0.1	49.5	155.5	310.5	104.1	471.8	10.6	174.2	1672.0	572.8	113.9
AXRHT529	JR-3	37.1	194.1	4.7	6.1	-0.3	0.5	0.4	51.8	157.8	309.2	103.2	472.0	11.0	174.5	1672.6	572.9	113.6
AXRHT549	JR-3	38.4	191.1	4.4	4.9	-1.6	0.4	-0.1	53.7	157.6	309.7	103.9	471.2	10.8	174.4	1671.7	572.9	113.4
AXRHT552	JR-3	37.7	193.5	4.5	6.5	-2.5	1.8	0.7	49.8	158.0	316.4	106.1	471.8	11.0	174.4	1671.9	572.9	113.4
	Average	*37.63*	*192.75*	*6.22*	*6.22*	*-1.32*	*1.14*	*0.65*	*52.93*	*157.40*	*310.27*	*104.59*	*471.67*	*10.63*	*174.29*	*1672.21*	*572.86*	*113.62*
	StDv	*0.40*	*1.71*	*2.88*	*0.71*	*0.69*	*0.66*	*0.70*	*2.64*	*0.83*	*2.38*	*1.02*	*0.39*	*0.43*	*0.20*	*0.73*	*0.28*	*0.16*
	% StDv	*1.06*	*0.89*	*46.33*	*11.48*	*51.97*	*57.93*	*107.97*	*4.98*	*0.53*	*0.77*	*0.97*	*0.08*	*4.01*	*0.11*	*0.04*	*0.05*	*0.14*

B.2. Electron Microprobe Analysis (EMPA)

30 micron thin sections were cut from select samples of each eruption-unit, and these were subsequently polished and carbon-coated prior to EMPA.

Mineral analyses were obtained on the most abundant mineral phases (feldspars, pyroxenes, and Fe-Ti oxides) at the Open University, Milton Keynes using a Cameca SX100 electron microprobe. An operating voltage of 20 kV and probe current of 20 nA (measured on a Faraday cage) with a 10 micron beam diameter were used for quantitative analysis. Data were reduced using the PAP correction routine of Pouchou & Pichoir (1985). Precision of feldspar and pyroxene data (the most abundant mineral phases) were determined by repeat measurements on representative crystals (Table B.3).

Table B.3. Major element (wt.%) data from repeat measurements of representative feldspar and pyroxene crystals.

Mineral	SiO_2 (wt.%)	TiO_2 (wt.%)	Al_2O_3 (wt.%)	Cr2O3 (wt.%)	FeO (wt.%)	MnO (wt.%)	MgO (wt.%)	CaO (wt.%)	Na_2O (wt.%)	K_2O (wt.%)	NiO (wt.%)	Total
Feldspar	57.17	0.04	25.68	0.01	0.38	0.00	0.02	8.33	6.34	0.78	0.01	98.77
Feldspar	57.87	0.03	25.61	0.00	0.37	0.00	0.03	8.30	6.32	0.79	0.02	99.34
Feldspar	57.78	0.04	25.79	0.00	0.33	0.00	0.02	8.25	6.32	0.78	0.01	99.32
Feldspar	57.58	0.00	25.75	0.00	0.35	0.00	0.01	8.48	6.41	0.78	0.00	99.36
Feldspar	58.03	0.04	25.63	0.00	0.37	0.00	0.01	8.22	6.48	0.79	0.00	99.58
Feldspar	57.73	0.05	25.87	0.01	0.45	0.00	0.02	8.22	6.40	0.82	0.00	99.58
Feldspar	57.62	0.04	25.07	0.00	0.39	0.00	0.03	7.56	6.68	0.93	0.01	98.33
Feldspar	58.03	0.04	25.10	0.00	0.38	0.01	0.03	7.45	6.53	0.94	0.00	98.52
Feldspar	57.95	0.02	25.18	0.00	0.37	0.00	0.02	7.63	6.64	0.92	0.04	98.77
Feldspar	56.94	0.04	26.00	0.00	0.42	0.00	0.01	8.46	6.28	0.73	0.02	98.91
ave.	*57.67*	*0.04*	*25.57*	*0.00*	*0.38*	*0.00*	*0.02*	*8.09*	*6.44*	*0.83*	*0.01*	
stdev	*0.36*	*0.02*	*0.33*	*0.00*	*0.03*	*0.00*	*0.01*	*0.39*	*0.14*	*0.08*	*0.01*	
2xstdev	*0.73*	*0.03*	*0.67*	*0.01*	*0.07*	*0.01*	*0.02*	*0.78*	*0.28*	*0.15*	*0.02*	
Pyroxene	49.26	0.39	1.07	0.00	18.83	0.58	10.33	17.26	0.25	0.00	0.00	97.97
Pyroxene	48.95	0.43	1.05	0.00	19.21	0.62	10.29	17.61	0.25	0.00	0.00	98.41
Pyroxene	49.00	0.48	1.06	0.00	18.56	0.59	10.40	17.60	0.29	0.00	0.02	98.00
Pyroxene	49.20	0.42	1.04	0.01	19.24	0.59	10.54	17.01	0.23	0.00	0.00	98.27
Pyroxene	49.33	0.43	1.05	0.00	19.03	0.56	10.46	17.41	0.25	0.00	0.01	98.52
Pyroxene	49.76	0.44	0.94	0.00	19.66	0.64	10.27	17.35	0.24	0.00	0.01	99.32
Pyroxene	50.20	0.36	0.94	0.00	19.04	0.60	10.53	17.56	0.23	0.00	0.00	99.47
ave.	*49.39*	*0.42*	*1.02*	*0.00*	*19.08*	*0.60*	*10.40*	*17.40*	*0.25*	*0.00*	*0.01*	
stdev	*0.45*	*0.04*	*0.06*	*0.00*	*0.35*	*0.03*	*0.11*	*0.22*	*0.02*	*0.00*	*0.01*	
2xstdev	*0.90*	*0.08*	*0.12*	*0.01*	*0.69*	*0.05*	*0.22*	*0.44*	*0.04*	*0.00*	*0.01*	

B.3. Laser Ablation-Inductively Coupled Plasma-Mass Spectrometry (LA-ICP-MS)

Due to the unknown ablation rates for individual mineral phases, 50 micron polished thin sections were cut from four select eruption-units in order to ensure the section was not penetrated during ablation.

Samples were ablated using a NewWave UP-213, 213 nm laser ablation system in imaged aperture mode. Ablated particulate material was analyzed by a Thermo X Series 2 Inductively Coupled Plasma-Mass Spectrometer. Helium was used as the laser cell transport gas (0.22 L min-1), which was blended with argon (0.83 L min-1) prior to entering the plasma. Instrumental parameters are detailed in Table B.4. A total of 31 elements (^{44}Ca, ^{45}Sc, ^{47}Ti, ^{51}V, ^{52}Cr, ^{57}Fe, ^{59}Co, ^{60}Ni, ^{69}Ga, ^{72}Ge, ^{85}Rb, ^{88}Sr, ^{89}Y, ^{90}Zr, ^{133}Cs, ^{137}Ba, ^{139}La, ^{140}Ce, ^{141}Pr, ^{146}Nd, ^{147}Sm, ^{153}Eu, ^{157}Gd, ^{159}Tb, ^{163}Dy, ^{166}Er, ^{172}Yb, ^{175}Lu, ^{208}Pb, ^{232}Th, ^{238}U) were collected, and six USGS micro-analytical glass standards (GSC-1G, GSD-1G, GSE-1G, BHVO-2G, BCR-2G, BIR-1G) were analysed at the beginning and end of each experiment and in between every 30 unknowns, effectively bracketing the unknowns with calibration standards. In addition to calibrating the unknowns using USGS glass standards, two additional internal standard-type calibrations were performed during and after analysis. The first was an instrumental drift/matrix suppression calibration, where a liquid internal standard (2 ppb of thallium standard in

2.0% trace grade HNO3) was used to visualize and correct for instrument drift and matrix suppression. The second calibration used actual major element concentration data measured via electron microprobe close to the laser pits to normalize the LA-ICP-MS concentration data to correct for matrix suppression, topographic effects and variation in laser-sample coupling. This calibration is a modification of the approach of Neff & Dudgeon (2006). CaO (wt.%) in the unknowns was used to apply a sample-specific correction factor to the LA-ICP-MS concentration data.

Table B.4. LA-ICP-MS operating parameters.

Laser Ablation Device	New Wave UP213 Nd:YAG
Wavelength	213 nm
Energy	0.6 mJ
Spot size	40 µm
Pre-ablation	150 µm
Fluence	7.35 J cm^{-2}
Rep rate	5 Hz
Dwell time	30 s
ICP-MS	Thermo X-II Series ICP-QMS
Detector	discrete dynode electron multiplier
RF power	1400 W
Plasma Ar gas flow rate	10.0 l min^{-1}
Auxiliary Ar gas flow rate	0.830 min^{-1}
Sample He gas flow rate	0.219 min^{-1}
Dwell Time per analyte	10.0 ms
Channels	1
Separation	0.02 AMU

B.4. $^{40}Ar/^{39}Ar$ feldspar geochronology

Feldspars were separated for argon geochronology from all rhyolitic units of the Kimberly borehole using standard magnetic separation techniques. These feldspars were then handpicked in order to avoid those with significant alteration and or inclusions that could affect analyses.

Samples and neutron flux monitors (Fish Canyon Sanidine) were placed in aluminium discs and stacked in quartz tubes. The relative positions of wells in the discs were precisely measured for later reconstruction of neutron flux gradients. The sample package was irradiated for 8 hours in the Oregon State University reactor, Cd-shielded facility. Fish Canyon Sanidine (28.172 ± 0.028 (1σ Ma, Rivera et al., 2011) was used to

monitor ^{39}Ar production and establish neutron flux values (J) for the samples. The neutron flux within a given disc is calculated by least-squares fitting of a surface to the J-monitors. Estimated errors in the neutron flux measurements are calculated from the residual deviation from the fitted surface.

Gas was extracted from samples using a mid-infrared CO_2 laser, with samples housed in a ZnS-window laser cell. Individual sample grains were loaded into a steel planchette containing 208 two millimeter diameter wells. Liberated argon was then purified of active gases (e.g., CO_2, H_2O, H_2, N_2, CH_4) using three Zr-Ti-Al getters; one at 25°C and two at 400°C. Data were collected on a GVi instruments ARGUS 5-collector mass spectrometer using a variable sensitivity faraday collector array in static collection (non-peak hopping) mode (Sparks et al., 2008, Mark et al., 2009). Time-intensity data are regressed to t_0 with second-order polynomial fits to the data. Mass discrimination was monitored by comparison to running-average values of an air standard. The average total system blank for laser extractions, measured once for every two unknowns, was 2.5 ± 0.3×10^{-16} mol ^{40}Ar, 2.5 ± 0.4×10^{-17} mol ^{39}Ar, 9.6 ± 2.1×10^{-18} mol ^{36}Ar (1σ over the temperature range where age information is extracted. All data are blank and interference corrected. The mass discrimination correction assumes a value of 298.56 ± 0.31 (1σ) for atmospheric argon (Lee et al., 2006; Mark et al., 2011).

B.5. U/Pb zircon geochronology

Zircons occurring in vitrophyre glass as free crystals, and as inclusions in ferromagnesian minerals were separated from basal vitrophyre of rhyolitic ignimbrites using standard heavy liquid and magnetic separation techniques. The majority of recovered zircons, regardless of size, are euhedral tetragonal dipyramids varying in length between 30 to 200 μm. Rhyolites with smaller quantities of zircon have smaller grains (e.g., Indian Springs Member). Zircon grains were mounted in epoxy along with fragments of the reference zircon GJ-1. U-Pb dating of zircons was performed at the Edinburgh Ion Microprobe Facility (EIMF) using the CAMECA IMS-1270 ion microprobe.

A primary ion beam of ~5 nA 16O2- created a beam diameter of ~25 μm and rastered over 15 μm^2 for two minutes to pre-clean the analysis area. The epoxy sample block was held under a vacuum and the surface was flooded with oxygen in order to double the yield of secondary Pb ions. A single electron multiplier was used in ion-counting mode to measure secondary ion beam intensities. Sputtered 206Pb+ ion yields, calculated from

measurements on reference zircons of known Pb concentration, ranged from 20 - 36 cps/ppm $^{206}Pb+$ /nA primary beam (equivalent to 5 - 9 cps/ppm for an O-beam with no oxygen flooding). The Th/U ratio was determined using ThO/UO ratio measured on the 91500 standard twice each day (fractionation of the ThO/UO ratio from the absolute value was approximately 4-5 %.). The internal reference zircon GJ-1, of known age 609 Ma (Jackson et al., 2004) was used to determine accurate U and Pb ion yields and measured after every 4 unknown analyses. All standards in a single session were averaged (minimum of 7 standards). A linear regression was applied (Kelly et al., 2008) to account for variations in U/Pb ratios, due to changes in instrument conditions. Instrumental mass fractionation was assumed to be 2 per mil per mass unit (based on previous measurements of glass standards). Total analytical time per spot was 27 min, pre sputtering (2 min), automatic centering of secondary ions (1 min), and analysis (24 min). From the GJ-1 standard we obtain an average $^{207}Pb/^{206}Pb$ ratio of 0.05993 ± 0.00011, which corresponds to an age of 604.1 ± 4.1 (2σ; 57 repeats).

Correction for in situ common lead (surface contamination) has been made by measuring the amount of 204Pb present and using a Stacy and Kramers (1975) estimation of terrestrial lead isotopic composition of modern day age. In addition the first 5 cycles during each spot analysis were omitted from any final age determinations. Only ages where common lead corrections were less than 3% were accepted (typically equivalent to >0.3 ppb 204Pb). Corrections for Th/U disequilibria were made assuming mineral to whole rock ratio of 0.11 by assuming a bulk rock Th/U ratio of 4 and using the average zircon Th/U ratio of 0.5. The largest corrections for 206Pb losses due to initial 230Th depletion were less than 1.3% with most being close to 1%.

B.6. Palaeomagnetic analysis.

A total of 10–14 drill-cores (10 cm in length, 2 cm in diameter) were taken from each cSRP eruption-unit in order to determine their palaeomagnetic polarity and their mean palaeomagnetic flow directions. Laboratory work was conducted by D.Finn and R.Coe at the University of California, Santa Cruz. Magnetic remanence measurement and automated progressive AF demagnetization up to 200 mT was performed on a 2G cryogenic magnetometer and Sapphire Instruments demagnetizer using a customized sample handler and software (Morris et al., 2009). Thermal demagnetization was carried out in a custom built oven housed in a magnetically shielded room along with the AF demagnetizer and cryogenic magnetometer. Fisher statistics (Fisher, 1953) and principal

component analysis (Kirschvink, 1980) were used to average individual sample directions and to calculate the best fit lines to demagnetization data, respectively. This enabled the generation of individual palaeomagnetic site mean directions of each eruption-unit sampled. These palaeomagnetic mean flow directions were then plotted as poles onto standard equal-area-projection stereonets, along with error circles considering the variance of all individual samples (e.g., 10–14 cores). In addition, mean palaeomagnetic flow directions, for each eruption-unit, were tilt corrected by measuring the present dip and strike of each unit, and rotating their respective sections back to horizontal (Finn, pers. comm.).

Appendix C

Data Tables

Table C.1. Major (wt.%) and trace element (ppm) data from rhyolitic members of the Rogerson Formation . Major element data is recalculated to 100% anhydrous.

	Grey's Landing Member							Brown's View Member				
Sample No.	RG-09-001A	RG-09-001B	GL-12.2-002	GL-12.2-004	BU-11.1-001	GL-12.2-001	GL-12.2-003	RG-09-010	RG-12.1-004	SSp-11.1-001	GL-12.1-001	RG-09-002
Lithology	upper lithoidal	upper lithoidal	upper lithoidal	upper lithoidal	vitrophyre	basal vitrophyre	basal vitrophyre	upper vitrophyre	upper vitrophyre	upper vitrophyre	vitrophyre	central lapilli-tuff
SiO_2	73.80	74.59	-	72.34	73.85	-	73.85	72.97	-	72.87	71.37	71.67
TiO_2	0.44	0.43	-	0.48	0.45	-	0.42	0.52	-	0.55	0.57	0.65
Al_2O_3	12.42	12.20	-	12.05	12.18	-	12.26	12.42	-	12.46	12.62	12.82
Fe_2O_3	3.68	3.56	-	3.86	3.65	-	3.50	3.38	-	3.53	4.19	4.26
MnO	0.06	0.05	-	0.07	0.06	-	0.06	0.05	-	0.05	0.07	0.08
MgO	0.23	0.14	-	0.27	0.21	-	0.26	0.33	-	0.40	0.37	0.53
CaO	1.22	0.94	-	1.94	1.22	-	1.23	1.29	-	1.46	1.67	1.83
Na_2O	2.90	3.27	-	3.59	3.06	-	2.96	2.60	-	2.44	3.09	2.82
K_2O	5.20	4.72	-	5.28	5.24	-	5.38	6.34	-	6.12	5.93	5.22
P_2O_5	0.06	0.08	-	0.11	0.07	-	0.06	0.09	-	0.11	0.10	0.13
SO_3	0.00	0.01	-	0.00	0.01	-	0.00	0.00	-	0.01	0.00	0.00
*LOI**	*2.51*	*0.45*	-	*0.84*	*2.28*	-	*2.42*	*2.36*	-	*2.25*	*2.40*	*2.25*
*Total**	*100.33*	*100.74*	-	*99.21*	*99.96*	-	*99.17*	*97.12*	-	*99.17*	*98.98*	*100.33*
ASI[a]	*0.99*	*1.01*	-	*0.80*	*0.95*	-	*0.95*	*0.93*	-	*0.95*	*0.87*	*0.95*
Rb	166.8	167.3	171.9	169.7	169.0	168.8	168.5	194.0	190.7	194.0	177.9	184.1
Sr	74.8	91.3	82.2	74.3	76.7	88.8	75.8	62.8	57.0	83.2	89.3	90.7
Y	75.8	76.0	80.8	75.5	75.3	76.6	75.5	59.3	60.1	59.8	67.1	63.5
Zr	670.1	661.1	631.8	648.7	686.0	676.5	693.2	533.6	545.6	583.7	626.3	619.1
Nb	55.0	54.2	55.1	55.2	55.3	54.4	55.3	47.0	47.9	47.3	48.0	47.0
Ba	1255.9	1751.6	1173.9	1253.8	1189.0	1257.1	1158.1	1133.5	1101.3	1257.8	1149.3	1177.2
La	86.7	92.6	84.4	83.5	85.0	88.4	88.0	77.3	79.1	77.1	80.6	81.2
Ga	18.3	17.9	18.9	19.4	19.4	19.2	18.7	17.7	17.4	18.1	20.1	19.0
Ce	172.4	172.1	169.3	164.3	168.6	170.1	164.4	152.9	155.7	151.5	160.5	160.6
Nd	71.8	76.8	73.0	73.0	69.5	72.0	72.9	60.7	60.2	61.4	66.3	65.0
Pb	26.9	25.0	27.0	28.0	25.6	26.1	27.4	23.9	26.0	26.8	25.6	26.6
Th	27.9	26.5	28.7	28.5	27.4	27.4	28.1	31.5	31.6	31.1	29.6	30.7
U	7.5	6.1	6.7	7.0	6.4	5.8	6.2	7.3	7.3	7.4	6.6	6.9
Th/Nb	0.5	0.5	0.5	0.5	0.5	0.5	0.5	0.7	0.7	0.7	0.6	0.7
Zr/Y	8.8	8.7	7.8	8.6	9.1	8.8	9.2	9.0	9.1	9.8	9.3	9.8

*Original total and Loss on Ignition (LOI). [a]ASI = Al/Ca-1.67*Na+K+P.

Table C.1. Major (wt.%) and trace element (ppm) data from rhyolitic members of the Rogerson Formation . Major element data is recalculated to 100% anhydrous. Continued...

	Brown's View Member				Rabbit Springs Member					
Sample No.	RG-09-003	SSp-11.1-002	RG-09-011	RG-12.1-003	RG-09-012	RG-12.1-002	RS-12.1-001	RG-09-013	RG-12.1-001	RG-10.1-005
Lithology	central lapilli-tuff	central lapilli-tuff	basal vitrophyre	basal vitrophyre	upper vitrophyre	upper vitrophyre	basal vitrophyre	basal vitrophyre	basal vitrophyre	xstal rich vitrophyre
SiO_2	71.27	71.67	72.03	-	73.10	-	74.45	75.60	-	73.06
TiO_2	0.66	0.65	0.60	-	0.49	-	0.41	0.33	-	0.43
Al_2O_3	13.37	12.90	12.62	-	12.48	-	12.01	12.00	-	12.97
Fe_2O_3	4.32	4.20	3.98	-	3.61	-	2.89	2.32	-	3.16
MnO	0.06	0.06	0.05	-	0.05	-	0.04	0.03	-	0.05
MgO	0.52	0.50	0.49	-	0.32	-	0.26	0.17	-	0.30
CaO	1.75	1.60	1.77	-	1.49	-	1.16	0.79	-	1.47
Na_2O	2.82	2.40	2.57	-	2.49	-	2.40	2.38	-	2.90
K_2O	5.10	5.87	5.76	-	5.90	-	6.32	6.36	-	5.59
P_2O_5	0.12	0.14	0.12	-	0.08	-	0.05	0.03	-	0.07
SO_3	0.00	0.00	0.01	-	0.00	-	0.00	0.00	-	0.01
*LOI**	*2.80*	*2.43*	*2.26*	-	*2.45*	-	*2.67*	*2.72*	-	*2.58*
*Total**	*100.36*	*100.36*	*100.06*	-	*99.71*	-	*99.54*	*100.07*	-	*100.20*
ASI[a]	*1.01*	*0.99*	*0.93*	-	*0.95*	-	*0.93*	*0.98*	-	*0.97*
Rb	170.5	185.4	187.2	180.0	192.1	195.8	205.0	212.6	210.7	-
Sr	91.2	93.9	89.9	80.6	82.5	71.8	53.0	38.5	42.8	-
Y	60.7	63.2	61.0	60.7	63.9	64.2	63.4	61.9	63.0	-
Zr	577.6	631.6	589.9	594.4	533.0	544.8	494.9	427.2	449.9	-
Nb	45.4	46.8	46.2	46.0	44.5	45.9	46.7	45.9	46.6	-
Ba	1082.2	1107.8	1135.9	1106.6	1402.7	1121.3	979.5	869.3	913.0	-
La	80.6	79.8	80.3	78.3	81.0	79.9	83.4	84.9	82.8	-
Ga	18.8	20.2	17.7	19.6	18.5	18.5	17.7	16.4	18.1	-
Ce	160.3	161.5	154.2	153.9	155.0	159.9	159.0	161.0	159.8	-
Nd	64.7	66.3	65.4	61.1	63.5	63.8	65.6	62.9	64.5	-
Pb	24.4	25.8	24.8	25.6	25.6	27.1	27.6	27.6	28.4	-
Th	29.7	29.7	29.3	28.9	30.3	31.4	33.3	34.8	34.2	-
U	6.6	6.8	6.1	6.2	6.5	6.8	7.0	7.5	7.0	-
Th/Nb	0.7	0.6	0.6	0.6	0.7	0.7	0.7	0.8	0.7	-
Zr/Y	9.5	10.0	9.7	9.8	8.3	8.5	7.8	6.9	7.1	-

*Original total and Loss on Ignition (LOI). [a]ASI = Al/Ca-1.67*Na+K+P.

Table C.1. Major (wt.%) and trace element (ppm) data from rhyolitic members of the Rogerson Formation . Major element data is recalculated to 100% anhydrous. Continued...

	Jackpot Member					
Sample No.	JP-10.1-005 upper	JP-10.1-001	RG-10.2-002	JP-10.1-002	JP-10.1-003	JP-10.1-004
Lithology	vitrophyre	lithoidal	lithoidal	lithoidal	lithoidal	lithoidal
SiO_2	74.43	73.36	76.25	75.60	75.24	76.48
TiO_2	0.38	0.46	0.37	0.34	0.32	0.33
Al_2O_3	12.27	12.42	11.67	12.37	12.44	12.21
Fe_2O_3	2.95	3.73	2.88	2.10	2.26	1.96
MnO	0.04	0.07	0.02	0.01	0.02	0.01
MgO	0.15	0.21	0.14	0.05	0.03	-0.03
CaO	1.04	1.34	0.69	0.69	0.73	0.54
Na_2O	2.27	3.13	2.83	3.07	3.34	3.12
K_2O	6.41	5.20	5.08	5.44	5.52	5.29
P_2O_5	0.05	0.07	0.07	0.28	0.09	0.07
SO_3	0.00	0.01	0.00	0.04	0.00	0.00
*LOI**	*2.83*	*2.47*	*0.57*	*0.90*	*0.54*	*0.51*
*Total**	*99.74*	*99.89*	*100.20*	*100.16*	*98.76*	*100.14*
ASI[a]	*0.98*	*0.94*	*1.03*	*1.04*	*0.98*	*1.04*
Rb	201.0	164.8	197.2	203.4	191.5	204.8
Sr	57.8	78.3	60.8	75.4	70.9	52.1
Y	65.3	64.4	62.9	81.3	83.5	75.9
Zr	532.5	531.2	529.0	532.9	556.1	547.4
Nb	45.3	46.1	45.2	47.6	47.5	51.2
Ba	1191.0	1175.1	1218.4	1350.8	1645.1	1109.2
La	80.0	84.6	82.4	92.6	108.8	107.0
Ga	18.1	18.3	18.7	21.2	22.2	21.1
Ce	160.6	172.3	158.3	190.5	225.4	206.3
Nd	66.0	74.2	64.9	80.0	89.9	88.0
Pb	27.6	25.7	26.8	25.1	27.5	29.6
Th	32.3	31.2	31.4	31.1	30.0	32.8
U	7.4	6.8	6.7	5.9	5.5	6.7
Th/Nb	0.7	0.7	0.7	0.7	0.6	0.6
Zr/Y	8.2	8.2	8.4	6.6	6.7	7.2

*Original total and Loss on Ignition (LOI). [a]ASI = Al/Ca-1.67*Na+K+P.

Table C.2. Major (wt.%) and trace element (ppm) data from rhyolitic members of the Cassia Formation . Major element data is recalculated to 100% anhydrous.

	Lincoln Reservoir Member											McMullen Creek Member	
Sample No.	MCM3-12.1-001	RC-10.1-007	UTC-12.2-001	DG-11.1-002	RC-10.1-008	RC-11.1-003	MCM3-12.1-002	ERC-12.1-004	TC-12.1-012	GC-12.2-005	GC-12.2-009	BCW-12.2-006	TC-12.1-005
Lithology	upper vitrophyre	top vitrophyre	upper lithoidal	vitrophyre	basal vitrophyre	basal vitrophyre	basal vitrophyre	basal vitrophyre	basal vitrophyre	basal vitrophyre	basal vitrophyre	upper orange ash	upper orange ash
SiO_2	72.50	72.34	-	72.81	73.30	73.72	73.43	-	72.70	-	-	-	-
TiO_2	0.51	0.50	-	0.48	0.44	0.45	0.45	-	0.49	-	-	-	-
Al_2O_3	12.69	12.75	-	12.65	12.56	12.37	12.34	-	12.42	-	-	-	-
Fe_2O_3	4.14	4.10	-	3.93	3.67	3.62	3.68	-	3.91	-	-	-	-
MnO	0.07	0.08	-	0.07	0.07	0.06	0.15	-	0.07	-	-	-	-
MgO	0.29	0.24	-	0.29	0.20	0.24	0.25	-	0.31	-	-	-	-
CaO	1.60	1.82	-	1.54	1.31	1.25	1.22	-	1.57	-	-	-	-
Na_2O	2.72	2.75	-	3.03	3.02	2.99	3.01	-	2.90	-	-	-	-
K_2O	5.40	5.31	-	5.13	5.35	5.23	5.40	-	5.55	-	-	-	-
P_2O_5	0.08	0.08	-	0.07	0.07	0.07	0.06	-	0.07	-	-	-	-
SO_3	0.00	0.03	-	0.01	0.02	0.01	0.00	-	0.00	-	-	-	-
*LOI**	*1.89*	*2.03*	-	*2.34*	*2.29*	*2.16*	*2.25*	-	*2.46*	-	-	-	-
*Total**	*99.22*	*100.19*	-	*100.33*	*100.27*	*100.28*	*98.97*	-	*98.82*	-	-	-	-
ASI[a]	*0.97*	*0.95*	-	*0.96*	*0.96*	*0.97*	*0.95*	-	*0.92*	-	-	-	-
Rb	159.3	161.6	167.4	161.5	166.4	166.8	162.9	158.5	161.9	176.3	170.4	166.5	172.1
Sr	105.8	119.0	96.5	99.8	82.7	83.1	80.6	93.9	91.3	68.8	80.8	78.0	63.8
Y	77.6	76.7	71.8	74.9	73.6	73.8	72.3	70.7	72.8	73.6	73.6	67.7	69.8
Zr	679.4	680.8	652.5	655.0	646.2	645.5	634.9	644.2	635.6	612.3	684.0	601.5	583.0
Nb	53.0	53.3	54.0	52.6	53.8	55.0	53.0	51.7	52.5	54.6	55.1	50.9	52.9
Ba	1156.7	1344.5	1293.0	1145.6	1155.5	1133.5	1210.4	1101.0	1093.5	1154.1	1185.6	1137.5	1148.8
La	85.4	88.0	85.4	83.9	84.5	86.5	81.7	78.8	82.5	83.2	88.7	80.2	84.0
Ga	19.7	21.6	19.4	20.7	19.5	18.4	18.9	18.9	18.9	18.3	19.4	18.2	18.2
Ce	165.1	170.5	164.9	165.8	173.4	166.0	165.7	157.9	162.1	168.2	162.1	163.0	164.7
Nd	73.8	74.1	69.3	70.2	74.4	74.8	69.6	67.4	71.3	72.7	73.2	68.1	69.2
Pb	24.6	24.9	25.2	25.0	25.9	24.6	25.0	24.8	25.0	26.4	27.2	26.9	28.2
Th	26.1	25.8	27.2	26.1	26.8	27.2	26.8	25.6	26.3	28.0	26.9	27.2	27.6
U	5.9	6.2	5.3	6.0	6.3	6.3	6.4	5.5	6.0	6.7	6.7	6.4	6.3
Th/Nb	0.5	0.5	0.5	0.5	0.5	0.5	0.5	0.5	0.5	0.5	0.5	0.5	0.5
Zr/Y	8.8	8.9	9.1	8.7	8.8	8.7	8.8	9.1	8.7	8.3	9.3	8.9	8.4

*Original total and Loss on Ignition (LOI). [a]ASI = Al/Ca-1.67*Na+K+P.

Table C.2. Major (wt.%) and trace element (ppm) data from rhyolitic members of the Cassia Formation . Major element data is recalculated to 100% anhydrous. Continued...

	McMullen Creek Member												
Sample No.	BCW-12.2-005	HG-11.2-001	RC-10.1-009	DG-11.1-001	CW-11.2-001	HG-11.2-002	RC-10.1-005	TC-12.1-004	TC-12.1-011	GC-12.2-004	GC-12.2-008	BCW-12.2-004	GC-12.2-003
Lithology	upper vitrophyre	upper vitrophyre	upper lithoidal	basal vitrophyre	basal vitrophyre	basal vitrophyre	basal vitrophyre	basal vitrophyre	basal vitrophyre	basal vitrophyre	basal vitrophyre	basal vitrophyre	lower grey ash
SiO_2	-	74.59	74.32	73.11	72.72	74.00	71.99	-	-	-	-	-	-
TiO_2	-	0.46	0.46	0.55	0.56	0.50	0.57	-	-	-	-	-	-
Al_2O_3	-	12.22	12.36	12.53	12.59	12.34	13.13	-	-	-	-	-	-
Fe_2O_3	-	3.21	3.31	3.80	3.94	3.42	4.08	-	-	-	-	-	-
MnO	-	0.05	0.05	0.06	0.07	0.04	0.07	-	-	-	-	-	-
MgO	-	0.21	0.17	0.35	0.37	0.26	0.33	-	-	-	-	-	-
CaO	-	1.09	1.11	1.58	1.68	1.22	1.78	-	-	-	-	-	-
Na_2O	-	2.68	3.16	2.95	2.78	2.55	2.91	-	-	-	-	-	-
K_2O	-	5.42	4.99	4.97	5.19	5.59	5.03	-	-	-	-	-	-
P_2O_5	-	0.06	0.07	0.09	0.10	0.07	0.10	-	-	-	-	-	-
SO_3	-	0.00	0.01	0.00	0.01	0.00	0.00	-	-	-	-	-	-
*LOI**	-	*1.92*	*1.18*	*2.32*	*2.40*	*2.87*	*2.28*	-	-	-	-	-	-
*Total**	-	*100.27*	*100.34*	*100.82*	*100.37*	*100.30*	*100.45*	-	-	-	-	-	-
ASI[a]	-	*1.00*	*0.98*	*0.97*	*0.96*	*1.00*	*0.98*	-	-	-	-	-	-
Rb	171.8	173.6	170.9	166.4	158.2	169.1	162.9	165.7	169.2	176.2	172.5	168.4	185.4
Sr	77.1	75.0	86.1	96.5	100.9	84.3	110.6	74.0	63.4	66.1	72.5	74.8	59.9
Y	69.3	65.0	118.0	68.8	67.6	64.2	67.9	66.5	68.3	67.5	67.3	68.2	68.4
Zr	638.4	611.9	631.0	643.4	632.3	607.7	643.5	600.3	586.2	582.1	585.5	608.5	594.6
Nb	52.8	51.9	53.0	51.0	49.5	50.9	50.1	50.5	51.2	51.5	51.4	51.3	52.9
Ba	1162.2	1188.6	1341.1	1138.0	1128.0	1207.7	1155.5	1075.8	1079.9	1101.8	1111.3	1107.3	1158.6
La	82.7	81.1	108.9	79.4	79.1	78.3	81.0	81.1	79.8	81.5	83.0	80.1	87.6
Ga	18.1	18.2	19.5	18.9	18.6	18.7	20.4	17.1	17.0	18.0	16.6	17.9	17.9
Ce	160.1	170.3	194.3	162.3	161.9	162.3	168.3	160.5	158.7	161.7	157.9	159.1	167.0
Nd	67.8	71.5	90.9	68.9	68.9	66.6	71.7	67.4	68.5	70.2	67.4	67.6	69.6
Pb	26.9	25.3	24.7	25.4	24.1	24.6	25.9	25.2	25.7	26.3	25.6	26.7	27.5
Th	27.6	27.1	28.3	26.5	25.4	26.8	26.4	26.7	27.3	28.3	27.7	27.5	28.2
U	6.5	5.9	7.5	6.4	5.9	6.3	6.6	5.9	6.8	6.3	6.4	6.2	5.7
Th/Nb	0.5	0.5	0.5	0.5	0.5	0.5	0.5	0.5	0.5	0.5	0.5	0.5	0.5
Zr/Y	9.2	9.4	5.3	9.3	9.3	9.5	9.5	9.0	8.6	8.6	8.7	8.9	8.7

*Original total and Loss on Ignition (LOI). [a]ASI = Al/Ca-1.67*Na+K+P.

Table C.2. Major (wt.%) and trace element (ppm) data from rhyolitic members of the Cassia Formation . Major element data is recalculated to 100% anhydrous. Continued...

	McMullen Creek Member		Indian Springs Member								Dry Gulch Member	
Sample No.	GC-12.2-007	GC-12.2-010	Q2-11.1-001	Q2-11.1-002	DG-11.1-003	RC-10.1-010	RC-10.2-001	CW-11.2-002	HG-11.2-003	IS-11.1-001	RC-10.2-002	DG-11.1-004	Q2-11.1-003
Lithology	lower grey ash	lower grey ash	vitrophyre	vitrophyre	vitrophyre	vitrophyre	vitrophyre	vitrophyre	vitrophyre	basal vitrophyre	fused tuff	upper vitrophyre	upper vitrophyre
SiO_2	-	-	73.42	73.78	73.69	74.81	73.20	72.55	72.72	72.80	-	75.53	75.35
TiO_2	-	-	0.44	0.44	0.42	0.41	0.46	0.50	0.51	0.48	-	0.33	0.36
Al_2O_3	-	-	12.40	12.28	12.23	12.25	12.41	12.51	12.57	12.51	-	12.11	12.13
Fe_2O_3	-	-	3.81	3.77	3.69	2.91	3.94	4.23	4.27	4.14	-	2.44	2.64
MnO	-	-	0.06	0.06	0.06	0.04	0.06	0.08	0.06	0.07	-	0.04	0.04
MgO	-	-	0.22	0.22	0.20	0.13	0.22	0.27	0.28	0.29	-	0.12	0.13
CaO	-	-	1.30	1.29	1.30	1.04	1.27	1.52	1.45	1.48	-	0.82	0.86
Na_2O	-	-	3.01	2.90	2.95	2.56	2.78	3.00	2.69	2.92	-	2.84	2.74
K_2O	-	-	5.27	5.18	5.37	5.79	5.58	5.25	5.35	5.21	-	5.73	5.70
P_2O_5	-	-	0.07	0.07	0.08	0.05	0.06	0.08	0.09	0.08	-	0.03	0.04
SO_3	-	-	0.00	0.01	0.01	0.00	0.01	0.00	0.00	0.02	-	0.00	0.00
*LOI**	-	-	*2.29*	*2.63*	*2.47*	*2.47*	*2.72*	*2.58*	*2.60*	*2.02*	-	*1.82*	*2.56*
*Total**	-	-	*100.37*	*100.68*	*100.26*	*100.24*	*99.47*	*98.21*	*100.33*	*100.50*	-	*100.76*	*100.67*
ASI[a]	-	-	*0.96*	*0.97*	*0.95*	*0.99*	*0.97*	*0.94*	*0.99*	*0.96*	-	*0.98*	*1.00*
Rb	172.6	177.6	178.5	180.0	179.9	177.8	179.1	173.4	172.8	-	183.7	200.5	190.6
Sr	74.5	63.1	77.8	75.0	73.8	64.5	79.7	90.3	98.8	-	71.7	49.0	54.4
Y	67.5	67.5	73.8	74.0	75.3	67.2	74.3	75.9	74.1	-	76.4	70.1	68.5
Zr	634.9	569.3	615.0	613.2	635.3	581.4	632.1	624.7	624.9	-	624.0	465.8	493.0
Nb	52.0	51.7	52.1	52.0	53.0	52.8	52.2	51.0	51.2	-	53.1	52.5	51.0
Ba	1126.9	1119.2	1127.8	1130.2	1158.9	1162.6	1143.3	1123.1	1165.9	-	1190.2	1066.6	1081.0
La	82.8	81.6	83.2	83.5	85.9	82.2	84.0	80.9	84.9	-	88.3	85.7	83.0
Ga	17.6	17.2	19.7	18.8	19.2	18.3	20.6	19.7	20.4	-	19.3	18.6	18.7
Ce	165.3	162.2	168.8	171.0	174.1	170.2	174.2	167.2	162.9	-	169.3	167.7	167.1
Nd	70.2	68.1	71.1	72.4	71.4	69.4	73.2	68.8	72.5	-	72.2	68.4	66.5
Pb	26.1	26.5	25.1	26.0	25.8	25.9	25.2	24.8	24.5	-	25.3	27.1	26.2
Th	27.5	27.2	28.9	29.2	29.6	28.4	28.5	27.9	27.9	-	29.5	31.9	30.2
U	6.9	6.4	7.1	6.7	7.2	6.8	6.6	6.6	6.8	-	7.0	7.4	6.8
Th/Nb	0.5	0.5	0.6	0.6	0.6	0.5	0.5	0.5	0.5	-	0.6	0.6	0.6
Zr/Y	9.4	8.4	8.3	8.3	8.4	8.6	8.5	8.2	8.4	-	8.2	6.6	7.2

*Original total and Loss on Ignition (LOI). [a]ASI = Al/Ca-1.67*Na+K+P.

Table C.2. Major (wt.%) and trace element (ppm) data from rhyolitic members of the Cassia Formation . Major element data is recalculated to 100% anhydrous. Continued...

	Dry Gulch Member						Little Creek Member						
Sample No.	CW-11.2-003	HG-11.2-004	NRC-11.2-001	NRC-11.2-003	SIS-12.1-004	Q2-11.1-004	UWS-12.1-002	RC-11.1-002	ERC-12.1-002	NRC-11.2-002	RC-11.1-001	RC-11.1-004	UWS-12.1-001
Lithology	purple lithoidal	purple lithoidal	purple lithoidal	purple lithoidal	purple lithoidal	purple lithoidal	upper vitrophyre	upper vitrophyre	vitrophyre	basal vitrophyre	basal vitrophyre	basal vitrophyre	basal vitrophyre
SiO_2	75.53	75.68	75.32	76.00	-	75.71	-	71.44	-	68.33	70.03	70.13	-
TiO_2	0.34	0.33	0.34	0.31	-	0.36	-	0.67	-	0.87	0.76	0.76	-
Al_2O_3	12.13	12.11	12.22	12.02	-	12.22	-	12.75	-	13.41	12.98	13.02	-
Fe_2O_3	2.57	2.51	2.66	2.40	-	2.60	-	4.34	-	5.72	4.94	4.98	-
MnO	0.02	0.03	0.04	0.03	-	0.04	-	0.06	-	0.08	0.07	0.07	-
MgO	0.14	0.07	0.10	0.14	-	0.09	-	0.57	-	0.99	0.72	0.73	-
CaO	0.86	0.60	0.65	0.63	-	0.67	-	1.88	-	2.73	2.26	2.27	-
Na_2O	3.18	3.20	3.30	3.17	-	3.17	-	2.65	-	3.03	2.87	2.87	-
K_2O	5.20	5.31	5.32	5.24	-	5.10	-	5.49	-	4.66	5.22	5.00	-
P_2O_5	0.04	0.15	0.04	0.06	-	0.04	-	0.14	-	0.19	0.16	0.16	-
SO_3	0.00	0.00	0.00	0.00	-	0.00	-	0.01	-	0.00	0.00	0.00	-
*LOI**	*0.62*	*0.39*	*0.50*	*0.50*	-	*0.22*	-	*2.14*	-	*1.74*	*1.99*	*1.97*	-
*Total**	*100.21*	*99.97*	*98.88*	*100.42*	-	*102.64*	-	*99.80*	-	*99.91*	*98.86*	*100.01*	-
ASI[a]	*0.98*	*1.02*	*0.99*	*1.00*	-	*1.03*	-	*0.94*	-	*0.91*	*0.91*	*0.92*	-
Rb	194.5	197.5	195.7	196.4	192.3	195.6	187.6	183.2	180.8	158.1	173.3	171.8	172.9
Sr	59.6	51.1	57.5	50.7	49.4	58.3	75.8	108.8	95.3	144.4	113.5	119.9	103.9
Y	70.9	90.0	70.9	68.6	57.6	67.5	60.9	61.0	63.6	64.0	62.3	63.2	60.0
Zr	490.5	484.8	521.4	474.8	437.5	502.0	587.1	616.6	640.4	704.9	642.6	655.6	616.6
Nb	51.8	52.6	53.5	52.1	50.8	52.5	46.2	45.6	45.9	43.4	43.6	44.0	43.9
Ba	1121.8	1162.7	1161.9	1144.5	1066.5	1037.9	1093.3	1372.3	1111.7	1136.8	1109.1	1159.6	1166.0
La	79.2	96.7	84.5	90.7	79.9	78.7	78.3	78.7	78.0	78.1	76.7	76.2	76.3
Ga	18.3	18.7	18.3	17.7	17.2	18.4	17.4	19.3	19.4	20.8	20.9	20.4	19.6
Ce	160.2	179.9	168.6	159.3	154.1	143.6	150.7	154.1	154.0	153.7	153.4	152.8	151.0
Nd	65.1	78.0	69.8	73.7	64.4	65.0	62.8	63.2	65.7	65.1	65.7	64.2	63.8
Pb	24.0	27.3	27.6	24.5	25.6	25.0	24.8	24.9	25.0	22.6	24.0	23.7	23.9
Th	31.1	32.1	31.3	30.6	31.1	31.5	29.8	28.5	29.0	26.1	27.9	27.4	27.5
U	6.2	7.3	6.8	6.1	5.9	6.3	6.8	6.7	7.1	6.2	6.5	6.2	6.3
Th/Nb	0.6	0.6	0.6	0.6	0.6	0.6	0.6	0.6	0.6	0.6	0.6	0.6	0.6
Zr/Y	6.9	5.4	7.4	6.9	7.6	7.4	9.6	10.1	10.1	11.0	10.3	10.4	10.3

*Original total and Loss on Ignition (LOI). [a]ASI = Al/Ca-1.67*Na+K+P.

Table C.2. Major (wt.%) and trace element (ppm) data from rhyolitic members of the Cassia Formation . Major element data is recalculated to 100% anhydrous. Continued...

	Wooden Shoe Butte Member											
Sample No.	RC-11.1-006	TC-12.1-008	TC-12.1-003	GC-12.2-006	GC-12.2-001	RC-10.1-003	ERC-12.1-001	RC-11.1-005	RC-10.1-002	BCW-12.2-003	TC-12.1-007	TC-12.1-002
Lithology	upper vitrophyre	upper vitrophyre	upper vitrophyre	vitrophyre	vitrophyre	Lower lithoidal	basal vitrophyre	basal vitrophyre	basal vitrophyre	basal vitrophyre	basal vitrophyre	basal vitrophyre
SiO_2	72.76	-	-	-	-	70.88	-	72.80	71.23	-	-	-
TiO_2	0.53	-	-	-	-	0.60	-	0.52	0.57	-	-	-
Al_2O_3	12.58	-	-	-	-	13.08	-	12.56	13.06	-	-	-
Fe_2O_3	3.86	-	-	-	-	4.62	-	3.90	4.33	-	-	-
MnO	0.05	-	-	-	-	0.05	-	0.06	0.06	-	-	-
MgO	0.28	-	-	-	-	0.36	-	0.33	0.38	-	-	-
CaO	1.35	-	-	-	-	1.96	-	1.41	1.88	-	-	-
Na_2O	2.78	-	-	-	-	3.46	-	2.83	3.02	-	-	-
K_2O	5.71	-	-	-	-	4.83	-	5.48	5.28	-	-	-
P_2O_5	0.09	-	-	-	-	0.12	-	0.10	0.13	-	-	-
SO_3	0.00	-	-	-	-	0.03	-	0.01	0.03	-	-	-
*LOI**	*2.35*	-	-	-	-	*1.62*	-	*2.34*	*2.37*	-	-	-
*Total**	*98.74*	-	-	-	-	*100.12*	-	*100.04*	*98.54*	-	-	-
ASI[a]	*0.96*	-	-	-	-	*0.91*	-	*0.96*	*0.94*	-	-	-
Rb	185.5	190.1	184.4	195.4	194.2	175.1	159.7	190.2	178.8	179.4	175.8	175.8
Sr	85.8	74.5	88.1	66.7	83.4	126.8	133.3	86.6	108.7	102.7	113.7	110.2
Y	71.3	70.1	72.7	67.0	68.3	58.4	71.6	70.5	68.0	69.2	68.3	68.6
Zr	663.4	672.5	698.1	618.1	602.6	696.6	666.1	633.6	637.8	646.0	671.7	645.4
Nb	50.9	52.0	51.4	51.9	49.8	48.2	44.6	51.1	48.6	48.7	48.1	47.9
Ba	1312.8	1221.5	1261.9	1188.0	1178.9	1229.7	1127.7	1233.1	1276.3	1185.8	1217.4	1186.1
La	87.5	83.6	85.7	84.5	81.8	82.4	78.7	83.2	92.0	87.0	84.0	82.6
Ga	20.6	19.2	20.1	18.7	18.8	20.7	20.6	19.8	21.5	20.5	20.0	20.2
Ce	168.5	172.2	171.2	163.0	164.0	160.7	153.4	172.8	124.3	163.4	160.0	160.0
Nd	71.8	73.1	72.2	67.3	67.5	65.3	67.3	68.9	75.1	71.2	68.9	66.3
Pb	26.2	27.4	26.6	28.4	27.3	25.0	23.4	26.6	26.0	27.3	24.9	25.8
Th	30.3	31.4	30.4	31.8	30.9	29.4	26.2	30.7	29.7	29.8	28.3	28.2
U	7.3	7.1	7.0	7.6	6.7	6.9	6.1	7.1	6.6	6.4	6.7	6.1
Th/Nb	0.6	0.6	0.6	0.6	0.6	0.6	0.6	0.6	0.6	0.6	0.6	0.6
Zr/Y	9.3	9.6	9.6	9.2	8.8	11.9	9.3	9.0	9.4	9.3	9.8	9.4

*Original total and Loss on Ignition (LOI). [a]ASI = Al/Ca-1.67*Na+K+P.

Table C.2. Major (wt.%) and trace element (ppm) data from rhyolitic members of the Cassia Formation . Major element data is recalculated to 100% anhydrous. Continued...

	Steer Basin Member				Big Bluff Member		Magpie Basin Member		
Sample No.	SIS-12.1-001	RC-10.1-001	RC-10.1-004	BCW-12.2-001	RC-11.1-008	RC-10.1-011	RC-10.2-005	RC-10.2-004	RC-10.2-006
Lithology	upper vitrophyre	upper lithoidal	vitrophyre	basal vitrophyre	upper vitrophyre	vitrophyre	upper vitrophyre	lower vitrophyre	fused tuff
SiO_2	-	72.41	72.28	-	76.15	74.82	75.68	75.72	-
TiO_2	-	0.58	0.53	-	0.31	0.31	0.29	0.30	-
Al_2O_3	-	12.90	12.58	-	12.44	12.09	12.17	12.19	-
Fe_2O_3	-	4.10	4.00	-	2.56	2.87	2.41	2.46	-
MnO	-	0.03	0.06	-	0.09	0.04	0.03	0.03	-
MgO	-	0.37	0.34	-	0.03	0.06	0.05	0.08	-
CaO	-	1.46	1.79	-	0.60	1.08	0.69	0.68	-
Na_2O	-	3.15	2.43	-	1.97	2.46	2.05	2.28	-
K_2O	-	4.89	5.87	-	5.82	6.24	6.61	6.25	-
P_2O_5	-	0.10	0.09	-	0.03	0.02	0.01	0.01	-
SO_3	-	0.00	0.03	-	0.00	0.00	0.01	0.01	-
*LOI**	-	*0.64*	*2.25*	-	*2.97*	*2.36*	*2.88*	*2.60*	-
*Total**	-	*100.38*	*100.47*	-	*112.01*	*100.37*	*99.85*	*100.08*	-
ASI[α]	-	*0.99*	*0.93*	-	*1.17*	*0.95*	*1.03*	*1.04*	-
Rb	186.6	187.4	194.8	197.0	216.2	213.7	235.2	232.9	230.0
Sr	90.1	104.5	90.8	67.6	32.3	46.1	31.7	31.4	29.0
Y	65.2	57.8	68.2	64.8	82.7	83.1	68.3	65.0	75.8
Zr	557.3	616.9	565.6	568.1	514.2	535.4	458.5	488.0	464.8
Nb	43.2	43.8	44.4	45.2	52.5	51.1	47.5	48.7	49.4
Ba	1178.6	1275.7	1205.8	1186.3	793.3	958.6	769.7	861.8	646.7
La	79.6	85.6	82.3	81.3	95.2	96.6	93.6	88.9	99.2
Ga	19.1	21.1	19.4	19.4	20.5	19.8	18.5	18.8	19.1
Ce	152.6	154.2	161.9	157.8	194.2	190.1	176.2	175.6	161.7
Nd	65.1	68.5	67.5	64.0	79.1	79.1	72.4	67.4	78.7
Pb	26.1	26.7	27.2	28.1	30.3	29.8	29.4	29.6	30.3
Th	29.7	29.5	31.0	31.2	34.6	34.1	35.3	34.9	38.3
U	6.7	5.0	7.3	7.2	8.7	7.8	7.9	7.7	8.6
Th/Nb	0.7	0.7	0.7	0.7	0.7	0.7	0.7	0.7	0.8
Zr/Y	8.5	10.7	8.3	8.8	6.2	6.4	6.7	7.5	6.1

*Original total and Loss on Ignition (LOI). [α]ASI = Al/Ca-1.67*Na+K+P.

Table C.3. Major (wt.%) and trace element (ppm) data from rhyolitic units of the Kimberley drill-hole. Major element data is recalculated to 100% anhydrous.

	Kimberly Rhyolite 1		Kimberly Rhyolite 2		Kimberly Rhyolite 3
Sample No.	A2·2102-2106	A2·6400-6411	A2·1419-1424	A2·1945.8-1953.2	A2·751.6-754
Lithology	upper vitrophyre	lower lithoidal	upper vitrophyre	basal vitrophyre	basal vitrophyre
SiO_2	68.00	68.17	74.16	74.22	69.60
TiO_2	0.80	0.81	0.35	0.34	0.70
Al_2O_3	13.40	13.40	12.75	12.58	13.52
Fe_2O_3	4.87	4.85	2.99	2.97	4.67
MnO	0.10	0.08	0.08	0.07	0.08
MgO	0.91	0.87	0.27	0.19	0.67
CaO	2.75	2.46	1.14	1.08	2.17
Na_2O	4.39	4.21	3.96	3.58	3.64
K_2O	4.62	4.98	4.27	4.92	4.81
P_2O_5	0.17	0.17	0.04	0.04	0.15
SO_3	0.00	0.00	0.00	0.00	0.00
*LOI**	*2.65*	*0.30*	*3.82*	*2.58*	*1.95*
*Total**	*99.75*	*99.50*	*99.59*	*99.49*	*99.54*
ASI[a]	*0.79*	*0.81*	*0.97*	*0.96*	*0.90*
Rb	156.8	154.4	173.9	182.8	172.2
Sr	122.7	124.5	66.7	65.5	104.1
Y	56.3	55.6	79.3	79.7	85.5
Zr	601.3	604.5	532.3	545.3	733.7
Nb	42.1	42.8	56.9	56.9	61.9
Ba	968.2	1046.2	1118.9	1113.4	1128.1
La	68.7	68.1	87.4	83.6	90.7
Ga	19.1	18.8	19.5	19.0	22.7
Ce	137.8	133.0	170.8	170.5	187.1
Nd	55.4	56.0	75.1	73.5	78.5
Pb	23.1	22.9	27.5	27.4	27.9
Th	24.5	24.7	27.6	28.1	27.9
U	5.7	5.6	6.1	6.4	6.1
Th/Nb	0.6	0.6	0.5	0.5	0.5
Zr/Y	16.7	10.9	6.7	6.8	8.6

*Original total and Loss on Ignition (LOI). [a]ASI = Al/Ca-1.67*Na+K+P.

Table C.4. Major (wt.%) and trace element (ppm) data from other rhyolitic units discussed in this thesis. Major element data is recalculated to 100% anhydrous.

	'Browns Bench 11'								'Oakley Hills 1
Sample No.	SWC-12.2-006	SWC-12.2-002	RG-10.2-003	NBB-11.2-002	UBB-12.1-001	UBB-12.1-002	SWC-12.2-001	SWC-12.2-005	OH-12.1-001
Lithology	upper lithoidal	vitrophyre	vitrophyre	vitrophyre	vitrophyre	vitrophyre	basal vitrophyre	basal vitrophyre	lower lithoidal
SiO_2	-	-	71.77	71.34	-	-	-	-	71.54
TiO_2	-	-	0.65	0.69	-	-	-	-	0.56
Al_2O_3	-	-	12.69	12.71	-	-	-	-	12.56
Fe_2O_3	-	-	4.19	4.38	-	-	-	-	3.94
MnO	-	-	0.06	0.06	-	-	-	-	0.06
MgO	-	-	0.49	0.62	-	-	-	-	0.40
CaO	-	-	1.70	1.94	-	-	-	-	1.70
Na_2O	-	-	2.81	2.73	-	-	-	-	3.79
K_2O	-	-	5.49	5.36	-	-	-	-	5.32
P_2O_5	-	-	0.12	0.14	-	-	-	-	0.12
SO_3	-	-	0.03	0.03	-	-	-	-	0.00
*LOI**	-	-	*2.25*	*2.18*	-	-	-	-	0.63
*Total**	-	-	*99.87*	*100.91*	-	-	-	-	98.67
ASI[a]	-	-	*0.94*	*0.93*	-	-	-	-	0.84
Rb	172.7	162.9	186.6	179.4	171.5	174.5	161.2	185.2	167.4
Sr	116.5	126.0	88.5	97.2	99.6	95.1	127.0	79.9	106.4
Y	62.7	63.9	63.5	63.3	62.1	60.9	62.3	61.7	70.7
Zr	636.9	656.4	624.5	624.6	616.8	609.8	642.8	593.3	660.7
Nb	44.9	44.3	47.0	46.3	44.3	45.1	43.5	46.3	50.6
Ba	1199.4	1145.7	1161.7	1156.7	1097.7	1103.4	1131.0	1174.2	1152.4
La	80.8	84.8	80.1	79.7	78.1	76.2	77.9	79.5	79.3
Ga	19.7	20.1	19.3	18.7	19.6	19.5	20.0	18.8	20.8
Ce	162.4	160.6	161.7	158.1	157.0	153.0	150.1	155.4	160.2
Nd	66.0	70.8	66.8	66.3	64.9	60.8	63.7	63.6	68.8
Pb	24.5	24.8	25.8	24.4	24.6	23.7	24.6	26.9	25.4
Th	28.4	27.8	30.1	29.3	28.0	28.5	27.2	31.1	26.7
U	6.0	6.8	6.8	6.3	6.7	6.5	6.6	7.5	6.1
Th/Nb	0.6	0.6	0.6	0.6	0.6	0.6	0.6	0.7	0.5
Zr/Y	10.2	10.3	9.8	9.9	9.9	10.0	10.3	9.6	9.3

*Original total and Loss on Ignition (LOI). [a]ASI = Al/Ca-1.67*Na+K+P.

Table C.4. Major (wt.%) and trace element (ppm) data from other rhyolitic units discussed in this thesis. Major element data is recalculated to 100% anhydrous. Continued...

	'Oakley Hills 2'		Three Creek Ignimbrite		Shoshone Falls Rhyolite
Sample No.	OH-12.1-003	OH-12.1-002	3C-10.2-002	3C-10.2-001	SHO-12.2-001
Lithology	upper lithoidal	basal vitrophyre	Lithoidal	Lower vitrophyre	lithoidal
SiO_2	72.69	72.75	73.65	74.02	68.76
TiO_2	0.49	0.48	0.45	0.44	0.73
Al_2O_3	12.46	12.44	12.32	12.33	13.49
Fe_2O_3	3.94	3.93	3.65	3.36	4.97
MnO	0.07	0.07	0.05	0.06	0.07
MgO	0.32	0.32	0.17	0.16	0.78
CaO	1.65	1.66	1.20	1.16	2.14
Na_2O	3.03	3.02	2.86	2.60	3.80
K_2O	5.27	5.25	5.58	5.81	5.10
P_2O_5	0.08	0.08	0.06	0.05	0.16
SO_3	0.00	0.00	0.01	0.01	0.00
*LOI**	2.34	2.19	0.97	1.87	0.40
*Total**	99.25	99.10	99.48	101.77	99.40
ASI[a]	0.92	0.92	0.96	0.98	*0.87*
Rb	158.9	158.9	169.6	173.8	171.7
Sr	93.5	93.5	85.2	78.8	108.5
Y	72.3	72.3	75.7	75.0	84.4
Zr	658.0	658.0	685.3	659.9	735.3
Nb	52.3	52.3	55.8	55.2	61.9
Ba	1146.7	1101.9	1212.4	1228.8	1165.5
La	75.3	80.9	89.0	86.9	94.7
Ga	18.8	18.9	19.9	18.8	22.6
Ce	153.1	163.0	172.5	177.2	185.1
Nd	65.9	68.8	74.8	72.2	80.1
Pb	24.9	24.9	26.5	25.9	29.1
Th	25.7	25.7	28.1	28.1	27.9
U	5.9	5.9	6.4	6.6	5.5
Th/Nb	0.5	0.5	0.0	0.0	0.5
Zr/Y	9.1	9.1	9.1	8.8	8.7

*Original total and Loss on Ignition (LOI). [a]ASI = Al/Ca-1.67*Na+K+P.

Table C.5. Average feldspar compositions from members of the Rogerson Formation. Values in brackets = data range

Member	*n*	SiO_2	TiO_2	Al_2O_3	Cr_2O_3	FeO	MnO	MgO	CaO	Na_2O	K_2O	NiO	An%	Or%
Plagioclase														
Greys Landing	90	58.79 *(55.47 - 61.69)*	0.03 *(22.72 - 25.99)*	24.63 *(0.00 - 0.07)*	0.00 *(0.36 - 0.88)*	0.47 *(0.00 - 0.06)*	0.01 *(0.00 - 0.06)*	0.03 *(0.00 - 0.11)*	7.59 *(5.19 - 9.24)*	6.57 *(5.82 - 7.07)*	0.91 *(0.64 - 1.029)*	0.00 *(0.00 - 0.03)*	36.90 *(31.19 - 43.45)*	5.26 *(3.62 - 7.87)*
Browns View	64	58.79 *(53.56 - 59.94)*	0.04 *(0.00 - 0.08)*	25.11 *(22.89 - 26.58)*	0.00 *(0.00 - 0.02)*	0.46 *(0.38 - 0.53)*	0.00 *(0.00 - 0.02)*	0.03 *(0.01 - 0.05)*	7.89 *(6.38 - 9.79)*	6.57 *(5.41 - 7.01)*	1.10 *(0.67 - 1.41)*	0.00 *(0.00 - 0.03)*	37.41 *(30.74 - 48.08)*	6.21 *(3.84 - 8.17)*
Rabbit Springs	53	59.37 *(55.34 - 60.67)*	0.03 *(0.00 - 0.06)*	24.86 *(22.080 - 27.35)*	0.00 *(0.00 - 0.02)*	0.39 *(0.28 - 1.21)*	0.00 *(0.00 - 0.02)*	0.02 *(0.00 - 0.18)*	7.22 *(5.93 - 9.76)*	6.92 *(5.73 - 7.25)*	1.19 *(0.64 - 1.55)*	0.00 *(0.00 - 0.02)*	34.12 *(28.60 - 46.67)*	6.68 *(3.54 - 9.03)*
Jackpot	42	61.12 *(58.54 - 72.40)*	0.02 *(0.00 - 0.13)*	24.15 *(20.21 - 25.89)*	0.01 *(0.00 - 0.08)*	0.47 *(0.26 - 2.95)*	0.01 *(0.00 - 0.06)*	0.01 *(0.00 - 0.09)*	6.85 *(4.87 - 8.53)*	6.18 *(5.17 - 7.52)*	1.17 *(0.83 - 1.83)*	0.01 *(0.00 - 0.05)*	35.23 *(26.50 - 42.03)*	7.20 (4.84 - 11.69)
Sanidine														
Rabbit Springs	22	65.50 *(61.21 - 64.40)*	0.04 *(0.00 - 0.07)*	19.52 *(18.36 - 18.96)*	0.00 *(0.00 - 0.00)*	0.17 *(0.12 - 0.21)*	0.00 *(0.00 - 0.01)*	0.00 *(0.00 - -0.05)*	0.67 *(0.39 - 0.89)*	4.32 *(3.93 - 4.42)*	9.77 *(8.82 - 9.87)*	0.00 *(0.00 - 0.02)*	3.36 *(2.06 - 4.68)*	57.75 *(54.58 - 60.91)*
Jackpot	14	66.51 *(65.59 - 70.01)*	0.07 *(0.00 - 0.17)*	19.06 *(18.65 - 19.93)*	0.00 *(0.00 - 0.02)*	0.17 *(0.12 - 0.41)*	0.01 *(0.00 - 0.04)*	0.00 *(0.00 - 0.00)*	0.68 *(0.32 - 1.06)*	4.40 *(4.12 - 4.81)*	9.09 *(8.38 - 10.24)*	0.01 *(0.00 - 0.04*	3.48 *(1.68 - 5.38)*	55.63 *(50.66 - 59.78)*

Table C.6. Average pyroxene compositions from members of the Rogerson Formation. Values in brackets = data range

Member	n	SiO_2	TiO_2	Al_2O_3	Cr_2O_3	FeO	MnO	MgO	CaO	Na_2O	K_2O	NiO
Pigeonites												
Greys Landing population 1	28	48.35 *(47.12 - 50.84)*	0.24 *(0.17 - 0.30)*	0.46 *(0.32 - 0.76)*	0.01 *(0.00 - 0.03)*	34.49 *(30.32 - 35.99)*	1.14 *(0.98 - 1.20)*	8.81 *(8.22 - 9.29)*	5.44 *(4.69 - 8.87)*	0.08 *(0.05 - 0.13)*	0.00 *(0.00 - 0.02)*	0.00 *(0.00 - 0.02)*
Greys Landing population 2	46	49.04 *(47.49 - 50.16)*	0.24 *(0.15 - 0.35)*	0.49 *(0.19 - 0.66)*	0.01 *(0.00 - 0.05)*	33.30 *(31.69 - 33.97)*	1.10 *(1.02 - 1.20)*	10.14 *(9.74 - 10.56)*	5.23 *(4.74 - 7.25)*	0.07 *(0.00 - 0.12)*	0.00 *(0.00 - 0.03)*	0.00 *(0.00 - 0.03)*
Browns View	73	48.75 *(45.75 - 52.02)*	0.20 *(0.13 - 0.28)*	0.40 *(0.34 - 0.92)*	0.00 *(0.00 - 0.03)*	30.17 *(27.56 - 30.86)*	0.91 *(0.82 - 0.95)*	13.50 *(12.88 - 13.82)*	3.93 *(3.52 - 6.85)*	0.07 *(0.02 - 0.31)*	0.00 *(0.00 - 0.11)*	-
Rabbit Springs	56	47.65 *(45.54 - 49.62)*	0.22 *(0.09 - 0.34)*	0.38 *(0.28 - 0.77)*	0.01 *(0.00 - 0.03)*	35.01 *(31.94 - 36.16)*	0.94 *(0.85 - 1.00)*	9.45 *(8.70 - 10.21)*	4.55 *(3.98 - 7.13)*	0.06 *(0.03 - 0.15)*	0.00 *(0.00 - 0.14)*	0.01 *(0.00 - 0.03)*
Jackpot	16	49.47 *(49.07 - 50.08)*	0.25 *(0.17 - 0.35)*	0.40 *(0.24 - 0.63)*	0.01 *(0.00 - 0.05)*	34.69 *(33.65 - 35.16)*	0.93 *(0.83 - 0.98)*	9.76 *(8.55 - 10.12)*	5.03 *(4.72 - 7.15)*	0.05 *(0.00 - 0.15)*	0.01 *(0.00 - 0.04)*	0.01 *(0.00 - 0.05)*
Augite												
Greys Landing population 1	11	48.98 *(47.68 - 50.19)*	0.35 *(0.28 - 0.47)*	0.82 *(0.61 - 1.19)*	0.01 *(0.00 - 0.06)*	24.37 *(23.19 - 26.27)*	0.78 *(0.73 - 0.89)*	7.57 *(7.28 - 7.97)*	16.07 *(14.07 - 17.08)*	0.21 *(0.17 - 0.25)*	0.01 *(0.00 - 0.05)*	0.01 *(0.00 - 0.05)*
Greys Landing population 2	14	49.53 *(48.70 - 50.21)*	0.39 *(0.35 -0.44)*	0.94 *(0.70 - 1.38)*	0.01 *(0.00 - 0.03)*	22.83 *(22.09 - 23.42)*	0.73 *(0.70 - 0.76)*	8.64 *(8.22 - 8.95)*	16.28 *(15.57 - 17.02)*	0.22 *(0.19 - 0.29)*	0.01 *(0.00 - 0.07)*	0.01 *(0.00 - 0.04)*
Browns View	40	49.49 *(47.05 - 51.49)*	0.36 *(0.26 - 0.58)*	0.96 *(0.74 - 1.73)*	0.01 *(0.00 - 0.03)*	17.87 *(17.12 - 18.57)*	0.54 *(0.49 - 0.57)*	10.85 *(9.67 - 11.20)*	17.89 *(16.92 - 19.30)*	0.25 *(0.21 - 0.32)*	0.00 *(0.00 - 0.06)*	0.01 *(0.00 - 0.03)*
Rabbit Springs	32	48.68 *(47.40 - 50.01)*	0.35 *(0.25 - 0.44)*	0.82 *(0.62 - 0.97)*	0.01 *(0.00 - 0.03)*	22.75 *(21.18 - 24.35)*	0.59 *(0.56 - 0.62)*	8.38 *(7.84 - 8.93)*	16.97 *(14.80 - 18.25)*	0.22 *(0.19 - 0.29)*	0.00 *(0.00 - 0.04)*	0.01 *(0.00 - 0.03)*
Jackpot	5	49.61 *(49.36 - 49.81)*	0.38 *(0.31 - 0.45)*	0.89 *(0.84 - 0.98)*	0.01 *(0.00 - 0.05)*	24.16 *(22.67 - 26.94)*	0.65 *(0.52 - 0.75)*	8.11 *(7.75 - 8.55)*	16.44 *(14.82 - 17.16)*	0.21 *(0.17 - 0.23)*	0.01 *(0.00 - 0.02)*	0.01 *(0.00 - 0.04)*

Table C.7. Average feldspar compositions from members of the Cassia Formation. Values in brackets = data range

Member	n	SiO_2	TiO_2	Al_2O_3	Cr_2O_3	FeO	MnO	MgO	CaO	Na_2O	K_2O	NiO	An%	Or%
Plagiodase														
Lincoln Reservoir	116	58.74 *(54.91 - 61.66)*	0.03 *(0.00 - 0.08)*	24.55 *(22.37 - 27.32)*	0.00 *(0.00 - 0.03)*	0.46 *(0.31 - 0.69)*	0.00 *(0.00 - 0.02)*	0.02 *(0.00 - 0.04)*	7.46 *(5.46 - 10.13)*	6.63 *(5.46 - 10.13)*	0.97 *(0.51 - 1.56)*	0.01 *(0.00 - 0.03)*	36.24 *(26.45 - 49.00)*	5.59 *(2.98 - 8.91)*
McMullen Creek	75	58.07 *(54.86 - 59.99)*	0.03 *(0.00 - 0.09)*	25.16 *(24.08 - 26.50)*	0.01 *(0.00 - 0.07)*	0.40 *(0.32 - 0.63)*	0.02 *(0.00 - 0.49)*	0.02 *(0.00 - 0.05)*	7.94 *(6.59 - 9.82)*	6.40 *(5.62 - 6.96)*	0.88 *(0.61 - 1.12)*	0.01 *(0.00 - 0.06)*	38.58 *(32.15 - 47.37)*	5.09 *(3.51 - 6.48)*
Indian Springs	36	58.34 *(55.06 - 60.61)*	0.03 *(0.00 - 0.08)*	25.34 *(24.21 - 26.86)*	0.01 *(0.00 - 0.04)*	0.41 *(0.29 - 0.53)*	0.01 *(0.00 - 0.07)*	0.01 *(0.00 - 0.04)*	7.93 *(6.78 - 9.47)*	6.35 *(5.56 - 6.83)*	0.85 *(0.60 - 1.10)*	0.01 *(0.00 - 0.05)*	38.81 *(33.45 - 46.76)*	4.93 *(3.51 - 6.43)*
Dry Gulch	29	57.66 *(55.89 -59.69)*	0.03 *(0.00 - 0.09)*	23.41 *(22.28 - 24.71)*	0.00 *(0.00 - 0.02)*	0.35 *(0.28 - 0.40)*	0.00 *(0.00 - 0.01)*	0.01 *(0.00 - 0.02)*	6.46 *(5.17 - 7.61)*	7.03 *(6.64 - 7.35)*	1.27 *(0.92 - 1.74)*	0.00 *(0.00 - 0.02)*	31.21 *(25.24 - 36.50)*	7.32 *(5.32 - 10.10)*
Little Creek	56	56.63 *(48.69 - 59.15)*	0.03 *(0.00 - 0.11)*	24.55 *(21.96 - 29.93)*	0.00 *(0.00 - 0.02)*	0.46 *(0.39 - 0.79)*	0.00 *(0.00 - 0.02)*	0.03 *(0.02 - 0.05)*	7.81 *(6.70 - 14.11)*	6.40 *(3.58 - 7.49)*	1.07 *(0.27 - 1.53)*	0.00 *(0.00 - 0.03)*	37.78 *(32.05 - 67.49)*	6.16 *(1.51 - 9.02)*
Wooden Shoe Butte	52	58.11 *(54.58 - 60.87)*	0.03 *(0.00 - 0.08)*	24.34 *(23.19 - 25.69)*	0.00 *(0.00 - 0.03)*	0.40 *(0.31 - 0.53)*	0.00 *(0.00 - 0.01)*	0.02 *(0.00 - 0.04)*	7.24 *(6.14 - 8.44)*	6.72 *(6.21 - 7.06)*	1.12 *(0.73 - 1.49)*	0.01 *(0.00 - 0.03)*	34.91 *(29.73 - 40.60)*	6.43 *(4.17 - 8.48)*
Steer Basin	70	59.78 *(55.46 - 63.25)*	0.02 *(0.00 - 0.05)*	24.16 *(20.71 - 25.31)*	0.01 *(0.00 - 0.05)*	0.37 *(0.26 - 0.64)*	0.01 *(0.00 - 0.07)*	0.01 *(0.00 - 0.09)*	6.97 *(5.20 - 9.00)*	6.58 *(5.55 - 7.33)*	1.24 *(0.46 - 2.76)*	0.01 *(0.00 - 0.06)*	34.23 *(25.93 - 43.40)*	7.28 *(3.84 - 17.75)*
Big Bluff	73	61.48 *(59.16 - 68.06)*	0.02 *(0.00 - 0.10)*	22.85 *(18.56 - 23.75)*	0.00 *(0.00 - 0.02)*	0.31 *(0.25 - 0.90)*	0.00 *(0.00 - 0.03)*	0.00 *(0.00 - 0.04)*	5.42 *(3.58 - 6.09)*	7.23 *(6.32 - 7.47)*	1.67 *(1.24 - 1.99)*	0.00 *(0.00 - 0.03)*	26.44 *(21.09 - 29.70)*	9.68 *(7.59 - 11.52)*
Magpie Basin	5	62.05 *(61.30 - 62.44)*	0.01 *(0.00 - 0.03)*	23.54 *(23.29 - 23.93)*	0.01 *(0.00 - 0.01)*	0.30 *(0.28 - 0.36)*	0.01 *(0.00 - 0.04)*	0.00 *(0.00 - 0.01)*	5.60 *(5.29 - 5.98)*	7.34 *(7.17 - 7.55)*	1.68 *(1.55 - 1.83)*	0.02 *(0.00 - 0.09)*	26.82 *(25.38 - 28.37)*	9.60 (8.73 - 10.54)
Sanidine														
Wooden Shoe Butte	5	65.65 *(65.35 - 65.83)*	0.09 *(0.03 - 0.16)*	18.80 *(18.55 - 19.05)*	0.01 *(0.00 - 0.07)*	0.16 *(0.11 - 0.20)*	0.00 *(0.00 - 0.01)*	0.00 *(0.00 - 0.00)*	0.49 *(0.35 - 0.66)*	4.16 *(3.92 - 4.44)*	9.54 *(8.90 - 9.87)*	0.01 *(0.00 - 0.03)*	2.53 *(1.81 - 3.38)*	58.60 *(55.09 - 61.25)*
Steer Basin	4	64.22 *(64.02 - 64.46)*	0.11 *(0.09 - 0.16)*	19.09 *(19.06 - 19.14)*	0.01 *(0.00 - 0.02)*	0.18 *(0.14 - 0.23)*	0.03 *(0.00 - 0.04)*	0.00 *(0.00 - 0.00)*	0.74 *(0.70 - 0.78)*	4.36 *(4.10 - 4.59)*	9.11 *(8.85 - 9.39)*	0.01 *(0.00 - 0.04)*	3.80 *(3.63 - 3.95)*	55.69 *(53.71 - 57.94)*
Big Bluff	35	63.99 *(63.40 - 64.55)*	0.04 *(0.01 - 0.07)*	18.85 *(18.67 - 19.02)*	0.00 *(0.00 - 0.02)*	0.14 *(0.10 - 0.22)*	0.01 *(0.00 - 0.03)*	0.00 *(0.00 - 0.00)*	0.72 *(0.60 - 0.89)*	4.44 *(4.29 - 5.00)*	9.18 *(8.38 - 9.54)*	0.01 *(0.00 - 0.03)*	3.66 *(3.06 - 4.53)*	55.51 *(50.37 - 57.25)*
Magpie Basin	20	64.68 *(63.75 - 65.57)*	0.08 *(0.01 - 0.15)*	19.21 *(18.78 - 20.07)*	0.01 *(0.00 - 0.05)*	0.14 *(0.09 - 0.27)*	0.00 *(0.00 - 0.02)*	0.00 *(0.00 - 0.02)*	0.77 *(0.47 - 1.44)*	4.69 *(4.18 - 5.66)*	8.96 *(6.85 -. 9.82)*	0.01 *(0.00 - 0.06)*	3.85 *(2.34 - 7.26)*	53.52 *(41.10 - 58.76)*

Table C.8. Average pyroxene compositions from members of the Cassia Formation. Values in brackets = data range

Member	n	SiO_2	TiO_2	Al_2O_3	Cr_2O_3	FeO	MnO	MgO	CaO	Na_2O	K_2O	NiO
Pigeonite												
Lincoln Reservoir Population 1	54	48.33 *(45.25 - 49.68)*	0.24 *(0.15 - 0.32)*	0.44 *(0.29 -0.71)*	0.01 *(0.00 - 0.02)*	35.35 *(33.46 - 37.25)*	1.17 *(1.09 - 1.26)*	8.76 *(7.84 - 9.43)*	5.00 *(4.50 - 6.18)*	0.07 *(0.04 - 0.11)*	0.00 *(0.00 - 0.02)*	0.00 *(0.00 - 0.02)*
Lincoln Reservoir Population 2	44	48.32 *(44.78 - 50.45)*	0.25 *(0.18 - 0.32)*	0.51 *(0.44 - 0.70)*	0.00 *(0.00 - 0.03)*	33.54 *(31.19 - 34.82)*	1.11 *(1.03 - 1.15)*	9.99 *(9.61 - 10.67)*	5.21 *(4.58 - 7.89)*	0.08 *(0.05 - 0.27)*	0.00 *(0.00 - 0.00)*	0.00 *(0.00 - 0.02)*
McMullen Creek	42	48.97 *(47.09 - 49.90)*	0.22 *(0.10 - 0.33)*	0.42 *(0.28 - 0.79)*	0.01 *(0.00 - 0.04)*	33.32 *(27.23 - 34.90)*	1.05 *(0.85 - 1.15)*	10.43 *(9.86 - 11.57)*	4.76 *(3.87 - 9.84)*	0.07 *(0.01 - 0.21)*	0.01 *(0.00 - 0.07)*	0.01 *(0.00 - 0.05)*
Indian Springs	34	48.87 *(46.08 - 50.28)*	0.21 *(0.10 - 0.36)*	0.41 *(0.21 - 0.95)*	0.01 *(0.00 - 0.07)*	33.53 *(30.67 - 34.58)*	1.06 *(0.97 - 1.15)*	10.36 *(9.05 - 13.14)*	4.43 *(3.81 - 5.93)*	0.07 *(0.00 - 0.15)*	0.02 *(0.00 - 0.13)*	0.01 *(0.00 - 0.07)*
Dry Gulch	20	46.21 *(44.64 - 47.49)*	0.21 *(0.16 - 0.26)*	0.34 *(0.28 - 0.44)*	0.00 *(0.00 - 0.02)*	35.68 *(34.41 - 36.30)*	1.14 *(1.08 - 1.18)*	8.94 *(8.68 - 9.11)*	4.50 *(4.26 - 5.57)*	0.06 *(0.05 - 0.08)*	0.00 *(0.00 - 0.00)*	0.01 *(0.00 - 0.03)*
Little Creek	27	48.43 *(46.77 - 51.03)*	0.20 *(0.14 - 0.29)*	0.41 *(0.38 - 0.45)*	0.01 *(0.00 - 0.03)*	30.21 *(29.42 - 30.68)*	0.90 *(0.86 - 0.95)*	13.67 *(13.21 - 15.47)*	3.91 *(3.68 - 4.13)*	0.07 *(0.04 - 0.17)*	0.00 *(0.00 - 0.00)*	0.01 *(0.00 - 0.04)*
Wooden Shoe Butte Population 1	7	48.68 *(48.31 - 49.40)*	0.19 *(0.12 - 0.27)*	0.37 *(0.30 - 0.47)*	0.00 *(0.00 - 0.03)*	35.77 *(34.93 - 36.13)*	1.02 *(0.97 - 1.04)*	9.41 *(9.31 - 9.66)*	4.38 *(4.04 - 5.14)*	0.06 *(0.05 - 0.08)*	0.00 *(0.00 - 0.00)*	0.01 *(0.00 - 0.03)*
Wooden Shoe Butte Population 2	26	47.57 *(45.20 - 49.56)*	0.23 *(0.18 - 0.30)*	0.45 *(0.38 - 0.95)*	0.00 *(0.00 - 0.02)*	33.68 *(32.24 - 34.25)*	0.97 *(0.91 - 0.99)*	10.49 *(9.77 - 10.72)*	4.60 *(4.15 - 5.84)*	0.07 *(0.04 - 0.15)*	0.01 *(0.00 - 0.17)*	0.01 *(0.00 - 0.03)*
Steer Basin	20	49.47 *(49.05 - 49.86)*	0.20 *(0.12 - 0.30)*	0.40 *(0.27 - 0.65)*	0.01 *(0.00 - 0.06)*	34.09 *(32.85 - 35.74)*	0.94 *(0.82 - 1.04)*	9.78 *(8.80 - 10.04)*	4.79 *(4.42 - 5.98)*	0.06 *(0.00 - 0.16)*	0.01 *(0.00 -0.04)*	0.01 *(0.00 - 0.04)*
Big Bluff	n/a	-	-	-	-	-	-	-	-	-	-	-
Magpie Basin	17	46.85 *(46.15 - 47.38)*	0.19 *(0.11 - 0.31)*	0.33 *(0.24 - 0.86)*	0.01 *(0.00 - 0.03)*	38.75 *(30.85 - 39.80)*	1.02 *(0.79 - 1.07)*	6.78 *(5.89 - 7.13)*	4.74 *(4.12 - 10.84)*	0.06 *(0.00 - 0.20)*	0.01 *(0.00 - 0.08)*	0.01 *(0.00 - 0.02)*
Augite												
Lincoln Reservoir Population 1	15	49.12 *(46.73 - 50.25)*	0.38 *(0.24 - 0.66)*	0.87 *(0.75 - 1.28)*	0.01 *(0.00 - 0.02)*	24.11 *(23.48 - 26.29)*	0.77 *(0.73 - 0.84)*	7.72 *(7.52 - 7.92)*	16.21 *(13.56 - 17.09)*	0.22 *(0.18 - 0.24)*	0.00 *(0.00 - 0.00)*	0.00 *(0.00 - 0.01)*
Lincoln Reservoir Population 2	18	48.84 *(46.59 - 50.36)*	0.38 *(0.30 - 0.47)*	0.94 *(0.78 - 1.36)*	0.01 *(0.00 - 0.03)*	23.31 *(22.80 - 24.09)*	0.75 *(0.72 - 0.79)*	8.44 *(7.82 - 8.88)*	16.14 *(14.94 - 16.95)*	0.22 *(0.17 - 0.26)*	0.00 *(0.00 - 0.00)*	0.01 *(0.00 - 0.03)*
McMullen Creek	17	49.25 *(47.66 - 50.66)*	0.37 *(0.27 - 0.48)*	0.88 *(0.63 - 1.05)*	0.01 *(0.00 - 0.04)*	22.24 *(18.31 - 30.31)*	0.68 *(0.53 - 0.92)*	9.58 *(8.92 - 10.88)*	15.65 *(8.09 - 17.91)*	0.22 *(0.12 - 0.28)*	0.00 *(0.00 - 0.02)*	0.01 *(0.00 - 0.06)*
Indian Springs	8	49.16 *(48.21 - 50.52)*	0.41 *(0.33 - 0.50)*	0.94 *(0.85 - 1.24)*	0.00 *(0.00 - 0.01)*	21.80 *(20.15 - 22.59)*	0.65 *(0.60 - 0.71)*	9.08 *(8.86 - 9.28)*	16.64 *(16.02 - 17.34)*	0.25 *(0.22 - 0.27)*	0.01 *(0.00 - 0.07)*	0.01 *(0.00 - 0.02)*
Dry Gulch	19	47.11 *(46.18 - 48.06)*	0.30 *(0.25 - 0.36)*	0.70 *(0.44 - 0.91)*	0.00 *(0.00 - 0.02)*	23.76 *(21.91 - 31.32)*	0.74 *(0.67 - 1.02)*	7.97 *(7.70 - 8.60)*	16.48 *(9.11 - 17.72)*	0.22 *(0.15 - 0.27)*	0.00 *(0.00 - 0.07)*	0.00 *(0.00 - 0.02)*
Little Creek	21	49.01 *(47.93 - 50.17)*	0.37 *(0.31 - 0.43)*	0.95 *(0.84 - 1.04)*	0.00 *(0.00 - 0.02)*	17.83 *(17.56 - 18.11)*	0.53 *(0.48 - 0.56)*	10.93 *(10.02 - 11.23)*	17.91 *(17.60 - 18.16)*	0.27 *(0.23 - 0.31)*	0.00 *(0.00 - 0.02)*	0.01 *(0.00 - 0.03)*
Wooden Shoe Butte	23	48.61 *(45.83 - 50.38)*	0.37 *(0.26 - 0.48)*	0.89 *(0.77 - 1.18)*	0.01 *(0.00 - 0.02)*	21.82 *(20.71 - 22.99)*	0.60 *(0.57 - 0.65)*	8.92 *(8.44 - 9.24)*	17.08 *(14.96 - 17.72)*	0.25 *(0.19 - 0.62)*	0.00 *(0.00 - 0.01)*	0.01 *(0.00 - 0.03)*
Steer Basin	8	49.76 *(48.19 - 50.37)*	0.34 *(0.28 - 0.40)*	0.82 *(0.73 - 1.04)*	0.01 *(0.00 - 0.02)*	22.61 *(21.76 - 23.83)*	0.60 *(0.53 - 0.64)*	8.44 *(8.09 - 8.64)*	16.57 *(15.35 - 17.03)*	0.21 *(0.13 - 0.28)*	0.01 *(0.00 - 0.02)*	0.02 *(0.00 - 0.03)*
Big Bluff	22	47.55 *(46.19 - 49.24)*	0.35 *(0.29 - 0.43)*	0.65 *(0.50 - 0.99)*	0.01 *(0.00 - 0.03)*	27.15 *(25.19 - 32.95)*	0.63 *(0.56 - 0.85)*	3.75 *(3.26 - 4.54)*	17.01 *(13.24 - 18.40)*	0.21 *(0.13 - 0.30)*	0.02 *(0.00 - 0.37)*	0.00 *(0.00 - 0.02)*
Magpie Basin	44	47.91 *(46.11 - 48.59)*	0.31 *(0.25 - 0.38)*	0.67 *(0.59 - 0.76)*	0.01 *(0.00 - 0.04)*	25.78 *(24.02 - 27.04)*	0.64 *(0.60 - 0.68)*	6.36 *(5.95 - 7.51)*	16.59 *(15.60 - 17.42)*	0.21 *(0.16 - 0.28)*	0.00 *(0.00 - 0.03)*	0.01 *(0.00 - 0.03)*

Table C.9. Average feldspar compositions from rhyolitic units of the Kimberly bore-hole. Values in brackets = data range

member	*n*	SiO_2	TiO_2	Al_2O_3	Cr_2O_3	FeO	MnO	MgO	CaO	Na_2O	K_2O	NiO	An%	Or%
Kimberly Rhyolite 1														
Plagioclase	72	57.35 *(54.55 - 59.05)*	0.04 *(0.00 - 0.10)*	23.07 *(21.97 - 24.56)*	0.00 *(0.00 - 0.04)*	0.43 *(0.38 - 0.51)*	0.00 *(0.00 - 0.01)*	0.00 *(0.00 - 0.05)*	6.94 *(6.05 - 9.02)*	6.95 *(6.04 - 7.30)*	1.21 *(0.82 - 2.29)*	0.00 *(0.00 - 0.03)*	33.12 *(29.15 - 43.02)*	6.88 *(4.56 - 13.13)*
Kimberly Rhyolite 2														
Plagioclase	3	59.18 *(58.68 - 59.49)*	0.04 *(0.03 - 0.07)*	21.67 *(21.29 - 22.03)*	0.00 *(0.00-0.01)*	0.29 *(0.25 - 0.34)*	0.01 *(0.00 - 0.02)*	0.01 *(0.00 - 0.01)*	5.18 *(4.86 - 5.64)*	7.70 *(7.62 -7.79)*	1.51 *(1.30 - 1.65)*	0.00 *(0.00 - 0.01)*	13.92 *(23.55 - 26.65)*	8.59 *(7.37 - 9.46)*
Anorthoclase	16	61.23 *(60.06 - 62.02)*	0.03 *(0.00 - 0.06)*	19.79 *(19.21 - 20.28)*	0.00 *(0.00 - 0.03)*	0.22 *(0.16 - 0.28)*	0.00 *(0.00 - 0.02)*	0.00 *(0.00 - 0.01)*	2.88 *(2.58 - 3.08)*	7.39 *(7.03 - 7.80)*	3.72 *(3.24 - 4.43)*	0.01 *(0.00 - 0.03)*	13.92 *(12.57 - 14.86)*	21.44 *(18.48 - 25.53)*
Sanidine	9	63.17 *(61.46 - 72.20)*	0.05 *(0.00 - 0.22)*	17.39 *(10.98 - 18.49)*	0.00 *(0.00 - 0.00)*	0.33 *(0.13 - 1.63)*	0.01 *(0.00 - 0.03)*	0.01 *(0.00 - 0.06)*	0.91 *(0.53 - 1.07)*	5.39 *(3.03 - 6.10)*	7.22 *(5.38 - 8.37)*	0.01 *(0.00 - 0.03)*	4.67 *(3.71 - 5.27)*	44.99 (40.50 - 51.62)
Kimberly Rhyolite 3														
Plagioclase	28	57.88 *(54.82 - 59.87)*	0.04 *(0.01 - 0.09)*	22.24 *(20.16 - 23.76)*	0.00 *(0.00 - 0.02)*	0.37 *(0.24 - 0.54)*	0.00 *(0.00 - 0.02)*	0.00 *(0.00 - 0.05)*	6.13 *(4.83 - 7.85)*	7.15 *(6.52 - 7.71)*	1.54 *(0.99 - 2.35)*	0.00 *(0.00 - 0.02)*	29.35 *(23.18 - 37.64)*	8.76 *(5.70 - 13.58)*
Sanidine	2	61.32 *(61.14 - 61.50)*	0.05 *(0.04 - 0.05)*	18.12 *(18.10- 18.15)*	0.00 *(0.00 - 0.00)*	0.19 *(0.18 - 0.20)*	0.00 *(0.00 - 0.00)*	0.00 *(0.00 - 0.01)*	0.84 *(0.80 - 0.89)*	4.91 *(4.86 - 4.95)*	8.06 *(8.03 - 8.09)*	0.01 *(0.00 - 0.02)*	4.42 *(4.24 - 4.60)*	49.65 *(49.20 - 50.10)*

Table C.10. Average pyroxene compositions from rhyolitic units of the Kimberly bore-hole. Values in brackets = data range

Member	*n*	SiO_2	TiO_2	Al_2O_3	Cr_2O_3	FeO	MnO	MgO	CaO	Na_2O	K_2O	NiO
Pigeonite												
Kimberly Rhyolite 1	18	48.91 *(48.27 - 49.68)*	0.24 *(0.17 - 0.29)*	0.41 *(0.38 - 0.44)*	0.01 *(0.00 - 0.03)*	29.25 *(28.95 - 29.68)*	0.94 *(0.92 - 0.98)*	16.63 *(16.36 - 16.82)*	1.76 *(1.72 - 1.79)*	0.03 *(0.00 - 0.08)*	0.00 *(0.00 - 0.00)*	0.01 *(0.00 - 0.03)*
Kimberly Rhyolite 2	4	46.52 *(46.12 - 46.89)*	0.19 *(0.16 - 0.24)*	0.26 *(0.20 - 0.37)*	0.00 *(0.00 - 0.00)*	37.87 *(36.73 - 38.51)*	1.54 *(1.47 - 1.60)*	7.59 *(7.06 - 9.08)*	4.10 *(3.48 - 4.37)*	0.07 *(0.03 - 0.10)*	0.00 *(0.00 - 0.00)*	0.00 *(0.00 - 0.00)*
Kimberly Rhyolite 3	19	48.22 *(46.78 - 49.21)*	0.20 *(0.14 - 0.23)*	0.30 *(0.25 - 0.42)*	0.00 *(0.00 - 0.03)*	30.66 *(29.63 - 31.42)*	1.09 *(1.03 - 1.14)*	13.40 *(12.78 - 13.71)*	3.84 *(3.66 - 5.12)*	0.06 *(0.01 - 0.12)*	0.00 *(0.00 - 0.00)*	0.01 *(0.00 - 0.00)*
Augite												
Kimberly Rhyolite 1	60	48.92 *(47.93 - 49.70)*	0.36 *(0.27 - 0.56)*	0.90 *(0.77 - 1.63)*	0.01 *(0.00 - 0.04)*	16.03 *(15.71 - 16.48)*	0.58 *(0.53 - 0.64)*	11.89 *(11.51 - 12.19)*	18.73 *(18.25 - 19.24)*	0.31 *(0.24 - 0.38)*	0.00 *(0.00 - 0.01)*	0.01 *(0.00 - 0.03)*
Kimberly Rhyolite 2	32	47.25 *(46.47 - 47.83)*	0.29 *(0.21 - 0.35)*	0.61 *(0.51 - 1.24)*	0.01 *(0.00 - 0.03)*	25.54 *(24.00 - 27.58)*	0.97 *(0.00 - 1.07)*	6.27 *(5.67 - 7.31)*	16.74 *(15.08 - 17.28)*	0.23 *(0.16 - 0.30)*	0.02 *(0.00 - 0.36)*	0.00 *(0.00 - 0.03)*
Kimberly Rhyolite 3	18	48.61 *(48.09 - 49.03)*	0.33 *(0.25 - 0.41)*	0.77 *(0.67 - 0.91)*	0.01 *(0.00 - 0.02)*	18.33 *(17.74 - 19.54)*	0.64 *(0.60 - 0.69)*	10.94 *(10.62 - 11.36)*	17.78 *(16.93 - 18.20)*	0.29 *(0.23 - 0.35)*	0.00 *(0.00 - 0.00)*	0.00 *(0.00 - 0.03)*

Table C.11. Average feldspar compositions from other rhyolitic units discussed in this thesis. Values in brackets = data range

Member	n	SiO_2	TiO_2	Al_2O_3	Cr_2O_3	FeO	MnO	MgO	CaO	Na_2O	K_2O	NiO	An%	Or%
Plagioclase														
'Three Creek Ignimbrite'	22	59.00 *(57.76 - 60.05)*	0.03 *(0.00 - 0.08)*	24.88 *(24.02 - 25.51)*	0.00 *(0.00 - 0.01)*	0.46 *(0.38 - 0.51)*	0.00 *(0.00 - 0.01)*	0.02 *(0.00 - 0.05)*	7.57 *(6.63 - 8.45)*	6.28 *(5.84 - 6.75)*	0.90 *(0.75 - 1.13)*	0.00 *(0.00 - 0.02)*	37.87 *(32.85 - 42.36)*	5.32 *(4.50 - 6.63)*
'Browns Bench 11'	17	59.91 *(59.31 - 60.99)*	0.03 *(0.00 - 0.08)*	24.86 *(24.29 - 25.43)*	0.01 *(0.00 - 0.04)*	0.46 *(0.38 - 0.53*	0.01 *(0.00 - 0.06)*	0.01 *(0.00 - 0.05)*	7.45 *(6.98 - 7.90)*	6.62 *(6.44 - 6.88)*	1.11 *(0.98 - 1.20)*	0.01 *(0.00 - 0.04)*	35.91 *(33.80 - 37.76)*	6.39 *(5.50 - 6.92)*

Table C.12. Average pyroxene compositions from other rhyolitic units discussed in this thesis. Values in brackets = data range

Member	n	SiO_2	TiO_2	Al_2O_3	Cr_2O_3	FeO	MnO	MgO	CaO	Na_2O	K_2O	NiO
Pigeonite												
'Three creek ignumbrite'	20	49.07 *(48.64 - 49.47)*	0.27 *(0.20 - 0.39)*	0.51 *(0.39 - 0.75)*	0.01 *(0.00 - 0.04)*	33.43 *(30.30 - 34.95)*	1.10 *(1.01 - 1.21)*	9.52 *(8.45 - 10.14)*	5.23 *(4,74 - 9.02)*	0.07 *(0.03 - 0.01)*	0.00 *(0.00 - 0.01)*	0.00 *(0.00 - 0.02)*
'Browns Bench 11'	17	51.29 *(50.48 - 51.83)*	0.21 *(0.12 - 0.83)*	0.39 *(0.26 - 0.66)*	0.01 *(0.00 - 0.05)*	29.91 *(29.47 - 30.41)*	0.95 *(0.86 - 1.01)*	13.81 *(13.27 - 14.06)*	3.91 *(3.77 - 3.99)*	0.06 *(0.00 - 0.13)*	0.02 *(0.00 - 0.09)*	0.02 *(0.00 - 0.08)*
Augite												
'Three creek ignumbrite'	8	49.74 *(49.36 - 50.00)*	0.39 *(0.35 - 0.44)*	0.90 *(0.84 - 0.96)*	0.01 *(0.00 - 0.03)*	22.88 *(22.29 - 23.90)*	0.74 *(0.73 - 0.78)*	8.49 *(8.29 - 8.67)*	15.84 *(15.03 - 16.05)*	0.22 *(0.19 - 0.28)*	0.00 *(0.00 - 0.00)*	0.00 *(0.00 - 0.02)*
'Browns Bench 11'	10	51.65 *(49.71 - 57.43)*	0.37 *(0.27 - 0.50)*	1.22 *(0.71 - 3.85)*	0.01 *(0.00 - 0.03)*	17.42 *(13.85 - 18.51)*	0.54 *(0.43 - 0.62)*	10.73 *(7.94 - 11.31)*	17.47 *(13.88 - 18.19)*	0.33 *(0.24 - 0.72)*	0.14 *(0.00 - 1.25)*	0.00 *(0.00 - 0.03)*

Table C.13. Results of $^{40}Ar/^{39}Ar$ geochronology laser fusion experiments of all rhyolitic units of the Kimberly bore-hole.

Kimberly Rhyolite 1 (A2-6400-6411)

Run_ID	Ar40_	Ar39_	Ar37_	Ar36_	Age	Age_Er
90624-07-44151	0.3908	0.0135	0.0007	0.00119	10.05	1.81
90624-08-44152	0.0455	0.0048	0.0002	0.00012	8.59	5.49
90624-10-44155	0.0663	0.0069	0.0003	0.00016	10.16	3.25
90624-11-44159	0.1069	0.0163	0.0007	0.00020	10.78	1.38
90624-12-44160	0.5041	0.0058	0.0002	0.00168	2.00	4.89
90624-13-44162	0.0949	0.0054	0.0003	0.00028	7.55	4.30
90624-14-44163	0.1155	0.0068	0.0004	0.00036	5.42	3.93
90624-15-44167	0.1339	0.0142	0.0005	0.00038	5.70	1.64
90624-16-44168	0.1445	0.0033	0.0001	0.00047	3.99	6.71
90624-17-44170	0.1209	0.0090	0.0003	0.00032	10.53	2.45
90624-18-44171	0.0422	0.0045	0.0002	0.00007	18.97	5.53
90624-19-44175	0.0346	0.0061	0.0002	0.00003	16.02	4.10
90624-20-44176	0.0791	0.0050	0.0003	0.00017	21.90	6.11
90624-21-44178	0.1012	0.0086	0.0003	0.00030	5.24	3.01
90624-22-44179	0.1070	0.0070	0.0003	0.00030	8.80	3.69
90624-23-44183	0.0654	0.0045	0.0002	0.00017	13.56	5.37
90624-24-44184	0.0938	0.0071	0.0002	0.00031	0.72	3.11
90624-25-44186	0.0813	0.0053	0.0002	0.00025	4.06	4.65
90624-26-44187	0.0476	0.0086	0.0004	0.00007	11.47	3.20
90624-27-44191	0.1813	0.0056	0.0002	0.00057	6.86	4.19
90624-28-44192	0.2766	0.0071	0.0003	0.00089	5.66	3.78
90624-29-44194	0.0366	0.0083	0.0004	0.00003	12.35	3.23
90624-30-44195	0.2257	0.0113	0.0004	0.00069	7.11	2.32
90624-31-44199	0.0399	0.0071	0.0003	0.00006	12.18	3.70
90624-32-44200	0.0871	0.0055	0.0003	0.00025	8.79	4.87

Kimberly Rhyolite 1 (A2-2102-2106)

90631-01-44275	0.0194	0.0075	0.0004	0.00005	3.18	2.23
90631-02-44276	0.0213	0.0082	0.0004	0.00008	-0.58	1.94
90631-03-44280	0.0237	0.0103	0.0005	0.00004	4.59	1.45
90631-04-44281	0.0265	0.0108	0.0005	0.00004	5.41	1.46
90631-05-44283	0.0289	0.0114	0.0005	0.00002	7.73	1.70
90631-06-44284	0.0077	0.0031	0.0001	0.00000	10.86	6.33
90631-07-44288	0.0133	0.0053	0.0003	0.00002	4.45	2.98
90631-08-44289	0.0169	0.0069	0.0003	0.00004	3.36	2.16
90631-09-44291	1.2511	0.1623	0.0000	-0.00002	28.78	0.09
90631-10-44292	0.0219	0.0093	0.0003	0.00001	8.13	1.44
90631-11-44296	0.0202	0.0079	0.0003	0.00000	9.53	2.11
90631-12-44297	0.0234	0.0100	0.0005	0.00002	6.37	1.94
90631-13-44299	0.0157	0.0065	0.0003	-0.00001	11.36	2.05
90631-14-44300	0.0048	0.0016	0.0001	0.00000	10.88	10.95
90631-15-44304	0.0149	0.0059	0.0003	0.00001	7.12	3.30
90631-16-44305	0.0166	0.0063	0.0002	-0.00002	13.30	2.50
90631-17-44307	0.0129	0.0053	0.0003	-0.00001	12.47	3.00
90631-18-44308	0.0228	0.0090	0.0005	0.00000	9.98	1.84
90631-19-44312	0.0315	0.0100	0.0005	0.00001	10.38	1.66
90631-20-44313	0.0217	0.0090	0.0004	-0.00002	11.30	1.84
90631-21-44315	0.0321	0.0128	0.0005	-0.00001	10.59	1.37
90631-22-44316	0.0241	0.0096	0.0005	-0.00001	10.20	1.92
90631-23-44320	0.0154	0.0066	0.0004	-0.00002	12.64	2.39
90631-24-44321	0.0208	0.0083	0.0004	-0.00003	13.15	1.70
90631-25-44323	0.0092	0.0026	0.0001	-0.00003	24.06	6.72
90631-26-44324	0.0164	0.0063	0.0003	0.00000	9.56	2.24
90631-27-44328	0.0336	0.0136	0.0005	0.00001	8.23	1.36
90631-28-44329	0.0199	0.0075	0.0004	-0.00001	11.35	2.71
90631-29-44331	0.0345	0.0139	0.0006	0.00002	8.16	1.48
90631-30-44332	0.0172	0.0072	0.0003	-0.00001	10.77	2.20
90631-31-44336	0.0168	0.0060	0.0003	-0.00001	12.85	4.78
90631-32-44337	0.0181	0.0062	0.0004	0.00001	10.14	4.22

Table C.13. Results of $^{40}Ar/^{39}Ar$ geochronology laser fusion experiments of all rhyolitic units of the Kimberly bore-hole. Continued...

Kimberly Rhyolite 2 (A2-1945-1953)

Run_ID	Ar40_	Ar39_	Ar37_	Ar36_	Age	Age_Er
90637-01-44339	0.0846	0.0357	0.0004	0.00006	6.94	0.64
90637-02-44340	0.0208	0.0085	0.0006	0.00003	5.07	3.34
90637-03-44344	0.1043	0.0442	0.0003	-0.00001	9.13	0.59
90637-04-44345	0.0624	0.0243	0.0004	0.00000	9.65	1.13
90637-05-44347	0.0906	0.0393	0.0005	0.00002	7.96	0.61
90637-06-44348	0.1055	0.0474	0.0003	0.00005	7.24	0.47
90637-07-44352	0.0796	0.0328	0.0002	0.00002	8.42	0.72
90637-08-44353	0.0769	0.0348	0.0004	0.00001	8.11	0.70
90637-09-44355	0.0434	0.0136	0.0005	0.00006	7.21	1.63
90637-10-44356	0.0196	0.0068	0.0004	0.00002	7.72	3.39
90637-11-44360	0.0375	0.0115	0.0005	0.00006	6.51	2.04
90637-12-44361	0.0600	0.0143	0.0007	0.00005	11.77	1.48
90637-13-44363	0.1337	0.0617	0.0004	0.00002	7.82	0.39
90637-14-44364	0.0682	0.0299	0.0003	-0.00002	9.09	0.78
90637-15-44368	0.1313	0.0490	0.0003	0.00005	8.79	0.49
90637-16-44369	0.0657	0.0292	0.0002	0.00003	7.31	0.80
90637-17-44371	0.0864	0.0395	0.0003	-0.00001	8.42	0.66
90637-18-44372	0.1067	0.0437	0.0003	0.00003	8.33	0.55
90637-19-44376	0.0578	0.0221	0.0003	0.00003	8.16	1.29
90637-20-44377	0.0897	0.0384	0.0003	0.00000	8.77	0.66
90637-21-44379	0.0607	0.0281	0.0002	0.00000	8.14	0.91
90637-22-44380	0.1426	0.0605	0.0004	0.00004	8.01	0.42
90637-23-44384	0.1177	0.0505	0.0003	0.00006	7.33	0.46
90637-24-44385	0.0351	0.0109	0.0004	0.00006	5.86	2.09
90637-25-44387	0.0620	0.0286	0.0002	0.00005	6.24	0.89
90637-26-44388	0.1033	0.0313	0.0002	0.00008	9.31	0.75
90637-27-44392	0.1200	0.0510	0.0002	0.00007	7.31	0.50
90637-28-44393	0.0787	0.0361	0.0002	0.00003	7.32	0.64
90637-29-44395	0.0966	0.0377	0.0002	0.00004	8.37	0.63
90637-30-44396	0.0364	0.0117	0.0005	0.00004	7.87	1.97
90637-31-44400	0.0679	0.0207	0.0002	0.00004	10.04	1.32
90637-32-44401	0.0188	0.0072	0.0003	0.00002	7.42	3.63

Kimberly Rhyolite 2 (A2-1945-1953)

90639-01-44559	0.10642	0.04608	0.00046	0.00003	8.01	0.62
90639-02-44560	0.03680	0.00988	0.00057	0.00002	11.36	2.37
90639-03-44562	0.22191	0.09767	0.00056	0.00007	7.67	0.26
90639-04-44563	0.18088	0.08106	0.00051	0.00006	7.49	0.34
90639-05-44567	0.14356	0.06440	0.00046	0.00009	6.84	0.39
90639-06-44614	0.15354	0.06715	0.00033	0.00005	7.81	0.39
90639-07-44615	0.15749	0.06434	0.00025	0.00003	8.67	0.42
90639-09-44618	0.12193	0.05391	0.00070	0.00005	7.38	0.49
90639-10-44622	0.09636	0.04319	0.00022	-0.00001	8.54	0.61
90639-11-44623	0.22354	0.09966	0.00034	0.00006	7.75	0.26
90639-12-44625	0.22714	0.10481	0.00014	0.00000	8.11	0.24
90639-13-44626	0.18271	0.07587	0.00030	0.00010	7.50	0.31
90639-14-44630	0.07283	0.02791	0.00063	0.00003	8.61	0.99
90639-15-44631	0.10881	0.04968	0.00029	0.00002	7.72	0.49
90639-16-44633	0.15178	0.06922	0.00016	0.00001	8.05	0.48
90639-17-44634	0.04703	0.01796	0.00051	0.00010	3.86	1.39
90639-18-44638	0.19486	0.08821	0.00016	0.00001	8.15	0.35
90639-19-44639	0.08935	0.03983	0.00041	0.00005	6.88	0.67
90639-20-44641	0.18251	0.08100	0.00014	0.00005	7.75	0.32
90639-21-44642	0.19410	0.08492	0.00027	0.00003	8.11	0.32
90639-22-44646	0.12867	0.05872	0.00026	0.00004	7.40	0.45
90639-23-44647	0.13064	0.05877	0.00032	0.00003	7.71	0.48
90639-24-44649	0.12135	0.05265	0.00023	0.00001	8.34	0.50
90639-25-44650	0.11037	0.04881	0.00026	0.00005	7.33	0.57
90639-26-44654	0.02358	0.01068	0.00003	0.00004	3.60	2.72
90639-27-44655	0.15735	0.06960	0.00029	0.00002	8.14	0.39
90639-28-44657	0.10665	0.04718	0.00027	0.00007	6.87	0.54
90639-29-44658	0.13142	0.05719	0.00020	0.00009	6.85	0.43
90639-30-44662	0.12495	0.05500	0.00032	0.00005	7.51	0.51
90639-31-44663	0.21317	0.09622	0.00009	0.00005	7.69	0.26
90639-32-44665	0.10145	0.04550	0.00024	0.00002	7.81	0.55
90639-33-44666	0.11780	0.05198	0.00031	0.00009	6.53	0.52
90639-34-44670	0.09257	0.03910	0.00032	0.00001	8.69	0.71
90639-35-44671	0.09310	0.04297	0.00036	0.00004	7.11	0.58
90639-36-44673	0.06238	0.02817	0.00018	0.00004	6.84	0.84
90639-37-44674	0.11104	0.04872	0.00027	0.00000	8.46	0.53

Table C.13. Results of $^{40}Ar/^{39}Ar$ geochronology laser fusion experiments of all rhyolitic units of the Kimberly bore-hole. Continued...

Kimberly Rhyolite 3 (A2-751-754)

Run_ID	Ar40_	Ar39_	Ar37_	Ar36_	Age	Age_Er
90631-01-44275	0.01938	0.00751	0.00040	0.00005	3.18	2.23
90632-01-44205	0.01723	0.00914	0.00032	-0.00006	13.94	2.28
90632-02-44206	0.02048	0.00979	0.00042	0.00004	3.34	2.29
90632-03-44210	0.02000	0.01078	0.00049	-0.00004	11.35	2.00
90632-04-44211	0.03162	0.01312	0.00058	0.00001	8.68	1.95
90632-05-44213	0.01705	0.00721	0.00039	-0.00002	12.12	3.31
90632-06-44214	0.03257	0.01371	0.00072	0.00004	5.70	1.52
90632-07-44218	0.01383	0.00736	0.00032	0.00002	3.86	3.13
90632-08-44219	0.01567	0.00926	0.00032	0.00002	4.03	2.40
90632-09-44221	0.00877	0.00344	0.00020	0.00000	8.19	6.23
90632-10-44222	0.03847	0.01207	0.00044	0.00003	8.94	1.77
90632-11-44226	0.01023	0.00500	0.00025	-0.00003	14.40	5.08
90632-12-44227	0.02045	0.00550	0.00029	0.00000	14.36	4.78
90632-13-44229	0.00835	0.00407	0.00021	-0.00002	14.04	5.82
90632-14-44230	0.01329	0.00400	0.00032	0.00002	8.09	5.34
90632-15-44234	0.02159	0.00970	0.00038	0.00000	8.51	2.81
90632-16-44235	0.02364	0.00920	0.00048	0.00001	8.42	2.24
90632-17-44237	0.01335	0.00598	0.00025	0.00002	5.01	3.70
90632-18-44238	0.01034	0.00579	0.00028	0.00001	4.91	3.56
90632-19-44242	0.01913	0.00676	0.00031	0.00001	8.41	3.38
90632-21-44245	0.01930	0.00672	0.00027	0.00000	10.57	3.17
90632-22-44246	0.01836	0.00538	0.00025	0.00006	1.08	4.58
90632-23-44250	0.00971	0.00408	0.00020	-0.00005	21.78	4.40
90632-24-44251	0.01480	0.00776	0.00053	0.00005	0.26	3.18
90632-25-44253	0.01322	0.00566	0.00049	0.00004	1.13	4.07
90632-26-44254	0.02761	0.00766	0.00031	0.00004	7.76	2.69
90632-27-44264	0.00518	0.00277	0.00009	-0.00001	11.76	7.26
90632-30-44270	0.01992	0.00749	0.00036	0.00003	6.39	3.64
90632-31-44272	0.00614	0.00318	0.00012	0.00000	6.66	8.68

Table C.14. U-Pb Geochronology data from select members of the Cassia Formation. Data obtained by SIMS analysis of zircons.

Sample and spot number	U (ppm)	Th (ppm)	Pb (ppm)	Th/U	^{204}Pb (ppb)	$^{207}Pb/^{206}Pb$	$\pm1\sigma$	$^{207}Pb/^{235}U$	$\pm1\sigma$	$^{206}Pb/^{238}U$	$\pm1\sigma$	Rho	$^{206}Pb/^{238}U$ [Ma]	$\pm1\sigma$ [Ma]	$^{206}Pb/^{207}Pb$ [Ma]	$\pm1\sigma$ [Ma]
McMullen Creek Member: RC-10.1-006 (20 zircons)																
McM2-RH1	91.2	48.6	0.55	0.13	0.28	0.0618	0.0106	0.0122	0.0021	0.0014	0.00004	0.1452	9.2	0.2	-	-
McM2-1-2	144.0	96.8	0.21	0.69	0.21	0.0323	0.0035	0.0062	0.0007	0.0014	0.00004	0.2380	9.0	0.2	-	-
McM2-2-1	73.0	34.5	0.10	0.48	0.14	0.0357	0.0052	0.0072	0.0011	0.0015	0.00006	0.2774	9.4	0.4	-	-
McM2-3-1	70.5	34.3	0.10	0.50	0.09	0.0509	0.0082	0.0100	0.0016	0.0014	0.00004	0.1579	9.2	0.2	-	-
McM2-4-1	116.4	88.9	0.16	0.78	0.09	0.0553	0.0069	0.0100	0.0013	0.0013	0.00003	0.1782	8.4	0.2	-	-
McM2-5-1	137.1	101.7	0.20	0.76	0.21	0.0354	0.0038	0.0066	0.0008	0.0014	0.00005	0.3067	8.8	0.3	-	-
McM2-6-1	133.5	74.4	0.20	0.57	0.06	0.0468	0.0066	0.0093	0.0013	0.0014	0.00005	0.2409	9.3	0.3	-	-
McM2-6-2	110.5	63.9	0.15	0.59	0.12	0.0393	0.0064	0.0074	0.0012	0.0014	0.00004	0.1806	8.8	0.3	-	-
McM2-6-3	66.3	32.0	0.08	0.50	0.12	0.0373	0.0082	0.0068	0.0015	0.0013	0.00004	0.1488	8.6	0.3	-	-
McM2-7-1	51.0	27.0	0.06	0.54	0.12	0.0311	0.0079	0.0057	0.0015	0.0013	0.00006	0.1693	8.6	0.4	-	-
McM2-8-1	2392.3	2947.5	4.95	1.26	1.65	0.0431	0.0017	0.0098	0.0005	0.0017	0.00004	0.5112	10.7	0.2	-	-
McM2-9-1	119.0	64.0	0.16	0.55	0.14	0.0407	0.0056	0.0074	0.0010	0.0013	0.00004	0.2075	8.5	0.2	-	-
McM2-10-1	139.5	98.1	0.22	0.72	0.08	0.0497	0.0035	0.0098	0.0007	0.0014	0.00004	0.3699	9.2	0.3	-	-
McM2-13-1	144.7	68.3	0.23	0.48	0.36	0.0371	0.0031	0.0080	0.0007	0.0016	0.00005	0.3653	10.1	0.3	-	-
McM2-14-1	97.5	60.9	0.14	0.64	0.19	0.0331	0.0075	0.0063	0.0014	0.0014	0.00004	0.1286	8.9	0.3	-	-
McM2-15-1	279.3	183.3	0.42	0.67	0.44	0.0502	0.0044	0.0101	0.0009	0.0015	0.00004	0.2725	9.4	0.2	-	-
McM2-16-1	265.6	138.3	0.40	0.53	0.25	0.0396	0.0031	0.0079	0.0006	0.0014	0.00003	0.2462	9.3	0.2	-	-
McM2-17-1	610.3	258.1	0.87	0.43	0.35	0.0438	0.0016	0.0085	0.0004	0.0014	0.00002	0.4181	9.1	0.2	-	-
McM2-18-1	343.4	305.9	0.52	0.91	2.19	0.0381	0.0054	0.0075	0.0011	0.0014	0.00003	0.1349	9.2	0.2	-	-
McM2-19-1	94.3	131.9	26.59	1.43	0.52	0.0917	0.0006	2.7116	0.0463	0.2143	0.00341	0.9306	1252	18	1462	12
McM2-19-2	72.5	42.1	0.09	0.60	0.23	0.0414	0.0064	0.0073	0.0012	0.0013	0.00004	0.2042	8.3	0.3	-	-
McM2-19-3	334.9	800.2	129.09	2.45	0.73	0.0916	0.0002	3.0978	0.0415	0.2453	0.00323	0.9822	1414	17	1459	4
McM2-20-1	136.8	111.8	0.19	0.84	0.17	0.0334	0.0037	0.0063	0.0007	0.0014	0.00004	0.2684	8.8	0.3	-	-
McM2-21-1	93.0	52.5	0.13	0.58	0.06	0.0410	0.0042	0.0078	0.0008	0.0014	0.00003	0.2332	8.9	0.2	-	-
Indian Springs Member: RC-10.1-010 (12 zircons)																
McM1-RH1	228.2	153.9	0.35	0.69	0.45	0.0515	0.0037	0.0100	0.0008	0.0014	0.00004	0.3625	9.0	0.3	-	-
McM1-RH2	112.2	83.1	0.16	0.76	0.33	0.0436	0.0060	0.0080	0.0011	0.0013	0.00004	0.1983	8.6	0.2	-	-
McM1-RH3	969.4	896.4	1.60	0.95	0.89	0.0407	0.0017	0.0079	0.0004	0.0014	0.00002	0.3451	9.1	0.1	-	-
McM1-RH4	158.4	126.0	0.23	0.82	0.27	0.0328	0.0048	0.0060	0.0009	0.0013	0.00003	0.1579	8.6	0.2	-	-
McM1-RH6	105.0	59.6	0.14	0.58	0.47	0.0399	0.0130	0.0077	0.0025	0.0014	0.00004	0.0896	9.0	0.3	-	-
McM1-6-1	149.7	119.1	0.14	0.82	0.88	0.0296	0.0190	0.0057	0.0037	0.0014	0.00003	0.0344	9.1	0.2	-	-
McM1-RH7	109.5	62.5	0.17	0.59	0.16	0.0449	0.0050	0.0096	0.0011	0.0015	0.00005	0.2686	10.0	0.3	-	-
McM1-RH9	87.1	44.8	0.12	0.53	0.22	0.0511	0.0085	0.0095	0.0016	0.0013	0.00005	0.2118	8.7	0.3	-	-
McM1-RH10	440.3	165.4	0.63	0.39	0.67	0.0444	0.0043	0.0087	0.0009	0.0014	0.00003	0.1920	9.1	0.2	-	-
McM1-11-1	188.1	158.4	1.21	0.86	0.56	0.0442	0.0018	0.0347	0.0015	0.0057	0.00008	0.3178	36.6	0.5	-	-
McM1-RH11	263.3	588.5	2.03	2.29	1.56	0.0257	0.0015	0.0179	0.0011	0.0050	0.00007	0.2291	32.4	0.4	-	-
McM1-RH5	268.2	102.3	1.43	0.39	0.66	0.0453	0.0009	0.0331	0.0008	0.0053	0.00007	0.5423	34.1	0.4	-	-

Table C.14. U-Pb Geochronology data from select members of the Cassia Formation. Data obtained by SIMS analysis of zircons. Continued...

Sample and spot number	U (ppm)	Th (ppm)	Pb (ppm)	Th/U	^{204}Pb (ppb)	$^{207}Pb/^{206}Pb$	$\pm1\sigma$	$^{207}Pb/^{235}U$	$\pm1\sigma$	$^{206}Pb/^{238}U$	$\pm1\sigma$	Rho	$^{206}Pb/^{238}U$ [Ma]	$\pm1\sigma$ [Ma]	$^{206}Pb/^{207}Pb$ [Ma]	$\pm1\sigma$ [Ma]
Little Creek Member: RC-11.1-004 (19 zircons)																
UWS-2-1	82.1	43.6	0.12	0.54	0.23	0.0343	0.0088	0.0069	0.0018	0.0015	0.00005	0.1315	9.4	0.3	-	-
UWS-3-1	87.5	37.2	0.15	0.44	0.08	0.0383	0.0049	0.0088	0.0011	0.0017	0.00004	0.1701	10.8	0.2	-	-
UWS-4-1	141.1	65.3	0.23	0.47	0.12	0.0462	0.0032	0.0101	0.0008	0.0016	0.00004	0.3815	10.2	0.3	-	-
UWS-6-1	97.8	71.2	0.17	0.75	0.06	0.0441	0.0040	0.0099	0.0009	0.0016	0.00003	0.2315	10.5	0.2	-	-
UWS-7-1	76.0	36.5	0.12	0.49	0.09	0.0501	0.0095	0.0107	0.0021	0.0015	0.00006	0.2065	9.9	0.4	-	-
UWS-8-1	198.6	90.8	0.33	0.47	0.24	0.0430	0.0053	0.0094	0.0012	0.0016	0.00005	0.2278	10.2	0.3	-	-
UWS-9-1	93.1	65.0	0.16	0.72	0.12	0.0366	0.0047	0.0081	0.0011	0.0016	0.00005	0.2531	10.3	0.3	-	-
UWS-10-1	176.3	172.0	0.29	1.00	0.25	0.0345	0.0025	0.0068	0.0005	0.0014	0.00002	0.1929	9.3	0.1	-	-
UWS-11-1	96.3	59.9	0.15	0.64	0.14	0.0532	0.0077	0.0114	0.0017	0.0016	0.00006	0.2688	10.0	0.4	-	-
UWS-12-1	168.9	97.4	0.30	0.59	0.19	0.0358	0.0037	0.0083	0.0009	0.0017	0.00004	0.2138	10.8	0.2	-	-
UWS-13-1	108.5	53.4	0.18	0.50	0.13	0.0403	0.0037	0.0093	0.0009	0.0017	0.00005	0.3026	10.8	0.3	-	-
UWS-15-1	643.0	678.3	1.19	1.08	0.15	0.0432	0.0015	0.0093	0.0003	0.0016	0.00002	0.3715	10.0	0.1	-	-
UWS-16-1	1313.7	1067.2	2.47	0.83	2.23	0.0410	0.0030	0.0094	0.0007	0.0017	0.00002	0.1592	10.7	0.1	-	-
UWS-16-2	113.8	62.4	0.18	0.56	0.09	0.0376	0.0026	0.0082	0.0006	0.0016	0.00004	0.3664	10.1	0.3	-	-
UWS-17-1	95.0	44.4	0.15	0.48	0.15	0.0369	0.0049	0.0078	0.0011	0.0015	0.00004	0.2059	9.9	0.3	-	-
UWS-18-1	90.3	50.6	0.14	0.57	0.00	0.0462	0.0038	0.0102	0.0009	0.0016	0.00004	0.3093	10.3	0.3	-	-
UWS-19-1	722.9	534.6	1.32	0.76	0.98	0.0456	0.0046	0.0104	0.0011	0.0016	0.00003	0.1596	10.6	0.2	-	-
UWS-20-1	192.3	104.0	0.33	0.55	0.08	0.0462	0.0033	0.0109	0.0008	0.0017	0.00004	0.3109	11.0	0.3	-	-
UWS-14-1	347.2	27.8	21.25	0.08	1.01	0.0903	0.0008	0.7893	0.0393	0.0634	0.00310	0.9839	396	19	1432	17
UWS-14-2	458.1	62.8	25.90	0.14	1.17	0.0925	0.0007	0.7331	0.0506	0.0575	0.00394	0.9948	360	24	1478	13
UWS-21-1	188.7	66.3	44.31	0.36	0.04	0.0900	0.0008	2.8715	0.0464	0.2315	0.00318	0.8497	1342	17	1424	17
UWS-21-2	592.5	690.3	194.77	1.20	0.80	0.0931	0.0002	3.4097	0.0375	0.2657	0.00288	0.9853	1519	15	1489	3

Table C.15. Model parameters and results from the simple mixing calculations (Chapter 4).

Mixing componant	**Fe (ppm)**	**Mg (ppm)**	**Rb (ppm)**	**Sr (ppm)**	**Zr (ppm)**
Average CRB*	93601	31568	22	317	174
Evolved mafic liquid (L_2)[b]	56596	5468	101	215	868
Parental magmas					
Magpie Basin Member[a]	17018.8	405.1	232.7	30.7	470.5
Dry Gulch Member[a]	17803.9	670.5	195.4	53.8	483.7
Results from simple mixing calcultation between the Magpie Basin Member and L_2. Concentrations after 10, 30 and 50% mixing.					
10%	20977.4	910.8	219.5	49.1	510.2
30%	28894.6	1922.2	193.2	86.0	589.8
50%	36811.8	2933.7	166.8	122.9	669.4
Results from simple mixing calcultation between the Dry Gulch Member and L_2. Concentrations after 10, 30 and 50% mixing.					
10%	21684.0	1149.7	185.9	69.9	522.2
30%	29444.1	2108.0	167.1	102.1	599.1
50%	37204.3	3066.4	148.2	134.4	676.0

*Columbia River Basalts data from Hooper & Hawkesworth (1993), [a]Average composition, [b]Concentrations after 80% fractionation of average CRB (Table C.16).

Table C.16. Results of Raleigh fractional crystallisation of average Columbia River Basalt. Grey bar shows the composition of the more-evolved liquid L2 used in subsequent mixing calculations. Fractionating mineral assemblage assumed to be Olivine (50%), Clinopyroxene (25%), and Plagioclase (25%).

% Crystallised	**Mg (ppm)**	**Fe (ppm)**	**Rb (ppm)**	**Sr (ppm)**	**Zr (ppm)**
80	5468	56596	101	215	868
60	11640	70284	52	254	435
40	18108	79778	35	281	290
20	24777	87282	27	301	218
0	31568	93601	22	317	174
Kd_{values}*					
Olivine	*6.600*	*1.850*	*0.010*	*0.010*	*0.003*
Plagioclase	*0.030*	*0.200*	*0.071*	*2.450*	*0.003*
Clinopyroxene	*1.700*	*3.000*	*0.031*	*0.060*	*0.001*

*Kd_{values} taken from compilation given at http://earthref.org/KDD/ and references therein

References

Allen, S.R., McPhie, J. (2003). Phenocryst fragments in rhyolitic lavas and lava domes. *J. Volcanol. Geotherm. Res.* 126:263–283.

Ambrose, S.H. (1998). Late Pleistocene human population bottlenecks, volcanic winter, and differentiation of modern humans. *J. Human Evol.* 34:623–651.

Anderson, A.L. (1931). Geology and mineral resources of eastern Cassia County, Idaho. *Idaho Bureau of Mines and Geology Bull.* 14:66p.

Andrews, G.D.M., Branney, M.J. (2005). Folds, fabrics, and kinematic criteria in rheomorphic ignimbrites of the Snake River Plain, Idaho: Insights into emplacement and flow. In: Pederson, J., and Dehler, C.M. (eds). Interior Western United States: *Geol Soc Am Field Guide 6*, pp 18.

Andrews, G.D.M., Branney, M.J., Bonnichsen, B., McCurry, M. (2008). Rhyolitic ignimbrites in the Rogerson Graben, southern Snake River Plain volcanic province: volcanic stratigraphy, eruption history and basin evolution. *Bull. Volcanol.* 70:269–291.

Andrews, G.D.M., Branney, M.J. (2011). Emplacement and rheomorphic deformation of a large, lava-like rhyolitic ignimbrite: Grey's Landing, southern Idaho. *Geol. Soc. Am. Bull.* 123:725–743.

Armstrong, R.L., Leeman, W.P., Malde, H.E. (1975). K-Ar dating, Quaternary and Neogene volcanic rocks of Snake River Plain, Idaho. *Amer. J. Sci.* 275:225–251.

Bachmann, O., Bergantz, G. (2008). The Magma Reservoirs that feed Super-eruptions. *Elements* 4:17–21.

Bailey, R.A. (1976). Volcanism, structure, and geochronology of Long Valley caldera, Mono County, California. *J. Geophys. Res.* 81:725–744.

Barry, T.L., Kelley, S.P., Reidel, S.P., Camp, V.E., Self, S., Jarboe, N.A., Renne, P.R. (2013). Eruption chronology of the Columbia River Basalt Group. *Geol. Soc. Amer. Spec. Pap.* 497: 45–66.

Best, M.G., Christiansen, E.H., Gromme, S. (2013). Introduction: The 36–18 Ma southern Great Basin, USA, ignimbrite province and flareup: Swarms of subduction-related supervolcanoes. *Geosphere* 9: 260–274.

Bonnichsen, B. (1982a). "Rhyolite lava flows in the Bruneau-Jarbidge eruptive center, southwestern Idaho." *Cenozoic geology of Idaho. Idaho Bur Mines Geol Bull* 26:283–320.

Bonnichsen, B. (1982b). The Bruneau-Jarbidge Eruptive Center, southwestern Idaho. In: Bonnichsen, B., Breckinridge, R.M. (eds). Cenozoic Geology of Idaho. *Idaho Bur. Min. Geol. Bull.* 26:237–254.

Bonnichsen, B., Citron, G.P. (1982). The Cougar Point Tuff, southwestern Idaho. In: Bonnichsen, B., Breckenridge, R.M. (eds). Cenozoic geology of Idaho. *Idaho Bur. Mines Geol. Bull.* 26:255–281.

Bonnichsen, B., Christiansen, R.L., Morgan, L.A., Moye, F.J., Hackett, W.R., Leeman, W.P., Honjo, N., Jenks, M.D., Godchaux, M.M. (1989). Excursion 4A: Silicic volcanic rocks in the Snake River Plain-Yellowstone Plateau province. In: Chapin, C.E., Zidek, J. (eds). Field excursions to volcanic terranes in the western United States; Volume II, Cascades and Intermountain West. *NM Bur. Mines. Mineral. Resourc. Mem.* 47:135–182.

Bonnichsen, B. (2000). on BBC *'Horizon'*.

Bonnichsen B, Godchaux MM (2002) Late Miocene, Pliocene, and Pleistocene geology of southwestern Idaho with emphasis on basalts in the Bruneau–Jarbidge, Twin Falls, and western Snake River Plain regions. In: Bonnichsen, B. et al. (eds). Tectonic and magmatic evolution of the Snake River Plain volcanic province. *Idaho Geol. Surv. Bull.* 30:233–312.

Bonnichsen, B., Leeman, W.P., Honjo, N., McIntosh, W.C., Godchaux, M.M. (2008). Miocene silicic volcanism in southwestern Idaho: geochronology, geochemistry, and evolution of the central Snake River Plain. *Bull. Volcanol.* 70:315–342.

Boroughs, S., Wolff, J., Bonnichsen, B., Godchaux, M., Larson, P. (2005). Large-volume, low-$\delta^{18}O$ rhyolites of the central Snake River Plain, Idaho, USA. *Geology* 33:821–824.

Boroughs, S., Wolff, J.A., Bonnichsen, B., Ellis, B.S., Larson, P. (2012). Evaluating models of the origin of Miocene low –$\delta^{18}O$ rhyolites of the Yellowstone/Columbia River large igneous province. Earth Plan. Sci. Lett. 313–314:45–55.

Branney, M.J., Kokelaar, B.P. (1992). A reappraisal of ignimbrite emplacement: progressive aggradation and changes from particulate to non-particulate flow during emplacement of high-grade ignimbrite. *Bull. Volcanol.* 54(6):504–520.

Branney, M.J., Kokelaar, B.P., McConnell, B.J. (1992). The Bad Step Tuff: a lava-like ignimbrite in a calc-alkaline piecemeal caldera, English Lake District. *Bull. Volcanol.* 54:187–199.

Branney, M.J., Kokelaar, P. (1994). Volcanotectonic faulting, soft-state deformation, and rheomorphism of tuffs during development of a piecemeal caldera, English Lake District. *Geol. Soc. Amer. Bull.* 106:507–530.

Branney, M.J., Kokelaar, P. (2002). Pyroclastic density currents and the sedimentation of ignimbrites. *Geol. Soc. Lond. Mem.* 27:1–143.

Branney, M.J., Bonnichsen, B., Andrews, G.D.M., Ellis, B., Barry, T.L., McCurry, M. (2008). 'Snake River (SR) -type' volcanism at the Yellowstone hotspot track: distinctive products from unusual, high-temperature silicic super-eruptions. *Bull. Volcanol.* 70:293–314.

Brown, D.J., Bell, B.R. (2013). The emplacement of a large, chemically zoned, rheomorphic, lava-like ignimbrite: the Sgurr of Eigg Pitchstone, NW Scotland. *Journal of the Geological Society*, 170 (5): 753-767.

Brown, R.J., Branney, M.J. (2013). Internal flow variations and diachronous sedimentation within extensive, sustained, density-stratified pyroclastic density currents flowing down gentle slopes, as revealed by the internal architectures of ignimbrites on Tenerife. *Bull. Volcanol.* 75(7):1–24.

Brueseke, M.E., Hart, W.K., Shoemaker, K.A. (2004). Re-evaluating the "Owyhee – Humboldt" eruptive centre: relationships between voluminous middle Miocene silicic volcanism and the Owyhee plateau. *Geol. Soc. Am. Abs.* w/Prog 36:97.

Brueseke, M.E., Hart, W.K., Heizler, M.T. (2008). Diverse mid-Miocene silicic volcanism associated with the Yellowstone–Newberry thermal anomaly. *Bull. Volcanol.* 70:343–360.

Brueseke, M.E., Hart, W.K. (2009). Intermediate composition magma production in an intracontinental setting: unusual andesites and dacites of the mid-Miocene Santa Rosa–Calico volcanic field, northern Nevada. *J. Volcanol. Geotherm. Res.* 188:197–213.

Bryan, S.E., Riley, T.R., Jerram, D.A., Stephens, C.J., Leat, P.T. (2002). Silicic volcanism: An undervalued component of large igneous provinces and volcanic rifted margins. In: Menzies, M.A et al. (eds). Volcanic Rifted Margins: Boulder, Colorado. *Geol. Soc. Am. Spec. Pap*. 362: 99–120.

Camp, V.E., Ross, M.E., Hanson, W.E. (2003). Genesis of flood basalts and Basin and Range volcanic rocks from Steens Mountain to Malheur River Gorge, Oregon. *Geol. Soc. Am. Bull.* 115:105-128.

Carrasco-Núñez, G., Branney, M.J. (2005). "Progressive assembly of a massive layer of ignimbrite with a normal-to-reverse compositional zoning: the Zaragoza ignimbrite of central Mexico." *Bull. Volcanol.* 68(1):3-20.

Cas, R.A.F., Wright, J.V. (1987). Volcanic successions: modern and ancient. Alan & Unwin, London, pp. 1–528.

Cathey, H.E., Nash, B.P .(2004). The Cougar Point Tuff: Implications for thermochemical zonation and longevity of high-temperature, large-volume silicic magmas of the Miocene Yellowstone hotspot. *J. Petrol.* 45:27–58.

Chetel, L.M., Janecke, S.U., Carroll, A.R., Beard, B.L., Johnson, C.M., Singer, B.S. (2011). Paleogeographic reconstruction of the Eocene Idaho River, North American Cordillera. *Geol. Soc. Amer. Bull.* 123:71–88.

Chesner, C.A. (2012). The Toba caldera complex. *Quaternary International* 258:5–18.

Christiansen, R.L. (2001). The Quaternary and Pliocene Yellowstone Plateau volcanic field of Wyoming, Idaho and Montana. *US Geol. Surv. Prof. Pap.* 729-G.

Christiansen, E.H. (2005). "Contrasting processes in silicic magma chambers: evidence from very large volume ignimbrites." *Geological Magazine* 142:669–681.

Christiansen, E.H., McCurry, M. (2008). Contrasting origins of Cenozoic silicic volcanic rocks from the western Cordillera of the United States. *Bull. Volcanol.* 70:251–267.

Coble, M.A., Mahood, G.A. (2012). Initial impingement of the Yellowstone plume located by widespread silicic volcanism contemporaneous with Columbia River flood basalts. *Geology* 40:655–658.

Decker, R.W. (1990). How often does a Minoan eruption occur? In: Hardy, D.A et al. (eds). *Thera and the Aegean World III,* pp 444–452.

De Silva, S.L., Francis, P.W. (1989). Correlation of large ignimbrites—two case studies from the Central Andes of Northern Chile. *J. Volcanol. Geotherm. Res.* 37(2):133–149.

Doherty, D.J., McBroome, L.A., Kuntz, M. (1979). Preliminary geological interpretation and lithologic log of the exploratory geothermal test well (INEL-1), Idaho National Engineering Laboratory. *U.S. Geol. Surv.* 9:79–1248.

Donoghue, E., Troll, V.R., Harris, C., O'Haloran, A., Walter, T.R., Perez Torrado, F.J. (2008). Low-temperature hydrothermal alteration of intra-caldera tuffs, Miocene Tejeda caldera, Gran Canaria, Canary Islands. *J. Volcanol. Geotherm. Res.* 176:551–564.

Drew, D.L., Bindeman, I.N., Watts, K.E., Schmitt, A.K., Fu, B., McCurry, M. (2013). Crustal-scale recycling in caldera complexes and rift zones along the Yellowstone hotspot track: O and Hf isotopic evidence in diverse zircons from voluminous rhyolites of the Picabo volcanic field, Idaho. *Earth and Plan. Sci. Lett.* 381:63-77.

Dueker, K., Stachnik, J., Yuan, H. Schutt, D. (2007). Image of Yellowstone magmatic history and lower crustal outflow. Abstracts with Programs, *Geol. Soc. Amer.* 39:202.

Eby, G.N. (1990). The A-type granitoids: a review of their occurrence and chemical characteristics and speculations on their petrogenesis. *Lithos* 26:115–134.

Ekren, E.B., McIntyre, D.H., Bennett, E.H. (1984). High-temperature, large volume, lava like ash-flow tuffs without calderas in southwestern Idaho. *US Geol. Surv. Prof. Pap.* 1272.

Ellis, B.S. (2009). Rhyolitic Explosive Eruptions of the Central Snake River Plain, Idaho – Investigations of the Lower Cassia Mountains Succession and surrounding areas. *Ph. D Thesis.* University of Leicester, U.K.

Ellis. B.S., Barry, T.L., Branney, M.J., Wolff, J.A., Bindeman, I., Wilson, R., Bonnichsen, B. (2010). Petrologic constraints on the development of a large-volume, high temperature, silicic magma system: the Twin Falls eruptive centre, central Snake River Plain. *Lithos* 120:475–489.

Ellis, B., Branney, M.J. (2010) Silicic phreatomagmatism in the Snake River Plain: the Deadeye Member. *Bull. Volcanol.* 72(10):1241–1257.

Ellis, B.S., Branney, M.J., Barry, T.L., Barfod, D., Bindeman, I., Wolff, J.A., Bonnichsen, B. (2012a). Geochemical correlation of three large-volume ignimbrites from the Yellowstone hotspot track, Idaho, USA. *Bull. Volcanol.* 74:261–277.

Ellis, B.S., Mark, D.F., Pritchard, C.J., Wolff, J.A. (2012b). Temporal dissection of the Huckleberry Ridge Tuff using the $^{40}Ar/^{39}Ar$ dating technique. *Quaternary Geochronology* 9:34-41.

Ellis, B.S., Wolff, J.A. (2012). Complex storage of rhyolite in the central Snake River Plain. *J. Volcanol. Geotherm. Res.* 211–212:1–11.

Ellis, B.S., Mark, D.F. (2013). 'Super-eruptions' and silicic volcanism from the Yellowstone volcanic field. *Geology Today* 29(4):133-137.

Ellis, B.S., Wolff, J.A., Boroughs, S., Mark, D.F., Starkel, W.A., Bonnichsen, B. (2013). Rhyolitic volcanism of the central Snake River Plain: a review. *Bull. Volcanol.* 75:745–764.

Elston, W.E., Seager, W.R., Clemons, R.E. (1975). Emory cauldron, Black Range, New Mexico, source of the Kneeling Nun Tuff. *Field Conf. Guide. N.M. Geol. Soc.* 26:283–292.

Engebretson, D.C., Cox, A., Gordon, R.G (1984). Relative motions between oceanic and continental plates in the Pacific basin. *Geol. Soc. Am. Spec. Pap.* 206:59 pp.

Ewart, A., Milner, S.C., Armstrong, R.A., Duncan, A.R. (1998). Etendeka volcanism of the Gobobseb Mountains and Messum Igneous Complex, Namibia, Parts I and II. *J. Petrol.* 39:191–253.

Ferguson, C.A., McIntosh, W.C., Miller, C.F. (2012). Silver Creek caldera - The tectonically dismembered source of the Peach Spring Tuff. *Geology.* 41:3–6.

Fisher, R.A. (1953). Dispersion on a sphere. *Royal Society of London Proceedings*. 217(A):295–305.

Fisher, R.V., Schminke, H.U. (1984). Pyroclastic rocks. New York, Springer-Verlag p.472.

Flexser, S. (1991). Hydrothermal alteration and past and present thermal regimes in the western moat of Long Valley caldera. *J. Volcanol. Geotherm. Res.* 48:303-318.

Geist, D., Richards, M (2013). Origin of the Columbia Plateau and Snake River plain: Deflection of the Yellowstone plume. *Geology* 21:789-792.

Green, J.C., Fitz, T.Z. (1993). Extensive felsic lavas and rheoignimbrites in the Keweenawan Midcontinent Rift plateau volcanics, Minnesota: petrographic and field recognition. *J. Volcanol. Geotherm. Res.* 54(3-4):177–196.

Hackett, W.R., Moye, F.J., Bonnichsen, B. (1989). Day 5 Silicic volcanism in the SRP-YP province. *New Mex. Bur. Mines Min. Res. Mem.* 47:160–167.

Hall, A. (1996). Igneous petrology. Longman, Harlow, p.551.

Harangi, S., Mason, P.R., Lukács, R. (2005). Correlation and petrogenesis of silicic pyroclastic rocks in the Northern Pannonian Basin, Eastern-Central Europe: In situ trace element data of glass shards and mineral chemical constraints. *J. Volcanol. Geotherm. Res.* 143(4):237–257.

Henry, C.D., Wolff, J.A. (1992). Distinguishing strongly rheomorphic tuffs from extensive silicic lavas. *Bull. Volcanol.* 54:171–186.

Hildebrand, R.T., Newman, K.R. (1985). Miocene sedimentation in the Goose Creek basin, south-central Idaho, northeastern Nevada and northwestern Utah. In: Flores, R.M. et al. (eds). Cenozoic paleogeography of the western U.S. Rocky Mountain Section. *Society of Economic Paleontologists and Mineralogists* p. 55–70.

Hildreth,W., Moorbath, S. (1988). Crustal contributions to arc magmatism in the Andes of Central Chile. *Contributions to Mineralogy and Petrology* 98(4):455–489.

Hildreth, W.E.S., Halliday, A.N., Christiansen, R.L. (1991). Isotopic and chemical evidence concerning the genesis and contamination of basaltic and rhyolitic magma beneath the Yellowstone Plateau volcanic field. *J. Pet.* 32(1):63–138.

Hildreth, W., Mahood, J. (1985). "Correlation of ash-flow tuffs." *Geol. Soc. Amer. Bull*. 96(7): 968-974.

Hildreth, W., Wilson, C.J.N. (2007). "Compositional zoning of the Bishop Tuff." *J. Pet.* 48(5): 951-999.

Honjo, N., McElwee, K.R., Duncan, R.A., Leeman, W.P. (1986). K-Ar ages of volcanic rocks from the Magic Reservoir eruptive center, Snake River Plain, Idaho. *Isochron/West* 46:15–17.

Honjo, N., Bonnichsen, B., Leeman, W.P., Stormer Jr, J.C. (1992). High temperature rhyolites from the central and western Snake River Plain. *Bull. Volcanol.* 54:220–237.

Hooper, P.R., Hawkesworth, C.J. (1993). Isotopic and geochemical constraints on the origin and evolution of the Columbia River Basalt. *J.Petrol.*34:1203–1246.

Hooper, P.R., Binger, G.B., Lees, K.R. (2002). Ages of the Steens and Columbia River basalts and their relationship to extension-related calc-alkaline volcanism in eastern Oregon. *Geol. Soc. Am. Bull.* 114:43-50.

Houghton, B.F., Wilson, C.J.N., Pyle, D.M. (2000) Pyroclastic fall deposits. *Encyclopedia of Volcanoes. Academic Press, New York*. pp 555-570.

Jackson, S.E., Pearson, N.J., Griffin, W.L., Belousova, E.A. (2004). The application of laser ablation-inductively coupled plasma-mass spectrometry to in situ U–Pb zircon geochronology. *Chemical Geology* 211:47–69.

James, D.E., Fouch, M.J., Carlson, R.W., Roth, J.B. (2011). Slab fragmentation, edge flow and the origin of the Yellowstone hotspot track. *Earth Plan. Sci. Lett.* 311:124–135.

Kauffman, J.D., Othberg, K.L., Garwood, D.L. (2010). Geologic map of the McHan Reservoir quadrangle, Camas and Gooding counties, Idaho. *Idaho Geological Survey Digital Web Map* 116, 1:24,000.

Kelly, N.M., Hinton, R.W., Harley, S.L., Appleby, S.K. (2008). New SIMS U–Pb zircon ages from the Langavat Belt, South Harris, NW Scotland: implications for the Lewisian Terrane mode. *J. Geol. Soc.* 165:967–981.

Kirschvink, J.L. (1980). The least-squares line and plane and the analysis of paleomagnetic data. *Geophysical Journal of the Royal Astronomical Society* 62:699–718.

Lanphere, M.A., Champion, D.E., Christiansen, R.L., Izett, G.A., Obradovich, J.D. (2002). Revised ages for tuffs of theYellowstone plateau volcanic field: assignment of the Huckleberry Ridge Tuff to a new geomagnetic polarity event. *Geol. Soc. Amer. Bull.* 114:559–568.

Lee, J.Y., Marti, K., Severinghaus, J.P., Kawamura, K., Yoo, H.S., Lee, J.B., Kim, J.S. (2006). A redetermination of the isotopic abundances of atmospheric Ar. *Geochimica et Cosmochimica Acta* 70:4507–4512.

Leeman, W.P., Annen, C., Dufek, J. (2008). Snake River Plain–Yellowstone silicic volcanism: implications for magma genesis and magma fluxes. *Geol. Soc. Lond. Spec. Publ.* 304:235–259.

Lindsay, J.M., de Silva, S., Trumbull, R., Emmermann, R., Wemmer, K. (2001). La Pacana caldera, N. Chile: a re-evaluation of the stratigraphy and volcanology of one of the world's largest resurgent calderas. *J. Volcanol. Geotherm. Res.* 106:145–173.

Lipman, P.W. (1984). The roots of ash-flow calderas in North America: windows into the tops of granitic batholiths. *J. Geophys. Res.* 89:8801–8841.

Lipman, P.W. (1997). Subsidence of ash-flow calderas: relation to caldera size and magma chamber geometry. *Bull. Volcanol.* 59:198–218.

Long, M.D., Till, C.B., Druken, K.A., Carlson, R.W., Wagner, L.S., Fouch, M.J., James, D.E., Grove, T.L., Schmerr, N., Kincaid, C. (2012). Mantle dynamics beneath the Pacific Northwest and the generation of voluminous back-arc volcanism. *Geochem. Geophys. Geosyst.* 13:Q0AN01.

Lowe, D.J. (2011). Tephrochronology and its application: a review. *Quaternary Geochronology*, 6(2):107–153.

Malde, H.E., Powers, H.A. (1962) Upper Cenozoic stratigraphy of the western Snake River Plain, Idaho. *Geol. Soc. Am. Bull.* 73:1197–1210.

Manley, C.R., McIntosh, W.C. (2002). The Juniper Mountain Volcanic Center, Owyhee County, Southwestern Idaho: age relations and physical volcanology. In: Bonnichsen, B., White, C.M., McCurry, M. (eds). Tectonic and magmatic evolution of the Snake River Plain Volcanic Province. *Idaho Geol. Surv. Bull.* 30:205–227.

Mark, D.F., Barfod, D.N., Stuart, F.M., Imlach, J. (2009). The ARGUS multi-collector noble gas mass spectrometer: Performance for $^{40}Ar/^{39}Ar$ geochronology. *Geochemistry Geophysics Geosystems* 10:1–9.

Mark, D.F., Stuart, F.M., de Podesta, M. (2011). New high precision measurements for the isotopic composition of argon. *Geochimica et Cosmochimica Acta* 75:7494–7501.

Marti, J., Diez-Gil, J.L., Ortiz, R. (1991), Conduction model for the thermal influence of lithic clasts in mixtures of hot gases and ejecta. *J. Geophys. Res.* 96(B13):21879–21885.

Mason, B.G., Pyle, D.M., Oppenheimer, C. (2004). The size and frequency of the largest explosive eruptions on Earth. *Bull. Volcanol.* 66: 735–748.

McClay, K.R., Ellis, P.G. (1987). Geometries of extensional fault systems developed in model experiments. *Geology* 15:341–344.

McCurry, M., Watkins, A.M., Parker, J.L., Wright, K., Hughes, S.S. (1996). Preliminary volcanological constraints for sources of high-grade, rheomorphic ignimbrites of the Cassia Mountains,

Idaho: implications for the evolution of the Twin Falls Volcanic Center. *Northwest Geol.* 26:81-91.

McCurry, M., Hayden, K.P., Morse, L.H., Mertzman, S. (2008). Genesis of post-hotspot, A-type rhyolite of the Eastern Snake River Plain volcanic field by extreme fractional crystallization of olivine tholeiite. Bull. Volcanol. 70:361–383.

McCurry, M., Rodgers, D.W. (2009). Mass transfer along the Yellowstone hotspot track I: petrologic constraints on the volume of mantle-derived magma. *J. Volcanol. Geotherm. Res.*188:86–98.

Michalek, M. (2009) Geological Map of parts of the Lake Hills and Carey Quadrangles, Blaine County, Idaho. *M.S. Thesis,* Idaho State University, USA. 1:12,000.

Milner, S.C., Duncan, A.R.., Whittingham, A.M., Ewart, A. (1995). Trans-Atlantic correlation of eruptive sequences and individual silicic volcanic units within the Paraná-Etendeka igneous province. *J. Volcanol. Geotherm. Res.* 69:137–157.

Morgan, W.J. (1971). Convection plumes in the lower mantle. *Nature* 230:42–43.

Morgan, L.A., McIntosh, W.C. (2005). Timing and development of the Heise volcanic field, Snake River Plain, Idaho, western USA. *Geol. Soc. Am. Bull.* 117:288-306.

Morris, E.R., Schillinger, W., Coe, R.S., Pluhar, C.J., Jarboe, N.A. (2009). Automating the 2G superconducting rock magnetometer for single-solenoid alternating field demagnetization. *Geochem. Geophys. Geosys.* 10(5).

Mytton, J.W., Williams, P.L., Morgan, W.A. (1990). Geologic map of the Striker 4 Quadrangle, Cassia County, Idaho. *U.S. Geological Survey Miscellaneous Investigations Series Map* I-2052, 1:48,000.

Nash, B.P., Perkins, M.E., Christensen, J.N., Lee, D.C., Halliday, A.N. (2006). The Yellowstone hotspot in space and time: Nd and Hf isotopes in silicic magmas. *Earth Plan. Sci. Lett.* 247:143–156.

Neff, H., Dudgeon, J.V. (2006). LA-ICP-MS Analysis of Ceramics and Ceramic Raw Materials from the Gila River Indian Community, Arizona. *Research Report: Institute for Integrated Research in Materials, Environments, and Society,* California State University, USA.

Newhall, C.G., Self, S. (1982). The volcanic explosivity index (VEI) – an estimate of explosive magnitude for historical volcanism. *J. Geophys. Res.* 87: 1231–1238.

Oakley, W.L., Link, P.K. (2006). Geologic map of the Davis Mountain Quadrangle, Gooding and Camas Counties, Idaho. *Idaho Geological Survey.* 1:24,000. *Idaho Geol. Surv. Geologic Map 49*.

Ochs, F.A., Lange, R.A. (1999). "The density of hydrous magmatic liquids." *Science* 283: 1314–1317.

O'Hara, M.J., Mathews, R.E. (1981). Geochemical evolution of an advancing, periodically replenished, periodically tapped, continuously fractionated magma chamber. *J. Geol. Soc*. 138:237–277.

Ort, M.H., Silva, S.L., Jiménez, C., Jicha, B.R., Singer, B.S. (2013). Correlation of ignimbrites using characteristic remanent magnetization and anisotropy of magnetic susceptibility, Central Andes, Bolivia. *Geochem. Geophys. Geosys.* 14:141–157.

Othberg, K.L., Kauffman, J.D., Gillerman, V.S., Garwood, D.L. (2012). Geologic Map of the Twin Falls 30 x 60 Minute Quadrangle, Idaho. 1:100,000.

Pankhurst, R.J., Leat, P.T., Sruoga, P., Rapela, C.W., Márquez, M., Storey, B.C., Riley, T.R. (1998). The Chon Aike silicic igneous province of Patagonia and related rocks in Antarctica: A silicic large igneous province. *J. Volcanol. Geotherm. Res.* 81:113–136.

Pearce, J.A., Harris, N.B.W., Tindle, A.G. (1984). Trace Element Discrimination Diagrams for the Tectonic Interpretation of Granitic Rocks. *J. Petrology.* 25(4):956–983.

Peng, X.. Humphreys, E.D. (1998). Crustal velocity structure across the eastern Snake River Plain and the Yellowstone swell. *J. Geophy. Res.* 103:7171–7186.

Perkins, M.E., Nash, W.P., Brown, F.H., Fleck, R.J. (1995). Fallout tuffs of Trapper Creek Idaho - a record of Miocene explosive volcanism in the Snake River Plain volcanic province. *Geol. Soc. Am. Bull.* 107:1484–1506.

Perkins, M.E., Williams, S.K., Brown, F.H., Nash, W.P., McIntosh, W. (1998). Sequence, age, and source of silicic fallout tuffs in middle to late Miocene basins of the northern Basin and Range Province. *Geol. Soc. Am. Bull.* 110:344–360.

Perkins, M.E., Nash, B.P. (2002). Explosive silicic volcanism of the Yellowstone hotspot: the ash fall tuff record. *Geol. Soc. Amer. Bull.* 114:367–381.

Pierce, K.L., Morgan, L.A. (1992). The track of the Yellowstone hot spot: Volcanism, faulting, and uplift. In: Link, P. K. et al. (eds). Regional Geology of Eatern Idaho and Western Wyoming. *Geological Society of America Memoir* 179.

Pierce, K.L., Morgan, L.A., Saltus, R.W (2002). Yellowstone plume head: postulated tectonic relations to the Vancouver slab, continental boundaries, and climate. In: Bonnichsen, B et al. (eds). Tectonic and Magmatic Evolution of the Snake River Plain Volcanic Province. *Idaho Geol. Surv. Bull.* 30:5-33.

Pouchou, J.L., Pichoir, F. (1985). "PAP" procedure for improved quantitative analysis. *Microbeam. Anal* 20:104–105.

Putirka, K.D., Mikalelian, H., Ryerson, F., Shaw, H. (2003). New clinopyroxene-liquid thermobaromers for mafic, evolved, and volatile-bearing lava compositions, with applications to lavas from Tibet and the Snake River Plain, Idaho. *Am. Mineral* 88:1542–1554.

Pyle, D.M. (1995). Mass and energy budgets of explosive volcanic eruptions. *Geophys. Res. Lett.* 5:563-566.

Pyle, D.M. (2000). Sizes of volcanic eruptions. In: Sigurdsson, H et al. (eds). *Encyclopedia of volcanoes.* Academic Press, pp 263–269.

Quane, S.L., Russell, J.K. (2005). Ranking welding intensity in pyroclastic deposits. *Bull. Volcanol.* 67:129–143.

Rampino, M.R., Self, S. (1992). Volcanic winter and accelerated glaciation following the Toba super-eruption. *Nature* 359:50–52.

Rampino, M.R., Ambrose, S.H. (2000). Volcanic winter and the Garden of Eden: the Toba super-eruption and the Late Pleistocene human population crash. *Geol. Soc. Am. Spec. Pap.* 345:71–82.

Reidel, S.P., Camp, V.E., Tolan, T.L., Martin, B.S. (2013). The Columbia River flood basalt province: stratigraphy, areal extent, volume, and physical volcanology. In: Reidel, S.P., Camp, V.E., Ross, M.E., Wolff, J.A., Martin, B.S., Tolan, T.L., Wells, R.E. (eds). The Columbia River flood basalt province. *Geol. Soc. Amer. Spec. Pap.* 497:1–43.

Renne, P.R., Balco, G., Ludwig, K.R., Mundil, R., Min, K. (2011). Response to the comment by W.H. Schwarz et al. on "Joint determination of K-40 decay constants and Ar-40*/K-40 for the Fish Canyon sanidine standard, and improved accuracy for Ar-40/Ar-39 geochronology" by Renne et al. (2010). *Geochimica et Cosmochimica Acta* 75(17).

Riley, T.R., Leat, P.T. (1999). Large volume silicic volcanism along the proto-Pacific margin of Gondwana: Lithological and stratigraphical investigations from the Antarctic Peninsula: *Geological Magazine* 136:1–16.

Rivera, T. A., Storey, M., Zeeden, C., Hilgen, F. J., & Kuiper, K. (2011). A refined astronomically calibrated $^{40}Ar/^{39}Ar$ age for Fish Canyon sanidine. *Earth and Plan. Sci. Lett.* 311(3):420–426.

Robock, A. (2005). Cooling following large volcanic eruptions corrected for the effects of diffuse radiation on trees. Geophys. Res. Lett. 32:L06702.

Robock, A. (2013). The Latest on Volcanic Eruptions and Climate. *Eos Trans Amer. Geophys. Union* 94: 305–306.

Rose, W.I., Chesner, C.A. (1987). Dispersal of ash in the great Toba eruption, 75 ka. *Geology* 15:913–917.

Rudnick, R.L., Gao, S. (2003). Composition of the continental crust. *Treatise on Geochemistry.* doi:10.1016/B0-08-043751-6/03016-4.

Rytuba, J.J., McKee, E.H (1984). Peralkaline ash flow tuffs and calderas of the McDermitt volcanic field, southeast Oregon and north central Nevada. *J. Geophys. Res.* 89:8616-8628.

Salvador, A. (eds). (1994). International Stratigraphic Guide: A guide to stratigraphic classification, terminology, and procedure. International Union of Geological Sciences and the Geological Society of America, Boulder, Colorado.

Self, S. (2006). "The effects and consequences of very large explosive volcanic eruptions." *Philosophical Transactions of the Royal Society A: Mathematical, Physical and Engineering Sciences* 364: 2073–2097.

Self S (2010) A new look at the deposits and eruption sequence of the Otowi Member, Bandelier Tuff Formation, Jemez Mountains, New Mexico. *Geol. Soc. Am.* 42(5):5.

Shervais, J.W., Vetter, S.K., Hanan, B.B. (2006). Layered mafic sill complex beneath the eastern Snake River Plain: evidence from cyclic geochemical variations in basalt. *Geology* 34:365–368.

Shervais, J.W., Hanan, B.B. (2008). Lithospheric topography, tilted plumes, and the track of the Snake River–Yellowstone hot spot. *Tectonics* 27:TC5004.

Shervais, J.W., Schmitt, D.R., Nielson, D., Evans, J.P., Christiansen, E.H., Morgan, L., Shanks, W.C.P., Prokopenko, A.A., Lachmar, T., Liberty, L.M., Blackwell, D.D., Glen, J.M., Champion, D., Potter, K.E., Kessler, J.A. (2013). First Results from HOTSPOT: The Snake River Plain Scientific Drilling Project, Idaho, U.S.A. *Scientific Drilling* 52:36-45.

Smith, R.L. (1960) Zones and zonal variations in welded ash-flows. *US Geol. Surv. Prof. Pap.* 354-F: 149–158. In: *New Mex. Geol. Soc. Spec. Pub.* (1980) 9.

Smith, C.L. (1966). Geology of eastern Mount Bennett Hills, Camas, Gooding, and Lincoln counties, Idaho: *University of Idaho Ph.D. dissertation.* 129 pp.

Smith, A.D. (1992). Back-arc convection model for Columbia River basalt genesis. *Tectonophysics* 207:269–285.

Soler, M.M., Caffe, P.J., Coira, B.L., Onoe, A.T., Kay, S.M. (2007). Geology of the Vilama caldera: a new interpretation of a large-scale explosive event in the Central Andean plateau during the Upper Miocene. *J. Volcanol. Geotherm. Res.* 164:27–53.

Sparks, R.S.J., Self, S., Walker, G.P.L. (1973). Products of Ignimbrite Eruptions. *Geology* 1(3): 115–118.

Sparks, R.S.J., Wilson, L. (1976). A model for the formation of ignimbrite by gravitational collapse. *J. Geol. Soc. London* 132: 441–451.

Sparks, R.S.J., Walker, G.P.L. (1977). The significance of vitric-enriched air-fall ashes associated with crystal-enriched ignimbrites. *J. Volcanol. Geotherm. Res.* 2:329–341.

Sparks, R.S.J., Self, S. and working group. (2005). Super-eruptions: global effects and future threats. *Rep Geol Soc London Working Group 2nd ed*. Geol. Soc. London, pp 24.

Sparks, R.S.J., Folkes, C.B., Humphreys, M.C.S., Barfod, D.N., Clavero, J., Sunagua, M.C., McNutt, S.R., Pritchard, M.E. (2008). Uturuncu volcano, Bolivia: Volcanic unrest due to mid-crustal magma intrusion. Amer. J. Sci. 308(6):727–769.

Spera, F.J., Crisp, J.A. (1981). "Eruption volume, periodicity, and caldera area: relationships and inferences on development of compositional zonation in silicic magma chambers." *J. Volcanol. Geotherm.* Res. 11:169-187.

Stacey, J. S., Kramers, J.D. (1975). Approximation of terrestrial lead isotope evolution by a two-stage model. *Earth Plan. Sci. Lett.* 26:207–221.

Steven, T.A., Lipman, P.W. (1976). Calderas of the San Juan Volcanic Field, southwestern Colorado. *US Geol. Surv. Prof. Pap.* 958:1–35.

Streck, M.J., Grunder, A.L. (1995). "Crystallization and welding variations in a widespread ignimbrite sheet; the Rattlesnake Tuff, eastern Oregon, USA." *Bull. Volcanol.* 57(3): 151–169.

Sun, S.S., McDonough, W.F. (1995). "The composition of the Earth." *Chemical geology* 120(3):223–253.

Swanson, D.A., Wright, T.L., Hooper, P.R., Bentley, R.D. (1979). Revisions in stratigraphic nomenclature of the Columbia River Basalt Group. *US Geol. Surv. Bull.* 1457–G.

Swanson, E.R., Kempter, K.A., McDowell, F.W., McIntosh, W.C. (2006). Major ignimbrites and volcanic centers of the Copper Canyon area: a view into the core of Mexico's Sierra Madre Occidental. *Geosphere* 2:125–141.

Troll, V.R., Emeleus, C.H., Donaldson, C.H. (2000). Caldera formation in the Rum Central Igneous Complex, Scotland. *Bull. Volcanol.* 62:301-317.

Valley, J.W., Kinny, P.D., Schulze, D.J., Spicuzza, M.J. (1998). "Zircon megacrysts from kimberlite: oxygen isotope variability among mantle melts." *Contributions to Mineralogy and Petrology* 133:1–11.

Watts, K.E., Bindeman, I.N., Schmitt, A. (2011). Large-volume rhyolite genesis in caldera complexes of the Snake River Plain: insights from the Kilgore Tuff of the Heise volcanic field, Idaho, with comparison to Yellowstone and Bruneau–Jarbidge rhyolites. *J. Petrol.* 52:857–890.

Whalen, J. B., Currie, K.L., Chappel, B.W. (1987). A-type granites: geochemical characteristics, discrimination and petrogenesis. *Contributions to Mineralogy and Petrology* 95: 407–419.

Whitaker, M.L., Nekvasil, H., Lindsley, D.H., McCurry, M. (2007). "Can crystallization of olivine tholeiite give rise to potassic rhyolites? - an experimental investigation." *Bull. Volcanol.* 70: 417-434.

Willcock, M.A.W., Cas, R.A.F., Giordano, G., Morelli, C. (2013). The eruption, pyroclastic flow behaviour, and caldera in-filling processes of the extremely large volume (> 1290 km^3), intra-to extra-caldera, Permian Ora (Ignimbrite) Formation, Southern Alps, Italy. *J Volcanol. Geotherm. Res.* 265: 102-126.

Williams, H. (1942). The geology of Crater Lake National Park, Oregon, with reconnaissance of the Cascade range southward to Mt Shasta. *Carnegie Inst.* Washington Pub 540, pp 162.

Williams, P.L., Mytton, J.W., Covington, H.R. (1990) Geologic map of the Striker 1 Quadrangle, Cassia, Twin Falls, and Jerome Counties, Idaho. *U.S. Geological Survey Miscellaneous Investigations Series Map* I-2078, 1:48,000.

Williams, P.L., Covington, H.R., Mytton, J.W. (1991) Geologic map of the Striker 2 Quadrangle, Twin Falls, and Cassia Counties, Idaho. *U.S. Geological Survey Miscellaneous Investigations Series Map* I-2078, 1:48,000.

Williams, P.L., Mytton, J.W., Morgan, W.A. (1999) Geologic map of the Striker 3 Quadrangle, Idaho and Nevada. *U.S. Geological Survey Miscellaneous Investigations Series Map* I-2633, 1:48,000.

Wilson, C.J.N., Houghton, B.F., McWilliams, M.O., Lanphere, M.A., Weaver, S.D., Briggs, R.M. (1995). Volcanic and structural evolution of Taupo Volcanic Zone, New Zealand: a review. *J. Volcanol. Geotherm. Res.* 68:1–28.

Wilson, C.J.N. (2001). The 26.5 ka Oruanui eruption, New Zealand: an introduction and overview. *J. Volcanol. Geotherm. Res.* 112:133–174.

Wilson, C.J.N., Hildreth, W. (2003) Assembling an ignimbrite: mechanical and thermal building blocks in the Bishop Tuff, California. *J. Geol.* 111:653–670.

Wright, K.E., McCurry, M., Hughes, S.S. (2002). Petrology and geochemistry of the Miocene tuff of McMullen Creek, central Snake River Plain. In: Bonnichsen, B., McCurry, M., White, C.M. (eds). Tectonic and magmatic evolution of the Snake River Plain volcanic province. *Idaho Geol. Surv. Bull.* 30:177–194.

Wood, S.H., Clemens, D.M. (2002). Geologic and tectonic history of the western Snake River Plain, Idaho and Oregon. In: Bonnichsen, B. et al. (eds). Tectonic and Magmatic Evolution of the Snake River Plain Volcanic Province. *Idaho Geol. Surv. Bull.* 30:69-103.

Worl, R.G., Kiilsgaard, T.H., Bennett, E.H., Link, P.K., Lewis, R.S., Mitchell, V.E., Johnson, K.M., Snyder, L.D. (1991). Geologic map of the Hailey 1 x 2 Quadrangle, Idaho. *US Geological Survey.* 1:250,000.

Youngquist, W., Haegele, J.R. (1956) Geological reconnaissance of the Cassia Mountains region, Twin Falls and Cassia Counties, Idaho. *Idaho Bureau of Mines and Geology pamphlet* 110: pp18.